Frittage de pièces de Polytétrafluoroéthylène (PTFE) compacté : Mécanismes physiques et modèles

Gabriel Guenoun

université PARIS-SACLAY

NNT : 2019SACLN054

Thèse de doctorat

école normale supérieure paris–saclay

PTFE compact sintering: Physical mechanisms and models

Thèse de doctorat de l'Université Paris–Saclay
préparée à l'Ecole Normale Supérieure Paris–Saclay

École doctorale n°579 : Sciences Mécaniques et Energétiques, Matériaux et Géosciences (SMEMAG)
Spécialité de doctorat : Solides, Structures et Matériaux

Thèse présentée à Cachan, le 27 novembre 2019, par

M. Gabriel Guenoun

Composition du Jury :

M. Olivier Lame Professeur, Mateis, INSA de Lyon	Rapporteur
M. Yann Marco Maître de conférences (HDR), IRDL, ENSTA Bretagne	Rapporteur
Mme Sandra Domenek Maître de conférences (HDR), GENIAL, AgroParisTech	Examinateur
M. Lucien Laiarinandrasana Professeur, Centre des Matériaux, Mines ParisTech	Président du jury
M. Jean-Yvon Faou Ingénieur R & D, Saint-Gobain Research Paris	Invité
M. Stéphane Roux Directeur de Recherche CNRS, LMT, ENS Paris-Saclay	Invité
M. Gilles Régnier Professeur, PIMM, Arts et Métiers ParisTech	Co-directeur de thèse
M. Nicolas Schmitt Professeur, LMT, UPEC	Directeur de thèse

université PARIS-SACLAY
ÉCOLE DOCTORALE
Sciences mécaniques et énergétiques, matériaux et géosciences (SMEMAG)

Titre : Frittage de pièces de Polytétrafluoroéthylène (PTFE) compacté : Mécanismes physiques et modèles

Mots clés : Science des polymères, Thermomécanique, Procédé, Modélisation, Cristallisation

Résumé : Le polytétrafluoroéthylène (PTFE) est un polymère semi-cristallin ayant de nombreuses propriétés remarquables avec notamment une excellente tenue thermique, un coefficient de frottement extrêmement faible et une grande résistance à la corrosion. Ces atouts lui valent d'être utilisé dans de nombreuses applications.

Sa mise en forme s'effectue par des procédés similaires à ceux utilisés pour les poudres métalliques. Dans l'un d'eux, la poudre de PTFE est compactée uniaxialement en pièces cylindriques. L'étape suivante est le frittage de la poudre compactée, au cours de laquelle les pièces sont chauffées au-delà de la température de fusion du polymère. Durant ce cycle thermique, les pièces subissent de grandes déformations causées notamment par la fusion et la recristallisation du PTFE. Les gradients thermiques couplés à ces déformations peuvent engendrer des incompatibilités mécaniques pouvant conduire à l'endommagement, voire à la rupture des pièces.

Cette thèse a permis d'apporter une compréhension plus fine des phénomènes physiques à l'œuvre durant le frittage du PTFE compacté par des observations et analyses microstructurales, et des essais de caractérisation thermique et mécanique. La relaxation de contraintes résiduelles, la fermeture de porosités et un phénomène de cristallisation secondaire ont ainsi été mis en évidence et génèrent des déformations libres de contraintes macroscopiques. Les propriétés mécaniques du matériau en température ont également été déterminées lors du frittage. Un modèle a été développé pour rendre compte de ces observations. Il a été intégré dans une simulation thermomécanique du procédé de frittage d'une pièce de référence. Le modèle a été validé par comparaison des résultats de la simulation à des mesures réalisées sur des expériences de laboratoire.

Enfin, un outil de simulation numérique par éléments finis a été développé. Il permet de déterminer les états de contrainte et déformation ainsi que la répartition des taux de cristallisation et des propriétés thermomécaniques au sein d'une pièce de PTFE compacté durant le cycle de frittage. A terme, cet outil pourrait permettre d'optimiser les paramètres du procédé industriel pour, par exemple, réduire le temps de frittage tout en s'assurant d'avoir des pièces non-endommagées et possédant les propriétés requises.

Université Paris–Saclay
Espace Technologique / Immeuble Discovery
Route de l'Orme aux Merisiers RD 128 / 91190 Saint-Aubin, France

université PARIS-SACLAY

ÉCOLE DOCTORALE
Sciences mécaniques et énergétiques, matériaux et géosciences (SMEMAG)

Title: PTFE compacts sintering: Physical mechanisms and models

Keywords: Polymer science, Thermomechanics, Process, Modeling, Crystallization

Abstract: Polytetrafluoroethylene (PTFE) is a semi-crystalline polymer with many outstanding properties including excellent thermal resistance, extremely low friction coefficient and high corrosion resistance. These advantages make it suitable for many applications.

It is shaped by processes similar to those used for metal powders. In one of them, the PTFE powder is uniaxially compacted into cylindrical parts. The next step is the compacted powder sintering process, in which the parts are heated above the melting temperature of the polymer. During this thermal cycle, the parts undergo large strains caused by the melting and the recrystallization of PTFE. Thermal gradients coupled with these strains induce mechanical incompatibilities that can lead to damage or even failure of the parts.

This study provides a more detailed understanding of the physical mechanisms at work during the sintering of compacted PTFE through microstructural observations and analyses, and thermal and mechanical characterization tests. The relaxation of residual stresses, the closure of porosity and a secondary crystallization mechanism have thus been highlighted and generate macroscopic stress-free strain (called *eigenstrain*). The mechanical properties of the material as function of temperature have been also determined during sintering. A model has been developed to take into account these observations. It has been integrated into a thermomechanical simulation of the sintering process of a reference part. The model has been validated by comparing the simulation results with measurements from a laboratory experiments.

Finally, a finite element numerical simulation tool has been developed. It is used to determine the stresses and strains as well as the distribution of crystallization rates and thermomechanical properties within a PTFE part compacted during the sintering cycle. In the long term, this tool could make it possible to optimize the industrial process parameters to reduce sintering time, for example, while ensuring that the parts are undamaged and have the required properties.

Université Paris–Saclay
Espace Technologique / Immeuble Discovery
Route de l'Orme aux Merisiers RD 128 / 91190 Saint-Aubin, France

Contents

Acknowledgments

Cette thèse aura été pour moi une expérience incroyable durant laquelle j'ai eu l'occasion de rencontrer, de côtoyer et de travailler avec des personnes fantastiques. Je tiens à les remercier très largement.

Merci aux membres de mon jury d'avoir accepté de prendre part à ma soutenance de thèse, et en particulier aux rapporteurs Yann Marco et Olivier Lame d'avoir lu si attentivement mon manuscrit. Merci Sandra Domenek pour ces échanges très intéressants et Lucien Laiarinandrasana d'avoir accepter de présider ce jury.

Nicolas, Gilles et Stéphane, je tiens à vous remercier tous les trois pour votre investissement, pour vos idées formidables et pour ces fameuses réunions toujours très fructueuses. Vous êtes mon trio de directeurs de thèse et j'en suis fier.

Je souhaite remercier Carole et Xavier pour m'avoir fait confiance dès le début en me confiant cette thèse. Merci ensuite à Jean-Yvon de m'avoir si bien encadré à Saint-Gobain, d'avoir pris autant à coeur le sujet et d'avoir fait le lien entre académique et industriel. A Saint Gobain Recherche, j'ai eu l'opportunité de travailler avec certaines personnes que je remercie : Carole, Rémi, Nicolas, Guillaume. Merci aussi à toute l'équipe TMM de m'avoir si bien accueilli. Ce projet n'aurait jamais pu avoir lieu sans l'investissement de certaines personnes chez Saint-Gobain à Willich. Merci Georges, Ansgar, Monika, Lina, André et toute l'équipe qui a toujours été très disponible et surtout à l'écoute pendant trois ans.

Un grand merci aux collègues de mes deux laboratoires ! Merci à tous les amis du LMT et surtout à mes camarades de bureau Myriam, Xuyang, Guillaume, Bhimal, Yanjun ... Merci Rémy, Boubou, Xavier, Marc pour votre aide avec toutes mes expériences. Merci aux amis du PIMM, notamment à mes camarades de bureau et à mes partenaires de foot. Lorsqu'il n'y avait pas d'expérience ou de rendez-vous prévu, c'était toujours difficile de choisir dans quel laboratoire se rendre ! Merci Gaëlle et Vincent pour votre aide sur la DSC et la DRX.

Je remercie aussi toutes les personnes qui m'ont aidé directement sur les expériences. Notamment pour les expériences à l'ESRF, merci à Nathalie, Nils, Isabelle, Sylvie et Sébastien. Pour la compaction isostatique de PTFE, merci Noël et Azziz du LPTMS à Villetaneuse. Merci Matheus, Caiuã et Achraf pour vos stages. Merci Rodrigo pour ces quelques discussions sur le PTFE depuis le Brésil. Merci Nicolas pour ces découpes jet d'eau sur le PTFE compacté.

Enfin, je remercie du fond du coeur mes parents, ma famille et mes amis. J'ai la chance d'être extrêmement entouré et c'est pour moi une grande source de bonheur et de motivation. Merci !

Domitille, merci pour ton soutien démesuré, ta joie de vivre et tant d'autres choses. Ce travail n'aurait pas été le même sans toi.

Introduction

Polytetrafluoroethylene (PTFE) is a semi-crystalline polymer used in numerous applications in our everyday life. Due to its (extraordinary) specific physico-chemical properties, this polymer is manufactured differently from the other thermoplastics. One of these processes consists in pressing as-polymerized PTFE powder into cylindrical preforms called billets. Pressed PTFE is also reffered to as green PTFE. The billets are later heated above PTFE melting temperature to obtain a "homogeneous" part by erasing interfaces between compacted powder grains. This process stage is called sintering. Sintered PTFE or melt-crystallized PTFE is therefore machined according to its applications.

This work focuses on the sintering of green PTFE and investigates the different mechanisms of deformation that take place. Models are developed for each mechanism in order to be able to simulate the thermomechanical behavior during sintering stage and to determine how to improve the process parameters.

In this introduction, a presentation of PTFE is made in section 1 with its discovery, its principal applications and its synthesis processes. The different manufacturing processes are detailed in section 2. A focus is made on PTFE sintering and the main challenges that it brings. Finally, the structure of the manuscript is presented in section 3.

1 Polytetrafluoroethylene

1.1 Discovery

Polytetrafluoroethylene (PTFE) was discovered by chance by Dr. Roy Plunkett of DuPont Company in 1938 [1]. While seeking for a new fluorinated refrigerant, he realized that the cylinder of tetrafluoroethylene (TFE) he was using had no more pressure in it. When he sawed the cylinder in half to check what was left in it, he found PTFE powder (Figure 1). The discovery of PTFE is a famous example of serendipity.

After several analyses of the white powder, he discovered that it corresponded to PTFE, the linear polymer obtained from TFE. It was then found that PTFE was very slippery, had no flow and was almost chemically inert. Processing methods were designed for PTFE based on metal powder processing. Those methods are still used nowadays, as evidenced by this work which deals with PTFE sintering for industrial applications.

PTFE was then used for the Manhattan project as a corrosion-resistant material to contain Uranium hexafluoride. For those reason, the US government kept the PTFE secret during World War II.

In 1947, DuPont started the commercial production of Teflon® (trademark for PTFE).

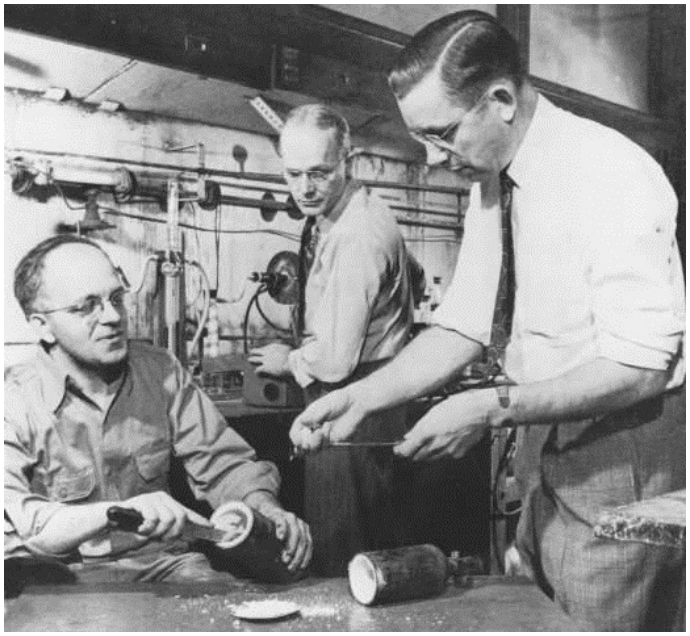

Figure 1: Discovery of PTFE by Dr. Plunkett (on the left) after sawing of the TFE cylinder. Image from the Hagley Museum and Library.

1.2 Properties

PTFE possesses numerous valuable properties. Those are mainly related to the atomic structure of fluorine and of the carbon chains.

Those properties are:

- High melting point [1]
- High thermal stability [1]
- Good mechanical properties at extreme temperatures (low and high)
- Chemical inertness [2, 3]
- Insolubility [3]
- Low coefficient of friction [4]
- Resistance to corrosion [2]
- Hydrophobicity [5]
- Flame resistance [6]
- Good weatherability [1]
- Low dielectric constant / good electrical insulator [1]
- Purity [1]

1.3 Applications

Plenty of industrial application were designed taking advantage of the properties of PTFE [1]. Among them are:

- Bearing (constrains relative movement and reduces the friction between moving parts) shown in Figure 2a
- Seals
- Thread seal tapes shown in Figure 2b

- Dry lubricants
- Outdoor application (ex: Gore-Tex®) shown in Figure 2c
- Food container (non stick)
- Coating (against corrosion) shown in Figure 2d
- Paints and inks
- Wire insulation

(a) (b)

(c) (d)

Figure 2: Different applications of PTFE: Saint-Gobain Norglide® bearings taken from *bearings.saint-gobain.com* (a), a PTFE thread seal tape taken from *rmmcia.fr* (b), a Gore-Tex jacket taken from *gore-tex.fr* (c) and a frying pan with a PTFE coating taken from *tefal.fr* (d).

1.4 Synthesis

Two commercial polymerization processes of TFE are commonly used: *suspension* polymerization and *emulsion* (or *dispersion*) polymerization.

In the case of *suspension*, TFE is polymerized in water with very small amount of dispersant under vigorous agitation. The dispersant is quickly consumed leading to the

PTFE to precipitate.

Granular resins (*fine cut* and *pelletized*) are derived from *suspension*. *Fine cut* resin is usually obtained by milling the raw suspension to obtain particles of size between 20 to 100 µm. This resin has an apparent density below 0.5 g/cm^3. *Pelletized* resin is produced by agglomeration of *fine cut* powder. Therefore, its particle size is usually around 500 µm and has an apparent density above 0.5 g/cm^3. Due to their different flowability, *fine cut* resin is also called *low flow* resin and *pelletized* resin is called *free flow* resin.

In the case of *emulsion*, TFE is polymerized in water with mild agitation and large quantities of dispersant.

PTFE *dispersion* is obtained by concentrating the generated emulsion solution and is used for coatings. *Fine powder* is produced by coagulation, then separation and finally drying of the colloidal particles of the emulsion solution. *Fine powder* is generally used for paste extrusion and is composed of particles around 500 µm in size.

2 Manufacturing process

Traditional thermoplastic manufacturing processes are not used for PTFE because of its extremely high viscosity in the molten state. This is also the case for high density polyethylene that is processed from nascent powders [7].

2.1 Overview of existing processes

Three manufacturing processes of PTFE are predominantly used: compression molding for granular PTFE, extrusion for PTFE fine powder (and granular PTFE), and coating of PTFE dispersion.

Compression molding

Granular PTFE resin is pressed into preforms in a mold at ambient temperature. Those preforms are often called billets which are hollow cylinders. Their diameter usually ranges between 75 to 500 mm and their height between 100 to 1200 mm [1]. They can weigh almost 500 kg. Then the preforms are sintered in ovens to make the PTFE particles coalesce and to remove the porosity originating from compaction.

The sintered billets can be machined to make final parts. They can be skived using a blade by making the billet turn around a mandrill to obtain PTFE films. Those films can reach thicknesses between 50 to 400 µm.

Fillers can be added to the PTFE powder to enhance the mechanical, the wear or other properties of the final product.

Extrusion

Unlike traditional thermoplastic extrusion processes, PTFE paste extrusion is performed with the help of a lubricant [1]. Mixing PTFE fine powder with a lubricant lowers the pressure needed for extrusion. This lubricant is removed after extrusion by evaporation (at a lower temperature than PTFE melting temperature). Other types of extrusion can also be performed such as tube extrusion.

The interest of extrusion is the high strain imposed to the PTFE particles thanks to the different reduction ratios in the extruder. It leads to fibrillation of PTFE particles inside

the paste giving rise to some kind of PTFE composite. Its properties can be anisotropic. By this way either the ductility or the stiffness can be increased in one direction.

The extrudate can be sintered or not depending on the desired properties. Thread seal tape is made out of unsintered PTFE tape.

Coating

PTFE coatings can be performed from PTFE dispersion. Coating enables to cover different surfaces and to protect them from corrosion. It is also extensively used for cookwares (Figure 2d) even though the formulation of such coatings is generally more complex with additives and other resins.

2.2 Challenges in the sintering of PTFE compacts

This work is focusing on compression molding of granular PTFE (low flow) and more specifically on the sintering part. During sintering, PTFE preforms are heated in an oven in order to melt the crystals, have the particles coalesce and close the porosity induced by compaction. Due to melting and crystallization, PTFE billets undergo large strains with the temperature evolution. The coupling of those strains with thermal gradients leads to mechanical incompatibilities as illustrated in Figure 3, that generate stresses. In this schematic example, a molten PTFE cylinder crystallizes on the surface creating a "rigid shell". Once the core of the cylinder cools down, it crystallizes as well constraining the "rigid shel". This stress can sometimes lead to damage or even failure of the billets.

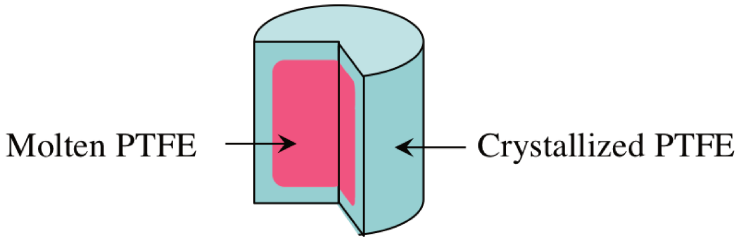

Figure 3: Sketch of a molten PTFE cylinder cooling down. The outer surface crystallizes creating a "rigid shell". Once the core crystallizes as well, it generates stresses by constraining the "rigid shell".

The origins of crack formation in billets are unknown. They could either form at compaction or at sintering. However their opening and probably their propagation are caused by the stresses established during sintering.

At LMT, compaction of PTFE was studied and modeled by Canto [8] and Fredy [9, 10]. Final density gradients were quantified at the end of the compaction by Fredy. Those variations could affect the sintering and be responsible of higher stress levels in the billet.

After sintering, the billets can be skived to obtain PTFE films. Defects can sometimes be observed at this stage.

The objectives of this thesis are to understand the physical mechanisms of deformation occurring in PTFE during the sintering and to be able to model them. The ultimate goal is to predict the state of a PTFE billet during sintering with a thermomechanical simulation using those models.

3 Structure of the study

The goal is to characterize the different elements necessary to perform a thermomechanical simulation of a PTFE compact sintering. Thus, it is essential to understand the different strain mechanisms that occur during sintering (Chapters 3 to 5) and to characterize the mechanical behavior for PTFE at different temperatures (Chapter 6). The simulation can then be developed using a thermomechanical model that reproduce the different mechanisms of deformation (Chapter 7). A finite element analysis framework is proposed and compared with various experiments (Chapter 8).

The content of each chapter is detailed below.

Chapter 1 - PTFE sintering: state of the art

Two different reviews are presented:

First, the different transitions and microstructural evolution of PTFE are exposed. A focus is made on crystallization mechanisms and crystallization kinetics models.

Second, models and simulations related to sintering of PTFE compacts are summarized.

Chapter 2 - Material and methods

The different experimental methods used during this work are described in this chapter. Differential scanning calorimetry (DSC) method and how to obtain a good baseline from it is explained. Thermomechanical analysis (TMA) technique is presented to measure the eigenstrain during sintering. X-ray diffraction (XRD) techniques and a convenient orientation measurement method is proposed. Then, visualization techniques such as scanning electron microscopy and X-ray microtomography are briefly introduced. Mechanical testings and dynamical mechanical analysis (DMA) are presented too. Finally, digital image correlation (DIC) and infrared spectroscopy techniques used for the analysis of the validation experiment are detailed.

Part I - Thermal uniformity

This part deals with the behavior of PTFE evolving with temperature in the case of thermal uniformity in the part.

Chapter 3 - Green PTFE behavior

Green PTFE compact behavior at heating is studied in this chapter. On top of the thermal expansion and eigenstrain due to melting, an irreversible mechanism due to residual stress relaxation is unveiled.

Chapter 4 - Void closure

In this chapter, the influence of the green PTFE compaction pressure on the initial porosity fraction is characterized. It reveals a void closure mechanism producing an eigenstrain opposed to the strain due to melting.

Chapter 5 - Melt-crystallized PTFE behavior

A singular crystallization kinetics is observed for molten PTFE with two independent crystallization mechanisms. As opposed to green PTFE, melt-crystallized PTFE under thermal cycle shows a more reversible (and isotropic) behavior.

Chapter 6 - Thermomechanical behavior

The mechanical properties of PTFE are investigated as function of temperature. The Young's modulus is measured at different temperatures for green and sintered PTFE. Viscous effects are found to be negligible and molten PTFE features elastomeric elasticity. An elastoplastic behavior is characterized for sintered PTFE.

Part II - Thermal inhomogeneity

This part deals with the behavior of PTFE evolving with temperature in the case of thermal inhomogeneity in the part. The addition of thermal gradient induces stresses inside the part. Thermomechanical simulations can try to evaluate this stress for any thermal loading.

Chapter 7 - Model equations: application to a semi-infinite PTFE part

The different models for the crystallinity kinetics, for the eigenstrain components and for the thermomechanical behavior are detailed and applied in a matlab simulation.

Chapter 8 - Finite element analysis of the sintering

A finite element (FE) method framework is set using the previous models in Abaqus® software. The FE analysis is compared to validation experiments to confirm its results.

Chapter 1

PTFE sintering: state of the art

This chapter contains a state of the art on the microstructural evolution of PTFE during sintering and of the elements of modeling needed to perform a thermomechanical simulation of PTFE sintering.

Contents

1 Microstructural evolution of PTFE during sintering

Polytetrafluoroethylene is subject to various microstructural modifications during sintering. Phase changes and glass transition have an impact on the final state of a sintered PTFE part. Melting and crystallization represent the most important phase change during sintering. Crystallinity and crystalline morphology are expected to evolve during these transitions. This section lists the different transitions likely to occur during the sintering cycle, then presents different observations on the evolution of crystallites during crystallization and finally exposes crystallization kinetic models of PTFE described in the literature.

1.1 Phase transitions

PTFE is a semi-crystalline polymer which means that part of its molecular chains are strictly organized into a crystal. For nascent PTFE powders, the crystallinity content can reach more than 90% and for sintered PTFE is usually around 50%. The crystallinity content refers to the fraction of ordered segments compared to the totality and is expressed here in mass fraction. The less ordered fraction is called amorphous phase as opposed to the crystalline structure.

The crystalline phase is subject to changes as function of temperature and pressure variations. The phase diagram of PTFE is presented in Figure 1.1 [11]. Four crystallines phases are known for PTFE and their structure is detailed in Figure 1.2. A double transition occurs around ambient temperature, from Triclinic phase II to Hexagonal phase IV above 19°C, and from Hexagonal phase IV to Pseudo-hexagonal phase I at 30°C [12]. Above 340°C, the crystal organization vanishes and the entire polymer becomes amorphous. This transition is called melting at heating and crystallization at cooling.

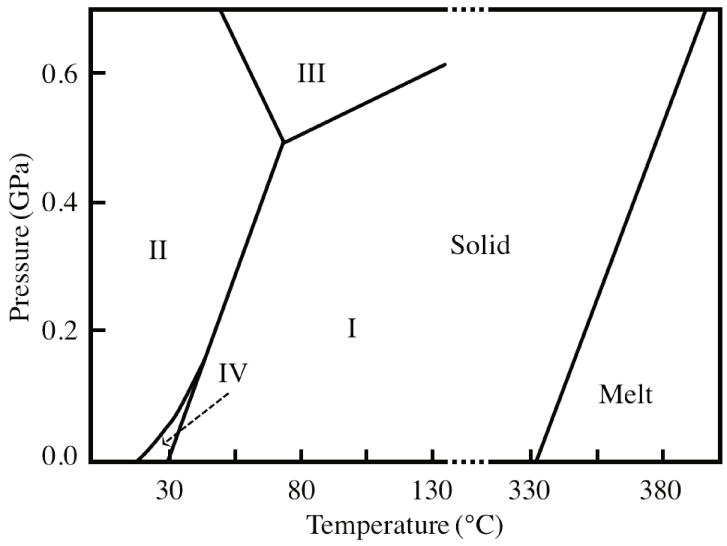

Figure 1.1: PTFE phase diagram. Based on [11].

At higher pressures (above 0.5 GPa), crystalline structure change from Hexagonal (or Triclinic) to Orthorhombic [13] (Figure 1.2). The crystalline transitions between phase II and phase IV, and between phase IV and phase I do not correspond to significant microstructural modification. The helical conformation of phase II is untwisted from 13 atoms per full turn to 15 atoms per full turn in phase IV and I [14]. Phase I is more mobile

than phase IV, and allows more angular motions (torsion) around the chain [15, 16].

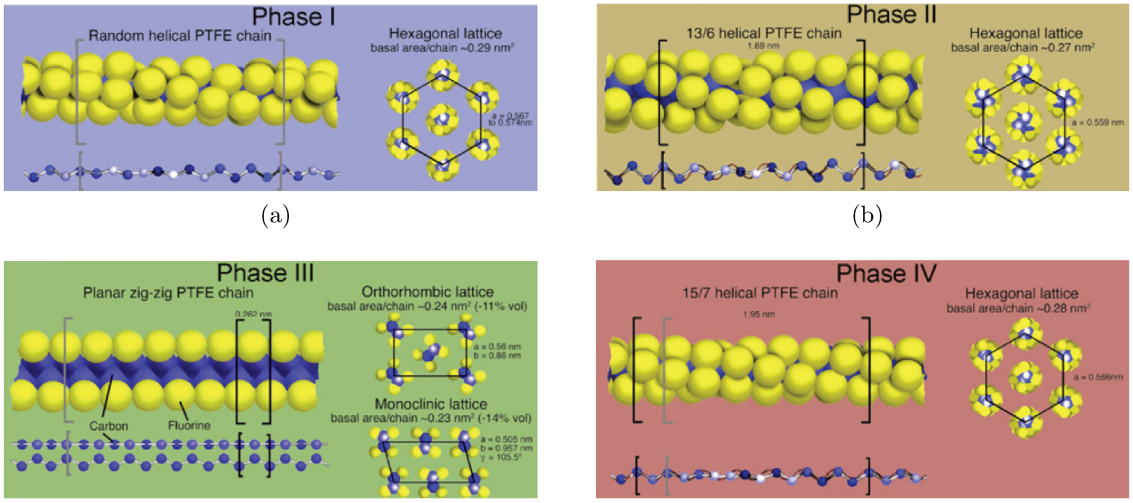

Figure 1.2: PTFE crystalline phases. Taken from [13].

PTFE chains are extremely long (about 20 µm) due to the high molecular weight (around 10^7 g/mol). This limits substantially the mobility of the polymer chains and therefore their ability to reorganize at phase changes. Torsion along the carbon chain remains the favorite possibility for reorganization. Conformational defects can move thanks to an helix reversal mechanism [17, 18]. PTFE chains being an helix, two chiral configurations exists (L and R). Switching from one to another within the same chain allows to reorganize the chains to form crystals. Illustrations of the different configurations and how the defects can move are presented in Figure 1.3. Figure 1.3c underlines that a crystal can only exist within same configuration L or R.

The other important transition in semi-crystalline polymers is the glass transition which concerns the amorphous phase[19]. The material is considered vitrous below the glass transition temperature (T_g) and in rubbery state above. In the rubbery state, the molecular chains in the amorphous phase presents a high mobility which decreases the viscosity of the material. The ductility is usually much higher and the stress is only carried by the entanglements between chains. In the vitrous state, the molecular chains have low mobility which makes the material more fragile.

In the case of PTFE, the exact position of the glass transition has long been and is still a subject of debate. Three transitions can be observed using dynamic mechanical analysis (DMA) tests (see Figure 1.4). The γ and α-transitions are related to the amorphous phase. The β-transition characterizes the double crystalline transition at ambient temperature. Some considers that the glass transition is the γ-transition around -110°C [20, 21] and others that it is the α-transition around 130°C [22, 23, 24, 25, 26].

More recent studies suggest that both γ and α transitions are related to two morphologies of amorphous phase: the rigid amorphous fraction (RAF) and the mobile amorphous fraction (MAF) shown in Figure 1.5. The RAF is the part of the amorphous phase at the vicinity of the crystalline phase. Conversely, the MAF is a fraction of the amorphous phase further away from the crystalline phase and therefore more mobile as less impacted by the crystals. The γ-transition corresponds to the glass transition of the MAF around -110°C and the α-transition corresponds to the glass transition of the RAF around 130°C [28, 27].

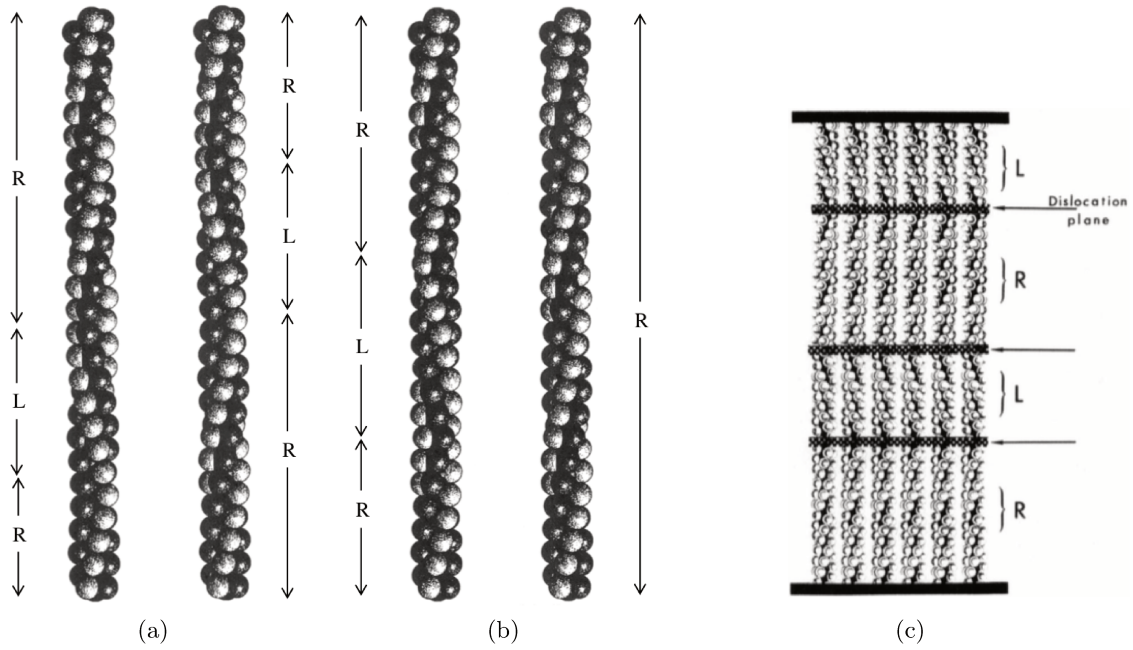

Figure 1.3: Illustration of helix configuration L and R in the same chain. A defect (configuration change) moves along a chain without changing the overall chain torsion (a). A defect can be created without changing the overall chain torsion (b). Taken from [17]. Crystals are formed with chains in the same configuration (c). Taken from [16].

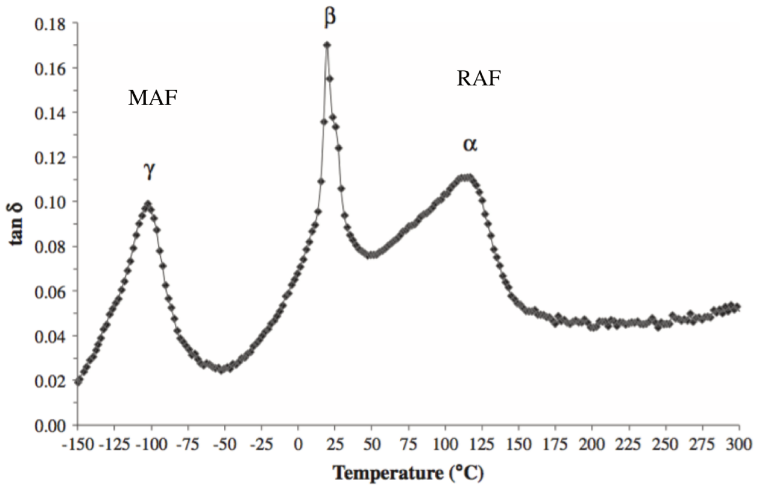

Figure 1.4: tan δ obtained with DMA experiment. The γ, β and α-transitions are observed with the different local maxima of tan δ. Taken from [27].

1.2 Crystalline lamellae formation and growth

Nascent PTFE is almost fully crystalline due to crystallization during polymerization. Extended-chain crystals are formed in these conditions [29, 30]. Figure 1.6 presents the difference between extended-chain crystals and folded-chain crystals. The former consists in stacks of chains or folded chains with a length between fold above 2 000 Å according to Wunderlich's definition [29] (Figure 1.6a). The latter is a stack of folded chains with a

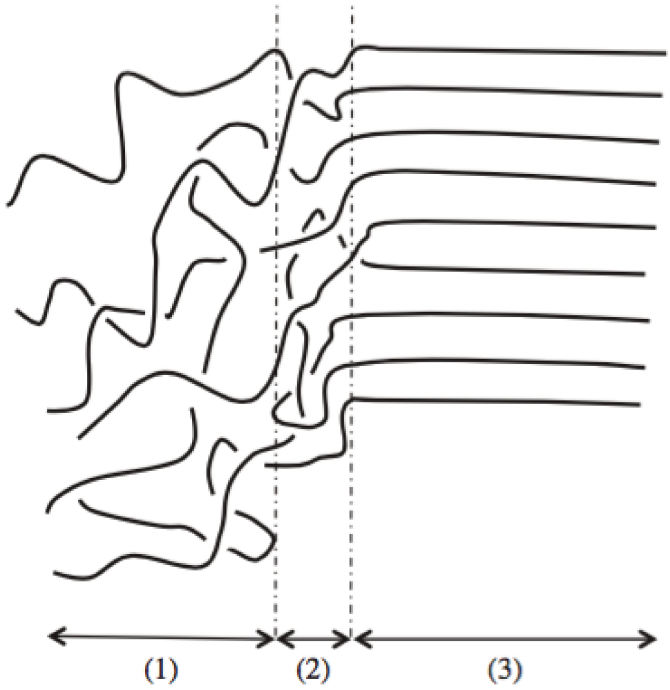

Figure 1.5: Sketch of PTFE semi-crystalline structure. (1) corresponds to the mobile amorphous fraction (MAF), (2) to the rigid amorphous fraction (RAF) and (3) to the crystalline phase. Taken from [27].

length between fold lower than 2 000 Å (Figure 1.6b). The distance between folds is the crystal lamellae thickness. It was shown by Geil et al. [31] that nascent particles are often folds of PTFE chains with a large lamellae thickness (above 2 000 Å).

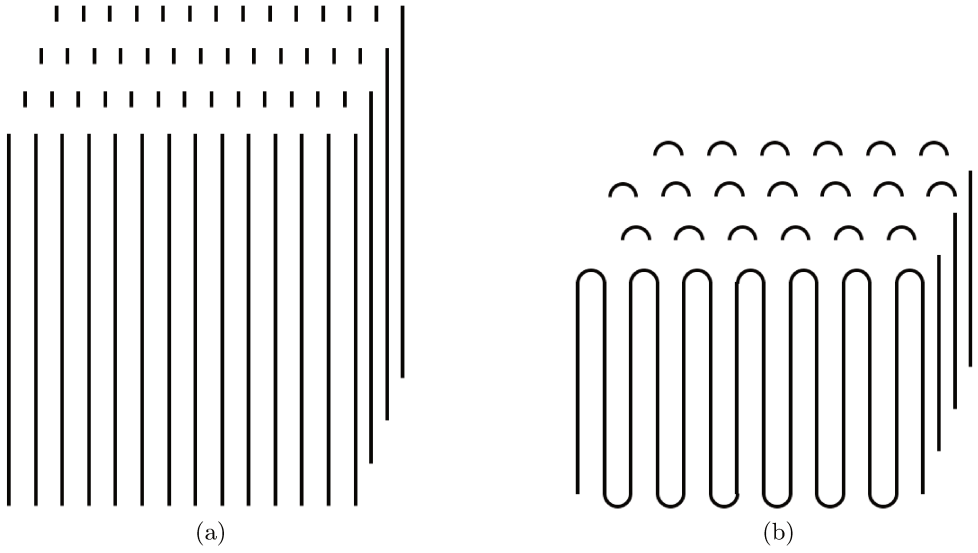

Figure 1.6: Sketch of an extended-chain crystal (a) and a folded-chain crystal (b).

During melting, PTFE chains lose their crystal organization and form a mesomorphic melt. The mesomorphic melt is a pseudo-structured state from which originates the future

crystals. According to Geil et al. [31], the chains start to reorganize and fold in the melt. Therefore, the time spent in the melt is important for the subsequent crystallization.

During the cooling of the melt, PTFE recrystallizes and form folded-chain crystals. Those lamellae can be observed via scanning electron microscopy (SEM) techniques as shown in Figure 1.7.

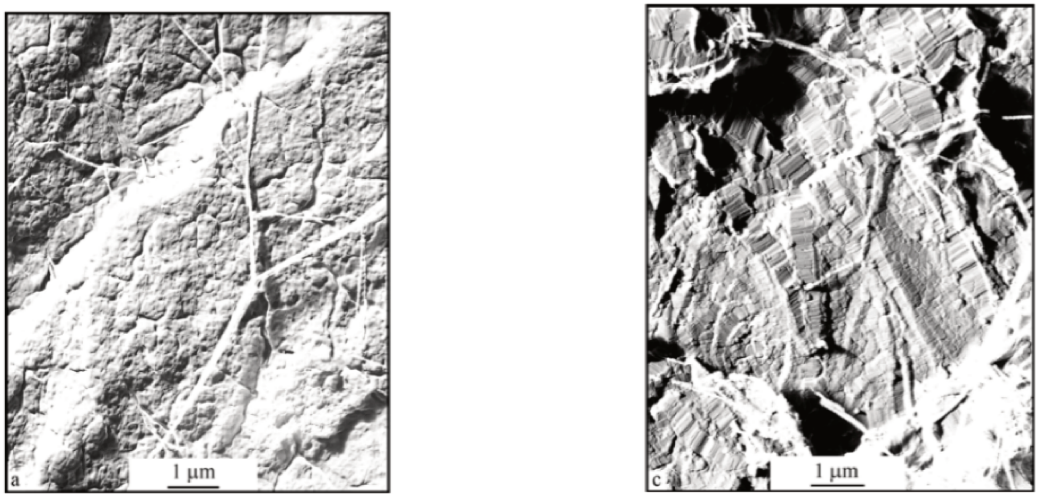

(a) (b)

Figure 1.7: SEM micrographs of sintered PTFE at 350°C for 10 min and quenched into water (a) and of sintered PTFE at 350°C for 30 min and slow cooled (b). Images taken from [31].

The temperature history at cooling seem has a pronounced effect on the crystal perfection and notably on the lamellae thickness (see Figure 1.7). Different studies observed this effect via SEM [32, 31, 30]. Figure 1.8 exposes this dependency from statistical analyses based on SEM micrographs. A clear increase of the lamellae thickness is shown as function of the temperature between 312 and 322°C (Figure 1.8a), as well as an increase with time spent at these temperature (Figure 1.8b).

The same tendency was obtained using differential scanning calorimetry (DSC) and X-ray scattering measurements [33]. Melting peak in DSC gives information on the lamellae size distribution thanks to Gibbs-Thomson equation [34, 35]:

$$T_m = T_m^0 \left(1 - \frac{2\sigma_e}{\Delta h_f l}\right) \tag{1.1}$$

where T_m is the melting temperature of the crystal, T_m^0 is the melting temperature of an infinite crystal, σ_e is the end surface free energy, Δh_f is the enthalpy of fusion per unit volume of crystal and l is the lamellae thickness.

Thanks to DSC analysis, this equation leads to a relation between melting temperature and crystallite size (Figure 1.9a). Therefore the lamellae thickness can be directly accessed from DSC measurements via the melting temperature. Figure 1.9b gives the melting temperature as function of the crystallization time for different temperatures. It appears that the evolution of the lamellae thickness with time is dependent on the crystallization temperature. This lead Ferry et al. [33] to conclude that at high temperature crystal perfection is more likely to happen due to higher thermal agitation. Conversely, at lower temperature viscosity increases leading to thinner lamellae.

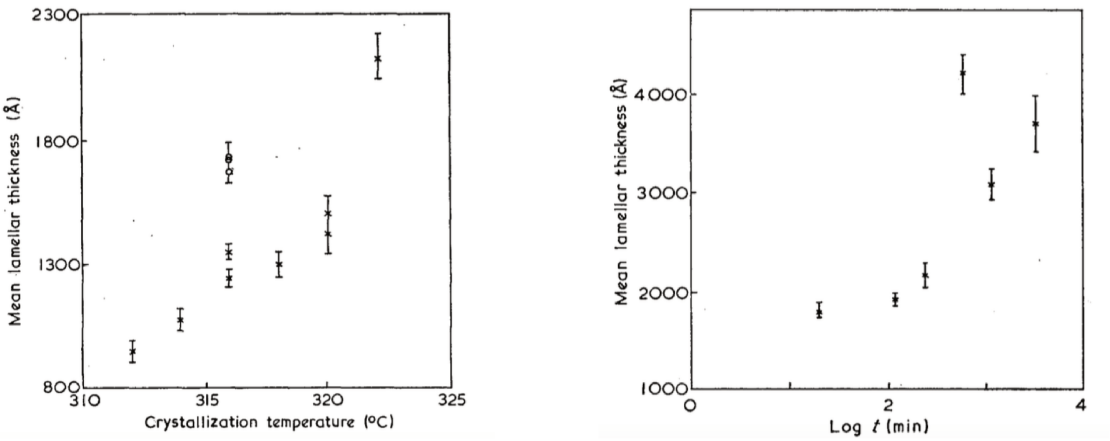

(a) (b)

Figure 1.8: Lamellae thickness as function of crystallization temperature for 20 min isotherm (a) and as function of crystallization time at 322°C (b). These results were obtained by Bassett [32] from SEM observations.

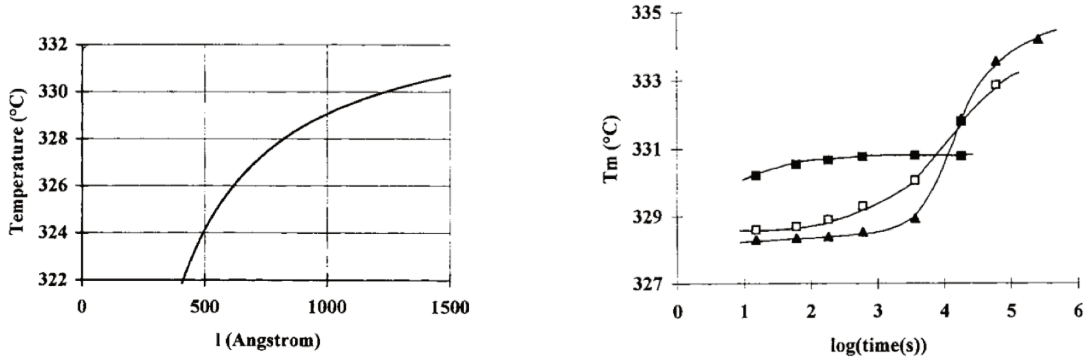

(a) (b)

Figure 1.9: Melting temperature as function of lamellae thickness (a) and temperature of the maximum of DSC melting peak as function of crystallization time, for different temperatures: 315°C (■), 320°C (□) and 323°C (▲) (b). Images taken from [33].

1.3 Crystallization kinetics

As previously shown with the evolution of the crystalline lamellae, the crystallization follows a specific kinetic law. It describes the evolution of the crystallinity content with temperature and time.

Crystallization kinetic models usually deal with competition between nucleation and growth of the crystals. Close to melting temperature, the nucleation is low as the probability to create a nuclei is almost equal to the probability to that a nuclei is removed. When the temperature decreases, the growth of the crystal is more favorable as the mobility of the chains is important. At even lower temperature, the nucleation becomes more important and the mobility is reduced.

The crystallization kinetics of polymers is often modeled with classical models. However it is very common to encounter a secondary crystallization mechanism which complicates

its modeling.

Avrami model

The most known model for crystallization kinetic is the Avrami model which describes spherulitic crystal nucleation and growth [36, 37, 38]. The Avrami model is relevant for isothermal crystallization and has been widely applied for metals and polymers crystallization. The Avrami equation estimates the relative crystallinity content $\alpha = \chi/\chi^{\infty}$ where χ is the crystalline mass fraction and χ^{∞} the crystalline mass fraction at the end of an isothermal crystallization:

$$\alpha(t) = 1 - \exp\left(-K\ t^n\right) \tag{1.2}$$

where $K(T)$ is the Avrami kinetic constant which depends on the isothermal temperature T and n is the Avrami exponent which characterizes both the growth dimension and the nucleation type (instantaneous or sporadic). The parameter n is a positive integer between 1 and 4. It is equal to the growth dimension for an instantaneous nucleation and to the growth dimension + 1 for a sporadic nucleation. For example, $n = 1$ corresponds to an instantaneous nucleation with a linear growth, and $n = 4$ to a sporadic nucleation with growth in the three dimensions.

The Avrami model relies on several assumptions:

- uniform nucleation;
- no volume change during transformation;
- complete transformation;
- constant growth rate during the transformation.

Ozawa model - constant cooling rates

Ozawa extended the Avrami model to anisothermal crystallization in the case of a constant cooling rate. This model is very convenient to analyze anisothermal DSC experiments. Those experiments are mandatory when the crystallization is fast and it is not possible to perform isotherms without initiating the crystallization. The equation of the Ozawa model [39] is defined as

$$\alpha(T) = 1 - \exp\left(-\frac{k(T)}{\phi^n}\right) \tag{1.3}$$

where $k(T)$ is the Ozawa kinetic constant and ϕ is the cooling rate.

The Ozawa model relies on the additional *isokinetic* hypothesis. It implies that the growth rate G and the nucleation rate $\dot{N}$ follow the same temperature evolution.

The Ozawa kinetic constant $k(T)$ is related to the Avrami kinetic constant $K(T)$ by the following equation:

$$K = \left(\frac{\mathrm{d}k^{1/n}}{\mathrm{d}T}\right)^n \tag{1.4}$$

Nakamura model - indifferent thermal history

Nakamura extended the Avrami model to any thermal history. This model is essential to simulate the evolution of the crystallinity content for a complex thermal loading such as the one observed by PTFE in a billet during sintering. The equation of Nakamura model [40] is

$$\alpha(t) = 1 - \exp\left(-\left\{\int_0^t \kappa\big(T(\tau)\big)\mathrm{d}\tau\right\}^n\right) \tag{1.5}$$

where κ is Nakamura kinetic constant and is related to the other kinetic constants via

$$\kappa = K^{1/n} = \frac{\mathrm{d}k^{1/n}}{\mathrm{d}T} \tag{1.6}$$

It can also be expressed using the differential expression which is more convenient for incremental computations

$$\frac{\mathrm{d}\alpha}{\mathrm{d}t} = n\ \kappa\big(T(t)\big)\left\{\int_0^t \kappa\big(T(\tau)\big)\mathrm{d}\tau\right\}^{n-1}(1-\alpha) \tag{1.7}$$

Kinetic constant evolution

Hoffman and Lauritzen proposed an expression for the growth rate G [34] as function of the temperature

$$G(T) = G_0 \exp\left(-\frac{U^*}{R(T-T_\infty)}\right)\exp\left(-\frac{K_g}{T\Delta T f}\right) \tag{1.8}$$

where G_0 is a constant, U^* is the activation energy for macromolecules movement (usually ranging between 4000−7000 J/mol [34, 41]), R is the gas constant and K_g is a parameter associated to nucleation. T_∞ is a temperature where any macromolecular movement is forbidden, and usually $T_\infty = T_g - 30$, where T_g is the glass transition temperature. $\Delta T = T_m^0 - T$ where T_m^0 is the melting temperature of an infinite crystal and f is defined by $f = 2T/(T_m^0 + T)$.

The first exponential term $\exp\left(-U^*/R(T-T_\infty)\right)$ conveys the diffusion process of the chains in the molten state. The further above T_∞ the temperature T, the higher the diffusion. The second exponential term $\exp\left(-K_g/T\Delta T f\right)$ is related to the nucleation at the surface of the crystalline lamella. The further below T_m the temperature, the faster the growth of the lamella. Those two terms balance each other producing a temperature function similar to an asymmetric Gaussian.

The same type of temperature evolution is generally chosen to characterize the kinetic constant $K(T)$ [42, 43, 44]. An illustration of the kinetic constant as function of temperature is proposed in Figure 1.10.

Secondary crystallization kinetics

Secondary crystallization mechanisms are also a very common feature in polymers [45, 46, 47, 48, 49]. Some models exist to try to capture the overall kinetics. Verhoyen proposed the *consecutive* Avrami model [50] which sums up to independent crystallization kinetics. The equation of the *consecutive* Avrami model is

$$\alpha(t) = w_1\big(1 - \exp\left(-K_1(t-t_{i1})^{n_1}\right)\big) + w_2\big(1 - \exp\left(-K_2(t-t_{i2})^{n_2}\right)\big) \tag{1.9}$$

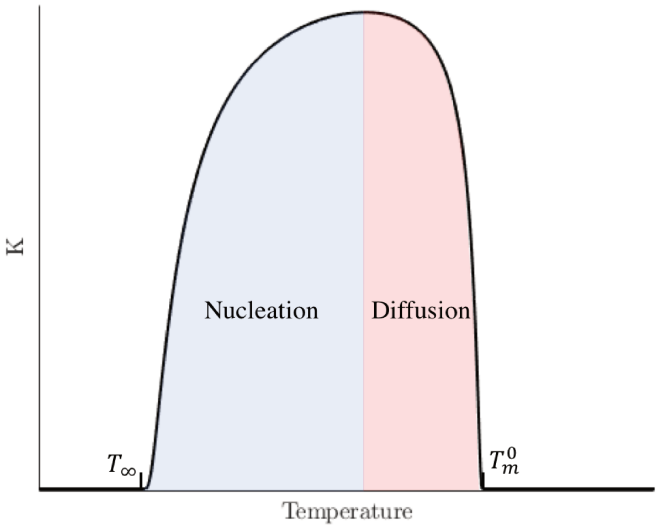

Figure 1.10: Illustration of the kinetic constant as function of temperature. The shape of the function is given by (1.8). The high temperature region is governed by the diffusion process and the low temperature region is governed by nucleation.

where w_1 and w_2 are weight factors related to each crystallization, K_1, K_2, n_1 and n_2 are respectively the Avrami kinetic constants and the Avrami exponents for each crystallization. t_{i1} and t_{i2} are the induction times respectively for the primary and the secondary crystallization.

The *consecutive* Avrami model is the extension of the *parallel* Avrami model introduced by Velisaris [51] with the addition of induction times. The inductions times (t_{i1} and t_{i2}) delay the start the primary and the secondary crystallization.

The secondary crystallization is usually a phenomenon that starts later and that is dependent on the primary crystallization. The Hillier model proposes to model the secondary crystallization kinetic with a convolution to the primary crystallization kinetic [52]. For that reason, the Hillier model is based on more physical assumptions than the consecutive Avrami model. The Hillier model can be written as:

$$\alpha(t) = w_1\big(1-\exp\left(-K_1 t^{n_1}\right)\big) + w_2 \int_0^t \frac{\partial}{\partial t}\Big(1-\exp\left(-K_1 \tau^{n_1}\right)\Big)\big[1-\exp\left(-K_2(t-\tau)\right)\big]\mathrm{d}\tau \tag{1.10}$$

In this model is that the secondary crystallization occurs in a domain linked to the primary crystallized domain. Such evolution is relevant in the case of lamellar thickening or in the case of interlamellar crystallization. The Hillier model is nevertheless usually more difficult to handle for experimental data fitting. For that reason, this model is less frequently used.

Those two models were presented for the isothermal case and can be extended to non-isothermal kinetics using Nakamura's formalism.

PTFE crystallization kinetics

PTFE crystallization kinetics via DSC experiments was first studied by Ozawa in 1981 [53] and later by Seo and by Wang et al. [54, 55]. Figure 1.11 shows the evolution of the relative crystallinity as function of the temperature for different cooling rates. As mentioned previously, the PTFE is shown to crystallize very quickly on a narrow temperature range (between 320°C and 300°C). The authors found out that the Avrami exponent n is close to 1 (1.5 in the case of Wang). It means that the crystallization has a linear growth with an instantaneous nucleation. This result is consistent with observations made by Symons [56] on linear growth crystallization using SEM observations. Ozawa mentioned that secondary crystallization could exist in PTFE and have an impact on the final crystallinity content.

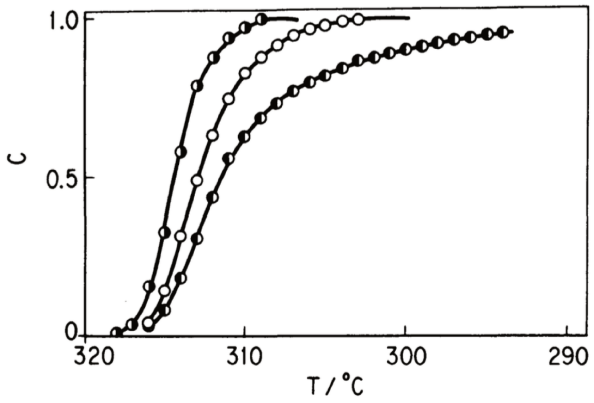

Figure 1.11: Relative crystallinity α as function of the temperature for different cooling rates: 0.9°C/min (◑), 2.9°C/min (○) and 4.5°C/min (◐). Image taken from [53].

Recent studies and perspectives

A more recent work explored crystallization of PTFE over a wide range of cooling rates using ultra fast scanning calorimetry (UFSC). UFSC allowed to reach cooling rates up to 800 000°C/s. The study showed it was impossible to prevent crystallization to happen even at very high cooling rates [57].

Others studies pointed out a reversible behavior during crystallization and second melting of PTFE (i.e. melting of melt-crystallized PTFE) [58, 59]. Figure 1.12 shows a DSC measurement performed by the authors. On the calorigram, it can be seen that the crystallization peak and second melting peak are spread over a broad temperature range. Using temperature modulated DSC (TMDSC), the authors found that the behavior between 220 and 310°C is reversible. The TMDSC revealed an "excess" of specific heat capacity that could be related to a reversible melting phenomenon.

The limitation of the Avrami/Nakamura model for the application to PTFE comes from the fact that the transformation is not always complete. The final crystallinity content of PTFE depends on the thermal history. In the different articles studying PTFE crystallization kinetics, the final value of α was set to 1 whereas χ^{∞} varies with cooling rates. It would be valuable to take this evolution into account within the kinetic model.

The recent studies showed a crystallization behavior between 220 and 310°C which was not integrated to any crystallization kinetic model. Therefore it would be interesting to consider this evolution in a model to truly appreciate the crystallinity content variation.

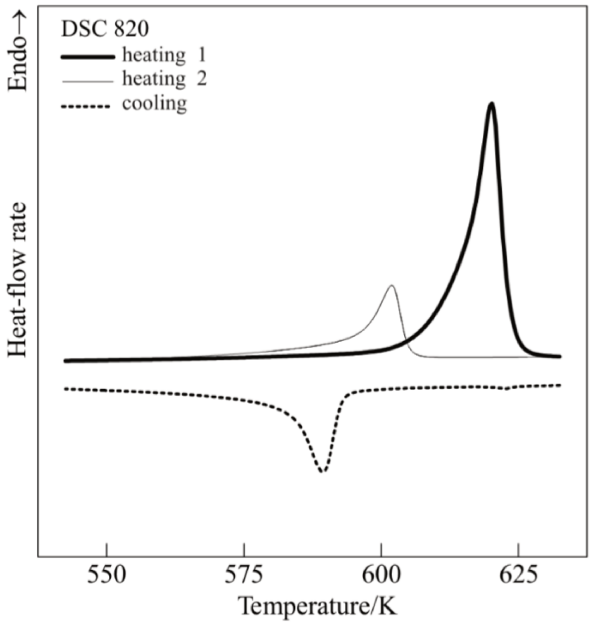

Figure 1.12: DSC calorigram obtained from nascent PTFE melted a first time, cooled down and melted a second time. The heating rate is 20°C/min and the cooling rate is 10 °C/min. The crystallization peak and secondary melting peak seems to extend on a broad temperature region. Figure taken from [59].

2 Mechanical analysis of PTFE sintering

This section reports the different elements from the literature necessary to establish a simulation of the sintering of PTFE. First mechanical properties for PTFE are exposed and then a list of different existing models and simulations are proposed.

2.1 Mechanical behavior of PTFE during sintering

Mechanical properties of sintered PTFE

Only a few papers exist on mechanical properties of PTFE. PTFE is known as being a polymer having quite low mechanical properties. Therefore it often needs to be enhanced by filler addition.

PTFE has a very high viscosity η in the molten state: 10^{11}–10^{12} Poise at 380°C [1]. Therefore it does not flow in the molten state. From DMA experiments shown in Figure 1.13a, the loss modulus (G") is always at least one magnitude order below the storage modulus (G'). It means that the material behaves as an elastic material at the frequency studied with very a short relaxation time.

Other authors studied the evolution of the Young's (E) modulus as function of temperature (Figure 1.14). Some results were obtained from tensile tests [61, 62] and others from compression tests [63]. The evolution of E is consistent when comparing between the different results. Young's modulus presents a slope discontinuity around 100° C which may be related to the α-transition. The same slope discontinuity can be observed in the DMA measurements from Figure 6.1. Besides, the evolution of E with the temperature can be

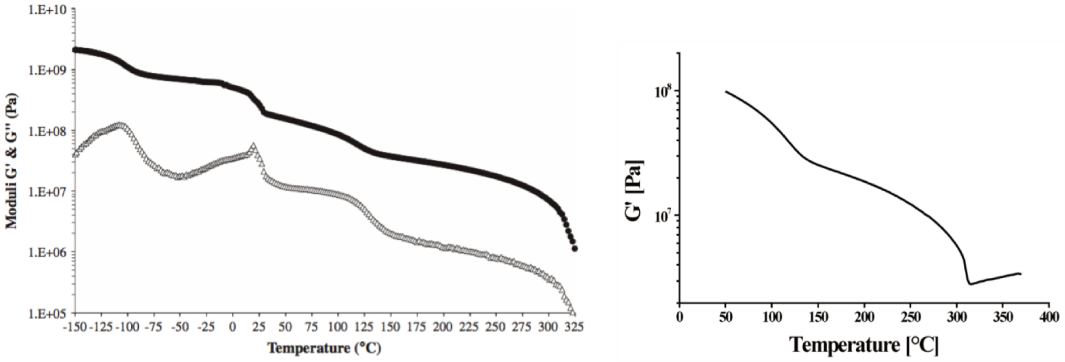

(a) (b)

Figure 1.13: Dynamic mechanical analysis of sintered PTFE in torsion. Storage modulus (■) and loss modulus obtained (△) at 1 rad/s (a) and storage modulus up to 370°C at 1 Hz (b). Image (a) taken from [27] and (b) from [60].

obtained from the evolution of the shear modulus (G) using the relation:

$$G = \frac{E}{2(1+\nu)} \tag{1.11}$$

where ν is the Poisson's ratio. This relation is valid for an isotropic material.

Poisson's ratio for PTFE is between 0.40-0.46 [62, 63, 1], and no mention of a variation with temperature is made. Therefore, the Young's modulus evolution obtained from the storage modulus (G') is consistent with Figure 1.14.

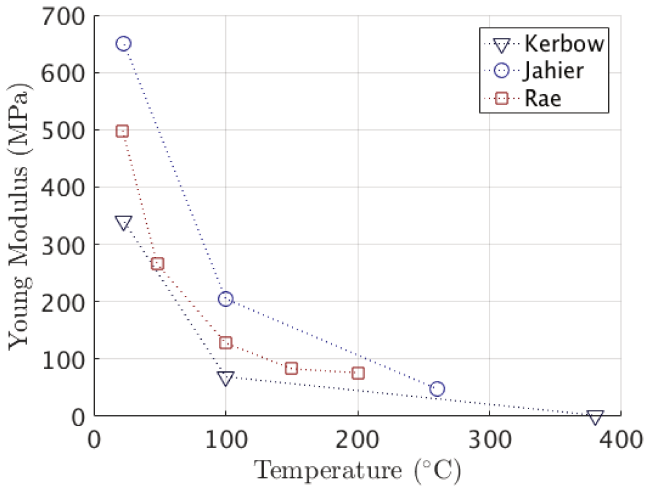

Figure 1.14: Young modulus of sintered PTFE obtained by different authors from tensile tests [61, 62] and from compression tests [63].

Crystal plasticity is an important deformation mechanism in PTFE. Crystalline planes slides against each other at a low energy cost. Thus, the crystal shear plasticity threshold is very low [64, 65]. It explains the low coefficient of friction of PTFE and the tendency of

PTFE crystals to form fibrils under shear [66, 67].

Sintered PTFE yield stress evolution with temperature has been investigated by several authors via tensile tests or compression tests [61, 68]. Figure 1.15 gathers those results in one graph. The evolution of the yield stress with temperature seems similar to the evolution of Young's modulus. In particular, the same slope discontinuity seems to be observed below 100° C which could correspond to the α-transition (glass transition of the RAF).

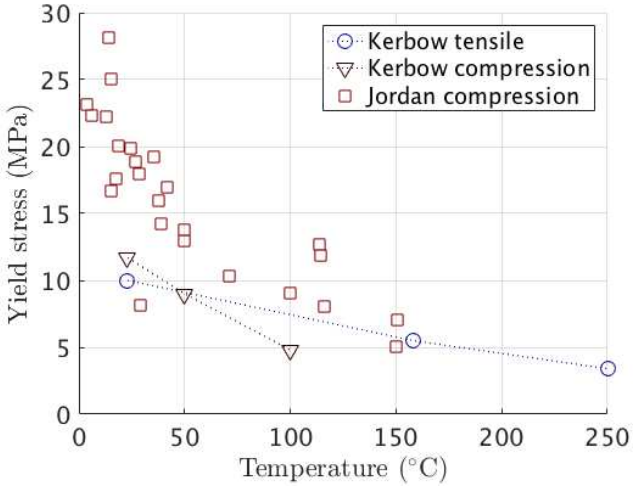

Figure 1.15: Yield stress of sintered PTFE as function of temperature measured by different authors: Kerbow et al. from tensile and compression tests [61], Jordan et al. from compression tests [68].

Mechanical models for PTFE

Some authors modeled the thermomechanical behavior of PTFE [69, 70]. They all decompose the behavior into two terms, one viscoelastic component and one viscoplastic component. In other words, a part of the strain is reversible, another is irreversible and both are time-dependent. A representation of the models used to describe behavior PTFE is shown in Figure 1.16.

Similarly Bergström modeled the thermomechanical behavior of PTFE with fillers for large strains using the Dual Network Fluoropolymer model [71]. This model was used to simulate the viscoelastic behavior and the viscoplastic behavior corresponding to irreversible chain sliding. The viscoelastic behavior is described by a combination of short term and long term relaxations. This model has been tuned using a set of specific experiments up to 200°C (uniaxial tension tests, uniaxial compression tests, volumetric compression tests and multiaxial small punch tests).

Mechanical properties of green PTFE after compaction

PTFE powder compaction 3D-behavior has been characterized by Canto [8] and Fredy et al. [9, 10] at room temperature using a triaxial machine. A Drucker-Prager/cap model was used to describe the mechanical behavior of PTFE during compaction. The mechanical properties of PTFE have been identified for different void ratios e (i.e. different levels of

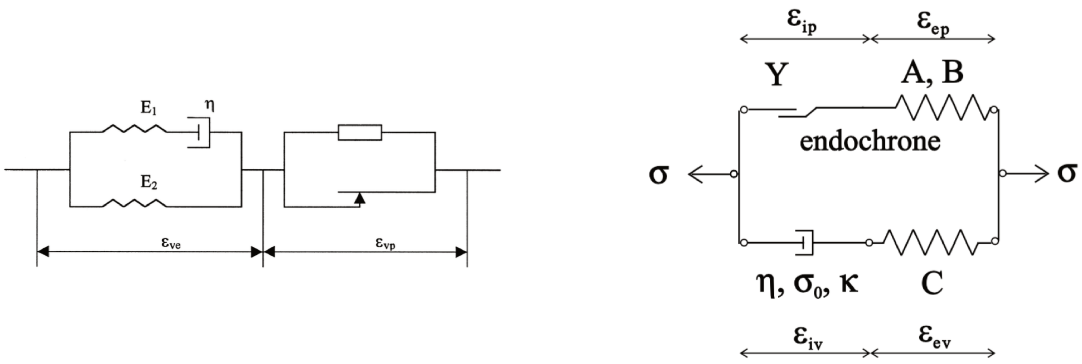

Figure 1.16: Representation of the rheological models used to describe behavior of PTFE. (a) from [69] and (b) from [70].

compaction) in order to complete this type of finite element simulations. The void ratio e is ratio between the volume of the voids and the volume of the solids, and is related to the porosity n by $e = n/(1-n)$. Figure 1.17 shows the evolution of Young's modulus and of Poisson's ratio as functions of the void ratio. It gives the evolution of the mechanichal properties during the compaction step. These results are particularly interesting when looking for the properties of PTFE compacts obtained from different compaction levels.

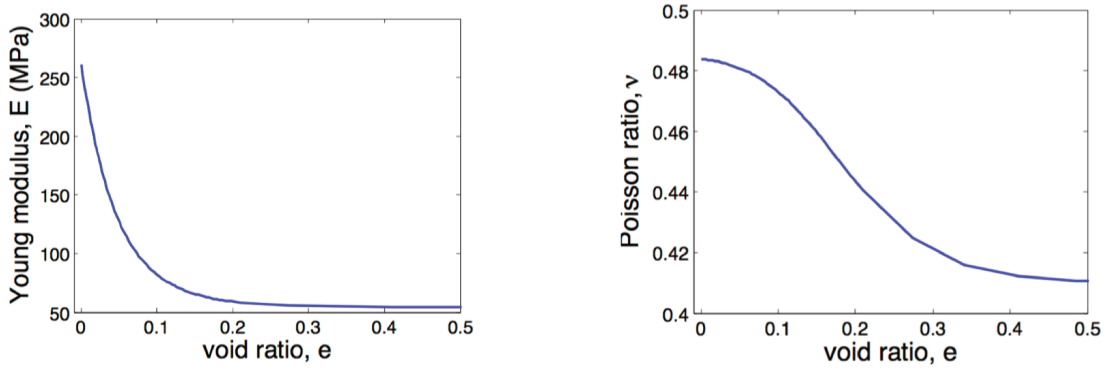

(a) (b)

Figure 1.17: Evolution of Young's modulus (a) and Poisson's ratio (b) as function of the void ratio for compacted PTFE powder. Results obtained from a hydrostatic test. Figures taken from [10].

Results from compaction simulation are useful for the simulation of the sintering step. Figure 1.18 shows the density distributions along the height of the green PTFE billet obtained for different compaction pressures. In particular, density distributions after compaction can be an input for refined sintering simulations. Due to the different mechanical response for different void ratios, it is very likely that density gradient modifies the stress state in PTFE billets during sintering.

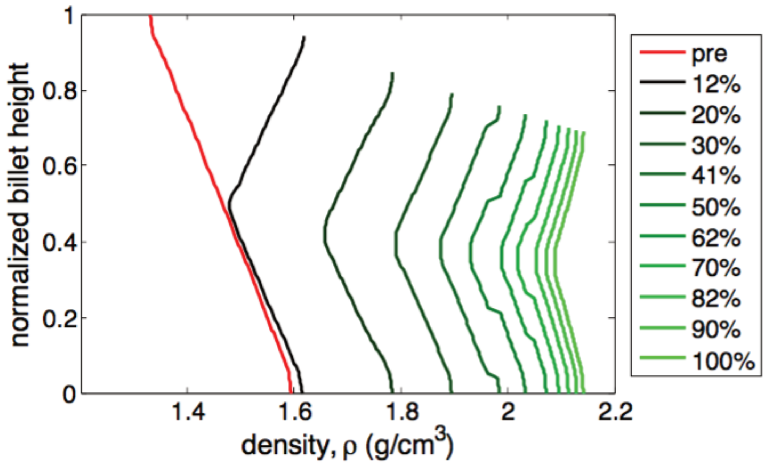

Figure 1.18: Density distributions along the eight of the PTFE billet after compaction. The density profiles are plotted for percentages of the maximal applied stress. Figure taken from [10].

2.2 Simulation of PTFE sintering

Strain mechanisms during sintering and model

A study by Canto [8, 72] investigated the deformation mechanisms during the sintering of cold-pressed PTFE compacts. Dilatometric experiments (or thermomechanical analysis) were performed on small PTFE compacts. The material used was a free flow resin. Both isostatic compaction and uniaxial compaction were studied.

The classical strain mechanisms during sintering are the thermal expansion and the strain caused by phase changes (melting and crystallization for PTFE). Figure 1.19 shows the measured thermal strain obtained for a uniaxial cold compact during sintering. It appears that the strain is anisotropic: the uniaxial compaction induced a transverse isotropic behavior.

An additional strain related to void closure was observed as shown in Figure 1.20 for an isotropically compacted sample. The subtraction of the strain of a sample without porosity to the strain of an initially porous sample reveals the existence of a void closure strain ε^{vc}. This shrinkage starts at melting. The void closure evolution are usually modeled considering surface tension and viscous behavior of the material [73]. In this article, a phenomenological model has been proposed:

$$\varepsilon^{vc} = \Delta\varepsilon^{vc}_{max}\left[1 - \exp(-a_{vc}t)\right] \quad H\big(T(t) - T_m\big) \tag{1.12}$$

with a temporal parameter a_{vc} and the strain related to the full closure of the porosity $\Delta\varepsilon^{vc}_{max}$ and H the Heaviside function.

Another effect was observed at heating corresponding to a "recovery" phenomenon. This effect is illustrated on Figure 1.21 where successive thermal cycle with increasing maximal temperature are performed on a uniaxially compacted sample. It appears that after the first cycles, the a permanent strain is observed. This strain corresponds to an expansion in the compaction direction and to a shrinkage in the transverse direction. The "recovery" is supposed to be related to the uniaxial pressing.

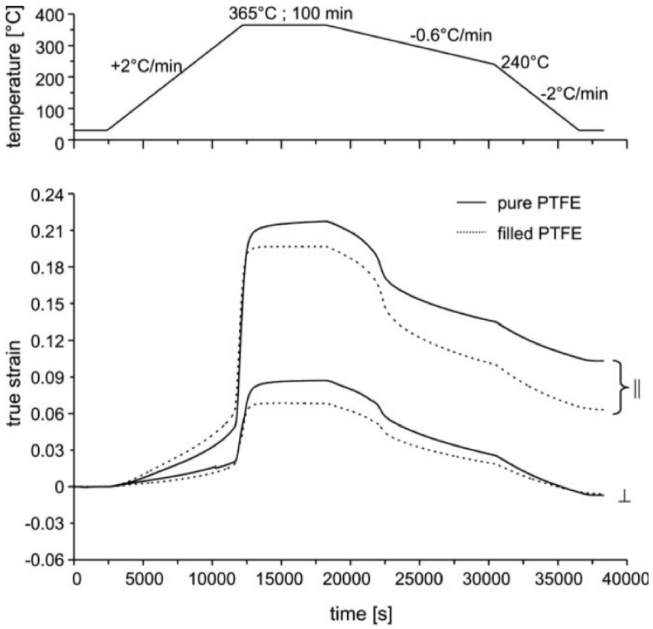

Figure 1.19: Thermal cycle and corresponding strain obtained from TMA experiment in compaction direction (∥) and in transverse direction (⊥). Figure taken from Canto [72].

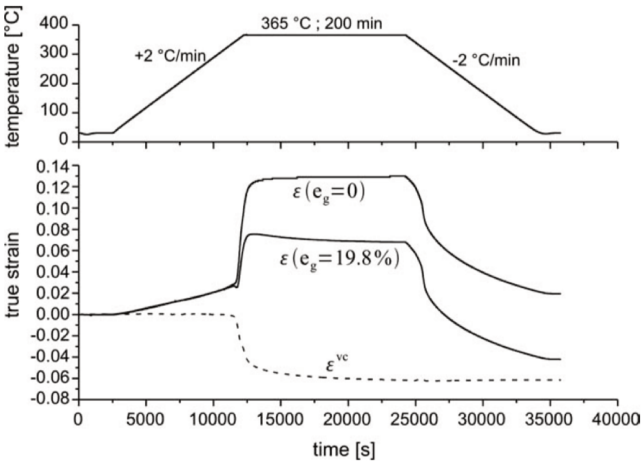

Figure 1.20: Thermal cycle and corresponding strain obtained from TMA experiment for two PTFE samples with different void ratios (i.e. different initial compactions). The subtraction of the two curves gives an evaluation of the strain related to void closure. Figure taken from Canto [72].

Finite element analysis

A mere finite element method analysis of the billet sintering is proposed by Andena [60]. The DSC, dilatometric results evolution of Young's modulus with temperature are taken as input for the simulation. The billet is represented with an asymmetric geometry.

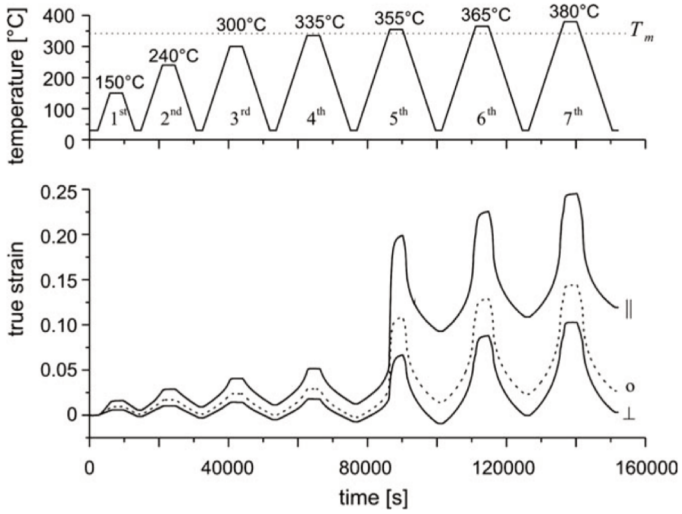

Figure 1.21: Thermal cycles with increasing maximal temperature and corresponding strain obtained from TMA experiment in compaction direction (∥), in transverse direction (⊥) and for an isotropic specimen. Figure taken from Canto[72].

First, the thermal simulation is done by computing the heat equation:

$$\rho c_p \frac{\partial T}{\partial t} + \nabla \left(-k \nabla T\right) = r \tag{1.13}$$

where ρ is the density, c_p is the specific heat, T the temperature, k is the thermal conductivity and r the heat source.

The values of the specific heat c_p are taken from the DSC measurements and its evolution with temperature is such that it incorporates the latent heats of fusion and crystallization. Therefore r is considered as null in the equation (1.13). The conductivity k is chosen linear with temperature.

Second, the thermal expansion coefficient is fitted from thermomechanichal analysis (TMA) experiments made on small compacted cylinders both in radial and axial directions. The behavior of green and recrystallized PTFE are supposed to be elastic. Using Young's modulus evolution with temperature obtained from a dynamic mechanical analysis (DMA) experiment, the stress can be computed inside the billet. Stress arises from the different of thermal expansion due to thermal gradients.

A Von Mises plastic behavior with low yield stress is added in the molten state. Therefore plastic strains form in the molten state resulting in residual stresses at end of the cooling. Residual stress maps can be computed as shown in Figure 1.22 .

This simulation has the advantage of carrying out a mechanical simulation of the PTFE billet sintering. The results are compared with residual stress measurements.

Prospective studies for improved PTFE sintering simulations

In order to be able to perform more accurate simulations of PTFE sintering, a better knowledge on the properties of green PTFE have to be acquired. Beside the behavior of molten PTFE was not studied.

Then a thermomechanical model for PTFE during sintering taking into account its viscoelastic, viscoplastic or elastoplastic behavior has to be defined. So far the existing

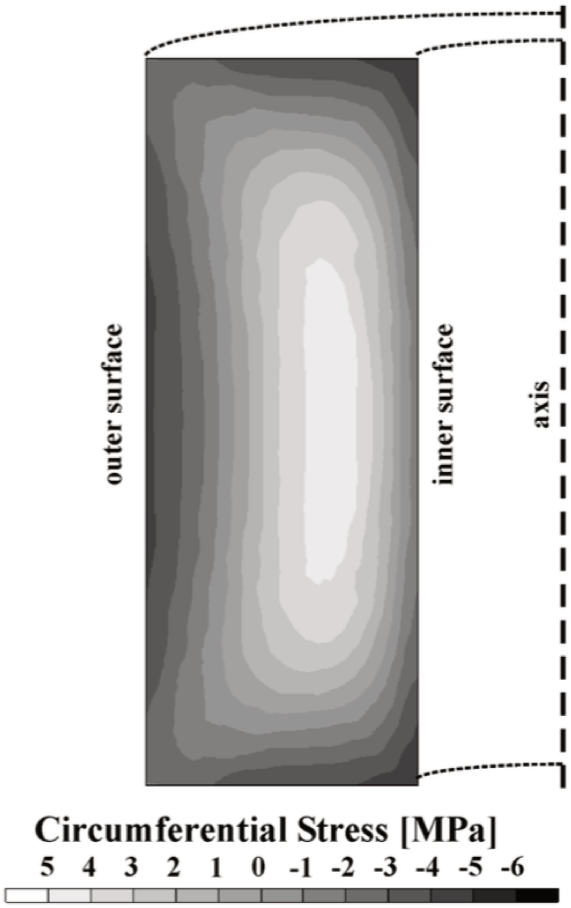

Figure 1.22: Circumferential residual stress map obtained from simulation of a billet sintering. Image taken from Andena [60].

models only reach 200°C.

The different thermal strain mechanism occurring during sintering could be modeled and especially to render the effect of crystallization kinetics.

Using those different models, a finer FE simulation could be developed. In particular, it could take into account variation of properties due to density gradients, and evaluate the effect of different crystallinity contents between core and edge. In Andena's simulation, the final residual stress is imposed by the plastic behavior of the molten state. As the whole billet has the same expansion coefficient, only the plastic strain can cause residual stresses in the end. This should be different when taking into account porosity closure and different crystallinity contents. It would also be interesting to investigate more on the properties of molten PTFE and get a precise mechanical model to improve the simulation.

Chapter 2

Material and methods

The material and the different experimental methods used to produce this PhD project are presented in this chapter.

Contents

Sections or subsections followed by an † are issued from the article:

PTFE crystallization mechanisms: Insight from calorimetric and dilatometric experiments, *to be submitted*

Sections or subsections followed by an • are issued from the article:

Orientation in transversely isotropic semi-crystalline polymer: application to uniaxially compacted PTFE, *to be submitted*

This chapter aims at presenting the material used in this study and the different experimental methods applied to characterized PTFE compacts behavior during sintering.

Section 1 deals with type of PTFE resin used and its pressing to form green parts. Differential scanning calorimetry (DSC) is presented in section 2. This technique is used to evaluate the thermal behavior, to characterize melting and crystallization in PTFE. In section 3, dilatometry is introduced to measure the thermal strain caused by a sintering cycle. An X-ray diffraction method for the characterization of the crystalline orientation in semi-crystalline polymers is described in section 4. Different observations methods detailed in section 5 were used to characterize and estimate the microstructure of PTFE compacts. Finally, the mechanical properties were evaluated thanks to different techniques and field measurement methods that are presented in section 6.

1 Material

1.1 PTFE resin

A fine cut (or low flow) granular PTFE resin was chosen. The initial crystallinity content of the powder is above 90 %. The molar mass of the powder is about 10^7 g/mol.

This type of resin is currently used for compaction molding and is suitable for compounding with fillers. More details on the difference between free flow, low flow resins and other type of PTFE powders are presented in Introduction .

On the SEM image of the PTFE powder in Figure 2.1, PTFE particles in the range of 20-100 µm can be observed. Those particles appear as fluffy flakes with a complex sub-microstructure (Figure 2.1b). The individual size of those elements is in the range of 100-500 nm. Therefore, two types of porosities can exist in the material after compaction, one *macro-porosity* to be linked with the particles size itself and a *micro-porosity* at a submicrometric scale. Chapter 4 deals with porosity and their evolution during sintering.

1.2 Thermal characterization

A calorigram of compacted PTFE is shown Figure 2.2. This experiment was performed on a differential scanning calorimeter with a 5 mg sample heated up at 20°C/min. The calorigram shows that the melting temperature of this resin is close to 340°C. It highlights an inflexion close to 250°C revealing a diffuse phase transition below the melting peak that could correspond to the melting of smaller crystals.

1.3 Sample preparation: cold pressing and slicing

In this work, PTFE compacts obtained (mostly) from uniaxial compaction are studied. Uniaxial pressing consists in filling a rigid die with PTFE powder and then compacting it by applying pressure with a piston. Figure 2.3 illustrates the powder compaction.

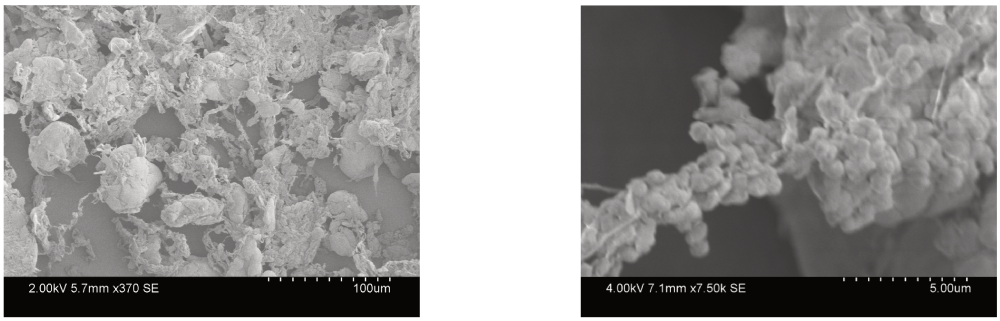

(a) (b)

Figure 2.1: SEM observation of the PTFE powder used for the experiments. (b) is a zoom of (a). The images are coming from an earlier work [10].

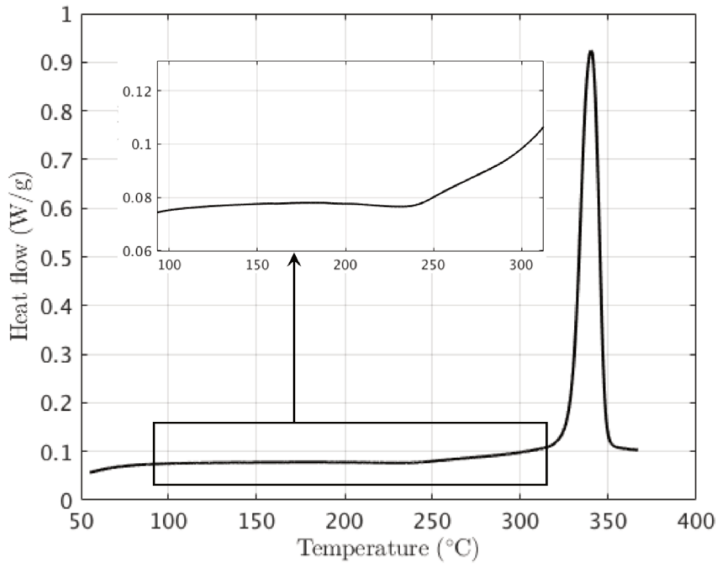

Figure 2.2: DSC melting peak of compacted PTFE powder. A zoom is shown at lower temperatures where a change is observed around 250°C

For all the experimental methods described in this chapter, the die of cross-section 8 mm × 8 mm was used to shape either cubes or rectangular blocks depending on the quantity of PTFE placed in the die. Density gradients and skin effects are induced by uniaxial compaction. The former is reduced by having a height as small as possible. The latter is considered to have little effect on dilatometry and is therefore neglected.

Another square die of section 35 mm × 35 mm was used to make 2 mm thick plates for the simulation validation experiment described later. A circular cross-section die with a diameter of 30 mm was used to make 20 mm high cylinders for another type of validation experiments (see Chapter 8).

The compaction was made on universal testing machine with an actuator displacement speed of 1 mm/min up to a given pressure. Then the actuator displacement was fixed for 5 min before unloading. The compaction pressure was mostly set at 50 MPa but samples were compacted at lower pressures to investigate the influence of the specimen green density

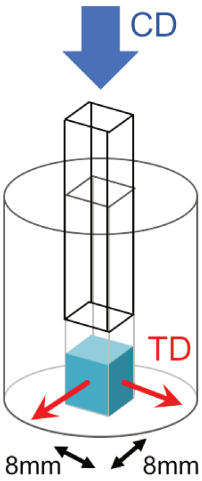

Figure 2.3: Uniaxial compaction of PTFE powder inside a metal die of 8 mm square section. The compaction direction (CD) and transverse directions (TD) are indicated.

on its dilatometric behavior during sintering in Chapter 4.

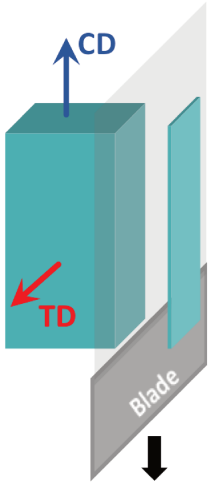

Figure 2.4: PTFE compacts are cut using a microtome to obtain 100 and 300 µm thick slices.

For differential scanning calorimetry (DSC) and for X-ray diffraction experiments (XRD), the PTFE blocks were sliced using a microtome (see sketch in Figure 2.4). 100 and 300 µm thick slices were obtained. The skin was always removed from the uniaxially pressed sample to measure only properties at the core. The cut were performed at ambient temperature. A preliminary cooling of the sample with liquid nitrogen could have been done to avoid any reorientation effects due to slicing. However no significant effect was noticed from the cut, so the cooling was not tested.

2 Differential scanning calorimetry (DSC)

2.1 Method description

Differential scanning calorimetry (DSC) is a thermal analysis method. It measures the heat energy uptake for a specific a thermal history. This method is used to characterize phase transitions. From the heat flow measurement, the transition temperature and the enthalpy associated can be estimated. For semi-crystalline polymers, this method is widely used to determine the glass transition, melting and crystallization [74, 75]. DSC is very convenient to study crystallization kinetic [76, 77].

The DSC method consists in measuring the temperature of the sample and of a reference sample, both placed in a precisely controlled oven. The temperature difference between the sample and the reference is related to the energy released or absorbed by the sample. At constant cooling or heating, it is linked to the specific heat capacity and latent heat of a phase change (see subsection 2.2).

To perform DSC on PTFE compacts, PTFE slices were punched into 5 mg disks. The thickness of the sample was limited to 100 µm to reduce thermal gradients (see subsection 2.3. The disk was placed in an standard aluminum pan (20 mg). A TA instruments Q10 was used for the DSC experiments. The heating and cooling rates were set between 0.5 to 20°C/min.

2.2 Crystallinity evaluation from DSC†

The specific heat of each phase, amorphous and crystalline, resp. $c_p^{\mathrm{am}}(T)$ and $c_p^{\mathrm{cr}}(T)$, can be well described as an affine variation with temperature. However the overall specific heat $\widetilde{c_p}$ is not linear with temperature during the crystallization as it depends on the crystalline mass fraction χ

$$\widetilde{c_p}(T,\chi) = \chi c_p^{\mathrm{cr}}(T) + (1-\chi)c_p^{\mathrm{am}}(T) \tag{2.1}$$

As the crystallinity content χ obeys a specific kinetic, it is not only dependent on temperature but also on thermal history, or during the DSC measurement performed at constant cooling rate, $\dot{T} = \phi$, on time and hence so does $\widetilde{c_p}$.

Ideally, the specific heat flux $\dot{q}$ extracted from a sample subject to melting or crystallization in a DSC experiment obeys

$$\dot{q} = \widetilde{c_p}\dot{T} + \Delta h^{\text{am-cr}}\dot{\chi} \tag{2.2}$$

where $\Delta h^{\text{am-cr}}$ is the specific heat of crystallization.

It is to be noted that both equations (2.1) and (2.2) are non-linearly coupled, so that the evaluation of χ during a DSC measurement at fixed cooling rate, $\dot{T} = \phi$, cannot be directly obtained. It is proposed to estimate χ from an iterative process where the above equations are progressively made consistent with each other at convergence through a fixed-point algorithm.

To evaluate the crystallinity content as a function of time (or temperature using the prescribed (constant) cooling rate $\dot{T} = \phi$), a baseline heat flux only due to the temperature change at fixed phase mass fraction, $\dot{q}_{\mathrm{base}}(t) = \widetilde{c_p}\dot{T}$, is introduced. However the measurement of c_p^{cr} for purely crystalline is not directly available for the computation of $\widetilde{c_p}$, so the asymptotic baseline of the recrystallized state $\dot{q}_{\mathrm{base}}^{\mathrm{recr}}(t)$ is used instead.

$$\dot{q}_{\mathrm{base}}(t) = \frac{\chi(t)}{\chi^\infty}\,\dot{q}_{\mathrm{base}}^{\mathrm{recr}}(t) + \left(1 - \frac{\chi(t)}{\chi^\infty}\right)\dot{q}_{\mathrm{base}}^{\mathrm{am}}(t) \tag{2.3}$$

where χ^{∞} is the estimated asymptotic crystallinity at room temperature evaluation of the recrystallized PTFE. $\dot{q}^{\text{recr}}_{\text{base}}(t)$ is related to $\widetilde{c_p}(T, \chi^{\infty})$ at the end of the crystallization which is dependent on $\dot{T} = \phi$.

The integration of $\dot{q}_{\text{exp}}(t)$ from which the baseline $\dot{q}_{\text{base}}(t)$ has been subtracted gives an evaluation of the crystallinity content $\chi(t)$ for a given cooling rate ϕ

$$\chi(t) = \frac{1}{\Delta h_{\text{am-cr}}} \int_{t_0}^{t} \left(\dot{q}_{\text{exp}}(t') - \dot{q}_{\text{base}}(t') \right) \mathrm{d}t' \tag{2.4}$$

where t_0 is the time of crystallization onset.

To initiate the determination of $\chi(t)$, a first evaluation is performed from the calorigram using a linear baseline for integration. Then, a new baseline is computed from Eq. (2.3), and from the latter, $\chi(t)$ is time integrated using Eq. (2.4). These two steps are repeated up to convergence to a fixed point, which requires typically no more than 2 to 3 iterations. This computation is performed in Chapter 5. Figure 5.2 shows the crystallization peak, the baseline at convergence and the integrated area.

2.3 Thermal gradient effects

In DSC experiments as the heating/cooling rates be significant compare to the sample thickness, thermal gradients can considerably modify the measurement. To gauge this effect, DSC experiments were performed on green PTFE at melting for various thicknesses at 20°C/min. The samples of different thicknesses were obtained by stacking PTFE disks in the DSC pan and therefore increasing the sample mass. Figure 2.5a shows the DSC signal for samples with different thicknesses. The melting peak widens due to thermal gradient as the thickness of the sample increases. Thermal gradients delay the heating in the core region causing a widening of the peak. This thermal delays effect on the melting peak can be retrieved by a mere thermal simulation. Figure 2.5b shows the melting peak simulated for a 100 µm and a 1 mm thick samples.

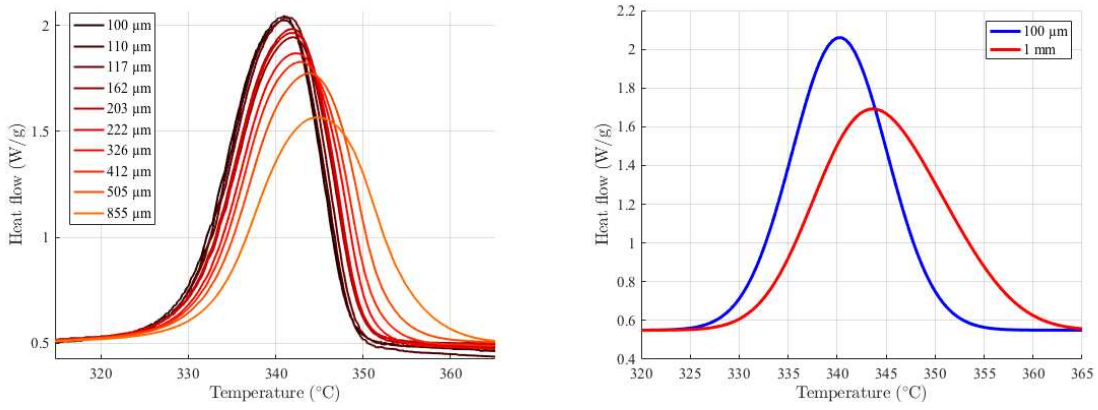

(a) (b)

Figure 2.5: DSC melting curves obtained for samples with different thicknesses at 20°C/min (a). A widening and a shift of the melting peak is observed for thicker samples. The same effect is retrieved with a thermal simulation of the DSC melting curve for 100 µm and 1 mm thick samples (b).

The same effect can be observed if the heating rate is too important. From the thermal simulation a sample heated up at 20°C/min the thermal gradient did not affect significantly the melting peak shape. Above 50°C/min thermal gradients are likely to modify the results for a 100 µm thick sample.

Therefore, one must be very careful when analyzing DSC results to be sure no thermal gradient effects are to be taken into account. At least, results should be compare in the same conditions (same thickness and heating/cooling rates). Studying crystallization kinetics requires to vary the cooling rates and thus the thermal gradient has to be carefully handle. It is important to choose sample thin enough and cooling rates not to high. Thus, the PTFE samples thickness was set at 100 µm and the heating/cooling rates did not exceed 20°C/min.

3 Dilatometric measurements

3.1 Method description

Dilatometry is a thermal analysis technique consisting in measuring the length or the volume evolution of a sample with temperature. Thermomechanical analysis (TMA) is the dilatometry method where the sample is maintained under a slight tension or compression during the thermal cycle. In practice, dilatometry is performed in a thermomechanical analyzer with load as small as possible to only ensure contact during measurement. Dilatometry is used to access thermal expansion coefficients and to study phase transitions.

For PTFE compacts, this experiment is able to reproduce sintering cycles at a small scale with quite uniform temperature in the specimen. During the sintering cycles, small PTFE cubes are melted and then recrystallized. The dilatometric measurements can also be compared to DSC measurements as they both give information on phase changes; here melting and crystallization (see Chapter 5).

For this work, PTFE cubic specimens were placed inside a thermomechanical analyzer TMA/SDTA 840 from Mettler Toledo. The oven controls the temperature and a probe placed on top of the sample measures its dimension (see Figure 2.6). The force applied by the probe was imposed at 0.01 N.

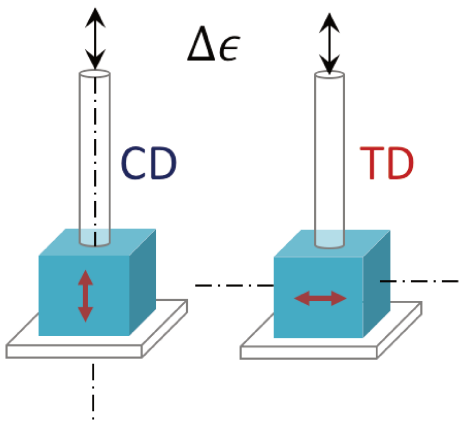

Figure 2.6: Measurement of the sample dimension variation during a thermal cycle in the compaction direction (CD) and in the transverse direction (TD).

Note that the dilatometric experiments on PTFE compacts were very repeatable inso-

far as the preparation conditions were the same. Dilatometric results appear to be sensitive to the compaction conditions. In particular, the powder temperature and maybe the hygrometry seem to modify the dilatometric behavior. To maintain the reproducibility of the experiments, the powder was stored at 4°C in a refrigerator before to compaction to remain below the crystalline phase transition at 19°C

Assuming a homogeneous state (from quasi-static temperature variations) the true (or logarithmic) strain ε_{ii} in direction i = CD *or* TD can be estimated from the displacement u_i and the initial size L_i, as

$$\varepsilon_{ii} \equiv \log\left(1 + \frac{u_i}{L_i}\right) \tag{2.5}$$

all along the thermal cycle (no implicit summation on index i). Note that this is the *mean* strain from the initial state considered as a reference, and the current state. Resorting to true strains allows us to change reference if so desired by mere subtraction of the strain of the newly chosen reference state.

The dilatometry test is performed on different samples, some to test the compaction direction (CD) and others for the transverse direction (TD) as the samples are transversely isotropic due to the uniaxial compaction (Figure 2.3).

From this transverse isotropy symmetry, the strain tensor is expected to be fully characterized by the TD and CD strain components. Choosing the third axis along the CD, the strain tensor assumes the following form

$$\boldsymbol{\varepsilon} = \begin{pmatrix} \varepsilon_{TD} & 0 & 0 \\ 0 & \varepsilon_{TD} & 0 \\ 0 & 0 & \varepsilon_{CD} \end{pmatrix} \tag{2.6}$$

3.2 Eigenstrain measurements†

In the dilatometric experiments, the temperature gradient was limited to a few degrees Celsius by choosing heating and cooling rates of maximum 2°C/min. Thermal computations showed that at this heating rate, the thermal gradient is maintained to 2°C between core and the edge of the specimen. Because of the homogeneity assumption and the assumption that the applied force is null, the measured strains are actually "eigenstrains" for constitutive law formulation of the thermo-mechanical behavior.

Eigenstrains correspond to the strains not related to external forces [78]. Among those stress-free strains are the thermal expansion and strain related to phase transformation. In practice, the eigenstrain is defined at the scale of the representative volume element (RVE). During phase transformations part of the microstructure can be constrained even if the stress is null at the scale of the RVE. The overall eigenstrain gathering the different eigenstrain components is expressed as ε^*_{ii}.

From the previous assumptions, the measured strains for PTFE compacts will be considered equal to the overall eigenstrain of PTFE,

$$\varepsilon_{ii} = \varepsilon^*_{ii} \tag{2.7}$$

During sintering, the eigenstrain of PTFE is caused by various physical mechanisms such as thermal dilation, phase change, void closure and residual stress relaxation. Those mechanisms will be studied in the next chapters (Chapters 3,4 and 5).

The volumetric strain is defined as

$$\varepsilon_v = \log\left(\frac{\upsilon}{\upsilon_0}\right) \tag{2.8}$$

with υ the specific volume and υ_0 the reference specific volume.

The crystalline mass fraction χ is also involved in ε_v as

$$\upsilon = \frac{1}{\rho} = \left(\frac{\chi}{\rho_{\text{cr}}} + \frac{1-\chi}{\rho_{\text{am}}}\right) \tag{2.9}$$

with ρ the total density, ρ_{cr} the density of the crystalline phase and ρ_{am} the density of the amorphous phase.

It can be shown that

$$\frac{\mathrm{d}\varepsilon_v}{\mathrm{d}T} = \frac{\mathrm{d}\chi}{\mathrm{d}T}\ \Delta\varepsilon_v^{\text{am-cr}} + f\ \beta_{\text{cr}} + (1-f)\ \beta_{\text{am}} \tag{2.10}$$

where $\Delta\varepsilon_v^{\text{am-cr}}$ is the volumetric strain induced by a crystallization, β_{cr} and β_{am} are the volumetric thermal expansion coefficient of respectively the crystalline and the amorphous phase, and f is the crystalline volume fraction related to χ via

$$f = \chi\,(\rho/\rho_{\text{cr}}) \tag{2.11}$$

with ρ the current density of the sample.

Due to the transverse isotropy of the sample, the volumetric strain can be computed via the strain in CD and TD:

$$\varepsilon_v = \varepsilon_{CD} + 2\varepsilon_{TD} \tag{2.12}$$

3.3 Crystallinity content evaluation from dilatometry

The same method than the one used to evaluate crystallinity content from DSC calorigrams 2.2 can be used for the dilatometric experiments. Equation (2.10) is modified to express the relative volume fraction $\tilde{f} = f/f^{\infty}$, where f^{∞} is the final volume fraction:

$$\frac{\mathrm{d}\varepsilon_v}{dT} = \frac{\mathrm{d}\chi}{\mathrm{d}T}\ \Delta\varepsilon_v^{\text{am-cr}} + \tilde{f}\ \beta_{\text{recry}} + (1-\tilde{f})\ \beta_{\text{am}} \tag{2.13}$$

with $\beta_{\text{recry}} = f^{\infty}\ \beta_{\text{cr}} + (1-f^{\infty})\ \beta_{\text{am}}$ the thermal expansion coefficient of recrystallized PTFE.

First β_{am} is obtained by fitting the measured thermal strain in the molten state. Then β_{recry} is evaluated by fitting the curve in the recrystallized state. A raw baseline is constructed with β_{am} and β_{recry}:

$$\begin{array}{lll} if & T > T_c, & \left(\frac{\mathrm{d}\varepsilon_v}{dT}\right)_{base} = \beta_{\text{am}} \\ if & T \leq T_c, & \left(\frac{\mathrm{d}\varepsilon_v}{dT}\right)_{base} = \beta_{\text{recry}} \end{array} \tag{2.14}$$

with T_c an evaluation of the temperature at which the crystallization starts.

Then a first estimate of the relative crystallinity fraction $\bar{\chi}_{exp} = \chi_{exp}/\chi_{exp}^{\infty}$ is obtained by subtracting $\left(\frac{\mathrm{d}\varepsilon_v}{dT}\right)_{base}$ to the variation of the measured strain $\left(\frac{\mathrm{d}\varepsilon_v}{dT}\right)_{exp}$ and after integration. Only the relative crystallinity fraction is obtained here as $\Delta\varepsilon_v^{\text{am-cr}}$ is not well evaluated.

From the first estimate of $\bar{\chi}$, a more realistic baseline can be computed:

$$\left(\frac{\mathrm{d}\varepsilon_v}{dT}\right)_{base} = \tilde{f}_{exp}\ \beta_{recry} + (1 - \tilde{f}_{exp})\ \beta_{am} \tag{2.15}$$

with $\bar{f}_{exp} = \bar{\chi}_{exp}(\rho_{exp}/\rho^{\infty}_{exp})$, where ρ^{∞}_{exp} is the density at the end of the experiment.

Using the new baseline, a better estimate of the relative crystallinity fraction $\bar{\chi}_{exp}$ can be obtained. The baseline generation process can be iterated to obtained an optimized baseline. This construction converges toward an evaluation of the relative crystallinity content $\bar{\chi}$.

An example of baselines generated with this methods is presented in Figure 5.9 in Chapter 5. Then the relative crystallinity content as function of temperature has been evaluated from dilatometry and compared to the one obtained from DSC in Figure 5.10.

4 X-Ray diffraction measurements (XRD)•

4.1 Method description•

X-ray diffraction (XRD) experiments provide information on the microstructure of semi-crystalline polymers [79, 80]. It gives access to the crystallinity content, the size of the crystalline domains and the preferred crystal orientations.

For this work, different configurations were used to study PTFE compacts morphology: a laboratory X-ray diffractometer and a synchrotron diffractometer at ESRF beam line D2AM BM02. From the former, experiments were done to analyze the crystallinity fraction and the orientation of the crystals. From the latter, in-situ experiment during crystallization were performed (see subsection 4.3 and Chapter 3). Figure 2.7a shows a X-ray diffractogram obtained at ESRF along 2θ. The peak of higher intensity correspond to the diffraction plane (100) of PTFE which is illustrated in Figure 2.7b. On the diffractogram, the broad bump below the (100) diffracting peak corresponds to the amorphous halo. Integrating both peaks enable to estimate the crystallinity content of the specimen (see Chapter 5).

In this chapter, XRD analysis was particularly used to quantify preferential crystal orientations. Characterization of the molecular orientation in a polymer is of prime importance when evaluating its (mechanical) properties. Moreover, this orientation results chiefly from processing conditions [82] and thus measuring it is essential to optimize the manufacturing in view of target applications.

In the case of semi-crystalline polymers, X-ray diffraction experiment is convenient for this purpose. The diffracted intensity in a certain direction can be related to the amount of crystals that meets Bragg's condition. The quantification of crystal orientation can be done using descriptors such as the Hermans orientation factor f_H which is constructed using the average of a square cosine of specific angles [83, 84] (its exact definition is provided in the next subsection 4.2). This factor is null when the object is isotropic and ranges from -0.5, when all the chains are perpendicular to the reference direction, to 1 when all the chains are aligned with it. It can also be seen as the projection of the molecular orientation probability distribution function (pdf) along the first order spherical harmonics $Y^0_1(\theta, \varphi)$ where θ is the polar angle wrt the reference direction, and φ the azimuthal angle. Even though it does not capture the complete information as it is only a projection of the orientation pdf, it reveals very convenient to compare different textures as they are condensed to a scalar.

Characterizing the orientation pdf is straightforward when a diffracting crystalline plane perpendicular to the chain direction is accessible via XRD measurements. However, it is

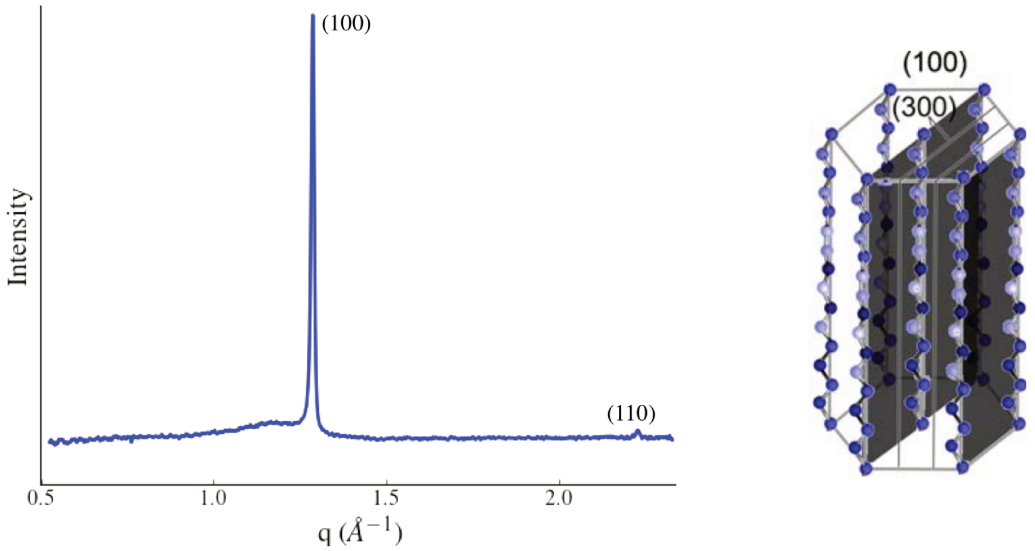

Figure 2.7: X-ray diffractogram along 2θ as function of the momentum transfer q (a). The peaks corresponding to the diffraction planes (100) and (110) are highlighted. Sketch of the (100) diffraction plane in a PTFE crystal taken from [81] (b).

hardly the case but diffraction planes including the chain direction are often accessible. It is often possible to quantify the molecular orientation pdf with diffraction measurements from two different crystalline planes. For example, the orientation of polyethylene (PE) chains can be obtained using the planes (110) and (200) [85, 86, 87, 88] via

$$\langle \cos^2 \theta_{PE} \rangle = 1 - 1.444 \, \langle \cos^2 \theta_{110} \rangle - 0.555 \, \langle \cos^2 \theta_{200} \rangle \tag{2.16}$$

Wilchinski [89] and then Sack [90] theorized the equations linking diffraction measurements to crystalline orientation. When no symmetry exist, defining two orientation factors is mandatory to represent a mean 3D orientation [91]. In the case where the analyzed diffraction planes contain the chain axis ($\boldsymbol{c}$ axis), two sets of planes are sufficient. Crystalline orientation was characterized in the case of polypropylene (PP) using diffraction planes (040) and (110) [92, 93], for polyvinylidene fluoride (PVDF) using the planes (110) and (020) [94], for PE (already mentioned) and for polyethylene terephthalate (PET) using plane (105) assuming it is perpendicular to the chain direction [95]. The same method can be used to characterize amorphous phase orientation from the amorphous halo [85]. The Hermans orientation factor relies on the second moment of orientation distribution and refinements can be made by taking into account the fourth moment [96].

In subsection 4.2, it will be shown that assuming 1) that the polymer crystals are statistically transversely isotropic along the chain direction and 2) that the processing conditions induce a transverse isotropy of the polymer chains, one can evaluate the chain orientation with no more than a single scan. In addition, high signal-to-noise ratio signals can be processed enabling faster acquisitions. This technique will be applied to measurements made on uniaxially compacted PTFE to eventually analyze an in-situ acquisition during crystallization in Chapter 5.

4.2 Orientation measurement in transversely isotropic semi-crystalline polymers•

General case

A good parameter for the orientation in polycrystalline material is $\langle \cos^2 \sigma \rangle$ the average square cosine of the angle σ between a given crystal axis $\boldsymbol{c}$ and a reference direction $\boldsymbol{Q}$. In the case of PTFE compacts, $\boldsymbol{Q}$ is chosen to be the compaction direction. The $\boldsymbol{c}$ axis corresponds to the direction of the macromolecule in the case of a polymer. In the latter case, let the $\boldsymbol{c}$ axis be one of the crystallographic direction, which is a common feature for semi-crystalline polymer crystals. The angles between $\boldsymbol{Q}$ and the other crystallographic directions a and b are denoted as δ and ϵ as shown in Figure 2.8.

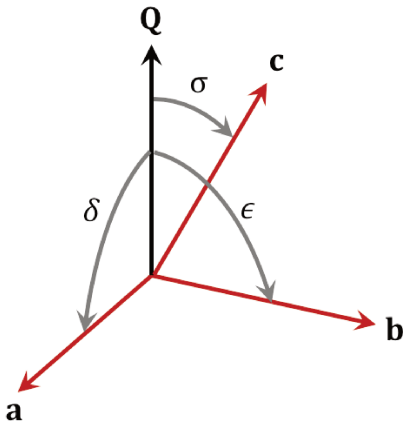

Figure 2.8: Angle definition between a reference direction Q and the crystal coordinate system (a, b, c).

However this parameter $\langle \cos^2 \sigma \rangle$ is usually not straightforward to obtain. Using X-ray diffraction, the orientation distribution of crystalline plane normals can be evaluated. This orientation is expressed through $\langle \cos^2 \phi \rangle$ where ϕ is the angle between $\boldsymbol{Q}$ and the normal $\boldsymbol{P}$ to the crystalline planes $\mathcal{P}$ for a given diffraction plane (hkl) (see Figure 2.9)

$$\langle \cos^2 \phi \rangle = \frac{\int_0^{\pi/2} \int_{-\pi}^{\pi} I(\phi, \psi) \cos^2 \phi \sin \phi \, \mathrm{d}\psi \mathrm{d}\phi}{\int_0^{\pi/2} \int_{-\pi}^{\pi} I(\phi, \psi) \sin \phi \, \mathrm{d}\psi \mathrm{d}\phi} \tag{2.17}$$

where $I(\phi, \psi)$ is the diffracted peak intensity for a sample orientation (ϕ, ψ).

$\langle \cos^2 \phi \rangle$ is related to the average of the cosines products of the angles characterizing the crystallographic directions (δ, ϵ and σ). This constitutes an equation with multiple unknowns depending on the observed crystalline plane [89]

$$\begin{aligned} \langle \cos^2 \phi \rangle \quad = \quad & e^2 \langle \cos^2 \delta \rangle + f^2 \langle \cos^2 \epsilon \rangle + g^2 \langle \cos^2 \sigma \rangle \\ & + 2ef \langle \langle \cos \delta \rangle \langle \cos \epsilon \rangle \rangle + 2fg \langle \langle \cos \epsilon \rangle \langle \cos \sigma \rangle \rangle \\ & + 2ge \langle \langle \cos \sigma \rangle \langle \cos \delta \rangle \rangle \end{aligned} \tag{2.18}$$

where e, f and g are coefficients related to the crystalline structure.

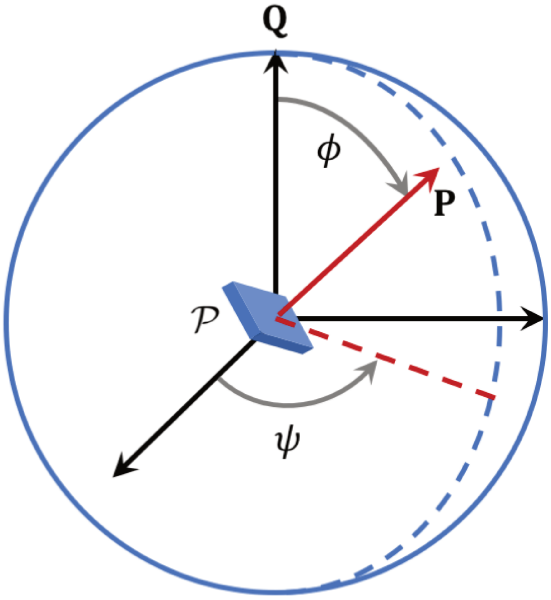

Figure 2.9: Definition of the angle ϕ between the reference direction $\boldsymbol{Q}$ and the normal $\boldsymbol{P}$ to a crystalline plane $\mathcal{P}$. The angle ψ characterizes the rotation of $\mathcal{P}$ around $\boldsymbol{Q}$.

The orthogonality relationship gives

$$\langle \cos^2 \delta \rangle + \langle \cos^2 \epsilon \rangle + \langle \cos^2 \sigma \rangle = 1 \tag{2.19}$$

Multiplying the peak measurements and using the crystalline symmetries enable to reach the required number of equations to solve the problem.

The Hermans orientation factor f_H is a common orientation descriptor based on $\langle \cos^2 \sigma \rangle$. It is the projection of the orientation along the second Legendre polynomial. The Hermans orientation factor expression is

$$f_H = \frac{1}{2} \left(3 \langle \cos^2 \sigma \rangle - 1 \right) \tag{2.20}$$

The Hermans orientation factor is null in the case of an isotropic configuration. It is equal to 1 if all the molecular chains are orientated in the Q direction and equal to -0.5 if all the chains are perpendicular to the Q direction. The definition of $\langle \cos^2 \sigma \rangle$ depends on the choice of Q. In the case of transverse isotropy, a restriction chosen in the next sections, it is straightforward to select Q along the preferential orientation axis. For a more complex orientation in three dimensions, defining two Hermans orientation factors can be necessary [91].

Diffracting plane containing the chain with statistical transverse isotropy hypothesis

Diffracting planes containing the crystal chain are often accessible with a high diffraction intensity. For example, the plane (110) in the case of PE, PP or PVDF or the plane (100) for PTFE are accessible for diffraction measurements. A new orthogonal coordinate system can be defined using the $\boldsymbol{c}$ axis containing the chain direction and a normal to the diffracting plane (axis $\boldsymbol{a}'$). The new coordinate system is presented in Figure 2.10 with the $\boldsymbol{b}'$ axis added to obtain an orthogonal system. δ' and ϵ' are the new corresponding angles between $\boldsymbol{Q}$ and the respective new axes $\boldsymbol{a}'$ and $\boldsymbol{b}'$.

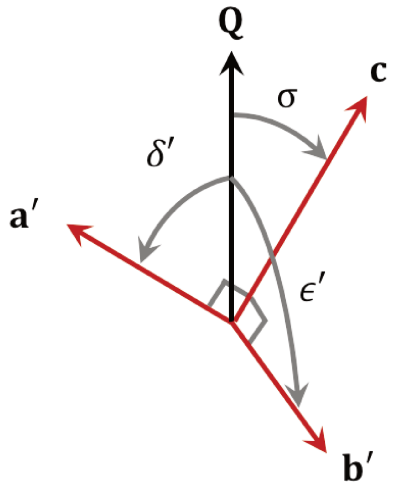

Figure 2.10: New coordinate system defined by $\boldsymbol{c}$ the chain direction and $\boldsymbol{a}'$ the normal to a diffracting plane containing $\boldsymbol{c}$. $\boldsymbol{b}'$ is constructed to create an orthogonal coordinate system, δ' and ϵ' are the angles between $\boldsymbol{Q}$ and the new axes.

The orthogonality relationship can be expressed using the new angles

$$\langle \cos^2 \delta' \rangle + \langle \cos^2 \epsilon' \rangle + \langle \cos^2 \sigma \rangle = 1 \tag{2.21}$$

Assuming that the axis $\boldsymbol{a}'$ is statistically equally distributed in the plane $(\boldsymbol{a}'\boldsymbol{b}')$ perpendicular to $\boldsymbol{c}$ allows to significantly reduce the unknowns. We call this assumption, the statistical transverse isotropy hypothesis, as it requires a statistical isotropy in the plane perpendicular to the chain direction. Therefore,

$$\langle \cos^2 \sigma \rangle = 1 - 2 \langle \cos^2 \delta' \rangle \tag{2.22}$$

The statistical transverse isotropy hypothesis is natural for polymers as the chain direction plays a very distinct role compare to the other directions. In some cases, this hypothesis can be confirmed by the very symmetry of the crystal. Such is the case for hexagonal crystals (such as PTFE). In some other cases where this hypothesis is not straightforward, it is necessary to validate it in the first place with an extra experiment in a perpendicular direction.

Due to the construction of the new coordinate system, the normal to the measured diffracted plane $\boldsymbol{P}$ is corresponding to the $\boldsymbol{a}'$ axis which is the normal to the crystalline plane of interest. Thus

$$\langle \cos^2 \phi \rangle = \langle \cos^2 \delta' \rangle \tag{2.23}$$

and finally

$$\langle \cos^2 \sigma \rangle = 1 - 2 \langle \cos^2 \phi \rangle \tag{2.24}$$

Transversely isotropic material

Furthermore, the material can be transversely isotropic due to process condition. This is the case for uniaxial compaction of PTFE powder. The transverse isotropy simplifies

further the diffraction measurement as it is no longer mandatory to access the full pole figure, but only a 2D measurement. Instead of recording the diffracted intensity $I(\phi, \psi)$ for both arguments, only the ϕ dependence is necessary as I is invariant with respect to ψ. Then equation (2.17) becomes

$$\langle \cos^2 \phi \rangle = \frac{\int_0^{\pi/2} I(\phi, \psi_0) \cos^2 \phi \sin \phi \, \mathrm{d}\phi}{\int_0^{\pi/2} I(\phi, \psi_0) \sin \phi \, \mathrm{d}\phi} \tag{2.25}$$

where I is obtained for only one configuration of $\psi = \psi_0$.

Hence the Hermans orientation factor can be computed as the scalar product of the measured diffractogram $I(\phi, \psi_0)$ with a simple trigonometric function $\cos(\phi)^2$. This provides a very noise-robust evaluation, which, in turn, is compatible with a fine temporal resolution for which very low signal-to-noise ratios are expected in the diffractogram. This is particularly beneficial when the measurement is done with a one-dimensional sensor by scanning along ϕ.

A mere quadrature of the integral shown in equation (2.25) can be performed at accordingly selected positions of ϕ in order to reduce the measurement uncertainty. This is particularly true when the X-ray diffraction is done with a one dimensional sensor by scanning along ϕ.

The transverse isotropy is a very common feature in polymer science. Combined with the statistical transverse isotropy hypothesis, very convenient crystalline orientation characterization can be achieved thanks to X-ray diffraction experiments. The experimental setup to perform such measurements is illustrated in the next section in the case of uniaxially compacted PTFE and the results are exposed in Chapter 5.

4.3 Experimental setups•

The PTFE slices used for the X-ray diffraction experiments are coming from compacted PTFE cubes. The uniaxial compaction induces transverse isotropy to the cube due to the axial symmetry of the process and the powder isotropy. Note that the die geometry (here cubic) could in principle modify this symmetry but in practice, it is safe to assume that transverse isotropy holds in the bulk material away from the specimen skin that may be affected.

The slices of PTFE are about 300 µm thick for the lab experiment and 100 µm thick for the experiment in the synchrotron facility. The reduction of thickness is linked to the heating plate used to restrain the thermal gradient. Those slices are such that they contain the compaction direction (CD) and the transverse direction (TD) (see Figure 2.4).

Orientations for green and sintered PTFE

Two samples were studied, one slice of green PTFE compact and one slice of PTFE that has been sintered. Sintering means PTFE was melted and then recrystallized. The objective was to determine whether sintering could modify the crystalline texture induced by uniaxial compaction.

Both samples were tested using a Philips X'Pert X-ray diffractometer with a copper source (with a generator voltage of 45 kV and a tube current of 40 mA). X-ray diffraction was performed in transmission with a θ-θ configuration (Bragg's condition) as shown in Figure 2.11. An azimuthal scan was done by varying ϕ over 180° at $2\theta = 18.3°$ corresponding

to PTFE diffraction peak (100). A single experimental value was obtained for each ϕ position. The position $\phi = 0°$ was chosen to correspond to CD and $\phi = 90°$ to TD.

The result of this experiment are presented in Chapter 5.

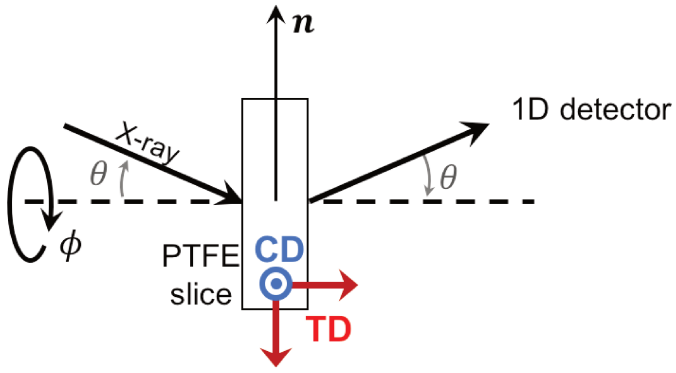

Figure 2.11: Sketch of the θ-θ diffraction setup. The sample is rotated along the horizontal axis to record the diffracted intensity along ϕ. The normal $\boldsymbol{n}$ is rotating in the PTFE slice from the compaction direction (CD) for $\phi = 0°$ to the transverse direction (TD) for $\phi = 90°$.

Evolution of orientation during *in-situ* crystallization

At the ESRF synchrotron facility, we had the opportunity to perform experiments on the D2AM line. Wide angles X-ray scattering experiments were carried out on 100 µm thick PTFE slices. The latter were placed on a Linkam heating stage THMS600 that can reach 150°C/min of heating/cooling rate. PTFE diffractograms were captured all along the crystallization thanks to the high intensity and high resolution of the beamline. Analyzing the crystalline peak during phase transformation gives access to the evolution of the crystallinity. It can then be compared to measurements made with differential scanning calorimetry (DSC). Similar *in-situ* experiments have been performed on other polymers to study the microstructural evolution during thermal treatment [97].

Another interesting piece of information provided by the *in-situ* measurement is the evolution of the crystalline orientation. The PTFE crystallization can be decomposed into primary and secondary crystallization mechanisms (as it is the case for many semi-crystalline polymers) [53, 46, 49]. The study of the crystalline texture gives the opportunity determine if both mechanisms induce the same orientation or not. Such information is essential to better understand the microstructural mechanisms responsible for the different crystallization processes and how they are related.

Figure 2.12 shows the diffraction setup used for the *in-situ* measurements. The X-ray source is perpendicular to the PTFE sample and the diffracted X-rays are collected with a 2θ angle on the 2D detector. The θ angle is related to a specific crystalline plane via Bragg's law. The integration of the crystalline peak along 2θ for each direction ϕ' gives access to $I(\phi', \psi_0)$.

Due to the 2θ angle tilt of the *in-situ* experimental setup (see Figure 2.12), the measurement does not give directly access to the diffracting intensity related to the compaction direction (CD). The normal to the diffracting crystalline plan cannot reach CD. $I(\phi', \psi_0)$ provides data on the integrated intensity $I(\phi, \psi_0)$ from $\phi = \theta$ to $\phi = 90°$ (using previous

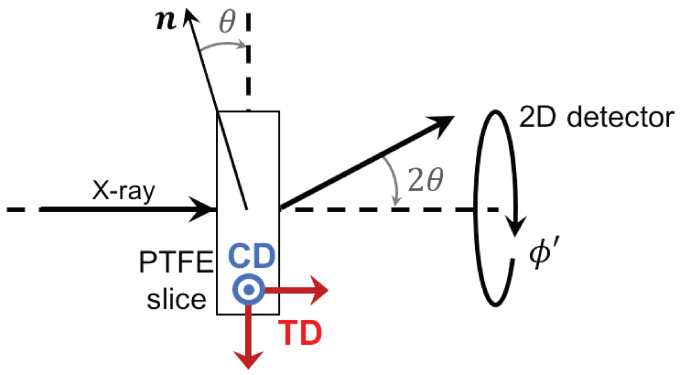

Figure 2.12: Sketch of the diffraction setup to obtain a 2D signal per capture. A drawback is that the diffraction normal is no more included in the plane of the PTFE slice.

definition, $\phi = 0°$ corresponds to CD and $\phi = 90°$ to TD). The variable change considered is $\cos\phi = \cos\phi' \cos\theta$. As the orientation is characterized by the Hermans function which is a projection of the cosine $\cos\phi$ along the second Legendre polynomial, the available information can be completed up to CD ($\phi = 0°$). The computation of the Hermans orientation factor f_H is then computed as described earlier.

The result of this experiment are presented in Chapter 5.

5 Microstructure observations

To better understand the physical mechanisms occuring during sintering, it is important to have a good knowledge of the microstructure of PTFE compacts. Microtomography and scanning electron microscopy (SEM) were used to characterize PTFE microstructure. Both techniques enable to evaluate the porosity level which has a great impact during melting (see Chapter 4).

5.1 Microtomography

X-ray microtomography is a nondestructive technique that gives access to the 3D imaging of the microstructure with a resolution around the micron [98]. It consists in taking different X-ray radiographies of a sample at various angles. Different algorithms exist in order to reconstruct the volume from the projections. The microstructure is accessible when the different constitutive elements have a different absorption coefficient, otherwise the contrast is null.

PTFE compacts were scanned using a laboratory microtomograph. Tomography scanning gives access to a quantification of the porosity which is higher than several microns in PTFE blocks. Chapter 4 focuses on the influence of the porosity on the thermal eigenstrain of PTFE during melting. Therefore it is important to be able to relate the compaction conditions to the porosity level. The type of porosity can also be observed in the limit of the scanning resolution (around few microns).

5.2 Scanning electron microscopy (SEM)

Scanning electron microscopy is an imaging technique giving access a nanometric resolution. An electron beam is used to scan the analyzed surface. The electrons interact with

the atoms at the surface. The electron can be received at different locations providing different types of information. The two common type of measured electrons are secondary electrons and backscattered electrons. The secondary electrons are useful for topography inspections and backscattered electrons are more interesting when it comes to distinguish different phases. A mix both types of electrons can also be used for imaging.

A low voltage scanning electron microscope Hitachi 4800 II was used to observed PTFE samples. Low voltage SEM gives good resolution on polymers without any conductive deposition on the surface [99]. PTFE compacts were cryofractured to access the bulk material with limited reorganization of the macromolecules on the splitted surface [100].

SEM scans reveal the PTFE microsctructure. It gives information on the porosity type for samples compacted at different pressures. Crystalline phase can also be observed via SEM. Those observations are interesting to understand crystallization mechanisms that take place in PTFE.

Environmental SEM (ESEM) is another type of SEM which is of interest for polymers as it gives the possibility to observe the sample without a vacuum chamber. For PTFE compacts with high porosity it could reduce the air pressure gradient which can affect the surface state by releasing the entrapped gas abruptly.

Transmission electron microscopy (TEM) is also an SEM alternative observation technique that could benefit the study of PTFE compacts. This type of microscopy gives information on the volume of the sample and is therefore more adapted to observe porosities. It can also achieve better resolutions. However the sample preparation is more difficult and only very thin slices can be analyzed.

6 Thermo-mechanical testings

6.1 Dynamic mechanical thermal analysis (DMTA)

Dynamic mechanical analysis (DMA) is a technique enabling to measure visco-elastic properties of materials [101]. Periodic stress or strain is applied to a small sample and respectively strain or stress is measured. The measured signal is analyzed. From the amplitude and the dephasing of the response, the storage and loss modulus are obtained. They characterize the elastic and viscous properties of the material. The amplitude and the frequency of the applied load can be varied to scan the properties of the material.

Dynamic mechanical thermal analysis (DMTA) enables to vary the temperature along the test. This test is widely used to characterize the viscoelastic behavior of polymers [102, 103].

Sintered PTFE beams of dimensions 8 mm $\times$ 8 mm $\times$ 20 mm wear clamped in the dynamic mechanical thermal analyzer (MCR 502 Anton Paar). The specimen was tested with a torsion device. This type of loading was the most convenient with this geometry. Bending, cpmpression or traction setups could be considered for other geometries. Green PTFE could not be tested as it is too brittle to be clamped without a breaking the sample.

Temperature scans between 30 to 370°C at heating (2°C/min) were made at fixed frequency and fixed amplitude (1 Hz and 1%) in Chapter 6 (see Figure 6.1). It gives the storage and loss modulus as functions of temperature. The damping curve highlights the phase transition of PTFE (β and γ transitions). The Young modulus evolution can be obtained from the storage modulus measurement.

Other tests were performed at fixed temperature and especially in the molten state to investigate the properties of the melt. Frequency scans were performed between 0.002 and

1 Hz at strain amplitude 1 and 10 %. This frequency range was chosen to investigate the long-term behavior. The temperature was varied between 310 to 360°C.

6.2 Compression tests in thermal chamber

Mechanical tests using a thermal chamber are necessary to evaluate the thermo-mechanical behavior of PTFE. An hydraulic universal testing machine (MTS TTC) with a thermal chamber was used to perform them (see Figure 2.13). The thermal chamber is a Carbolite Gero furnace with a three thermal zone control of maximal temperature 800°C and features five windows at 45° from each other. The interest of those windows is to lighten the sample and to capture images (either visible or infrared light) to perform digital image correlation (DIC) and measure the temperature field. The image acquisition can be performed during thermal cycle, during mechanical testing or both at the same time. The optical camera used for the experiments was a Canon EOS 70D and the infrared camera was a Jade from CEDIP Infrared Systems.

Figure 2.13: Thermal chamber placed on an hydraulic universal testing machine. The thermal chamber features five windows (whose normals make an angle of 45° with respect to its neighboring window) to perform optical acquisitions and to light up the sample.

Compression tests were performed on PTFE blocks. Compression plates with an insulating part were used (see Figure 2.14). The aim of those insulating part is to reduce the thermal gradient unfortunately present in the sample during the test. Due to size of the apparatus and the necessity to cool the actuator and the load cell, thermal gradients are

inevitable. Isothermal test are more adapted to the mechanical testing. The tests have to be performed after a sufficient waiting time to ensure that the temperature is uniform and stable with time in the sample and in the testing device. Anisothermal are achievable as well but the evaluation sample temperature is more difficult.

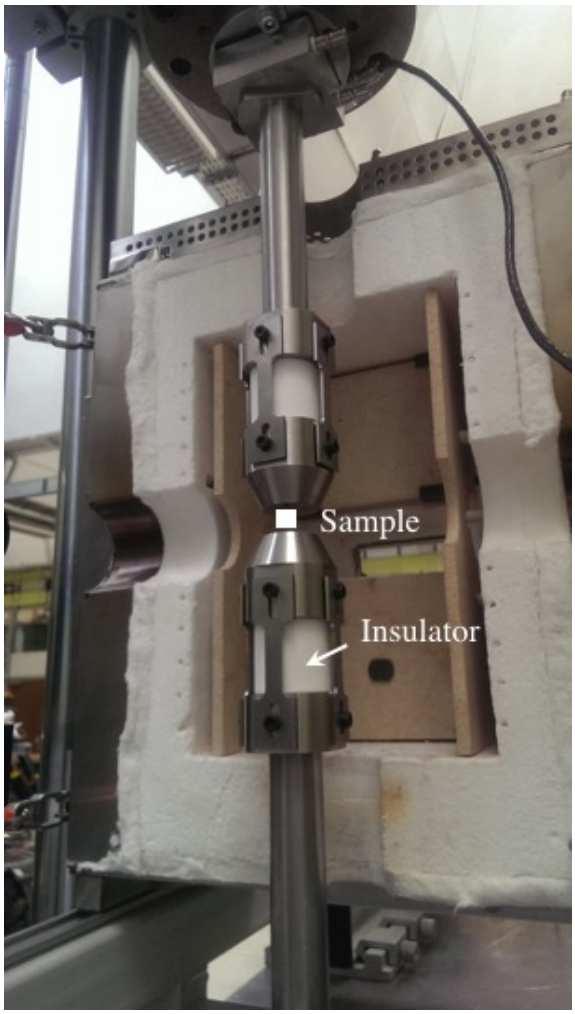

Figure 2.14: Compression plates placed in the thermal chamber. The rear part of the thermal chamber has been removed for the picture. The white insulating parts were designed to reduce the thermal gradient in the sample.

Different thermocouples were placed in the oven. For some experiments thermocouples were placed inside the PTFE sample, however this affects the thermal conditions and modifies boundary conditions of the test. Infrared measurements were taken to evaluate the sample temperature field through germanium windows. The interest of infrared measurements is to access not only the temperature but also the thermal gradient inside the part.

Compression tests were performed on small PTFE cubes (8 mm) and on bigger PTFE blocks (20 mm $\times$ 20 mm $\times$ 40 mm). Those experiments are analyzed in Chapter 6.

The elastic properties can be evaluated for both sintered and green PTFE. Green PTFE properties are usually more challenging to obtain as the material is very brittle. Different

types of loadings are needed to evaluate the non linear behavior (visco-elastic, visco-plastic or elasto-plastic) of the material as function of temperature.

6.3 Digital image correlation

Digital image correlation is a method that uses optical images to perform displacement field measurements. Two images of the surface of a material are compared to determine the transformation required to register one image onto the other one [104].

An image can be defined as a scalar function giving the gray level at each discrete point of coordinate $\boldsymbol{x}$. $f(\boldsymbol{x})$ and $g(\boldsymbol{x})$ denote respectively the original image and the deformed one. The displacement field is noted $\boldsymbol{u}(\boldsymbol{x})$. The assumption of conservation of the optical flow (conservation of the gray levels) ensures that

$$f(\boldsymbol{x}) = g\left(\boldsymbol{x} + \boldsymbol{u}(\boldsymbol{x})\right) \tag{2.26}$$

$\boldsymbol{u}$ can be estimated by minimizing the cost function

$$\Phi = \int_{\Omega} \Big(f(\boldsymbol{x}) - g(\boldsymbol{x} + \boldsymbol{u}(\boldsymbol{x})) \Big)^2 \mathrm{d}\boldsymbol{x} \tag{2.27}$$

where Ω is the studied domain.

DIC is often conducted locally to determine independently the displacements of zones of interest (subsets of pixels).

Global DIC is an alternative approach which consist in solving the problem over the entire studied domain by ensuring that the displacement can be decomposed along specific spatial functions such as finite element shape functions [105]. The displacement can therefore be expressed as

$$\boldsymbol{u}(\boldsymbol{x}) = \sum_{\alpha,\Psi} a_{\alpha n} \Psi_n(\boldsymbol{x}) e_\alpha \tag{2.28}$$

with $a_{\alpha n}$ the amplitudes, Ψ_n the shape functions and e_α the unit vectors in direction α.

The minimization of the cost function Φ using a (quasi-)Newton's method, leads to a linear system that can be written as

$$\boldsymbol{M}\boldsymbol{a} = \boldsymbol{b} \tag{2.29}$$

where $\boldsymbol{a}$ corresponds to the correction of the current estimate of the displacement field, $\boldsymbol{M}$ to a matrix and $\boldsymbol{b}$ is a second member proportional to the *residual* (i.e. the difference between the deformed image corrected with the current determination of the displacement field and the reference image).

Mechanical regularization can be added to the global DIC cost function in order to enforce the mechanical admissibility of the measured displacement field [106]. The relative weight of the regularization term with respect to the DIC cost function defines (the fourth power of) a regularization length and can be tuned during the iterative solving of the DIC problem.

The optical flow rests on the conservation of gray levels/brightness and can reveal to be unsuited for different images. Artifacts, external lightning or change in the surface absorption coefficient can modify the gray level distribution. Brightness and contrast corrections can be added to the DIC problem to account for those changes [107]. It is useful in the case of PTFE which becomes translucent in the molten state.

DIC was used to obtain displacement field measurements on the surface of PTFE specimens inside an oven during the thermal treatments.

6.4 Infrared thermography

Infrared thermography measurement is a technique that gives access to the temperature field at the surface of an object by measuring its emission of (IR-) light within a given range of wavelengths.

The intensity of the perceived radiations R_p of an opaque body can be expressed as [108]

$$R_p = \epsilon\ R_t + (1 - \epsilon)\ \Phi \tag{2.30}$$

where ϵ is the emissivity of the analyzed surface, R_t is the spectral exitance and Φ is the intensity of the surrounding radiations reflected by the analyzed surface. The spectral exitance R_t corresponds to the energy flux radiated by the observed surface at a temperature T. The Stefan-Boltzmann law states that

$$R_t = \sigma_{SB}\ T^4 \tag{2.31}$$

where $\sigma_{SB} = 5.67 \times 10^{-8}\ \mathrm{Wm^{-2}\ K^{-4}}$.

Usually, the observed surface is covered with black paint in order to increase the emissivity and to make it as uniform as possible. Therefore the surface emissivity is approximated as being unity, and the IR camera is calibrated with a black body ($\epsilon = 1$) over the expected temperature range. Finer calibrations can even be achieved by correcting additional effects such as camera housing temperature leading to a significant reduction in the measurement uncertainties [109, 110].

For the sintering experiment of a PTFE plate in an oven (detailed in Chapter 8), the required measurement precision is only of a few degrees Celsius due to the wide range of temperature swept and due to the model parameters uncertainties. Besides, the PTFE plate cannot be covered by black paint because of the large expansion of the material during sintering. Instead, PTFE surface was sprayed with black paint to form a speckle used for DIC. Therefore, a basic calibration was performed to relate the speckled PTFE surface temperature to the digital levels. A separate experiment was conducted where the surface temperature was measured simultaneously with a thermocouple placed inside the PTFE plate close to the surface and by infrared measurements. Figure 2.15 shows the digitial levels corresponding to the region measured by the thermocouple as a function of the temperature measured by the thermocouple. The evolution was extrapolated with an exponential fit to cover the temperature range between 150 and 400°C. The extrapolation potentially induces significant errors for temperature far from the measured ones. Some adjustments will be made to try to overcome these errors in Chapter 8.

In this work, thermography measurements were used to access the complete experimental conditions during sintering thereby offering a safe ground for comparing quantitatively the FE analysis with measurements made on a validation experiment in Chapter 8.

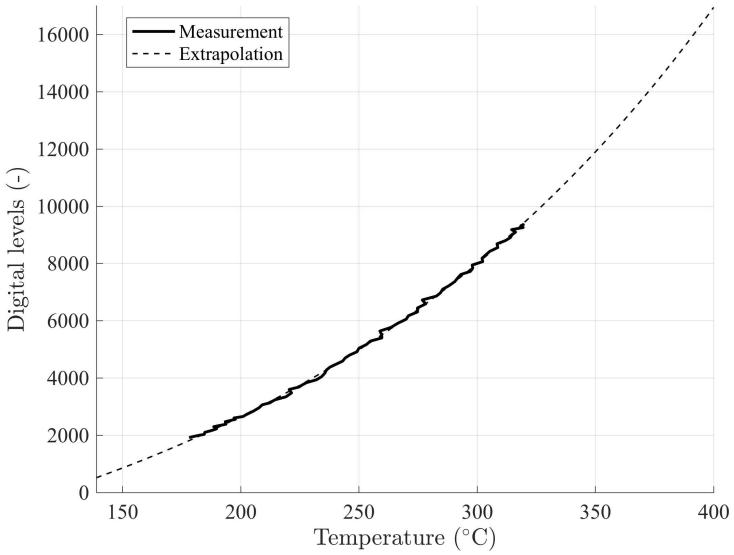

Figure 2.15: Relation between digital levels measured on PTFE plate surface and its temperature. This relation has been obtained from a specific experiment and extrapolated over a broader temperature range.

Part I

Thermal uniformity

Monochrome bleu, Yves Klein, Centre Pompidou

Chapter 3

Green PTFE behavior: residual stress relaxation

This chapter analyzes the thermal (eigen)strain of green PTFE before it completely melts. An original mechanism of residual stress relaxation occurring at first heating is described.

Contents

Sections or subsections followed by an * are issued from the article:

Thermal cycling of cold-pressed PTFE compacts: Reversible and irreversible behavior, *Polymer Testing*, 2019 [111]

1 Introduction

Green PTFE is an assembly of deformed particles. Oedometric compaction process is generally used for convenience compared to isostatic compaction process. However uniaxial pressing induces orientation effects. The dimensions of the part are constrained in the transverse directions (TD) whereas in the compaction direction (CD), the part is widely deformed. It will be shown in Chapter 5 that oedometric compaction induces a crystalline orientation. The macromolecules are more preferentially orientated in TD.

During a thermal cycle, green PTFE deforms due to different physical mechanisms. Among them, melting, thermal expansion and porosity closure are responsible of the overall thermal eigenstrain [72]. This chapter aims to study the overall eigenstrain (concept defined in Chapter 2) of a PTFE compact through arbitrary thermal histories, and to unravel the role of different mechanisms.

Dilatometry measurements during thermal cycles reveal an unexpected evolution of the eigenstrain, formally similar to elasto-plasticity, that can be decomposed into reversible and irreversible parts. A descriptive model is developed in section 2 to express this strain as a function of the maximum experienced temperature. The tensorial aspect of the reversible and irreversible parts of the eigenstrain is studied and reveals the anisotropy induced by the initial cold pressing. This observation translates into a swelling of the material as a result of internal stress relaxation, suggesting the creation of micro- or meso-porosity. This behavior was observed below melting and a discussion on its extension to the melting itself is proposed in section 3.

2 Behavior of nascent PTFE below melting*

Material, sample preparation and the dilatometric experimental method are mentioned in Chapter 2. It will be assumed that in the PTFE samples compacted at 50 MPa, the level of *macro-porosity* can be neglected (this will be discussed in next Chapter 4). Moreover, no porosity was observed using X-ray computed microtomography with 1 µm resolution. Another impact of the compaction is the induced orientation texture. As the PTFE is uniaxially compacted in a mold, the crystals are reoriented in the transverse directions (perpendicular to the compaction direction). A Herman's orientation factor for the chains orientation of -0.09 was determined in the compaction direction via X-Ray diffraction [112] (see Chapter 5).

In this section, successive thermal cycles with an increasing maximal temperature were chosen to investigate the strain behavior of compacted PTFE powder under thermal treatment below melting temperature. The thermal path consisted of three successive cycles reaching, respectively, 175°C, 250°C and 300°C (Figure 3.1a). The heating and cooling rates were 1.5°C/min and the holding time at maximal temperature was 30 min for each cycle. The PTFE specimen was held for 5 min at 25°C before each new cycle. A final cycle ended the thermal path to complete the sintering of the sample, with the same heating and cooling rates with a longer plateau of 100 min above the melting temperature at 370°C.

In this paper, $\theta = T - T_0$, refers to the temperature variation counted from the reference temperature T_0 which was chosen to be 25°C.

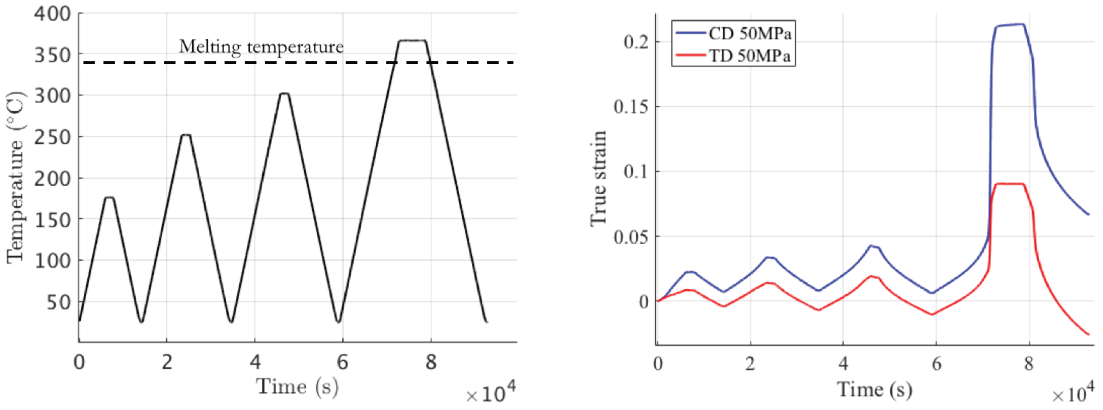

(a) (b)

Figure 3.1: Thermal cycle applied to the small PTFE block (a) and related measured true strain in compaction direction (CD) and transverse direction (TD) as function of time (b).

Figure 3.1b shows the true strain curves for CD and TD as function of time.

2.1 Reversible and irreversible eigenstrain decomposition*

The major strain variations are observed during the last thermal cycle at the end of the test and correspond respectively to melting and crystallization of PTFE compact as crystalline phase is denser than amorphous phase. The strain due to crystallization stretches on a longer temperature range than melting. The melting mechanism is essentially controlled by the crystallite size distribution of the PTFE resin [34]. In contrast, the crystallization is ruled by different mechanisms that depend on the cooling rate. The crystallization mechanism is a complex and not fully understood topic due to the presence of secondary crystallization [53, 54]. Because of this, the present study does not address melting and crystallization mechanisms, but rather focuses on the earlier stages prior to melting which, although simpler, reveal unexpected manifestations of stress relaxation already observed by Canto et al. [72]. Nevertheless, the last cycle that goes above melting temperature is shown in some of the following figures in order to see the very strong effect of sintering.

The CD and TD strains versus time are shown in Figure 3.1b with the reference chosen at the initial state at temperature T_0. A first observation is that the CD and TD directions show very different strains, even in the first three cycles. This means that the cold uniaxial compaction process induces pronounced anisotropy [60, 10, 113, 114]. After successive cycles, the sample tends to dilate in the compaction direction (CD), and to contract in the transverse direction (TD), and the apparent coefficient of thermal expansion appears to differ in these two directions, again a manifestation of compaction-induced anisotropy.

When plotted as a function of temperature rather than time, as done in Figure 3.2, it is observed again that sintering has a very major impact on the dilatometric behavior and, as mentioned above, the present study focuses on the pre-melting behavior, as shown in Figures 3.2b and 3.2d. In this first subsection, any of the principal eigenstrain, CD or TD, is considered independently without index.

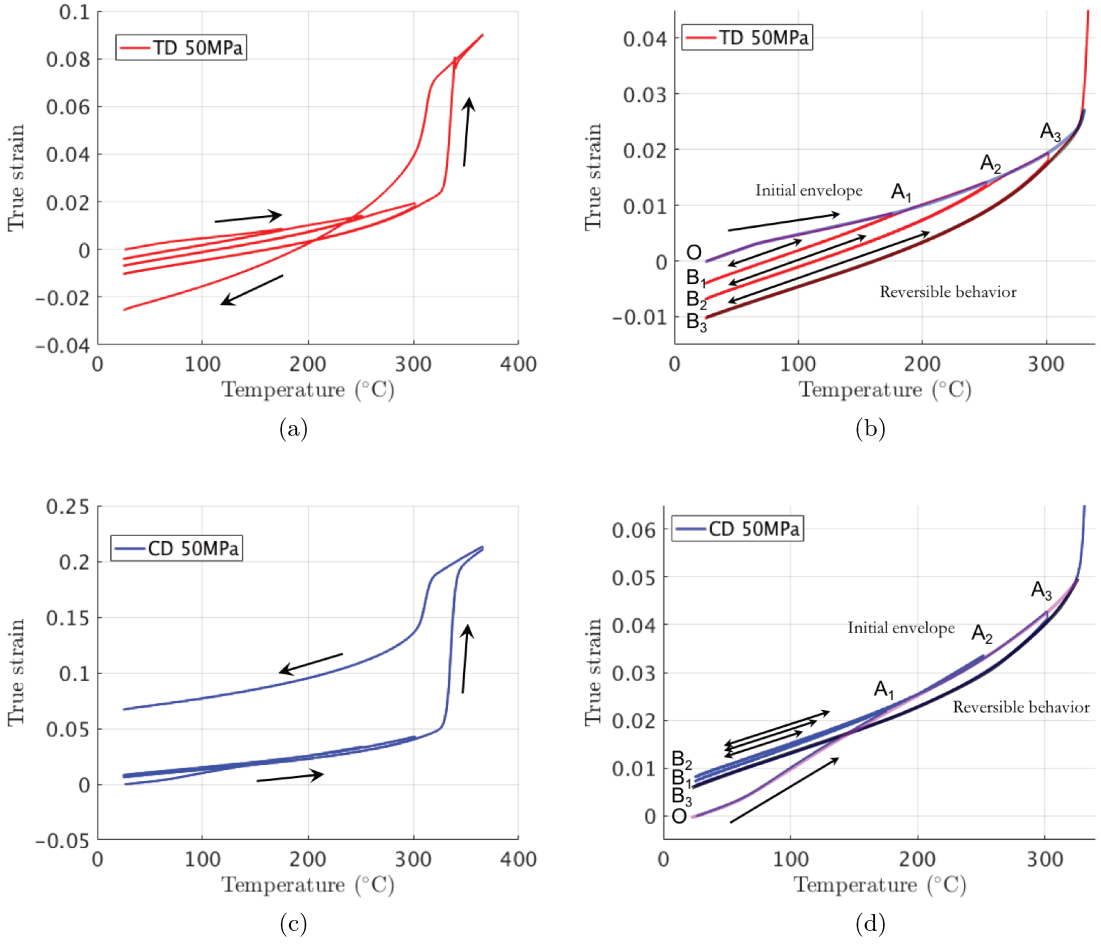

Figure 3.2: (a) Measured true strain in TD; (c) Measured true strain in CD; (b) zoom of (a) and (d) zoom of (c) on the three rst cycles prior to melting, where the followed path is $O - A_1 - B_1 - A_1 - A_2 - B_2 - A_2 - A_3 - B_3 - A_3$. Branches $A_i - B_i$ appear to be reversible behaviors valid when the temperature remains lower than that of point A_i.

These figures first show that, even in the absence of phase transformation, the thermo-mechanical behavior is *not* a reversible thermal dilation, in as much as the thermal eigenstrain is not given by a single function of the temperature variation. However, when the temperature variation is decreased from any previously experienced peak value τ, then a one-to-one relationship between eigenstrain and θ is observed, as can be seen for all branches $B_i - A_i$ in Figure 3.2b or 3.2d. These curves seem, however, to depend on but in a rather simple way: mere translations along the strain axis allow all reversible branches to superimpose exactly. This observation suggests that two parameters are needed to characterize the thermo-mechanical eigenstrains: 1) the current (relative) temperature, θ, along a reversible path and 2) the maximum previously experienced relative temperature,

$$\tau(t) = \max_{t' \leq t} [\theta(t')] \tag{3.1}$$

that controls the overall translation of the thermal response. Moreover, an additive

decomposition of the overall thermal eigenstrain into two contributions can be made:

$$\varepsilon[\theta(t)] = \varepsilon^{\text{rev}}(\theta(t)) + \varepsilon^{\text{irr}}(\tau(t)) \tag{3.2}$$

where ε^{rev} is the thermal expansion that only depends on the instantaneous relative temperature, θ, and ε^{irr} is an irreversible eigenstrain that only depends on the maximum of the previously encountered relative temperature. Note that the notation $[\theta(t)]$ refers to a functional dependence over the entire (past) temperature history, whereas $(\theta(t))$ refers to a function dependence on the scalar instantaneous variation of temperature occurring at time t.

This additive strain decomposition is formally reminiscent of the one encountered in (rate-independent) elasto-plasticity, but where relative temperature plays the role of stress. Introducing the functions defining the reversible and irreversible eigenstrains for $i \in \{\text{CD}, \text{TD}\}$:

$$\begin{array}{rcl} \varepsilon_i^{\text{rev}}(\theta) & = & f_i(\theta) \\ \varepsilon_i^{\text{irr}}(\tau) & = & g_i(\tau) \end{array} \tag{3.3}$$

It is easy to have access these functions experimentally by noting the following property: In the thermal cycles, one can select those instants of time noted t^+ where $\tau(t^+) = \theta(t^+)$. For those, the eigenstrain obeys

$$\begin{array}{rcl} \varepsilon_i(\theta(t^+)) & \equiv & \varepsilon_i^{\text{envel}}(\theta(t^+)) \\ & = & \varepsilon_i^{\text{rev}}(\theta(t^+)) + \varepsilon_i^{\text{irr}}(\theta(t^+)) \\ & = & f_i(\theta(t^+)) + g_i(\theta(t^+)) \end{array} \tag{3.4}$$

This relation is the "envelope" curve (path $O - A_1 - A_2 - A_3$) of Figures 3.2b or 3.2d and drawn in purple. Conversely, the longest descending temperature ramp ($A_3 - B_3$), corresponds to instants of time noted t^- for which τ is frozen to the temperature reached at point A_3, τ_3, and hence

$$\begin{array}{rcl} \varepsilon_i(\theta(t^-)) & \equiv & \varepsilon_i^{\text{desc}}(\theta(t^-)) \\ & = & \varepsilon_i^{\text{rev}}(\theta(t^-)) + \varepsilon_i^{\text{irr}}(\tau_3) \\ & = & f_i(\theta(t^-)) + g_i(\tau_3) \end{array} \tag{3.5}$$

Thus the reversible eigenstrain function is obtained (for $\theta < \tau_3$) as

$$f_i(\theta) = \varepsilon_i^{\text{desc}}(\theta) - \varepsilon_i^{\text{desc}}(0) \tag{3.6}$$

while the irreversible part is

$$g_i(\theta) = \varepsilon_i^{\text{envel}}(\theta) - f_i(\theta) \tag{3.7}$$

An illustration of the evaluation of these eigenstrains in the TD and CD directions is given in Figure 3.3.

The irreversible part of the eigenstrain g_i is very close to 0 up to about 60°C, just as if the PTFE sample had already experienced such a maximum temperature in its past. In some way, the function g encodes a memory of the sample. However, it may be that the effect of temperature can also be obtained with time through similar, but now thermally activated, irreversible microscopic events. This temperature-time analogy has, however, not been studied herein.

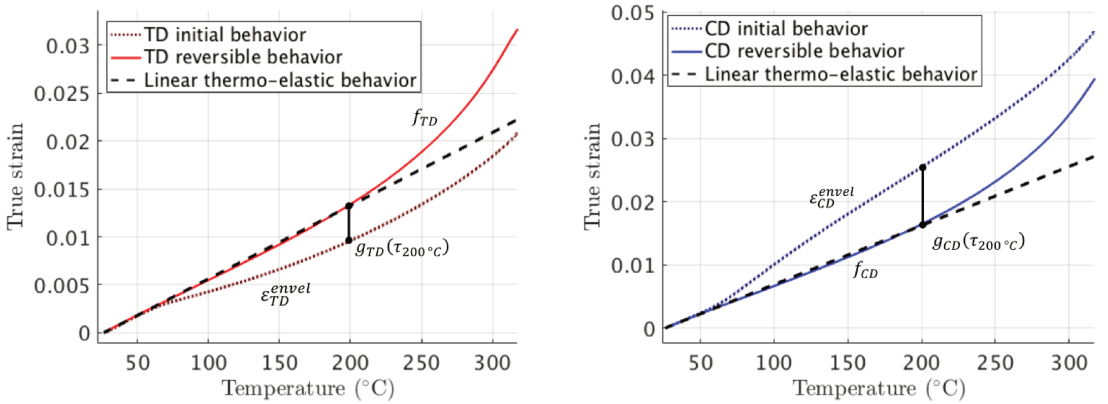

Figure 3.3: Evaluation of the overall eigenstrain split in the reversible and irreversible contributions for (a) the TD direction and (b) the CD direction.

Both CD and TD directions obey the same formalism, thereby reducing the full history dependent behavior to four (reversible and irreversible parts, CD and TD directions) scalar functions. However, they show very different quantitative contributions. This sheds some light on the subtle question of anisotropy.

The quantification of anisotropy can be done from the direction of the path followed by eigenstrains in strain space. The symmetry of the problem reduces the tensorial nature of the strain tensor to only two components CD and TD.

From 200°C and above, some new features that were not visible at lower temperatures begin to appear. First, the reversible part is very close to linear up to 200°C, and markedly non-linear (yet still reversible) above. Second, a more and more pronounced gap appears at temperature reversal points of the cycles (Figure 3.2), suggesting the progressive relevance of viscous effects that could be neglected at lower temperatures [24]. Third, the irreversible part of the eigenstrain seem to reveal higher and higher densification, which may be due to a different phenomenon than in the low temperature regime where a net expansion is observed. One may speculate that the collapse of nano-cavities may take place and contribute to the irreversible mechanism at such high temperatures. The melting of smaller crystals suggested by the calorigram shown in Chapter 2 (see Figure 2.2) around 250°C may help close nano-cavities.

The plots of the irreversible and thermo-elastic (reversible) eigenstrains in CD and TD against each other are shown in Figure 3.4. In such plots, an isochoric (isovolumic) transformation is a straight line of slope -2 because of the transversely isotropic character of the specimen.

In Figure 3.4a, the irreversible eigenstrain contribution corresponds at low temperature to a fixed direction in strain space, so that the ratio of volumetric to deviatoric strain is constant and positive (meaning an irreversible swelling). Because no phase transformation is expected in this range of temperature, such an effect could correspond to the opening of nanopores. The scale of those pores is termed nano to signify submicrometric, as they are not seen in X-ray computed micro-tomography. It would be interesting to use small angle X-ray scattering to investigate this point. At about 200°C, a contraction character begins to set in and, as mentioned above, it could correspond to the closing of nano-cavities.

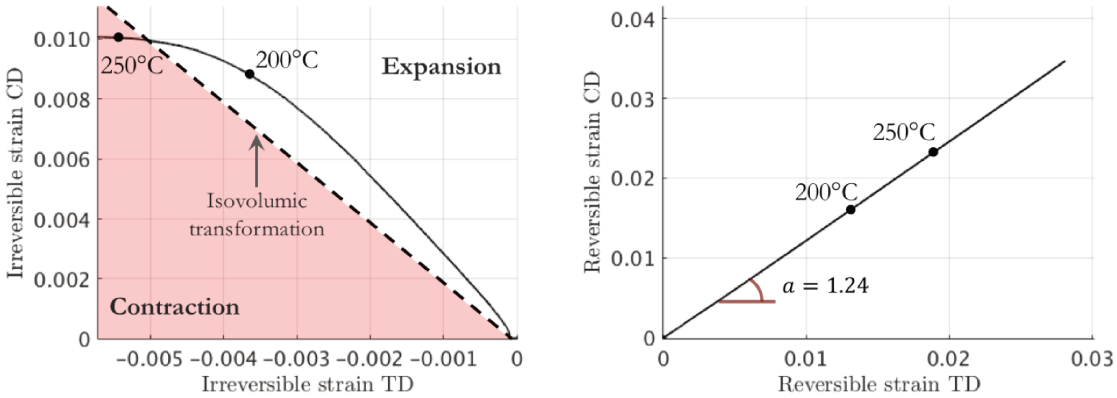

Figure 3.4: Residual stress relaxation in CD as function of the residual stress relaxation in TD for the (a) irreversible and (b) reversible eigenstrains.

The thermo-elastic eigenstrain contribution shown in Figure 3.4b is remarkably linear and reveals anisotropic dilation. Unlike the irreversible eigenstrain, this behavior remains linear at higher temperatures (at 250°C and above). This indicates that the origin of the anisotropy is different for the reversible and irreversible contributions. For the reversible eigenstrain, which can be associated to the thermal expansion, the anisotropy may be induced by the crystalline texture caused by the compaction. A possible origin of the irreversible eigenstrain anisotropy is discussed in the next subsection.

2.2 Proposed mechanisms for irreversible eigenstrains*

In order to distinguish the respective contribution of two categories of porosities (*macro* and *micro*) mentioned in Chapter 4 varying the compaction pressure provided some insight. At the highest compaction pressure considered in this study, 50 MPa, no *macro-pores* are observed to remain in the compacted sample (see Chapter 4). In contrast, we supposed that for lower pressures, (pressures down to 10 MPa were tested) some *macro-porosity* is left after compaction as the density is not saturated (see Figure 4.1). However, it is observed to be stable when the temperature is varied, up to temperature close to fusion, where surface tension leads to closure of the pores. For lower temperatures, *macro-pores* when they exist seem not to play any significant role. Besides, for these different compaction pressure, the dilatometry experiment revealed a similar irreversible expansion behavior. Therefore, the latter characteristic is believed to be due to the densification that takes place at the nanoscale. This is consistent also with the observation that no porosity became visible at the 1 µm scale resolution from tomography of samples compacted at 50 MPa, after the thermal cycles of the dilatometry experiment. The irreversible expansion due to the thermal cycle did only generate submicrometric pores.

From the above observations, it is deduced that the mechanism for the irreversible expansion of the sample:

- has to find its origin in the initial cold mechanical compaction;
- has to result from the deformation of the constitutive particles;

- has to involve a stored mechanical energy that will allow to compete with the surface tension cost of creating a pore;
- has to correspond to a metastable state becoming unstable under a temperature rise.

These points led us to propose a mechanistic scenario whereby the closing a *micro-pores* goes together with an internal stress field (where the potential elastic energy is stored).

Porosity (at least supermicrometric) disappears during compaction under a macroscopic oedometric strain, as sketched in Figure 3.5a. Elementary particles are thus deformed plastically, so that they come together and stick from interparticle adhesion (Figure 3.5b), that opposes residual stress due to the deformation of particles. The oedometric compression induces polarization of these internal stresses, as shown in (b). As temperature increases, such contacts may snap open, with a local kinematics that is illustrated in Figure 3.5c. Even if locally rather complex rearrangement of grains may exist, the net effect of a local contact opening can be inferred from the classical "Eshelby" problem, where an inclusion embedded in an elastic matrix undergoes a plastic strain [115]. Actually, all complications coming from the local details of such events can be accounted for by a multipolar expansion of Eshelby type terms vanishing with distance to the inclusion center r as $r^{-\alpha}$ with $\alpha \geq d$ where $d = 3$ is the space dimension. The dominant contribution is the only one that survives at the macroscopic scale and is precisely the usual "Eshelby" solutions, that contains three elementary purely deviatoric components polarized along x, y or z and one isotropic term (dilation of the inclusion). A finite density of such inclusions will produce, at a macroscopic scale, a strain reflecting the symmetry of the locally locked residual stress. In our case, it is expected that the macroscopic strain released by these local contact break-ups is simply opposed to the oedometric compaction, in agreement with the observed irreversible thermal eigenstrain.

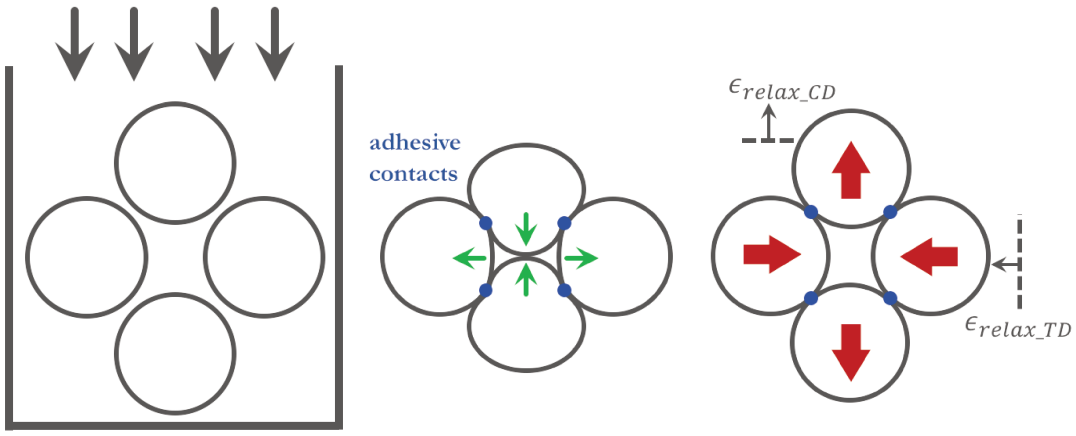

Figure 3.5: Sketch representing PTFE particles uniaxially compacted (a). The particles deform and trap residual stress. The compacted sample is removed from the mold (b) and is relaxed by applying a thermal treatment (c).

It is important to note that this elementary stress field involves a tension at the scale of the *micro-pore* (nm range) that has to be counter-balanced by a compression at a further distance. However the latter stress field decreases very fast with the distance r to the initial pore (Eshelby outer field decaying as r^{-3}). This is to be contrasted with a structural internal stress field (such as a skin compression balanced by a bulk traction as produced

e.g. by thermal tempering or shot-peeing). As a result, it is not possible to reveal these internal stresses by cutting or drilling because the net effect of introducing a free surface has to balance out at the scale of the *micro-pores*. Hence ideally no more than a nano-roughness should be expected. Nevertheless, when a spatially uniform distribution of such locked-in internal stresses is freed a uniform macroscopic strain is expected, consistently with the observed irreversible dilation.

At high temperature, the elastic properties of the material are expected to soften, (possibly involving viscous relaxation) and surface tension of nanocavities may proceed with a similar mechanism.

2.3 Sintered PTFE*

In order to highlight the specificities of the green compact, a similar dilatometry experiment was performed on a compacted PTFE sample first sintered with a thermal cycle above melting temperature and 100 min hold time at 370°C. Then, a similar temperature cycling (as shown in Figure 3.1a) was applied to the sintered specimen. The strains in CD and TD corresponding to the three thermal cycles are shown in Figure 3.6 as a function of the temperature. Those strains reveal no irreversibility during the successive cycles. This suggests that most residual stresses have been relaxed after the melting of PTFE, and no residual stress susceptible to be relaxed by thermal activation has been regenerated during the recrystallization. The sintering of PTFE leads to the loss of granular structure as the particles interfaces are merged during melting and recrystallization. This could also explain that no residual stress can be trapped in the same way as for the compacted nascent powder.

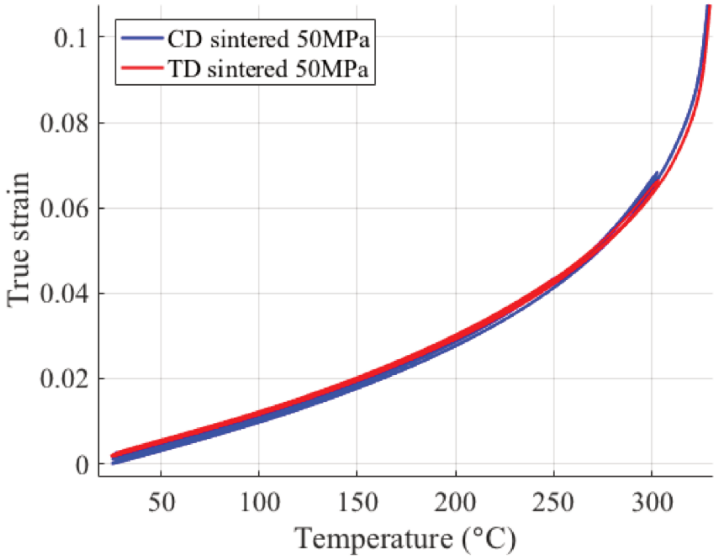

Figure 3.6: Measured true strain in CD and TD for a sintered PTFE cube during successive thermal cycles below melting temperature.

Also, the behavior appears to be isotropic [72], the expansion comes mainly from the amorphous phase which is more likely to be isotropic, and the recrystallized PTFE is much more amorphous (around 50 %) than nascent PTFE (more than 90 % crystalline). It is then also important to note that the thermal expansion is very different from sintered

PTFE and green compact of PTFE due to this difference of crystallinity content, so that these results cannot be used to compare with the reversible part of the unsintered sample. The thermal expansion stops being linear with temperature above 130°C, which may be due to the glass transition of RAF. This transition may impact sintered PTFE more than nascent PTFE as the amorphous fraction is much more important after sintering [23]. Around 250°C, the curvature of the strain may be explained by other phenomena such as melting of smaller crystals coming from secondary crystallization.

3 Behavior of nascent PTFE at melting

Previous results and discussions have been focused on the behavior of PTFE below melting. When looking at the behavior during melting, it appears that the strain increases very suddenly at fusion of PTFE crystals. The density difference between PTFE crystal and its amorphous phase explains this large strain; the density of PTFE crystals being $\rho_{cr} = 2.302$ g/cm^3 and the one of amorphous phase being $\rho_{am} = 2.0$ g/cm^3 at ambient temperature [61]. Figure 3.7a shows the measured strains during a sintering cycle in CD and TD. The PTFE sample was heated up to 370°C, maintained for 100 min at this temperature and cooled down to ambient temperature. The heating and cooling rate was 2°C/min. It appears that the melting strain presents a different signature in CD and TD. To quantify this anisotropy, Figure 3.7b shows the strain in CD as function of the strain in TD. The slope of this curve characterizes the anisotropy of the eigenstrain.

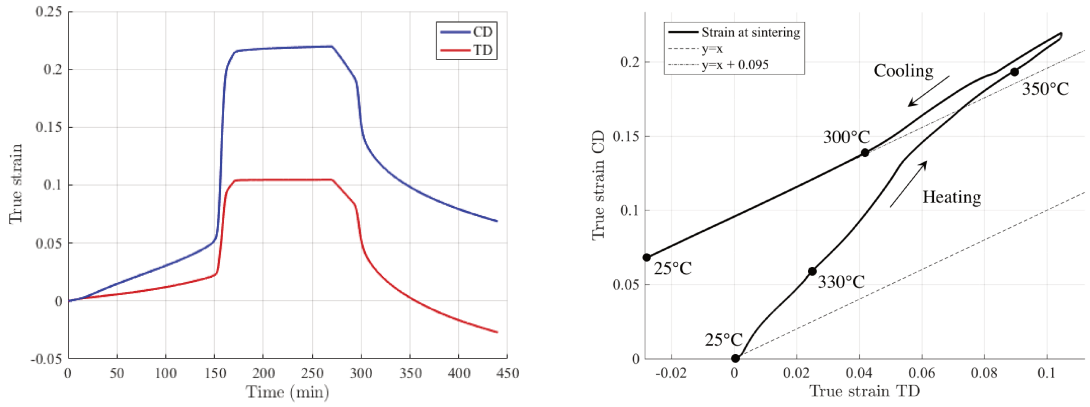

(a) (b)

Figure 3.7: (a) Measured strain in CD and TD during a sintering cycle as function of time; (b) Strain in CD as function of the strain in TD compared to curve $y = x + \delta$ representing an isotropic behavior.

In Figure 3.7b, the lower the part of the curve represents the heating. The residual stress relaxation mechanism discussed earlier occurs for a strain TD below 0.02 (for a temperature below 300°C). The part of the curve related to melting, between 330 and 350°C, presents a similar anisotropy than at lower temperatures. Above 350°C, the behavior is still anisotropic but only concerns the thermal expansion of molten PTFE.

Similarly to the melting strain, the crystallization strain is anisotropic (upper part of the curve in Figure 3.7b) but with a lower slope than for melting. From X-ray diffraction measurements in Chapter 5, it is shown that green and recrystallized PTFE have similar

crystalline orientations (at least at phase change). Therefore, both melting and crystallization strains should be almost equally anisotropic. The observed difference of slopes suggests that residual stress relaxation continues during melting resulting in a higher anisotropy of the overall eigenstrain.

It is very likely residual stress relaxation diminishes as the melting completes. The PTFE grain interfaces fade away due to melting and thus all the residual stresses are relaxed. It could explain the decrease of the slope in Figure 3.7b and therefore of the anisotropy at the end of the melting. Some anisotropy remains due to the anisotropic thermal expansion of molten PTFE.

Discussion on the evolution of the anisotropy during cooling and links with crystallization will be made in Chapter 5.

During melting, the different mechanisms involved in the overall eigenstrain are:

- the strain due to melting ;
- the thermal expansion that depends on the crystallinity content;
- the residual stress relaxation generating an irreversible strain;
- the void closure that suppresses the initial porosity due to compaction and also the porosity induced by residual stress relaxation due to a weak the surface tension in the molten state (mentioned previously and more detailed in Chapter 4).

4 Conclusions and perspectives*

Compacted nascent PTFE powder presents a peculiar behavior under thermal cycling. In addition to a reversible thermo-elastic contribution, an irreversible contribution has been shown. The latter is progressively erased by previous thermal treatment at higher and higher temperatures. Such behavior is formally reminiscent of an elasto-plastic behavior, with an additive decomposition of strains between the reversible and irreversible parts. Moreover, both of these strains reveal anisotropic behavior that is due to the preceding cold compaction process of nascent PTFE powder. Remarkably, after sintering, the irreversible part disappears, and the anisotropy (that still exists in the microstructure) has no visible manifestation in the next thermal cycles studied. It is speculated that the irreversible part of the thermal eigenstrain is due to local stress relaxation mechanisms, occurring at a submicrometer scale. Above 250°C, other mechanisms appear that modify the strain behavior of PTFE, such as possible porosity closure. To refine those observations and deepen the understanding of this phenomenon, it would be interesting to study the residual stress relaxation of PTFE with different multiaxial compactions such as hydrostatic or biaxial compaction. This should have an effect on the anisotropy of the relaxation strain by modifying the residual stress formation.

The evolution of the eigenstrain anisotropy of green PTFE suggests that the same relaxation mechanism continues during melting. This effect seems to reduce during melting as PTFE grain interfaces blur. Other eigenstrain mechanisms are then also present: strain due to crystal fusion, thermal expansion and void closure.

Chapter 4

Void closure

This chapter investigates the impact of the initial porosity on the overall thermal eigenstrain of green PTFE during melting.

Contents

1 Introduction

Sintering is known as an essential step of the manufacturing process of green PTFE compact as it induces particles coalesence and void closure. Sintered PTFE parts are then much more homogeneous and can be shaped. At melting, PTFE expands suddenly driving the enclosed air out. It results in closing the existing porosity in the PTFE compacts. Therefore, the porosity closure is one of the eigenstrain mechanisms taking place during sintering.

Green PTFE compacts are inherently an assembly of deformed nascent PTFE particles. Air is entrapped during compaction (and probably even before) in between the PTFE particles. The fraction of porosity changes with the compaction level. In this work, only the uniaxial compaction is studied.

Porosity has already been evoked in the previous chapter, as it appears when PTFE expands and releases residual stresses. In this previous case, the generated porosity was a *micro-porosity* (no more than a few microns). In this chapter, *macro-porosity*, whose size is comparable with the size of the PTFE particles (about 50 µm), is also considered.

This chapter deals with the impact of the porosity on the behavior of PTFE during sintering. Observations and estimations of the porosity are presented in section 2. Section 3 aims at showing this effect in terms of (eigen)strain during the thermal cycle. A simple model is exposed to take this phenomenon into account.

2 Porosity estimation

In order to estimate and characterize the porosity in PTFE compacts, different methods were used. First, the porosity fraction can be estimated from the compaction stress-strain curve. Then the nature of the porosity was determined from scanning electron micrographs. Finally, X-ray microtomography and light diffusion methods were used to quantify the amount of porosity in green PTFE samples.

2.1 Compaction

PTFE compacts were uniaxially pressed in a mold with a square section (8 mm × 8 mm) at 1 mm/min. From the stress-displacement curve obtained during compaction, the evolution of the apparent density with the compaction pressure is computed and shown in Figure 4.1. This evolution does not take into account the elastic compression of the sample. The asymptotic slope for higher pressures defines the compression coefficient of PTFE. By subtracting this effect, one could observe that an maximal density is almost reached for sample compacted at 50 MPa [8, 10].

Nascent PTFE is very close to a perfect crystal with a crystallinity content χ around 90 %. The apparent density ρ is related to χ via equation (2.9). At ambient temperature, the density of the PTFE crystal ρ_{cr} is 2.302 g/cm^3 and the density of the amorphous phase ρ_{am} is about 2.0 g/cm^3 [1]. The density of PTFE compact corresponding to zero porosity ρ_{max} is then 2.26 g/cm^3. Using this value, the porosity n can be determined from the apparent density ρ

$$n = 1 - \frac{\rho}{\rho_{max}} \tag{4.1}$$

and is shown in Figure 4.1 as the coordinate axis on the right. It seems that for the maximal compaction state achievable (above 50 MPa), the porosity is not null. Again,

removing the elastic compression effect would increase the values of porosity for higher pressures.

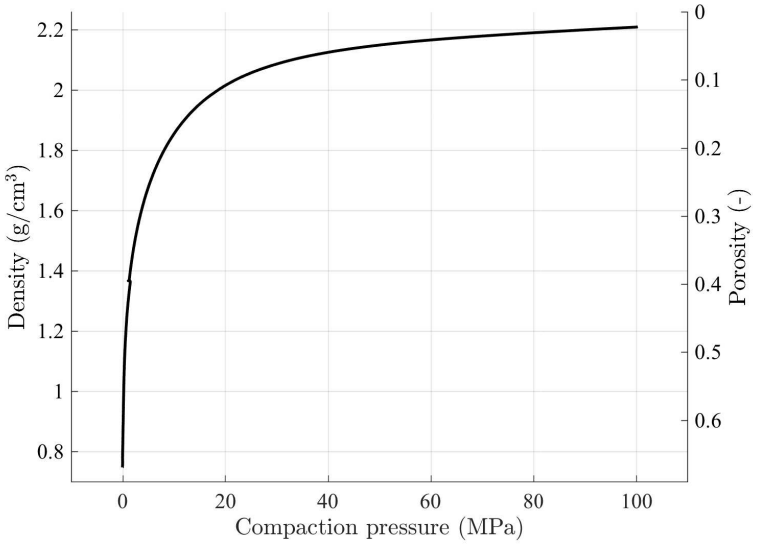

Figure 4.1: PTFE compact apparent density and porosity as functions of the compaction pressure. The evolution is obtained from the compaction stress-displacement curve and the elastic compression has not been removed.

In this study, the influence of compaction speed was not studied. However it is very likely that it has an effect on the final density. Similarly, applying pressure during a certain amount of time could lead to densification. For the rest of the work, the compaction pressure will correspond to the maximum pressure achieved without any pressure holding. Only the displacement is held for 5 min before removing the sample from the die. Other interesting viscous effects could exist from densification in pressure plateau.

2.2 Scanning electron microscopy

PTFE samples compacted at 5 MPa and at 50 MPa were cryofractured. They were cooled down in a liquid nitrogen bath before being splitted up. The cryofractured samples were analyzed using a scanning electron microscope (SEM) Hitachi 4800 II.

Figure 4.2 shows SEM micrographs at different magnifications for the 5 MPa-pressed sample on the left and the 50 MPa-pressed sample on the right. PTFE particles are supposed to be around 20 to 100 µm diameter (producer specifications for this PTFE resin). From the images, these particles seems to be made of agglomerates of smaller particles (about 1 to 5 µm).

For the lower compaction sample (5 MPa), a significant amount of large cavities are observed. Those cavities are about the size of the bigger PTFE particles (around 20 µm in Figure 4.2a and 4.2c). This large porosity will be defined as the *macro-porosity*. For the higher compaction sample (50 MPa), less porosity of this size is observed as the particles seems to be packed more closely (Figure 4.2b and 4.2d).

On both samples small cavities of the size of the small particles can be seen (around 5 µm in Figure 4.2c and 4.2d). Even a smaller porosity could be defined in Figure 4.2e at

the junction of small particles packs. Those porosities, smaller than 5 µm, will be defined as the *micro-porosity*.

5 MPa 50 MPa

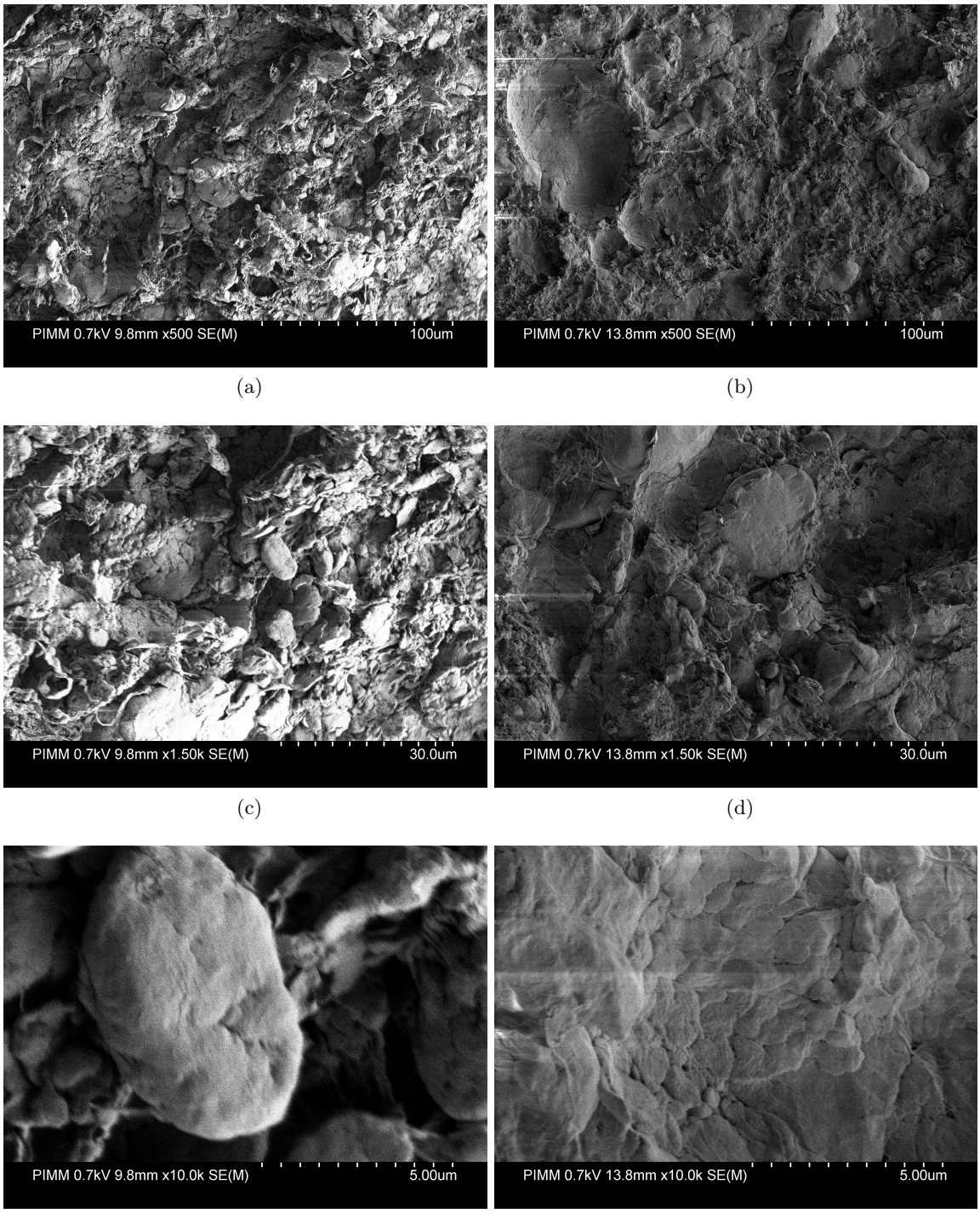

Figure 4.2: SEM pictures of cryofractured green PTFE compacts for two compaction levels: (a), (c), (e) at 5 MPa and (b), (d), (f) at 50 MPa. Three magnifications are proposed: x500 for (a,b), x1500 for (c,d) and x10000 for (e,f).

Note that several pictures have artefacts due to scanning as PTFE retains electrons during the acquisition.

2.3 Microtomography

The porosity can be observed thanks to microtomography. Air is less absorbing X-rays than PTFE, therefore a contrast can be obtained to estimate the porosity in PTFE compacts.

PTFE cylinders are uniaxially pressed in a circular section mold of diameter 35 mm at various pressures (5, 10, 20 and 30 MPa). Every sample is made of 19 g of PTFE powder. The specimens are scanned in a X-ray microtomograph with a resolution of 25 µm. Figure 4.3 shows a section of each reconstructed volume. The mean gray level which can be related to the density, increases with the compaction pressure, confirming the evolution observed in Figure 4.1. Furthermore, a "speckle" can be noticed in the reconstructed sections. It certainly means that there are local variations of the density related to porosity at a lower scale.

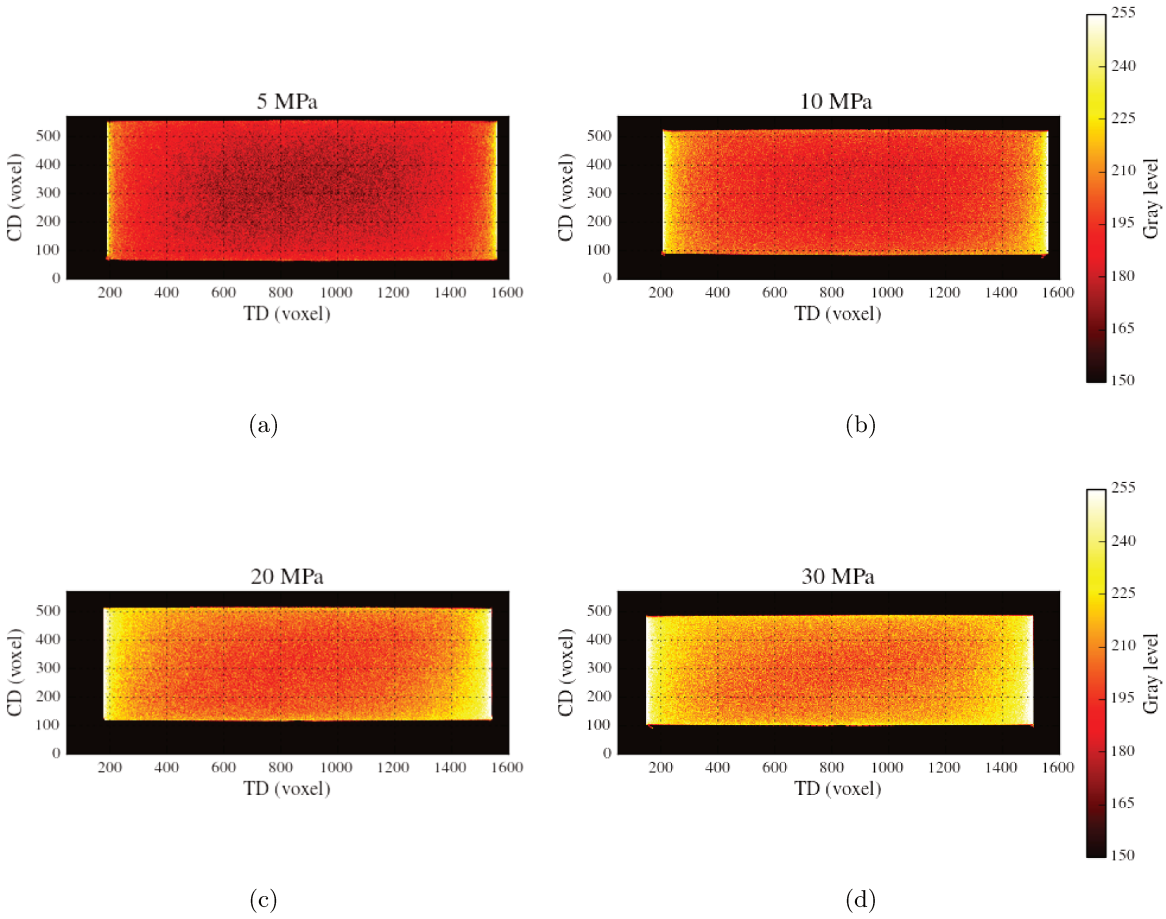

Figure 4.3: Microtomography sections of the reconstructed volumes for PTFE cylinder compacted at different pressures: (a) 5 MPa, (b) 10 MPa, (c) 20 MPa and (d) 30 MPa. The intensity is expressed in gray levels.

Intensity gradients can be observed in the compaction direction (CD) and in the trans-

verse direction (TD). However, this effect is an artifact that is caused by the interface PTFE-air.

It would be interesting make some scans with finer resolutions (lower than 25 µm) to really observed the porosity in order to evaluate its size and shape.

2.4 Light diffusion analysis

Light diffusion allowed to quantify the porosity more globally. Figure 4.4 shows four PTFE compacts for various compaction pressures (50, 20, 5 and 1.5 MPa). Their color is different, especially the 50 MPa sample that seems almost translucent. The color differences between the sample is related to their light diffusion properties.

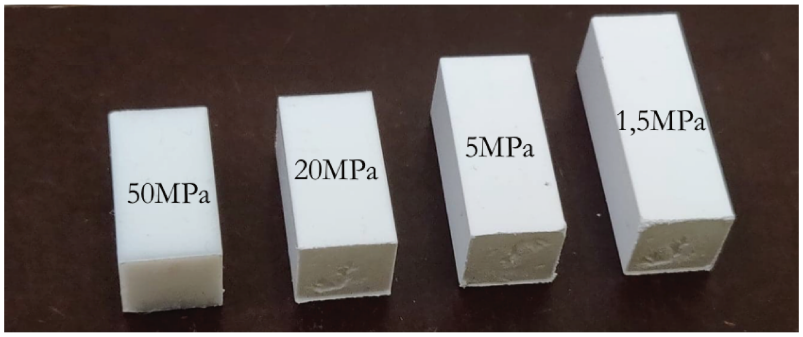

Figure 4.4: Picture of 1 g PTFE compacts for various compaction pressures (50, 20, 5 and 1.5 MPa). It appears that the light diffusion is evolving with the compaction. The difference is obvious for the 50 MPa sample.

The porosity in the PTFE sample acts as a diffusive agent. Therefore measuring the diffusion of transmitted light (or even reflected) could be used as tool to quantify the porosity level or even to characterize it [116].

Figure 4.5a shows a small angle diffractogram obtained using X-ray radiation (from SOLEIL synchrotron facility) from a green PTFE sample. A diffusion halo is observed with no characteristic peaks. This measurement was made on a PTFE slice containing only the transverse directions so that the diffusion halo is isotropic. The integrated intensity over a fixed range of q is plotted for different green samples (uniaxially compacted at 10, 20 and 50 MPa) in Figure 4.5b. The same measurements were also performed on the sintered PTFE samples compacted at the same pressures.

It appears that the intensity decreases with the compaction pressure. However the relation between the transmitted intensity is also depending on the sample thickness which explains the fluctuations on green PTFE measurements. Sintering seems to significantly reduce the porosity as the diffusion level drops for samples of same thickness (300 µm). The transmission coefficient is also modified by the crystallinity content (which is smaller in sintered PTFE). Therefore it is not possible to estimate the porosity from those measurements. However the initial compaction does not impact the final diffusion intensity after sintering and therefore the final porosity is the same regardless of the inital porosity. It seems that sintering closes up the porosity.

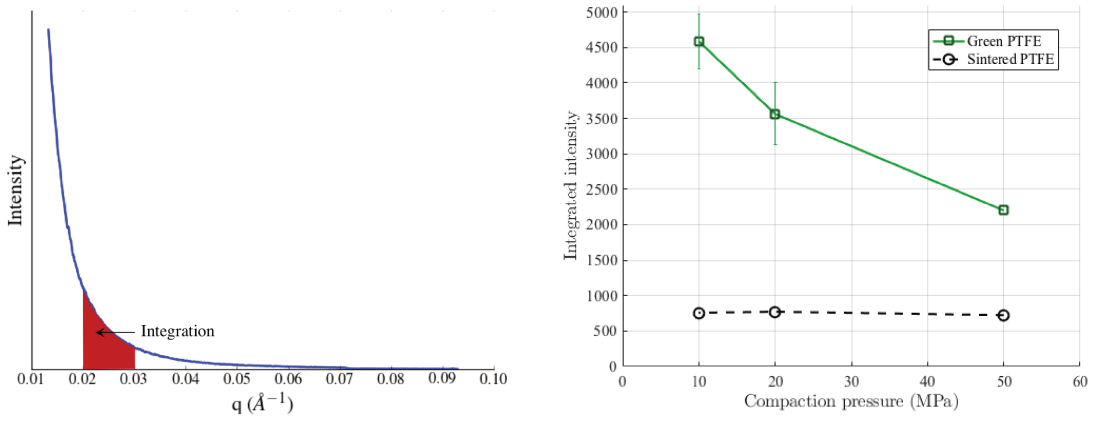

(a) (b)

Figure 4.5: a) Small angles X-ray diffractogram and integration zone in the diffusion halo. b) Integrated X-ray intensity obtained on green PTFE compacts at 10, 20 and 50 MPa, and on the respective sintered specimens.

3 Void closure signature in dilatometry

The dilatometric experiment presented in Chapter 2 were also used to characterize the influence of the porosity on PTFE overall thermal eigenstrain. Different uniaxial compaction pressures were tested: 50, 20, 10, 5 and 1.5 MPa. The volumetric strain ε_v is considered. ε_v can be computed from the true strain measured in compaction direction (CD) and transverse direction (TD) due to the transverse isotropy of the part: $\varepsilon_v = \varepsilon_{CD} + 2\varepsilon_{TD}$.

The volumetric strain for the PTFE samples at different compaction levels is shown in Figure 4.6. The main difference occurs at melting. The strain due to melting seems to be less important for less compacted samples. A decrease is observed in the plateau for the low compaction samples (1.5, 5 and 10 MPa).

The 50 MPa-pressed sample is considered as the reference. The reason for this choice is that a similar dilatometric experiment was performed on a 100 MPa-pressed and the results were almost superimposed. Therefore, it is assumed that the lower porosity content is reached for a 50 MPa-pressed sample. The component of the strain related to porosity can be obtained by subtracting the 50 MPa eigenstrain to the other curves. The outcome of the subtraction is a strain only corresponding to void closure.

The volumetric void closure strain is shown in Figure 4.7a. As expected, it reveals that the major strain occurs exactly during melting. In the case of higher compaction (20 and 10 MPa), almost all the void closure happens during melting. For lower compactions (5 and 1.5 MPa), the void closure pursues even during the plateau (above melting temperature T_m). Note that the void closure strains present some shifts or bumps (mostly at crystallization). Those effects are related to the construction of the subtracted curves. It means the measured temperature differs slightly between the two experiments (the considered experiments and the subtracted one).

A first order model depicts most of the phenomenon. It can be assumed that the porosity is closed as soon as the melting temperature is reached (see Figure 4.7b). The model can even be slightly refined by delaying the void closure during the melting by applying

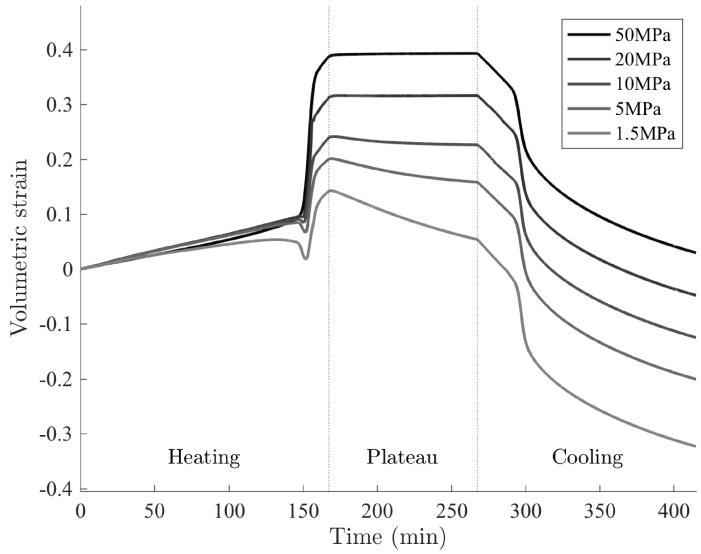

Figure 4.6: Measured volumetric true strain as function of time for different uniaxial compaction levels (50, 20, 10, 5 and 1.5 MPa).

a strain proportional to the melting strain. It would also be easier to implement in a simulation as it would smooth the strain variation.

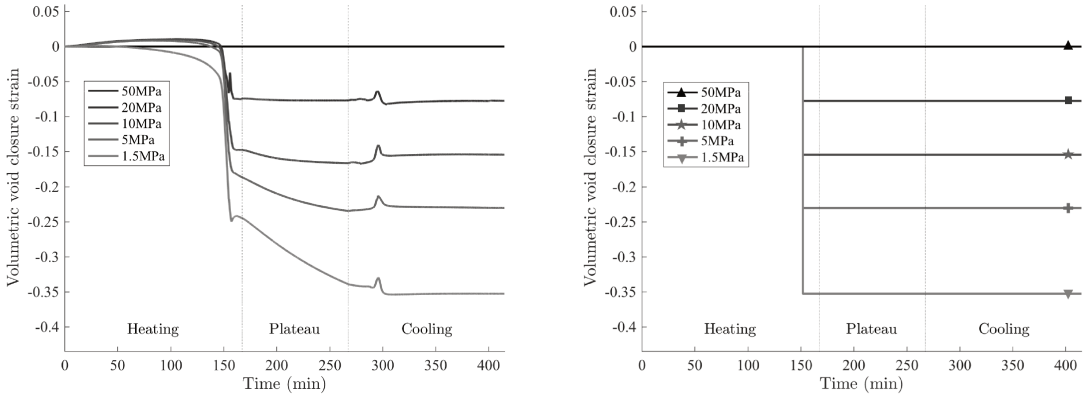

(a) (b)

Figure 4.7: Strain related to volumetric void closure for different uniaxial compaction levels (50, 20, 10, 5 and 1.5 MPa). The curves are obtained form Figure 4.6 by assuming the 50 MPa specimen has no porosity (a). A simple model making the void closure happening instantaneously at melting is presented (b).

To take into account the time dependence of the volumetric void closure strain ε_v^{vc}, Canto [72] suggested to fit the curves with a decreasing exponential law:

$$\varepsilon_v^{vc}(t) = \Delta\varepsilon_{max}^{vc}\left[1 - \exp(-t/t_{vc})\right] \quad H\big(T(t) - T_m\big) \tag{4.2}$$

where $\Delta\varepsilon_{max}^{vc}$ is the strain related to the total porosity closure, t_{vc} is a time that char-

acterizes the evolution of the void closure, H the Heaviside function and T_m the melting temperature. $\Delta\varepsilon^{vc}_{max}$ can be estimated thanks to the initial density value (see Figure 4.1).

This model does not seem to describe accurately the void closure evolutions presented in Figure 4.7a. Also the PTFE resin used by Canto (free flow) was different than the one used for this study (low flow) and it has a lower granulometry. It rather seems that the behavior should be decomposed into two terms: one term related to a closure happening instantaneously during melting and one term that is time dependent. Thus,

$$\varepsilon^{vc}_v(t) = \zeta\left(1-\bar{\chi}(t)\right)\Delta\varepsilon^{vc}_{max} + (1-\zeta)\,\Delta\varepsilon^{vc}_{max}\left[1-\exp(-t/t_{vc})\right]\,H\big(T(t)-T_m\big) \quad (4.3)$$

where ζ is the fraction of strain occurring instantaneously at melting and $\bar{\chi} = \chi/\chi_0$ is the relative crystallinity content at melting with χ_0 the crystallinity content of nascent PTFE.

t_{vc} and ζ seem to depend on the compaction level. One can imagine that the gas pressure in pores is higher for higher compaction pressures and that the time for the gas to get released t_{vc} is lower. For ζ, the compaction pressure dependence is less evident. It is related to the ability to close the porosity instantaneously at melting and the capacity to retain gas in the bulk.

The final volumetric void closure strain $\Delta\varepsilon^{vc}_{max}$ can be estimated from the compaction curve (from Figure 4.1) by considering the porosity is completely closed. Again, an error is made as the elastic compression was not deducted from the compaction curve. The final volumetric void closure strain $\Delta\varepsilon^{vc}_{max}$ can also be measured from the final value of the volumetric void closure strain curves (Figure 4.7a). Those two types of evaluation of $\Delta\varepsilon^{vc}_{max}$ are presented in Figure 4.8. It reveals a gap for the 5 and 1.5 MPa samples. From the evolution of the volumetric void closure strain of these samples from the TMA experiment shown in Figure 4.7a, it appears that the void closure was not finished when the cooling started. Therefore some porosity remained in the sintered sample. The plateau duration would have to be increased for low compaction samples to ensure a complete closure of the porosity.

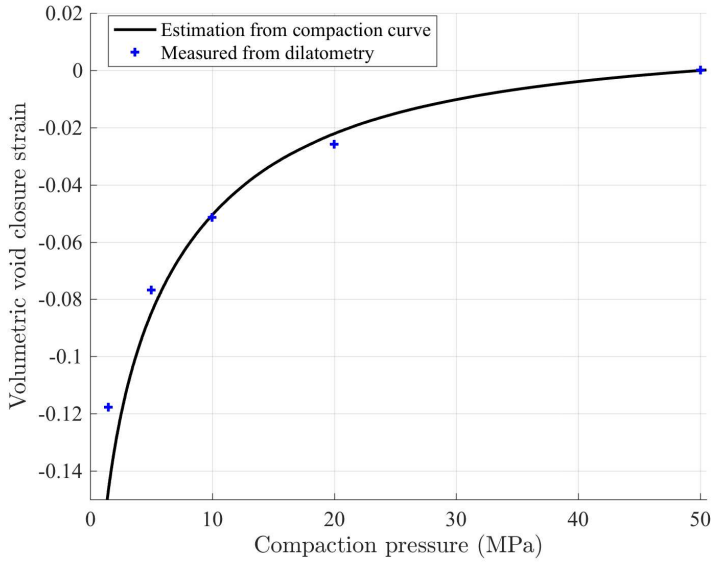

Figure 4.8: The final volumetric void closure strain $\Delta\varepsilon^{vc}_{max}$ estimated from the compaction curve (Figure 4.1) and measured from the TMA experiments (Figure 4.7a).

As already mentioned in Chapter 2, the PTFE overall thermal eigenstrain is anisotropic. Figure 4.9 presents the measured strain in dilatometric experiments in CD and TD for the different uniaxial compaction levels (50, 20, 10, 5 and 1.5 MPa). The eigenstrain seems almost identical for every samples below melting in CD and TD. In this stage of the heating, the overall eigenstrain is a combination of thermal expansion and residual stress relaxation (see Chapter 3). This behavior is anisotropic due to the powder compaction and it seems that the anisotropy is not influenced by the compaction pressure above 1.5 MPa. For the 1.5 MPa compact, the behavior is slightly different closer to melting. It would suggest that above 1.5 MPa, the residual stresses trapped by the deformed PTFE particles reach a maximum and the anisotropy of the overall eigenstrain is set. The extra pressure closes the porosity without changing this anisotropy. Therefore, it means that the crystalline texture is set as well.

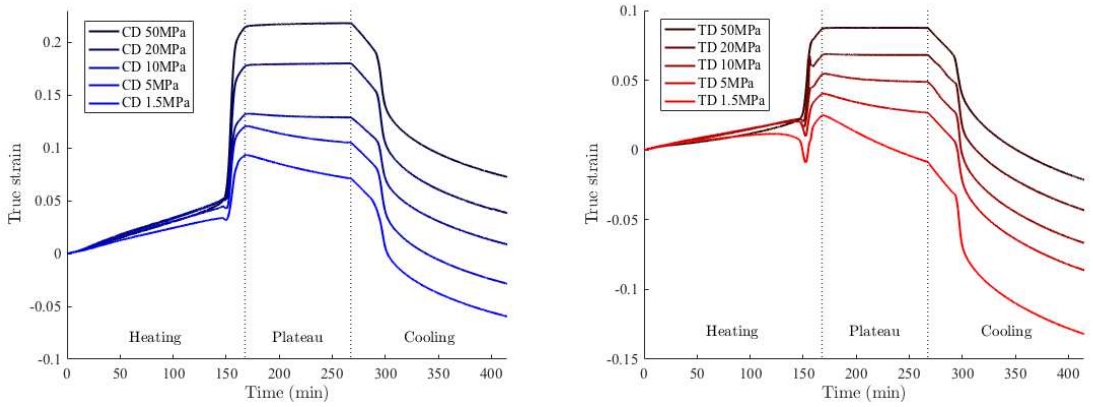

(a) (b)

Figure 4.9: Measured true strain as function of time for different uniaxial compaction levels (50, 20, 10, 5 and 1.5 MPa) in compaction direction (CD) and in transverse direction (TD).

Same type of computation than for the volumetric component can be made to evaluate the contribution of the void closure in each direction (CD and TD). The eigenstrain relative to the 50 MPa sample is subtracted to each other curves. Figure 4.10 shows the void closure strain in CD and TD for the different compaction pressures tested. It appears that the void closure strain is anisotropic as well. The anisotropy of the void closure strain originates from the anisotropy of the strain due to melting. As the melting strain is larger in CD than in TD, it is natural that the voids are more preferentially closed in CD than in TD.

The final value of the void closure strain for CD and TD as function of the compaction pressure is presented in Figure 4.11. The anisotropy can be quantified by the ratio of the strain in CD over the strain in TD. This ratio seems to decrease for the lower compactions. One could think that this reduction of the anisotropy of the void closure strain is related to the reduction of the anisotropy in general (for the 1.5 MPa sample). However when looking at Figure 4.10, it appears that the two porosity closure behaviors described earlier with equation 4.3 have different contributions in CD and TD. The instantaneous void closure with melting seems to be anisotropic whereas the time dependent porosity closure looks to be similar in CD and TD. The isotropy of this behavior could be explained by the fact that this behavior is governed by gas diffusion which does not imply orientation effects.

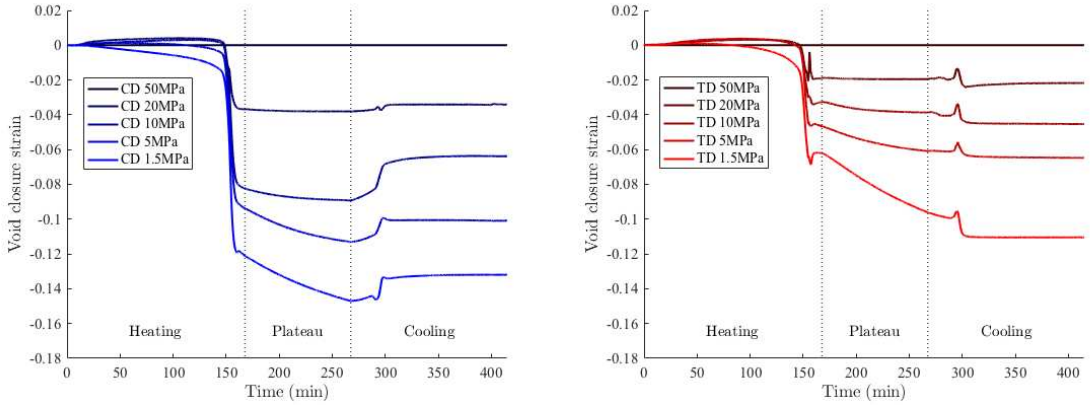

(a) (b)

Figure 4.10: Strain related to void closure for different uniaxial compaction levels (50, 20, 10, 5 and 1.5 MPa) in CD and in TD. The curves are obtained from Figure 4.9 by subtraction of the 50 MPa curve to each curve for each direction.

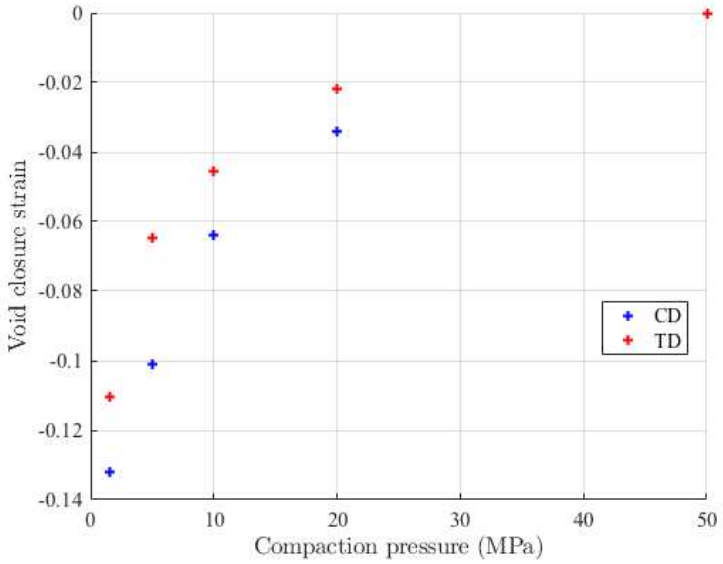

Figure 4.11: Void closure strain measured in the compaction direction (CD) and in the transverse direction (TD).

The illustration of the volumetric component of the void closure strain in Figure 4.12 summarizes the previous observations. The void closure strain is coming from two mechanisms, the first one is a sudden porosity closure due to melting. The corresponding strain is proportional to the melting strain and possess the same anisotropy. During melting, the air is pushed out by convection effects. The second mechanism is due to gas (air) diffusion. In the molten state, the remaining trapped air diffuses out. The corresponding strain is therefore time-dependent and isotropic.

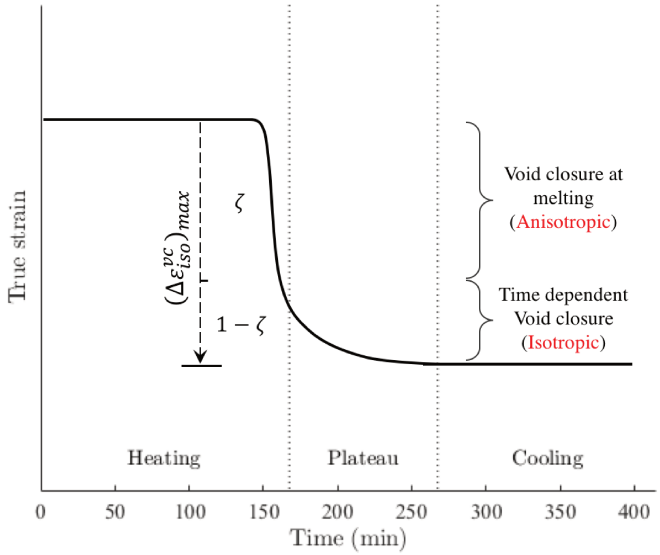

Figure 4.12: Illustration of the volumetric component of the void closure strain as function of time. The first part of the strain is proportional to the melting strain and the second part is related to gas diffusion. The first one is anisotropic similarly to the melting strain and the second one is isotropic.

4 Conclusions and perspectives

In this chapter, the porosity and its influence during sintering was studied. Different forms of porosities are present in PTFE compacts: *macro-porosity* around 20 µm and *micro-porosity* lower that 5 µm. The amount of porosity, and particularly the *macro-porosity*, is directly depending on the compaction level.

A light diffusion method was presented. It allows to estimate the density via optical measurements. Results were shown using X-ray diffusion but the same method could be generalized to visible light diffusion. Associated to a thickness control, it could enable inline density measurements for films. Light absorption is also an alternative to evaluate porosity in particular using X-ray tomography.

The porosity plays a significant role during sintering as voids are closed during melting. The overall thermal eigenstrain can drop drastically at melting due to this phenomenon (from 20 % for a sample compacted at 50 MPa to less than 10 % for a 1.5 MPa sample, in the compaction direction). It has been shown that two void closure mechanisms appear to be involved. The first one occurs simultaneously with melting. The other one seems to be time dependent and its share of the total void closure strain increases for samples compacted at lower pressure. This time-dependent phenomenon is probably related to gas diffusion. Therefore, ensuring the total removing of the enclosed air would require sufficient time in the plateau. Otherwise one could imagine these entrapped air pockets to be at origins of cracks during the cooling part of the sintering. Moreover, the time required to let the air out may depend on the wall thickness of the part. The time spent above melting may have to be adjusted in function of the part dimension.

Chapter 5

Behavior of PTFE from melt: crystallization and second melting

The crystallization of PTFE is investigated in this chapter. A secondary crystallization mechanism is observed and a crystallization kinetic model is proposed. The influence of the crystallization mechanisms on the overall thermal eigenstrain is analyzed.

Contents

Sections or subsections followed by an † are issued from the article:

PTFE crystallization mechanisms: Insight from calorimetric and dilatometric experiments, *to be submitted*

Sections or subsections followed by an • are issued from the article:

Orientation in transversely isotropic semi-crystalline polymer: application to uniaxially compacted PTFE, *to be submitted*

1 Introduction

After its first melting, PTFE properties are extensively modified. Its nascent (almost perfect) crystallinity is lost forever and the granular state of green PTFE no longer exists. After crystallization, it is called melt-crystallized PTFE in contract to as-polymerized PTFE [117]. This chapter aims to address the original crystallization kinetic behavior for PTFE and its influence on the overall thermal eigenstrain of melt-crystallized PTFE.

First, crystallization kinetics of PTFE from melts is studied in section 2, and then the anisotropic behavior of melt-crystallized PTFE is discussed in section 3.

2 Crystallization of PTFE from melt

2.1 Calorimetric measurements†

DSC experiments have been performed to study the crystallization kinetics of PTFE. Nascent PTFE samples were first melted at 375°C for 300 s and then cooled down at various cooling rates (0.5, 1, 2, 5 and 10°C/min).

A calorigram is presented in Figure 5.1 with heating and cooling rates of 10°C/min. The first melting peak is presented in dark red and the crystallization peak in blue. The light red peak corresponds to the melting peak of the recrystallized PTFE.

The first melting peak is quite narrow (between 325 and 355°C) and occurs at a higher temperature than the second melting peak (between around 250 and 330°C) . This is attributable to the high crystallinity of nascent PTFE with large crystal lamellae. The nascent powder is crystallized upon polymerization which explains its high crystallinity ($\simeq$ 90%) with a very low density of entanglements. The second melting peak is much smaller as recrystallized PTFE ($\simeq$ 30 to 50%).

The crystallinity peak in blue can be integrated with respect to time to evaluate the latent heat due to crystallization. The final crystallinity content χ can be estimated and compared to the latent heat of fusion from the second melting peak. Both calculations lead to an evaluation close to 35% of crystallinity for the cooling rate of 10°C/min. The same integration method allows one to evaluate the crystallinity content as function of temperature. The crystalline fraction at a given temperature corresponds to the partial temporal integration of the crystallization peak between the start of the crystallization and the given temperature.

The method to evaluate the DSC baseline during crystallization has been described in Chapter 2. Figure 5.2 shows the crystallization peak, the baseline at convergence computed using the method described in Chapter 2, and the integrated area. From this integration, one can determine the crystallinity content as function of temperature.

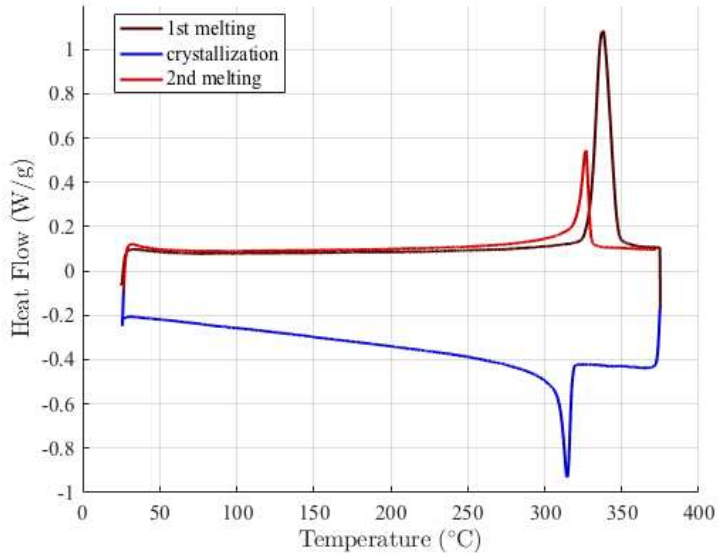

Figure 5.1: DSC calorigram obtained from green PTFE with heating/cooling rates of 10°C/min. A second heating was performed to melt recrystallized PTFE. The first heating stage is shown in dark red, first cooling in blue, second heating is light red.

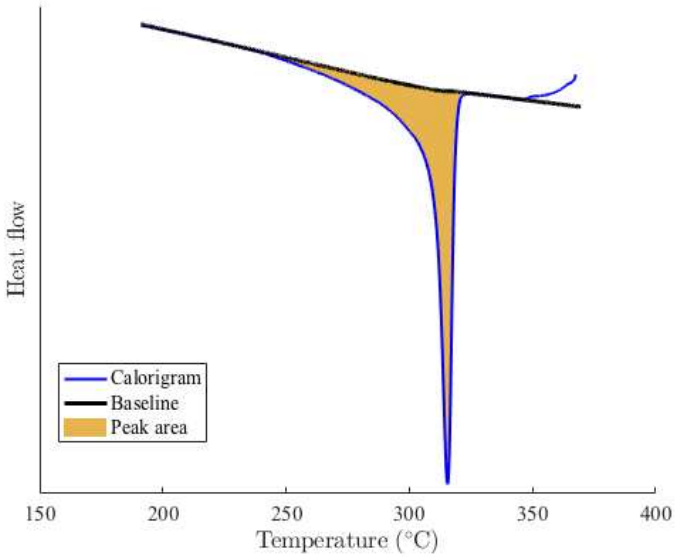

Figure 5.2: Computed baseline to perform the crystallization peak integration for a molten PTFE sample cooled down at 10°C/min.

2.2 Crystallization dependence with cooling rate†

The crystallinity content χ evolution with temperature was obtained for various cooling rates thanks to the DSC experiments (Figure 5.3). As already noted in previous works [33, 72], the final crystallinity content is dependent on the cooling rate. The crystallization temperature onset is estimated to be 318°C almost independently on the cooling rate.

The crystallinity increases very rapidly over 5-10°C. Basset observed growth of the

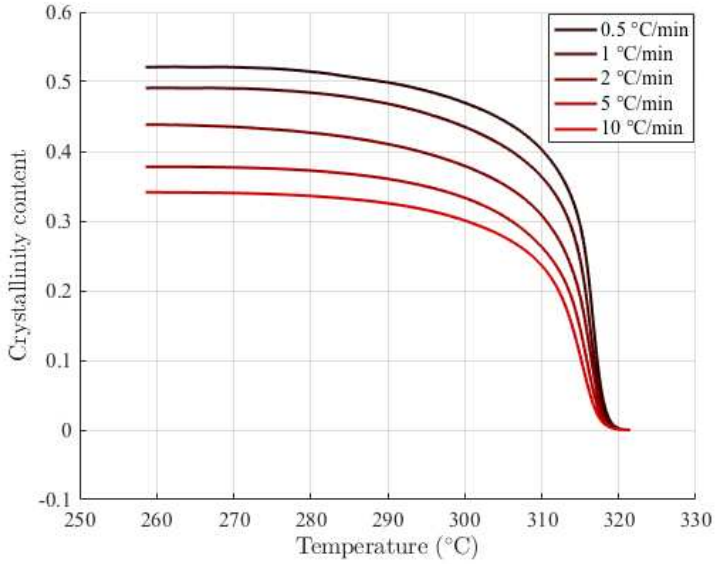

Figure 5.3: Crystallinity content χ evolution during crystallization for various cooling rates.

lamellae with time spent in the similar temperature range [32]. At lower temperatures, the crystallinity content continues to step up, but much slower over a range of 50°C. The marked difference between those two stages suggests that a secondary crystallization mechanism takes place.

Secondary crystallization mechanisms are usually encountered as a different mechanism driven by the primary crystallization [52, 46, 49]. However, surprisingly, PTFE's secondary crystallization seems to be independent of the primary crystallization as its contribution to crystallinity is observed not to depend on the cooling rate as shown in Figure 5.4. It appears that shifting the crystallinity versus temperature curves, measured for the different cooling rates, to reach the same final level collapses all data onto a single master curve. This figure suggests that this secondary stage (between 315 and 260°C) is identical.

Hence, the primary crystallization is responsible for the final crystallinity content variations obtained after different thermal histories.

Two DSC experiments were designed to secure the previous conclusions. To confirm that the secondary crystallization is independent on the cooling rate, a DSC was performed at a different cooling rate only in the temperature region of the secondary crystallization (Figure 5.5). To confirm that the primary crystallization is dependent on the time spent between 320 and 310°C), an isotherm is added at 317°C (Figure 5.6). The obtained results are compared to a control experiment.

Figure 5.5 shows a DSC experiment on a melted PTFE sample cooled down to ambient temperature. The initial cooling rate is 10°C/min and is turned down to 5°C/min below 310°C. Then the crystallized PTFE sample is heated above its melting temperature. The melting peak can be compared to the one of the control experiment where a PTFE sample was integrally cooled down at 10°C. It appears that the melting peaks are superimposed (Figure 5.5b) which means that the final crystallinity contents are the same. This observation confirms that secondary crystallization is not dependent on the cooling rate and that the final crystallinity is due to the thermal history in the primary crystallization temperature region.

The difference between the heat flow $\dot{q}$ of the experiment and the reference below 310°C

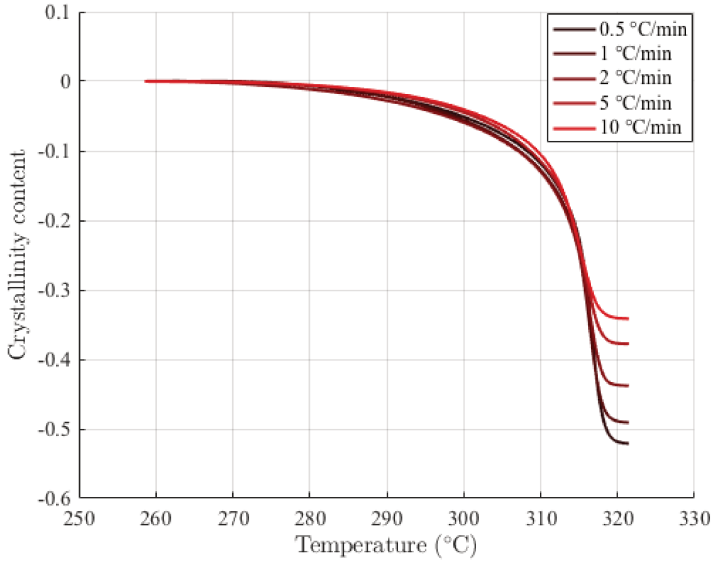

Figure 5.4: Crystallinity content χ evolution for various cooling rates shifted to reach the same final level. It appears that the measurements between 315 and 260°C for all cooling rates are almost coincident.

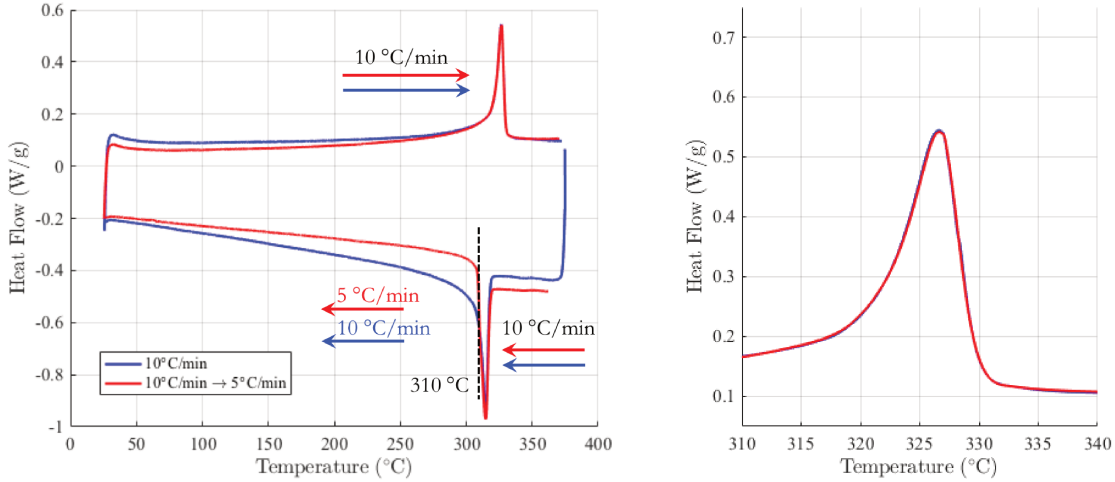

(a) (b)

Figure 5.5: DSC experiment to test the secondary crystallization mechanism. A molten PTFE sample is cooled down at 10°C/min until 310°C and then cooled down at 5°C. The sample is then heated up at 10°C/min and its melting peak is compared to the reference sample exclusively cooled down at 10°C/min (a). A zoom is made on the melting peaks (b).

is cause by the dependence of $\dot{q}$ on $\dot{T}$. Ideally, the DSC signals $\dot{q}$ obtained at cooling could be divided by $\dot{T}$ (see equation (2.2) in Chapter 2) and appear to be similar if the behavior is the same for the secondary crystallization. However, in practice it is not possible to do as an additional offset coming from the DSC setup is present in the measurement. This

offset would have to be removed before the division.

Similarly, the two signals at heating appear to be slightly different at low temperature. This difference is due to the additional offsets present in the two measurements. These offsets could come from the different thermal contacts. The heating signals can be treated to remove the baseline (as mentioned for crystallization) in order to extract the melting peaks for both experiments. This post-treatment confirms that the two peaks are similar.

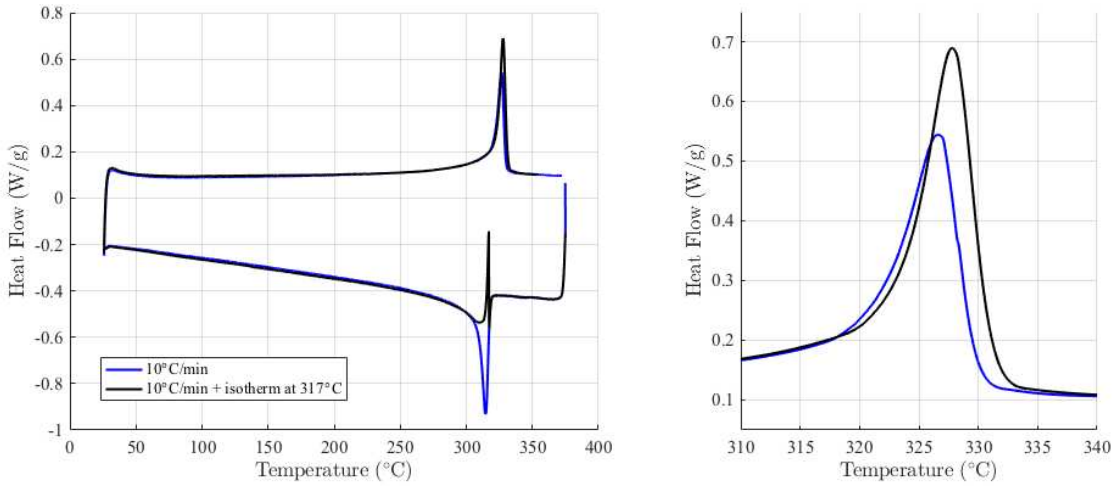

(a) (b)

Figure 5.6: DSC experiment to test the primary crystallization mechanism. A molten PTFE sample is cooled down at 10°C/min until 317°C, is held at this temperature for 2 hours and then is cooled down at 10°C/min. The sample is then heated up at 10°C/min up to its melting peak and is compared to the reference sample merely cooled down at 10°C/min(a). A zoom is made on the melting peaks (b).

Figure 5.6 shows a DSC experiment where a melted PTFE sample is cooled down to 317°C at 10°C/min, held for two hours at 317°C and then cooled down at 10°C/min to ambient temperature. Further on, the crystallized PTFE sample is heated back above its melting temperature. The melting peak is compared to the same control experiment where a PTFE sample was cooled down at 10°C without interruption. This comparison (Figure 5.6b) suggests that the hold time increased the final crystallinity content and consequently affected the overall crystallinity content.

2.3 Crystallization kinetic model

From the previous observations on the crystallization, a kinetic model can be established. Modeling the crystallization kinetics is important to take into account crystallinity effects in a complete simulation of PTFE compacts sintering. The choice has been made to use Avrami/Ozawa models [36, 39] to describe the crystallization kinetics. In the case of PTFE, the crystallinity content increases for lower cooling rates (for the studied cooling rates). Therefore one can not assume that the transformation is always complete as it is supposed in Avrami and Ozawa model.

To model the primary and the secondary crystallizations, the first choice was to use Hillier's model. Hillier's model depicts a secondary crystallization that grows along the

primary. However, the secondary crystallization observed in PTFE is independent on the primary one.

Therefore, a simple sum of two crystallinity evolutions is chosen to represent the evolution of the overall crystallinity content χ:

$$\chi = \chi_1^\infty \, \alpha_1 + \chi_2^\infty \, \alpha_2 \tag{5.1}$$

where α_1 is the transformation level of the primary crystallization, α_2 is the transformation level of the secondary crystallization, χ_1^∞ and χ_2^∞ are the crystallinity content associated respectively to the primary and secondary crystallizations for a complete transformation. Note that $\chi_1^\infty + \chi_2^\infty < 1$ as the final crystallinity content is never 100 % due to chain entanglements and other defects.

Primary crystallization

The primary crystallization is described by an Avrami/Ozawa model for constant cooling rates ϕ,

$$\alpha_1(T) = 1 - \exp\left(-k_1(T)/\phi^n\right) \tag{5.2}$$

where k_1 is the Ozawa kinetic constant for the primary crystallization and n is the Avrami exponent.

k_1 is related to the Avrami kinetic constant K_1 with the relation:

$$K_1 = \left(\frac{\mathrm{d}k_1^{1/n}}{\mathrm{d}T}\right)^n \tag{5.3}$$

and due to the instantaneous nucleation K_1 can be modeled by the Hoffman and Lauritzen expression [34, 43, 44]:

$$K_1(T) = K_0 \exp\left(-\frac{U^*}{R(T - T_\infty)}\right) \exp\left(-\frac{K_g}{T\Delta T f}\right) \tag{5.4}$$

The primary crystallization kinetics is described with the Ozawa model for constant cooling rates. The same parameters can be used to obtain the crystallization kinetics for any thermal history using Nakamura formalism (see Chapter 2) [40].

Secondary crystallization

To capture the evolution of the secondary crystallization, α_2 is expressed as

$$\alpha_2(T) = 1 - \exp\left(-k_2(T)\right) \tag{5.5}$$

with k_2 a second order polynomial function of the temperature, in the temperature range of the secondary crystallization:

$$\begin{aligned} &if \quad T > T_{c_2}, && k_2(T) = 0 \\ &if \quad T_{\infty_2} < T \leq T_{c_2}, && k_2(T) = a(T - T_{c_2})^2 + b(T - T_{c_2}) \\ &if \quad T \leq T_{\infty_2}, && k_2(T) = a(T_{\infty_2} - T_{c_2})^2 + b(T_{\infty_2} - T_{c_2}) \end{aligned} \tag{5.6}$$

where T_{c_2} is the secondary crystallization temperature and T_{∞_2} is a temperature below which the secondary crystallization is stabilized.

Model identification

The crystallization model was identified on the crystallinity evolution obtained from the DSC measurements 5.3 using a Gauss-Newton method. For the first step of the procedure, the primary crystallization parameters were adjusted by manipulating crystallinity evolution subtracted from a crystallinity evolution at a given cooling rate. Hence, the experimental contribution of the secondary crystallization evolution was removed as it is similar for any cooling rate. Only the primary crystallinity was remaining and could be fitted. Then the primary crystallization parameters were fixed to adjust the secondary crystallization parameters. Finally, a complete optimization was performed on all the parameters using the previously obtained parameters as an initial guess. The results of the model fitted on the experimental curves is represented in Figure 5.7.

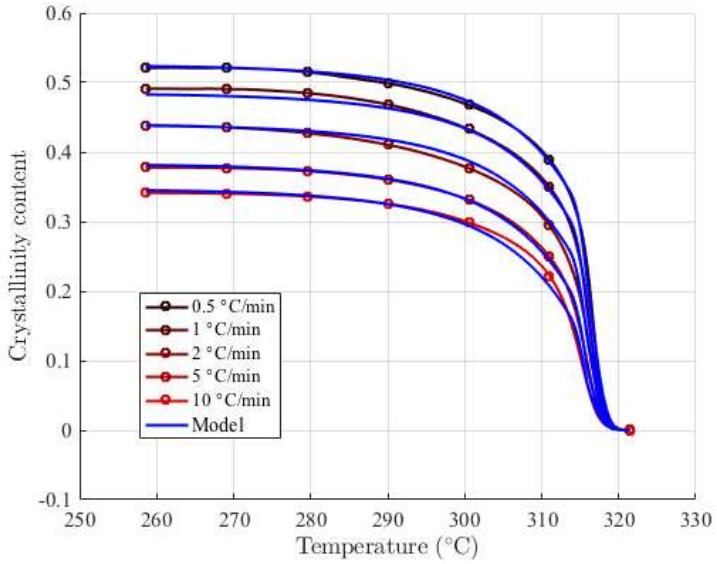

Figure 5.7: Crystallization kinetic model fitted on the crystallinity content evolution experimental curves for different cooling rates.

The evolution of the primary and of the secondary crystallinity compared to the experimental data is shown in Figure 5.8. The model gives an evolution of the primary crystallinity that depends on the cooling rate. It provides a temperature-dependent secondary crystallinity evolution. The shape of the secondary curve is similar to the shape at low temperatures of each experimental crystallinity evolution.

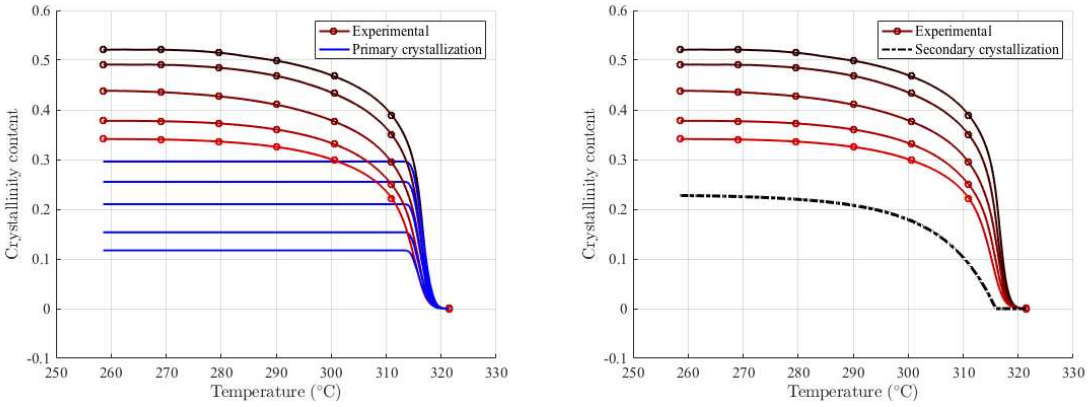

(a) (b)

Figure 5.8: Primary crystallization (a) and secondary crystallization (b) fractions of the kinetic model. The primary crystallization depends on the cooling rate whereas the secondary crystallization is only temperature dependent.

The model parameters obtained from the fit are presented below.

Parameters:

- $\chi_1^\infty = 0.355$
- $K_0 = 1337\ \mathrm{s}^{-n}$
- $U^* = 36.76\ \mathrm{J/mol}$
- $K_g = 5.148\ 10^4\ °\mathrm{C}^2$
- $T_\infty = 312.5°\mathrm{C}$
- $T_m = 326.5°\mathrm{C}$
- $n = 0.5$
- $\chi_2^\infty = 0.237$
- $T_{c_2} = 315.9°\mathrm{C}$
- $T_{\infty_2} = 250°\mathrm{C}$
- $a = -7.81\ 10^{-4}\ °\mathrm{C}^{-2}$
- $b = -0.101\ °\mathrm{C}^{-1}$

The Avrami exponent n found for the primary crystallization is 0.5. This non-integer value tends to prove that the Avrami/Ozawa model is not really adapted to represent this phenomenon. However the value is close to 1 meaning that the crystallization is more or less a one dimension growth which has been already mentioned for PTFE. Several authors identified a n equal to 1 using an Ozawa model for PTFE crystallization, however it seems that they normalized the crystallinity content with a final crystallinity content depending on the cooling rate [53, 54, 55].

The identified value of the activation energy U^* is surprisingly low compared to classical value for polymers (between 4000 and 7000 J/mol [34, 41]). Also the value of T_∞ is not corresponding to any glass transition of PTFE but to a temperature where all chain mobilities are freeze or not sufficient to go on crystallization process. Those parameters are probably not physical but they serve to describe the kinetic function K_1 related to primary crystallization. The primary crystallization is contained in the narrow temperature region between 326.5°C and 312.5°C.

For the secondary crystallization, the starting temperature T_{c_2} is 315.9°C. Below $T_{\infty_2} =$ 250°C, the crystallinity level is frozen. The choice of T_{∞_2} is not crucial as close to this temperature, the crystallinity content do not evolve much. It was necessary to set a rough approximation of this temperature to identify the parameters a, b and T_{c_2}.

As previously mentioned, $\chi_1^\infty + \chi_2^\infty = 0.592$ is largely inferior to 1. It traduces the fact that recrystallized PTFE is much less crystalline that as-polymerized PTFE. With this model the maximum crystallinity level achievable for recrystallized PTFE is 59.2 %.

2.4 Equivalence between dilatometric and calorimetric measurements

Similarly to DSC calorigrams, the evolution of the thermal eigenstrain at cooling contains information on the crystallinity content evolution. Confronting results from DSC and dilatometry are often used to consolidate the observations [118].

The dilatometric measurements and a method to evaluate the crystallinity from those measurements are described in Chapter 2.

An example of a dilatometric baselines reconstructed in order to evaluate the crystallinity content is shown in Figure 5.9 along with the evolution of the strain measured during cooling as function of temperature. As described in Chapter 2, a first baseline is generated and an optimized baseline is obtained after iterating the procedure giving access to the crystallinity content evolution. The baselines are shown in term of strain (instead of temperature derivative of the strain) for sake of clarity.

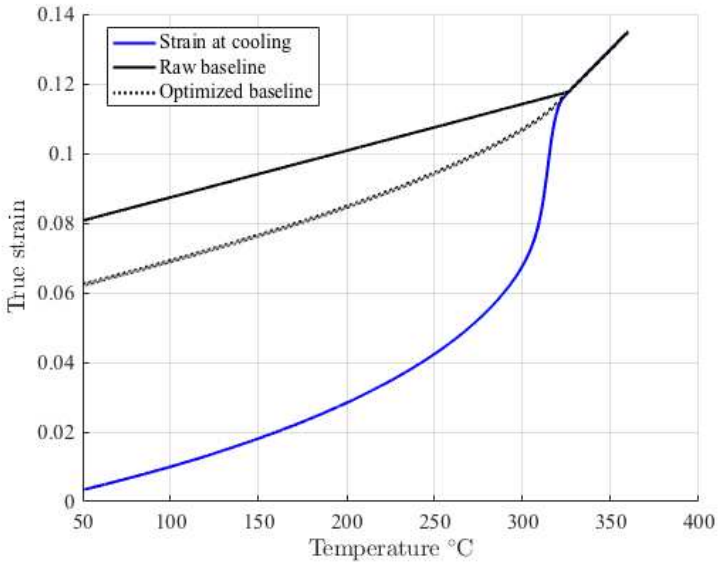

Figure 5.9: Baseline construction to evaluate crystalinity content evolution via dilatometric experiments.

There are some approximations due to this method as the crystalline volume fraction f is supposed to vary with thermal expansion whereas χ remains constant. However this method leads to very satisfying results. Figure 5.10 shows the relative crystallinity content evolution for a cooling at 2°C/min obtained from TMA and DSC experiments. The two results are extremely similar. It justifies the possibility to compare the evolutions measured in DSC with the behavior observed in dilatometric experiments.

Figure 5.10b shows a zoom of the crystallinity content evolution close to crystallization temperature. The evolution is slightly less abrupt for the evolution from the TMA experiment. This difference could be explained by thermal gradient effects. The entire PTFE block does not melt in the same time and therefore the thermal eigenstrain signature of melting is slightly delayed. It also seems to start at lower temperatures for the curve from TMA. This difference could be due to a gap between the temperature measurements in TMA and in DSC.

Note that the choice of the baseline integration is very dependent on the choice of the crystallization starting point and final point. This is especially true for DSC where the baseline is very tricky to determine.

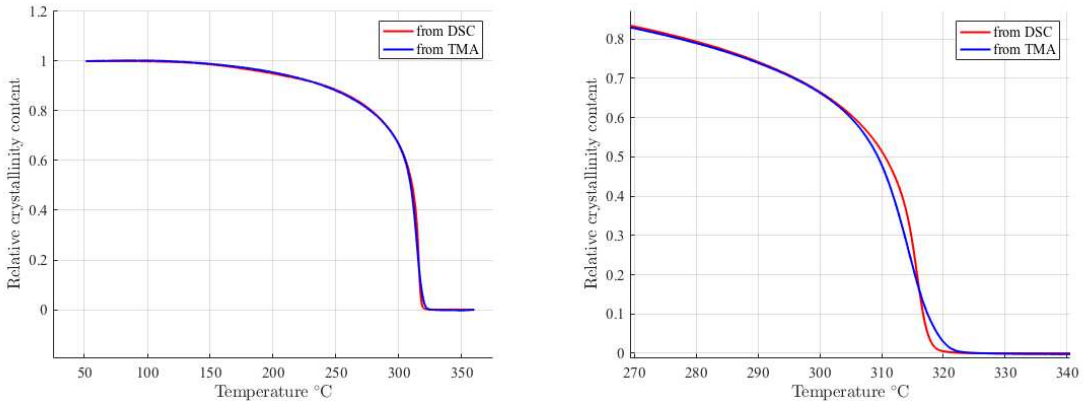

(a) (b)

Figure 5.10: Crystallinity content evolution obtained by dilatometric experiments (TMA) and by DSC experiments (a). Zoom of (a) around the crystallization temperature (b).

The evaluation of the crystallinity level is possible a posteriori using the density of crystalline and amorphous phase at ambient temperature. This method is then equivalent to the density evaluation via Archimedes's principle. However this method is less precise than with DSC as it is very sensitive to the density measurement.

3 Anisotropic behavior

3.1 Anisotropic thermal eigenstrain†

Overall thermal eigenstrain measurements also provide information on the phase change due to the density variation. At 25°C, the density of the PTFE crystal is 2.302 g/cm^3 and the density of the amorphous phase is about 2.0 g/cm^3 [61]. Therefore large variations of the sample dimensions are measured at melting and crystallization via TMA.

The same type of thermal cycle as in DSC was performed on a PTFE sample in a TMA instrument: a first heating, a plateau, a cooling and then a second heating. The heating and cooling rates were set at to 2°C/min to limit the thermal gradients from the skin to the core of PTFE sample. The PTFE sample was melted a first time and held at 375°C for 100 min (Figure 5.11a). Further, the melted sample was cooled down at ambient temperature and then heated up again. The displacement in the compaction direction

(CD) and in the transverse direction (TD) were measured on two different samples as an transverse isotropic behavior is expected due to the uniaxial compaction process.

Figure 5.11 shows the measured true strains (in CD and TD) as functions of time. The strain reference has been set at the end of the cooling. It can be set by a mere translation along the strain axis thanks to the choice of logarithmic (Hencky) strains. The first striking feature observed in Figure 5.11b is the symmetry between the cooling and the second heating. The anisotropy of the first heating was studied in an earlier study and was shown to be related to residual stress relaxation originating from cold compaction [72, 111].

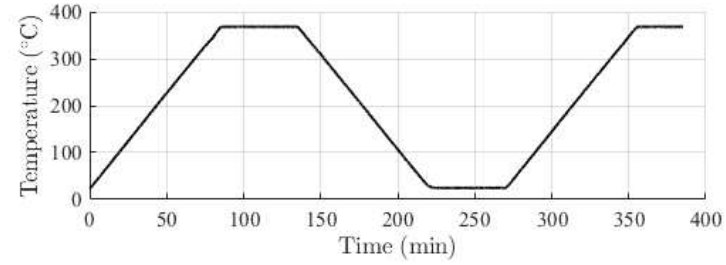

(a)

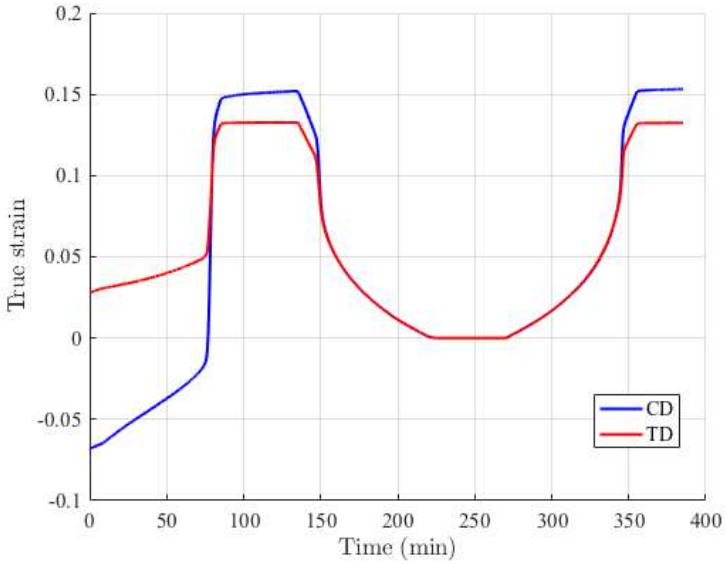

(b)

Figure 5.11: (a) Thermal cycle imposed for the TMA experiment. (b) Measured true strain of the PTFE samples (50 MPa-pressed) during the thermal cycle in CD and TD. The reference state for strain evaluation is chosen at the end of the sintering period (at 250 min).

This symmetry can be highlighted more quantitatively by plotting the strains measured in the cooling and the second heating stages as a function of temperature (see Figure 5.12). Below 300°C, the cooling strain and the second heating strain are almost perfectly superimposed. In this temperature range, the overlap means that the crystallization is reversible and shows no hysteresis. This result is consistent with earlier observations [59].

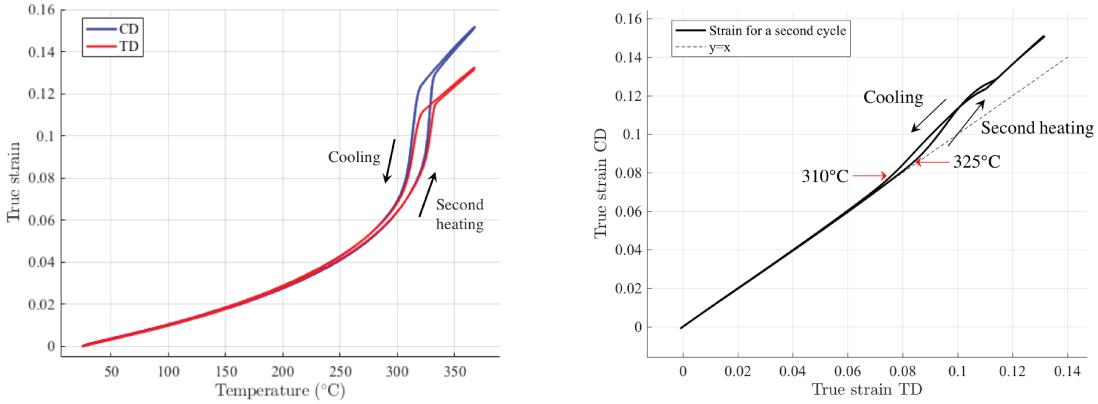

(a) (b)

Figure 5.12: (a) Measured strain (CD and TD) as function of temperature, for the cooling and the second heating (of a melted PTFE sample uniaxially compacted at 50 MPa); (b) Strain in CD as function of strain in TD compared to curve $y = x$ representing an isotropic behavior.

Plotting the CD and TD curves (resp. shown in blue and red) one against the other, in Figure 5.12b, provides information on the anisotropy. The slope of the curve quantifies the anisotropy of the strain. Therefore, the strain at cooling and at the second heating are isotropic below respectively 310°C and 325°C. Above this temperature, the curve can no more be superimposed with the curve $y = x$ that characterizes an isotropic behavior. It shows that the secondary crystallization induces an isotropic behavior which is reversible meaning it is the same at cooling and heating. Conversely, the primary crystallization appears to lead to an anisotropic behavior similarly to melting, reminiscent of the initial crystalline orientation (see next subsection 3.2). The observed hysteresis is related to the primary crystallization, which is not reversible.

Furthermore, Figure 5.12b also reveals that the thermal expansion of the amorphous phase is anisotropic whereas the thermal expansion of the recrystallized PTFE is isotropic. This is a surprinsing paradox for PTFE. In most cases, polymer melts have a completely isotropic behavior and once recrystallized, an orientation may be generated and induce an anisotropic behavior. In the case of uniaxially compacted PTFE, the opposite occurs. The exact reason for this behavior is not completely understood. It is almost certain that PTFE melt is still orientated due to the low mobility of the molecular chains however the reason for an isotropic behavior after crystallization is unclear.

Based on previously published results [32, 33, 31], and on the above reported experiments, it may be concluded that the primary crystallization consists in the formation of large crystal bands that thickens with time as temperature decreases between 320 and 310°C. This first phase transformation is rate limited and exhibits the large scale anisotropy induced by the initial cold compaction, which does not completely vanish after melting. In contrast, the secondary crystallization displays no hysteresis, so that it depends only (and instantaneously) on temperature. Thus it can be considered as an equilibrium reversible process. It is thus plausible that it consists in the nucleation-free [59] formation of many small crystals certainly of random orientation (as it induces an isotropic behavior), and hence not related to the primary crystals.

3.2 Crystalline orientation measurement•

X-ray diffraction measurements are analyzed using the sample preparation and the method described in Chapter 2.

Orientation for green and sintered PTFE

Experimental data sets obtained for both samples (green and sintered) using the laboratory X-ray diffractometer are presented in Figure 5.13. The two signals reveal anisotropic crystalline textures as the intensity is higher in CD than in TD. The sintered PTFE seems to have a lower anisotropy than green PTFE.

By using the method described in Chapter 2, the Hermans factor can be evaluated for both samples. For green PTFE, $f_H = -0.083$, and for sintered PTFE, $f_H = -0.043$. This indicates that the orientation of the PTFE crystals is suprisingly low and, as expected, mostly perpendicular to the $\boldsymbol{Q}$ direction chosen to be the oedometric compaction direction. The value of f_H is quite far from that of a complete orientation in the transverse plane ($f_H = -0.5$). It reveals that even though compaction involves large strains in PTFE powder, it only reorients slightly the chains. It also shows that sintering reduces the crystalline texture. The melting stage might allow the macromolecule chains to relax and somehow to reduce the preferential orientation induced by compaction.

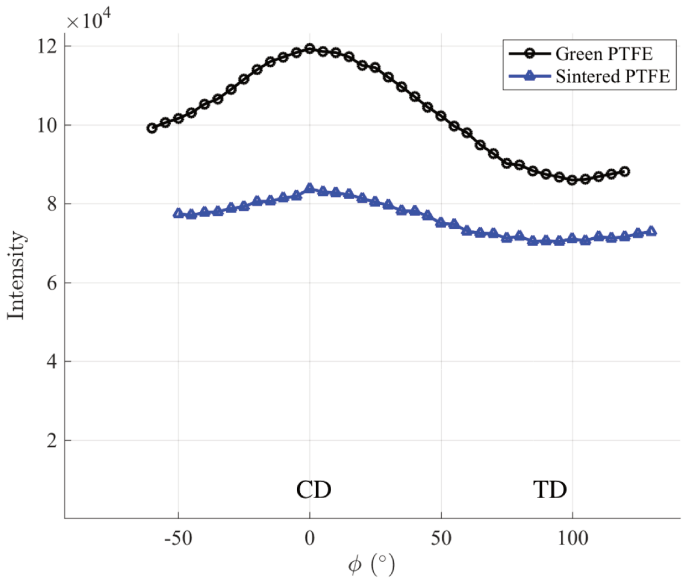

Figure 5.13: Integrated diffracted signal along peak (100) as function of ϕ for a green PTFE sample and for a sintered PTFE sample (both uniaxally compacted at 50 MPa) measured at room temperature on a laboratory X-ray diffractometer.

Studying the evolution of the crystalline texture at crystallization could provide insights on the different mechanisms. Evaluating the Hermans orientation factor with the method described herein allows one to measure the crystalline orientation in *in-situ* experiments.

Evolution of orientation during *in-situ* crystallization

The same type of experiment was conducted during the cooling stage of a melted PTFE sample using synchrotron radiation at the ESRF facility to perform an *in-situ* experiment.

The purpose of this experiment is to evaluate the evolution of the crystalline orientation during crystallization.

The evolution of f_H during cooling at 10°C/min from 370°C to ambient temperature is presented in Figure 5.14. The initial value of the Hermans orientation for the green PTFE (at room temperature) is $f_H = -0.093$ and is indicated on the Figure. The evolution of the crystalline peak intensity is shown to assess the evolution of the crystallization. It appears that the crystalline orientation sets in at a very early stage of crystallization (320°C). This early orientation is comparable to the one of the green PTFE and even seems to reach higher absolute values. Below 270°C, the orientation reduces significantly to reach $f_H = -0.073$. The values measured during this experiment are slightly higher than the one measured in the previous experiment before and after sintering. It could be explained by the fact that the PTFE slices are thinner and therefore some parasitic orientation could be induced by the cutting process. The overall evolution is similar for the two experiments, and in all cases, sintering is seen to reduce the crystalline texture.

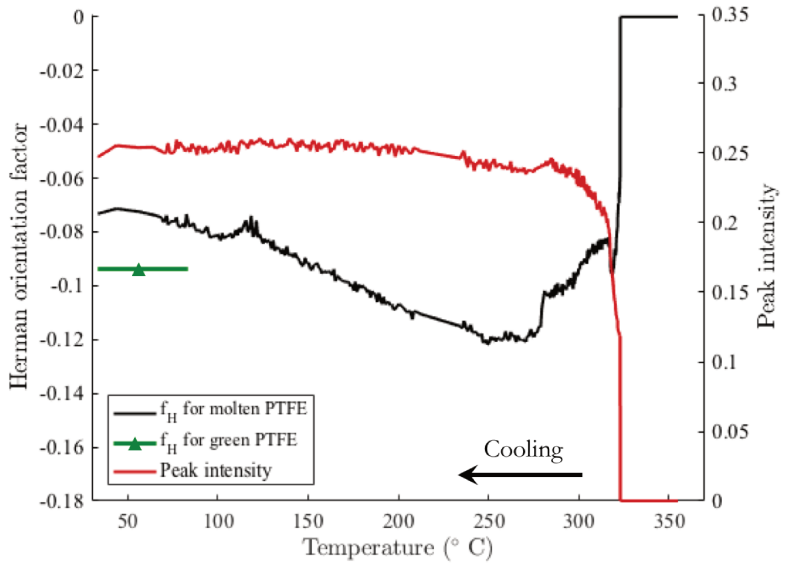

Figure 5.14: Evolution of the Hermans orientation factor of molten PTFE during cooling at 10°C/min compared to its value for green PTFE before melting. The evolution of the crystalline peak intensity is presented to gauge the evolution of the crystallinity.

Note that the temperatures indicated are subject to high uncertainties as the measurement was difficult to perform. The thermal gradient from the surface of the hot stage and the outer surface of the PTFE sample can be very high (more than 30°C between the two surfaces). The results should be treated with caution and considered as qualitative data on the evolution of the crystalline orientation during crystallization. A few aberrant data points were removed between 210°C and 235°C for the sake of clarity.

The herein proposed evolution suggests that primary crystallization preserves the crystalline orientation induced by uniaxial compaction. It is less easy to conclude for the secondary crystallization as the indicated temperature is only approximate. However the clear trend is a reduction of orientation as temperature is decreased. It could mean that secondary crystallization produces crystals which are more isotropically distributed, thereby decreasing the overall orientation. The orientation tends to decrease even after the end of crystallization. This could be related to the "glass transition" around 120°C [28, 27].

Below 120°C, the orientation seems stable.

3.3 Secondary crystallization as non linear heat capacity†

Because the secondary crystallization appears to be an equilibrium phenomenon, with no history (or time) dependence, it could be included into a non-linear dependence of the heat capacity of the crystal phase with temperature. Thereby, its calorimetric contribution was included into an effective c_p so as to define another baseline $\dot{q}_{\text{base}}$ in DSC analyses as illustrated in Figure 5.15. From the DSC data, from whatever prescribed temperature-time evolution, there is no way to distinguish this analysis from the earlier one (shown in Figure 5.2).

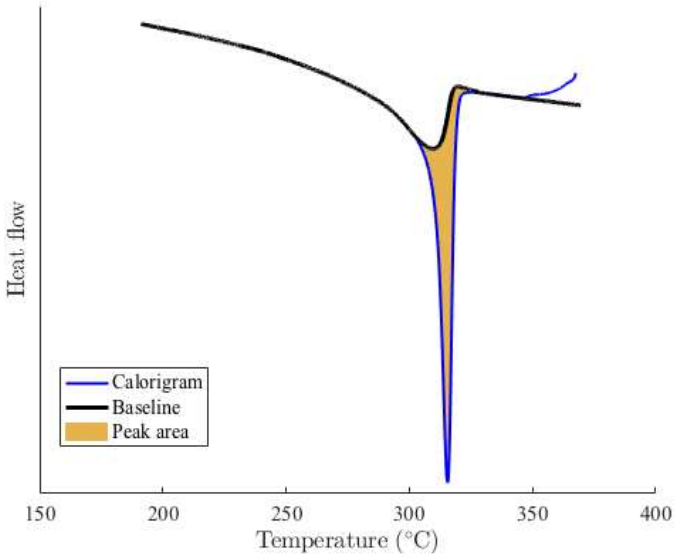

Figure 5.15: Modified baseline from DSC experiment with a non linear shape at lower temperature to fit the lower part of the crystallization peak. Such baseline enables the measurement of the primary crystallization only through the peak integration (to be compared with Figure 5.2).

Likewise, the eigenstrain component imposed by the secondary crystallization could be replaced by an isotropic thermal expansion coefficient $\beta(T)$ depending on the temperature instead of a constant one (see equation (2.10) in Chapter 2).

By construction, both descriptions give equivalent results to predict calorimetric and dilatometric experiments with PTFE. The only way to assess that the alleged variations of c_p or of β with T are due to a secondary crystallization is to measure the final crystallinity content. Crystallinity measurements on PTFE are not considered as very accurate [119] but trends are consistent.

Different measurements of the final crystallinity content are gathered in Figure 5.16 as a function of the cooling rate. Some measurements are coming from the DSC peak integration taking into account the secondary crystallization (first procedure). In addition, data from wide angle X-Ray scattering (WAXS) performed at the European synchrotron radiation facility (ESRF), are presented. The crystalline peak and the amorphous halo are integrated on the diffractogram, providing respectively I_{cr} and I_{am}. The ratio $I_{\text{cr}}/(I_{\text{cr}}+I_{\text{am}})$ gives a second estimate of the crystallinity content. On those WAXS measurements, the

uncertainty is quite high due to the choice of the baseline. A consistent methodology was applied and the observed trend is consistent with the DSC measurements. A third evaluation was obtained after sintering on the TMA machine by density measurements using Archimedes' principle. The crystallinity is evaluated from the value of the density knowing the density of the amorphous and the crystalline phase. The result was averaged over three experiments. All resulting data are consistent with the other measurements.

The crystallinity results confirm that the values obtained by DSC taking into account the secondary crystallization give the correct crystallinity content. Without the secondary crystallization, the DSC values would drop by 25%, reaching a value too small to be consistent with the other measurements.

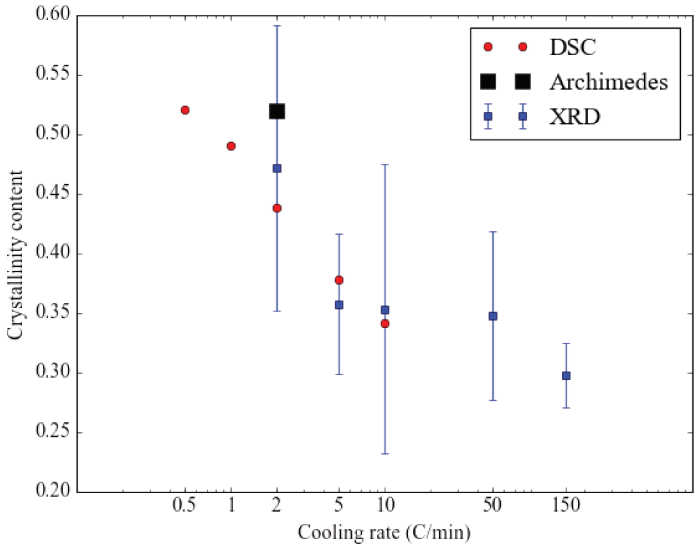

Figure 5.16: Final crystallinity content measured via DSC, XRD and Archimedes density measurement for different cooling rates.

4 Conclusions and perspectives

PTFE presents a singular crystallization behavior that can be decomposed into two mechanisms. The primary one has its own temperature rate dependence that controls the final crystallinity content as the cooling rate is changed. The secondary one is only related to temperature and is reversible.

The primary crystallization is responsible for an eigenstrain that keeps (at least) part of the crystalline orientation induced by the initial compaction. As PTFE molecular chains are very long, it is expected that they keep their large scale orientation even in the molten state. Primary crystals could be originating from the polymer chains whose large scale orientation is inherited from the preparation stage (cold pressing) to form crystalline bands. Those bands would thicken with time as temperature is lowered. On the contrary, the secondary crystallization induces an isotropic engeinstrain. It could be related to small crystals independent from the primary crystals that are at thermal equilibrium.

From X-ray diffraction observations, it appears that the crystalline orientation decreases at cooling. This result is consistent with the hypothesis that secondary crystals are evenly oriented. However the decrease seems to continues with cooling until the second glass

transition (related to RAF).

A crystallization kinetic model based on Avrami/Ozawa equations was developed to reproduce the behavior of molten PTFE at cooling. It takes into account the primary and secondary crystallization mechanisms. This model has some limits due to the non-compliance with the hypothesis of complete transformation of the Avrami model. Another kinetic model should be designed for better predictions. However this model is sufficient for the analyzed cooling rates range and can be easily implemented in a simulation.

It was shown that DSC and dilatometric experiments give equivalent information on the crystallinity content evolution. An similar crystallinity content evolution with temperature was obtained by DSC and dilatometric experiments. This equivalence is important to consolidate the observations on PTFE crystallization and it is also convenient to simulate the thermal eigenstrain behavior of PTFE for any thermal history (see Chapter 7).

From a broader view, the eigenstrain behavior is very different between as-polymerized PTFE (first heating) and melt-polymerized PTFE (cooling and second heating). For as-polymerized PTFE, the eigenstrain is affected by the residual stress relaxation due to the compaction stage. This leads to very anisotropic eigenstrains. For melt-polymerized PTFE, the eigenstrain is only anisotropic in the molten state and in the first part of the crystallization (or melting of the primary crystals). At lower temperature, the secondary crystallization, melting and thermal expansion are isotropic and reversible. This paradoxical behavior of PTFE is still unclear. In the molten state, PTFE chains do have not enough mobility to wipe out the orientation induced by compaction. However the reason why PTFE has an isotropic behavior after crystallization is unclarified.

Observing PTFE crystallization via *in-situ* test using scanning electron microscopy or atomic force microscopy (AFM) would be very interesting. The thickening of the primary crystals could be observed and the secondary crystals would probably be too small to be seen. However, the absence of visual change in the secondary crystallization temperature range would support this hypothesis.

Chapter 6

Thermomechanical behavior of PTFE

The mechanical behavior of PTFE is studied in this chapter for both green and sintered PTFE at different temperatures. An unexpected memory effect is observed and a thermomechanical model for PTFE is proposed.

Contents

1 Introduction

Literature on PTFE mechanical behavior is not as wide as for other polymers. The only data on the elastic properties of PTFE concerns sintered PTFE. One of the reasons for the lack of information on green PTFE compacts is that it depends on the compaction state (as shown in Chapter 1 and especially in Figure 1.17) and therefore on its density. It is also tricky to measure due to the brittleness of such specimen which are difficult to shape. PTFE is assumed to be a visco-elastic material and even visco-plastic in the molten state. Complex models have been developed. Some of them take into account chain sliding leading to irreversible strains and viscoelastic response related to the network [70, 71]. Those models are usually for temperatures below 200°C which is lower than the sintering temperature (around 370°C). The plastic behavior of PTFE is facilitated by the very low plasticity threshold of its crystals [64, 65].

Mostly uniaxial compression tests in the compaction direction (in the case of uniaxially compacted sample) are performed in this chapter. Poisson's ratio is supposed to be constant with temperature and the anisotropy of the mechanical properties is neglected. Elasticity measurements at ambient temperature were made in the compaction and transverse directions, and only small differences was observed between them.

This chapter aims at evaluating the mechanical properties necessary for the simulation of the sintering process. Therefore, the elastic and viscoelastic behaviors are analyzed as function of temperature in section 2. Then the elastoplastic properties are characterized for different temperatures in section 3. Finally, element of thermomechanical modeling of PTFE during sintering are proposed in section 4.

2 Elasticity and viscoelasticity

Dynamic mechanical analysis and compression tests are performed at different temperatures to evaluated the viscoelastic and the elastic behavior of PTFE.

2.1 Dynamic mechanical thermal analysis (DMTA) measurements

Sintered PTFE sample were tested using a dynamic mechanical thermal analysis (DMTA) apparatus. More details on this method are presented in Chapter 2.

A first test was made at 1 Hz with 1% of strain amplitude between 30 and 370°C at heating of 2°C/min. Figure 6.1 shows the storage (G') and the loss moduli (G'') as function of temperature. At the analyzed frequency, the loss modulus is always lower than the storage modulus by at least one decade. It means that the viscous effect is negligible at this frequency so that sintered PTFE can be considered as an elastic medium.

The damping ($\tan\delta = G''/G'$) is also shown. This quantity is interesting to study the different transitions and second glass transition can be noticed thanks to the local maximum of the damping at 130°C (mentioned in Chapter 1).

Other DMA tests were made using the DMTA to characterize the viscous properties for longer characteristic times at different isotherms. The storage and loss moduli were acquired for frequencies ranging between 0.002 and 1 Hz for 1% strain amplitude in the molten state (360°C) and in the partially recrystallized PTFE (310°C) with an estimated crystallinity content of 35%. Their evolutions are shown in Figure 6.2. Very similar results were obtained for a strain amplitude of 10% at 360°C.

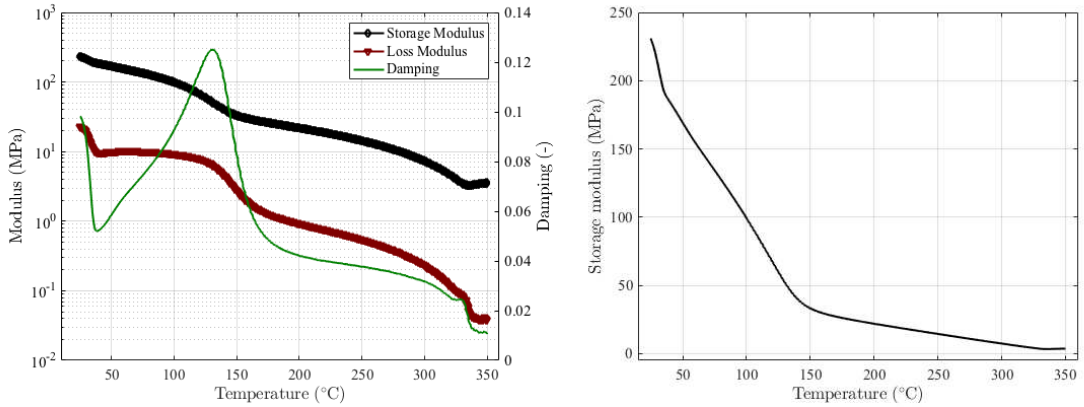

(a) (b)

Figure 6.1: (a) Measured storage modulus, loss modulus and damping evolution with temperature on sintered PTFE (at 1Hz, 1% amplitude and 2°/min). (b) Focus on the storage modulus evolution with temperature.

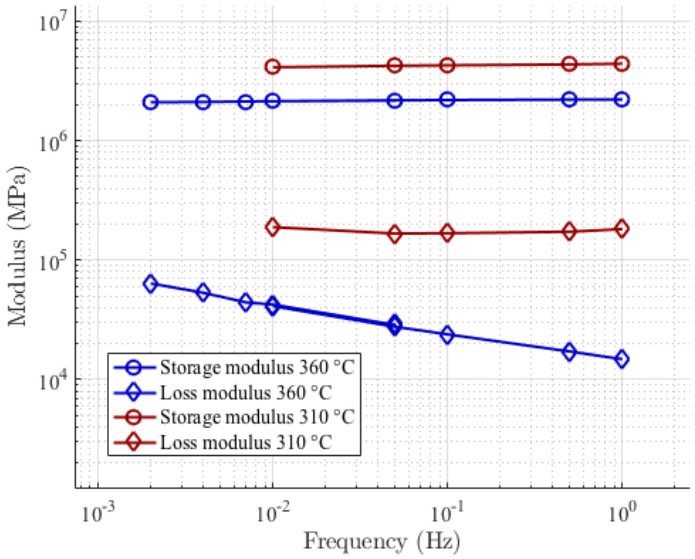

Figure 6.2: Storage modulus and loss modulus as function of the frequency for molten PTFE (360°C) and for partially recrystallized PTFE (310°C).

For both temperatures, the storage modulus does not vary much with frequency. The loss modulus is increasing with a decreasing frequency (*i.e.* at longer characteristic time) at 360°C. However even for the lower characteristic time which corresponds to 8 min, the loss modulus is more than 10 times lower than the storage modulus. A linear extrapolation would give a characteristic time of 10^8 s (more than 3 years) to make the storage and loss moduli intersect. It means that relaxation times of PTFE are so long that viscous effects would not affect a sintering cycle of a characteristic time close to one day. From those results, it can be concluded that PTFE behaves as an elastic material in the molten on the contrary to the common perception.

In the recrystallized state, the loss modulus seems to vary even less than in the molten state. Thus the characteristic relaxation time would be even longer than for molten PTFE.

Therefore, viscoelastic properties can be neglected for PTFE for usual applications. However, the DMTA experiments were only performed on sintered PTFE. Green PTFE compacts are too brittle to be clamped in the apparatus. Other measurements are then necessary to estimate the elastic properties of green PTFE.

2.2 Compression tests inside thermal chamber

Compression tests were performed in a thermal chamber placed on a universal testing machine. Small PTFE cubes (8 mm × 8 mm × 7.5 mm) compacted at 50 MPa were tested in the compaction direction during a thermal cycle. The samples were heated up to the melting temperature at 2°C/min. The same test was also performed at cooling at 2°C/min. Cyclic loading/unloading were applied in the elastic regime (strain below 1 %) controlled at 1 µm/s. The Young's modulus was evaluated from the slope of the measured stress-strain curves as function of temperature.

Figure 6.3 shows the evolution of the Young's modulus obtained from the compression tests on green and on sintered PTFE. It appears that the green PTFE has a similar Young's modulus than for sintered PTFE below 100°C. Above 100°C which is close to the second glass transition (α-transition around 130°C) [28, 27], the Young's modulus of sintered PTFE drops drastically. Conversely, for green PTFE it decreases more gently with temperature. The reason for this difference may be related to crystallinity level. As green PTFE is almost fully crystalline, it is less affected by the glass transition (where the amorphous phase goes in the rubbery state). In contast, sintered PTFE is almost 50 % amorphous and therefore is very impacted by the glass transition.

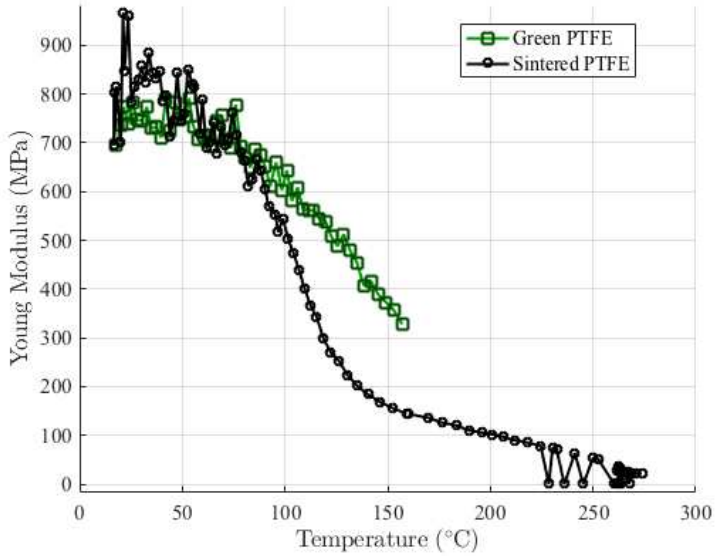

Figure 6.3: Young's modulus for green PTFE compacts and sintered PTFE obtained with compression tests in thermal chamber during sintering cycle. The compression direction corresponds to the compaction direction. The samples were compacted at 50 MPa.

Although this measurement method is convenient to estimate the Young's modulus,

there are some issues on the temperature control. Indeed only the oven temperature was controlled. Thus, the temperature indicated in Figure 6.3 is not truly the sample temperature but only an estimation from the thermocouples placed inside the oven close to the sample. The Young's modulus estimations are obtained on a broader temperature region for the sintered PTFE as it profited from the measurement at heating and cooling. The measurement for green PTFE could only be made at heating before PTFE is melted. Furthermore, as this is an anisothermal testing, thermal gradients can exist in the sample especially with the contact of the metal compression plates. Therefore Young's modulus is evaluated for an inhomogeneous sample.

Despite the temperature inhomogeneities, the evolution and the values of the Young's modulus shown in Figure 6.3 are consistent with the storage modulus measurements from DMTA in Figure 6.1b. Only the evolution below 50°C is different. This might be due to the thermal inertia of the thermal chamber at the beginning of the heating.

To obtain more accurate measurements, isothermal mechanical testings were performed in the same thermal chamber on bigger PTFE samples. Those samples were compacted isostatically up to 35 MPa with a different PTFE resin (Free flow resin Teflon® 807-N) instead of the low flow resin. The dimensions of the samples are 20 mm × 20 mm × 40 mm (Figure 6.4). Testing bigger parts allowed us to improve the accuracy of the measurement with the force sensor. Besides, measuring the strain from the displacement of the actuator can be slightly erroneous due to the deformation of the whole testing device. Thus, the displacement measurements were obtained using digital image correlation (DIC) using Correli™ software (see Chapter 2). The interest of using DIC is to access directly the strain field on the sample surface.

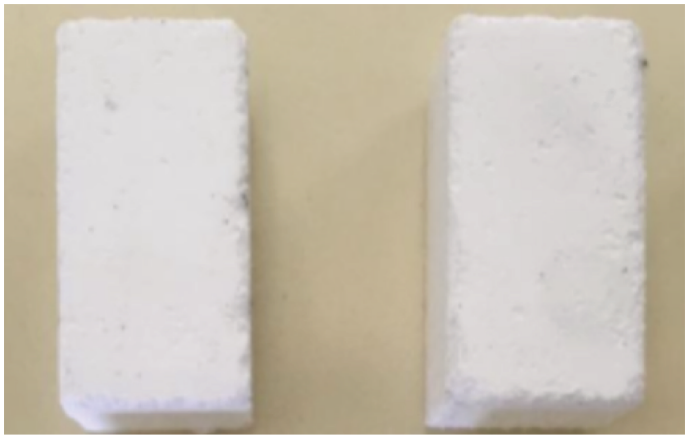

Figure 6.4: Isostatically compacted PTFE samples (up to 35 MPa) of dimensions 20 mm × 20 mm × 40 mm. Free flow resin was used for those samples instead of low flow in the rest of the work.

Each sample was compressed in the thermal chamber at different isotherms. A holding time of about half an hour was performed before testing to ensure the thermal homogeneity of the part. The same cyclic loading in the elastic regime were applied as in the previous experiment. The Young's modulus is then evaluated at different temperatures for green and sintered PTFE.

Figure 6.5 shows the evolution of the Young's modulus as function of temperature. The same trend is observed than in the previous experiment between the green and sin-

tered PTFE behaviors. Sintered PTFE elastic modulus decreases more than green PTFE's around 100°C. The values of the Young's modulus are slightly lower than the one measured in the previous experiment. This difference may be due to the different resins tested. The values of Young's modulus measured in all the experiments remain in the range of Young's modulus identified in the literature [62, 61, 63].

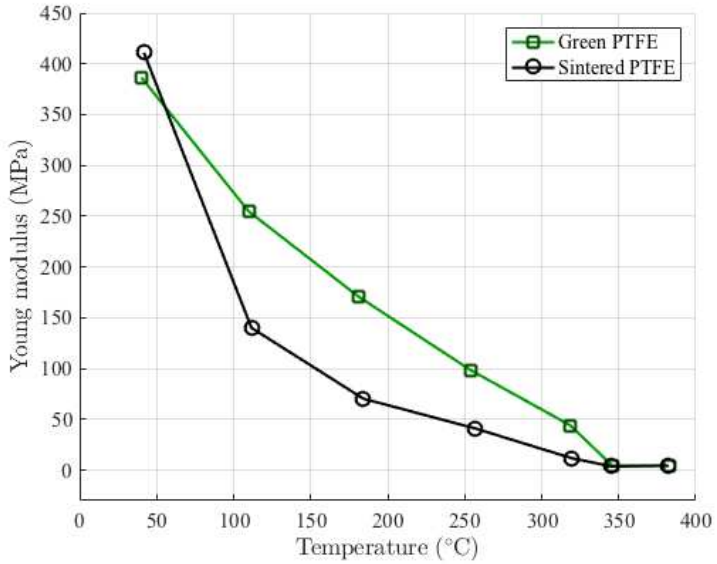

Figure 6.5: Young's modulus for green PTFE compacts and sintered PTFE obtained with compression tests in thermal chamber at different isotherms. Those results are obtained on a different resin (free flow resin) than for the rest of the work.

To simulate PTFE compact sintering, the values of the Young's modulus are set from the DMTA experiment in Figure 6.1b. The evolution from sintered PTFE is applied to green and sintered PTFE for simplicity. A simple improvement of the model consists in adapting the measured evolution of green PTFE modulus with temperature to the simulation. Besides, green PTFE elastic properties also depend on the compaction state (see Chapter 1). Fredy measured the Young's modulus and the Poisson's ratio as functions of the void ratio [10]. This Young's modulus evolution is extrapolated over temperature using the results from DMTA (on sintered PTFE) for the simulation. The extrapolation is performed using the condition that the properties in the molten state do not depend on the initial void ratio. This condition ensue of the assumption that the entire porosity is closed simultaneously with melting. The Poisson's ratio is considered constant with temperature until melting and is set as determined by Fredy in the simulation. After melting, it is fixed at the Poisson ratio value of green PTFE with no porosity ($\nu = 0.48$).

3 Plasticity

Irreversible strains are generated during mechanical loadings when the stress exceed a stress threshold. This section tries to characterize the plasticity in PTFE and to link it to crystallization. Then an interesting memory effect related to PTFE plasticity is exposed.

3.1 Plasticity evolution with crystallization

When the PTFE is loaded above a certain macroscopic yield stress, an overall "plastic" strain occurs in the semi-crystalline polymer. This "plastic" strain results from the local phase deformations (amorphous phase and crystalline phase).

In comparison to other families of materials, such as ceramics and metals, the macroscopic yield stress is low. This can be explained by the fact that at the local scale, a low energy is required to generate slip in crystallographic planes of the crystallites. Consequently, the local shear stress threshold is very low.

The local sliding in the crystallites is also responsible for low coefficient of friction of PTFE.

Uniaxial compression tests were performed to evaluate the plastic behavior of PTFE as function of temperature. Sintered PTFE samples were compressed in a thermal chamber at different isotherms. The sample was compressed successively at increasing loads with (almost) complete unloading in between. The unloadings were not complete to keep the contact between the plates and the sample. The tests were performed at seven temperatures: 100, 150, 200, 250, 275, 300 and 330°C.

The stress strain curves obtained at 100°C and for another sample at 330°C are shown in Figure 6.6.

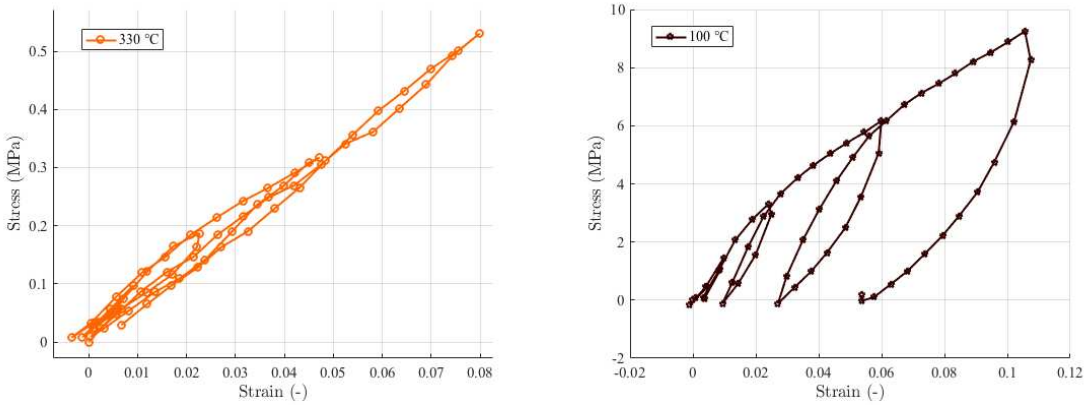

(a) (b)

Figure 6.6: Stress-strain curves from compression tests with different unloadings in the molten state at 330°C (a) and in a recrystallized state at 100°C (b).

The behavior of (previously sintered) PTFE at 330°C in the molten state is quasi purely elastic. The loadings and unloadings curves are almost superimposed (Figure 6.6a). Its Young's modulus corresponds to the rubbery modulus of PTFE around 6 MPa already measured from DMA in Figure 6.2.

Sintered PTFE shows an elastoplastic behavior at 100°C. In Figure 6.6b, it can be seen that after a certain load, PTFE does not retrieve the initial position after unloading. Therefore irreversible strains (or plastic strains) appear that can be measured at unloading. A yield stress is observed at about 2 MPa. Above this stress level, a plastic strain is generated. Plasticity is generated at higher stresses, and a hardening behavior increases the yield stress with the plastic strain.

Note that the hysteretic loops at unloading and reloading (in Figure 6.6b) could be assimilated to viscous effects. However this non linear behavior is most likely caused by

plasticity. Due to the fact that the threshold is seen from different direction at loading and unloading, it creates a hysteresis. To rule out the hypothesis that it is related to viscous effects, the same experiment should be done at different strain rates and give the same result.

The envelop stress-strain curves (unloading removed) are gathered in Figure 6.7 for the different temperatures (100, 150, 200, 250, 275, 300 and 330°C). The behavior evolves smoothly from an elastic behavior to an elastoplastic behavior. The hardening region can be noticed at stresses above the slope discontinuity. It appears that the elasticity limit is characterized by a strain that is similar for every curves which is slightly below 2%.

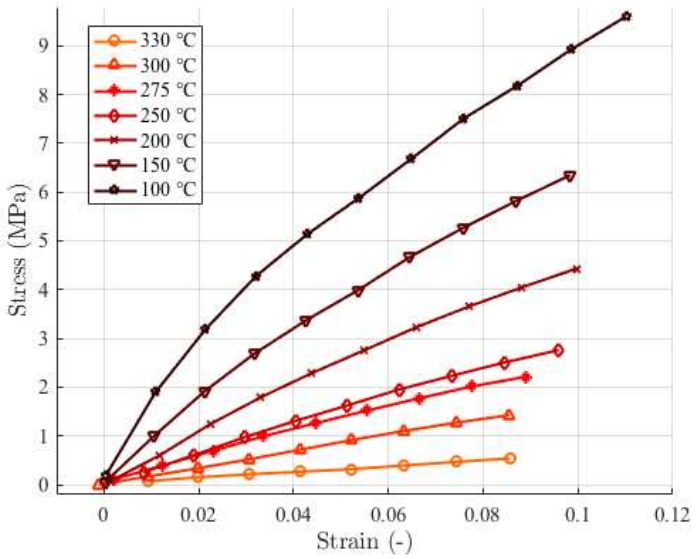

Figure 6.7: Envelop of the stress-strain curves obtained from compression tests at different temperatures.

3.2 Memory effect

As molten PTFE appears as a perfect elastic material, the following question arises: what happens to the plastic strain during melting?

To answer this question, a specific experiment was conducted as illustrated in Figure 6.8. A sintered PTFE plate was picked (35 mm × 35 mm × 2 mm) and was significantly bent at room temperature (Figure 6.8b). After 6 hours, the PTFE plate was still bent and almost no recovery was observed (Figure 6.8c) This relaxing step was performed to discard viscous effects. Then the sample was subjected to a thermal cycle similar to a sintering thermal treatment (heating up to 370°C at 4°C/min). The plate was suspended vertically in order to avoid any gravity effect. After complete melting, the plate recovered its initial flat shape. The recrystallized specimen is shown in Figure 6.8d and it has the same shape than before bending.

During the thermal cycle, the plate was observed and it appeared that a part of the strain was recovered even before melting (at low temperatures).

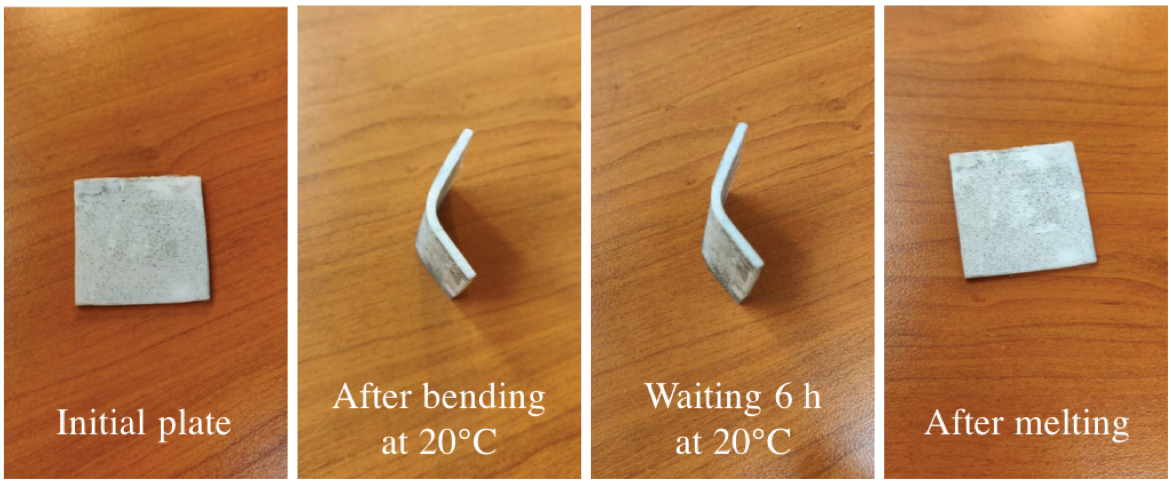

(a) (b) (c) (d)

Figure 6.8: Photos of the shape memory experiment. A 2 mm thick PTFE plate (a) is bended at ambient temperature (b). 6 hours after, the sample is still bended (c). The plate is heated above PTFE melting temperature in an oven and then cooled down, the plate recovered from the bending (d).

An attempt of explanation of this shape memory effect of PTFE is proposed through the microstructure evolution. Figure 6.9 shows a sketch of PTFE microstructure related to the previous memory experiment (Figure 6.8).

In the molten state, PTFE acts as an elastomer due to its high molar mass. The long macromolecules of PTFE form an entangled chains network (Figure 6.9a). Consequently molten PTFE presents an entropic elasticity. When PTFE recrystallizes, crystals freeze the shape of the PTFE specimen by forming physical crosslinks (Figure 6.9b).As previously mentioned, PTFE crystals have a very low shear plasticity threshold [64, 65]. Thus when the specimen is deformed, crystalline lamellae slide to form a new stable crystalline configuration. The amorphous phase is constrained and remains elastic which results in very low stress due to its low elastic modulus. The deformed configuration is then maintained due to crystal sliding strain (Figure 6.9c). The melting of the deformed PTFE specimen erases the crystalline arrangement and restores the elastomeric network of the previous molten state. The network recovers its initial undeformed configuration as it is a more stable state for the macromolecules (Figure 6.9d).

The shape memory effect is a common phenomenon in different polymers. It is usually linked to the glass transition. The polymer specimen is deformed in the rubbery state and cooled down below its glass transition temperature T_g to freeze its shape. Once heated up above T_g, the polymer recovers its initial shape.

In the case of PTFE, the effect is different. The temperature considered for the effect is the melting temperature T_m instead of T_g. More importantly, the specimen can be either deformed in the molten state or in the recrystallized state and still recover from its strain. A memory effect as been already been observed for PTFE close to the double crystalline transition at 19 and 30°C [70]. This effect could have the same origin but with a crystalline transition instead. It may be responsible of the first part of the recovery observed at lower temperature during the shape memory experiment.

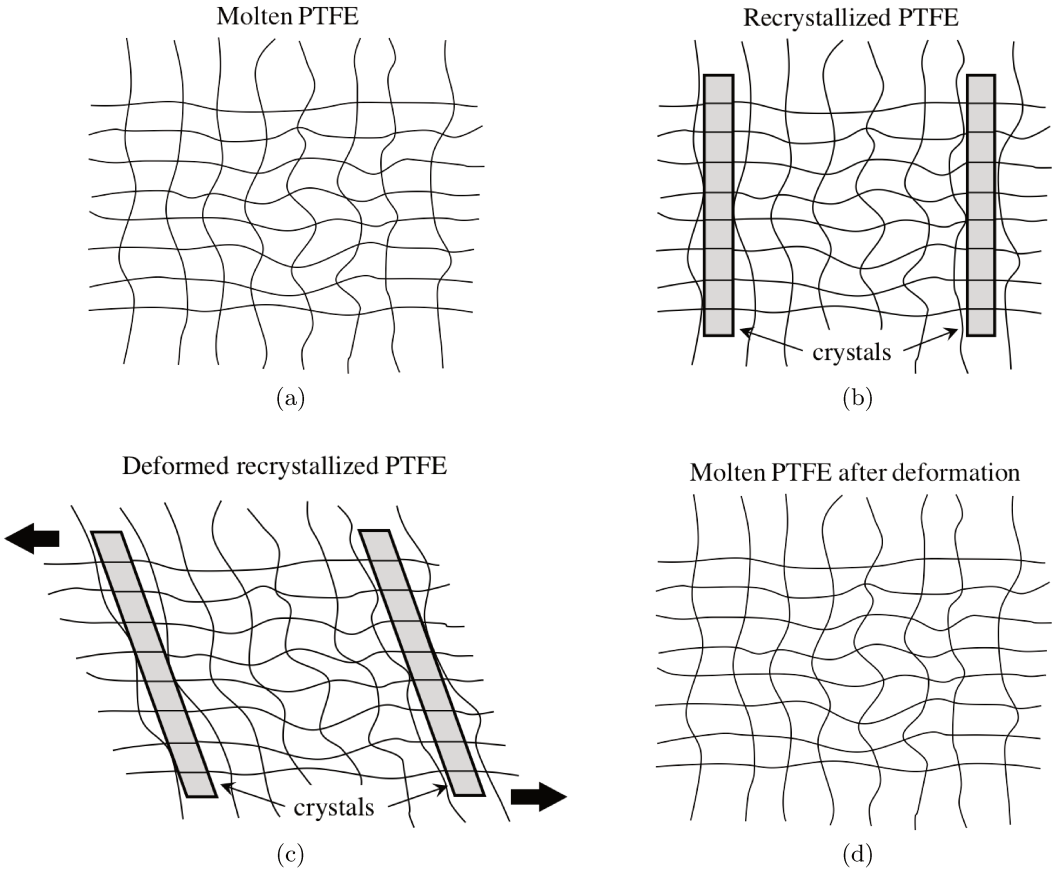

Figure 6.9: Interpretation of the memory effect. Molten PTFE is a network of macromolecule chains connected via entanglements (a). When PTFE cools down, it crystallizes, and crystals stiffen the network (b). "Permanent" deformation is possible due to high crystal plasticity and the strain is stored thanks to the new crystal arrangements (c). Melting removes the crystalline areas and allows the network to retrieve its initial configuration (d).

4 Thermomechanical model

Elements of thermomechanical modeling for PTFE are presented in this section, for green and then for sintered PTFE.

4.1 Green PTFE

The plastic and damage behavior of green PTFE was not studied in this work and therefore for the simulation by finite element method shown in Chapter 8, green PTFE was modeled as an isotropic elastic material:

$$\boldsymbol{\sigma} = \boldsymbol{C}(T, n_0) : \boldsymbol{\varepsilon}_e \tag{6.1}$$

where σ is the stress tensor, $\boldsymbol{C}$ is the stiffness tensor, depending on temeprature and on the initial porosity n_0 and $\boldsymbol{\varepsilon}_e$ the elastic strain tensor.

The total strain tensor $\boldsymbol{\varepsilon}$ can be decomposed into different terms,

$$\boldsymbol{\varepsilon} = \boldsymbol{\varepsilon_e} + \boldsymbol{\varepsilon_p} + \boldsymbol{\varepsilon}^* \tag{6.2}$$

with $\boldsymbol{\varepsilon_p}$ the plastic strain tensor and $\boldsymbol{\varepsilon}^*$ the overall eigenstrain tensor. For green PTFE, only elasticity is modeled and therefore $\boldsymbol{\varepsilon_p}$ is neglected. Moreover, the eigenstrain is not considered in this chapter but will be added in the simulations in Chapters 7 and 8.

The elastic properties are related to the Young's modulus (E) that was evaluated in the previous section for green PTFE as function of temperature and Poisson's ratio (ν). Measurements of E were made on PTFE will very little initial porosity (see Chapter 4). Fredy measured the evolution of the Young's modulus with porosity n at ambient temperature T_{amb} and is shown in Chapter 1

From the evolution of $E(T, n_0 = 0)$ and $E(T_{amb}, n)$, the evolution of $E(T, n)$ is extrapolated assuming that the Young's modulus in the molten state does not depends on the initial porosity n_0. This assumption could be challenged as the porosity can take time before a complete closure (see Chapter 4).

Linear elasticity enables to link the shear modulus (G) to the Young modulus and Poisson's ratio ν via

$$E = 2G\,(1 + \nu) \tag{6.3}$$

The Poisson's ratio of PTFE is estimated between 0.41 and 0.48 depending on the void ratio [10]. Therefore, the evolution of the shear storage modulus can be compared to the Young's modulus measured via compression tests. The two measurements gives close values of the elastic modulus.

In the next chapters, the evolution of the Young's modulus of green PTFE with temperature will be taken as the ones of sintered PTFE, and are still extrapolated for the different porosities using Fredy's results. The correct evolution was not taken into account as these results were obtained afterwards. However the error made by this difference is not very significant as the two evolutions are close.

4.2 Sintered PTFE

Concerning sintered PTFE, an elastoplastic behavior was observed. A Von Mises plasticity criterion is chosen, in a first approximation, with a hardening law for the plasticity threshold surface [120].

The increment of strain tensor $\mathrm{d}\boldsymbol{\varepsilon}$ can then be split in two parts: an elastic strain increment $\mathrm{d}\boldsymbol{\varepsilon}_e$ and a plastic strain increment $\mathrm{d}\boldsymbol{\varepsilon}_p$ from equation (6.2).

Under loading, the material remains elastic as long as the stress tensor does not reach the elastic limit surface defined by

$$f(\boldsymbol{\sigma}) = 0 \tag{6.4}$$

with f the plasticity criterion.

An isotropic elastic behavior is defined as in equation (6.1) when $f(\boldsymbol{\sigma}) < 0$. The behavior is also elastic when the following condition is satisfied

$$\frac{\partial f}{\partial \boldsymbol{\sigma}} : \mathrm{d}\sigma < 0 \tag{6.5}$$

It corresponds to an unloading step.

When the stress tensor reaches the plastic criterion $f(\boldsymbol{\sigma}) = 0$ and when

$$\frac{\partial f}{\partial \boldsymbol{\sigma}} : \mathrm{d}\boldsymbol{\sigma} > 0 \tag{6.6}$$

then plastic flow occurs.

Here, as only uniaxial compression tests are available, von Mises plasticity with associated flow rate and isotropic hardening was considered.

The increment of plastic strain tensor is given by equation

$$\mathrm{d}\boldsymbol{\varepsilon}_p = \mathrm{d}\lambda \frac{\partial f}{\partial \boldsymbol{\sigma}} \tag{6.7}$$

where $\mathrm{d}\lambda$ is a hardening parameter and $\frac{\partial f}{\partial \boldsymbol{\sigma}}$ defines the direction of plastic flow which is co-directional to the normal vector to the plastic surface in the stress space (normality condition).

To close the set of constitutive equations, during the plastic flow the stress remains on the yield surface which shape varies with the hardening so that the consistency condition must be satisfied

$$\mathrm{d}f = \frac{\partial f}{\partial \boldsymbol{\sigma}} \mathrm{d}\boldsymbol{\sigma} + \frac{\partial f}{\partial \boldsymbol{\varepsilon}_p} \mathrm{d}\boldsymbol{\varepsilon}_p = 0 \tag{6.8}$$

It defines the flow direction.

The Von Mises plasticity criterion is expressed

$$f(\boldsymbol{\sigma}) = \sigma_{VM} - \sigma_s(p, T) \tag{6.9}$$

with σ_{VM} the Von Mises stress

$$\sigma_{VM} = \sqrt{\frac{3}{2}\, \boldsymbol{\sigma}_d : \boldsymbol{\sigma}_d} \tag{6.10}$$

where $\boldsymbol{\sigma}_d$ is the deviatoric stress tensor

$$\boldsymbol{\sigma}_d = \boldsymbol{\sigma} - \frac{1}{3} \mathrm{tr}\boldsymbol{\sigma} \mathbf{1} \tag{6.11}$$

and with σ_s the stress characterizing the plasticity threshold surface and $p = \int |\mathrm{d}\varepsilon_p|$ the accumulated plastic strain.

The hardening is expressed in σ_s with

$$\sigma_s(p, T) = \sigma_Y(T) + H(T)\ p \tag{6.12}$$

with σ_Y the yield stress and H the hardening modulus.

The evolution of the hardening modulus with temperature can be evaluated from the envelop stress-strain curves (from Figure 6.7). The values of the Young's modulus and the hardening modulus as functions of temperature are shown in Figure 6.10. The two

moduli are measured from the slopes of the stress-strain curves respectively at the very beginning and at the end of the loading (see sketch in Figure 6.10). Note that the values for the Young's modulus are lower than the values measured previously. It is caused by the measurement at loading (instead of unloading). Additional effects such as compression of the overall testing device, are present which reduces the measured value of the Young's modulus.

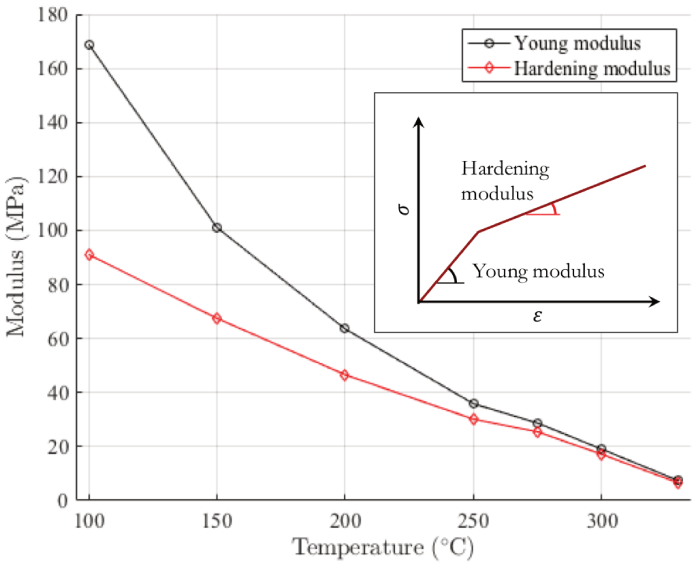

Figure 6.10: Hardening and Young's moduli of sintered PTFE as function of temperature. The two moduli can be read on the stress-strain envelop curve.

It was observed that the yield stress σ_Y is related to a strain ε_Y that is invariant on temperature. Thus,

$$\sigma_Y(T) = E(T)\,\varepsilon_Y \tag{6.13}$$

The use of Von Mises plasticity is questionable as it corresponds to an isovolumic plasticity model. More experiments with different loading paths should be performed to justify or not such modeling. Concerning green PTFE, it is almost evident that such model is not correct. The model used by Fredy et al. [9, 10] for powder compaction was a Drucker-Prager-cap model which implies an effect of the hydrostatic pressure on plasticity.

5 Conclusions and perspectives

It was shown that the viscoelastic behavior of sintered PTFE can be neglected from DMTA experiments. The evolution of the Young's modulus of PTFE with temperature was characterized in this chapter. The elastic properties are lower for sintered PTFE than green PTFE above the second glass transition temperature (α-transition). This difference is attributable to the difference in crystallinity fraction as nascent PTFE is almost fully crystalline and sintered PTFE about 50% crystalline.

Molten PTFE seems almost purely elastic. This elasticity is similar to the entropic elasticity of elastomers. In the recrystallized state, PTFE appears to be elastoplastic and

the share of "permanent" strain increases at lower temperatures. An interesting shape memory effect of PTFE comes from this behavior and ability of the crystalline planes to slide to new stable configurations. This memory effect induced by the elastomeric properties of PTFE, to the crystallization that freezes the shape and to the high deformability of PTFE crystals.

A thermomechanical model is proposed for PTFE. For green PTFE only linear elasticity is considered and for sintered PTFE an elastoplastic model is defined with a hardening law evolving with temperature. The Young's modulus chosen for green PTFE varies with temperature and initial porosity using the measurement obtained from Fredy [10].

From this work, different perspectives can be envisioned:

A more complete study on the properties of green PTFE could be considered. Plasticity in green PTFE is likely to be significant (in particular for low initial density). However different origins of the plasticity could exist: crystal plasticity, particles reorganization and even compaction. The presence of a time-dependent elastic behavior could be non-negligible in green PTFE probably due to the presence of air entrapped that diffuse through the bulk.

The elastoplastic model with Von Mises plasticity criterion could be challenged to evaluate its validity in other loading paths. Also the viscoplastic behavior was not considered in this work but could exist in green and sintered PTFE. It may not be worth modeling for sintering simulations but an effect could probably be characterized as function of temperature.

The evolution of the elastic properties with the crystallinity content was omitted. It would be very interesting to link the elastic modulus with crystallinity [121] and therefore with the crystallization kinetic model developed previously. If differences are appreciable, they could have an impact in the final stress state of a sintered PTFE billet.

The uniaxial compaction induces a transverse isotropic microstructure that impacts the mechanical properties as well. This effect was not studied here but it would be interesting to evaluate it and to see if the same anisotropic effects are observed for plasticity.

Lastly, characterizing a failure criterion for PTFE would be very interesting in order to perform more complete simulation of billet sintering. However establishing a failure criterion for PTFE is complex. In the sintering state, failure seems to be difficult to achieve as PTFE crystal unwind extensively to reach very high deformations. In the green state however, failure criterion would depend on the porosity level and on temperature.

Part II

Thermal inhomogeneity

Convergence, Jackson Pollock, Albright-Knox Art Gallery

Chapter 7

Model equations: application to a semi-infinite PTFE part

The equations of the model for PTFE sintering are developed in this chapter. To illustrate the different elements of the model, thermal treatment simulations are performed in the special (simple) case of a core extracted from the central part of the PTFE billet, and where the distance to the free surface, along the core axis is the only relevant spatial coordinate as the billet can be assimilated to a semi-infinite media with oedometric conditions and with no characteristic length but the crystallization front depth.

Contents

1 Introduction

The different physical mechanisms and models described in the previous chapters can be used for the simulation of the sintering process. This chapter combines the different model equations and proposes a simple simulation inspired from PTFE billet sintering.

One can consider a core of PTFE billet in its central part (i.e. away from the top or bottom sides, see Figure 7.1a). For a small enough core diameter (as compared to the billet radius and wall thickness), the billet can be assimilated to a semi-infinite half-space and hence, the core is confined by its surrounding so that its transverse strain is null (as for an oedometric test). It means that $u_y(x) = u_z(x) = 0$ (with u_i the displacement in the direction i). A sketch of the semi-infinite PTFE media $x > 0$ is represented in Figure 7.1b where x corresponds to the transverse direction (TD) and z to the compaction direction (CD). The other direction y is also a TD due to the uniaxial pressing of the billet. Thanks to the oedometric conditions, the only non-zero displacement component is $u_x(x)$ and is subjected to a traction free condition $\boldsymbol{\sigma}.\boldsymbol{n} = 0$ at the free surface, $x = 0$. The use of a symmetry condition $y \to -y$, imposes $\sigma_{yz} = 0$ and thus, the stress can only be built transversely. Therefore the only mechanical variables of interest are ε_{xx}, σ_{zz} and σ_{yy}.

The simulation can be easily implemented in Matlab (for example) via a finite difference method. The semi-infinite media can be discretized along x with an increment dx (see Figure 7.1b).

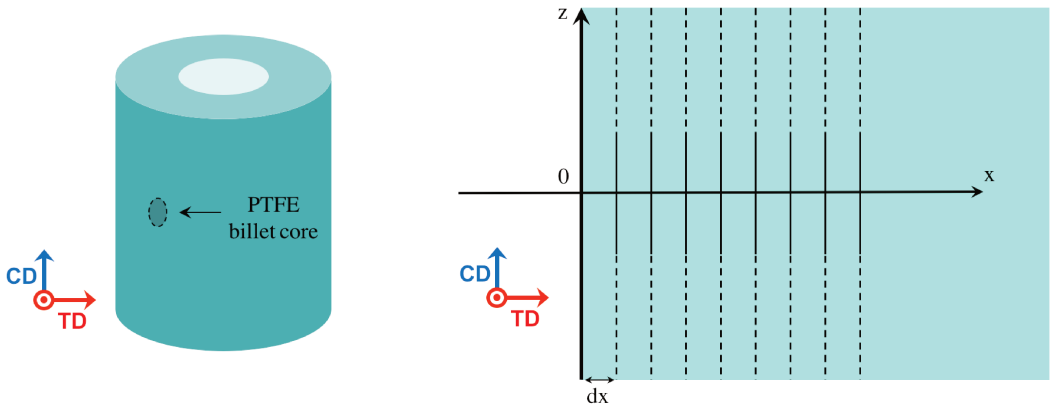

(a) (b)

Figure 7.1: Illustration of the core of PTFE billet (a) and its representation as a semi-infinite media (b). It is discretized with different elements in direction x for simulation purposes.

To model sintering, two different cases are to be addressed: heating of green PTFE above melting temperature and cooling of molten PTFE. In the former case, as-polymerized PTFE compact is heated from the surface $x = 0$ up to 385°C at 1°C/min and maintained at this temperature for a while. In the latter case, PTFE in the molten state at 385°C is suddenly in contact with the outside at ambient temperature (30°C) from the free surface.

In this chapter, the different bricks of the simulation are exposed. First the thermal simulation and the crystallinity content simulation are presented. The two simulations require to be computed together due to coupling. Then the eigenstrain simulation is detailed with a decomposition along the different physical mechanisms. Last, the thermomechanical

behavior is modeled, the depth profile of the stress σ_{zz} and its time evolution are evaluated.

2 Thermal and crystallinity simulation

2.1 Heat equation

The first step of the simulation consists in computing the temperature at any position (depth) x and time t. The latter is ruled by the heat equation

$$\rho c_p \frac{\partial T}{\partial t} + \partial_x \left(-k \partial_x T\right) = r \tag{7.1}$$

where ρ is the density, c_p is the specific heat, T the temperature, k is the thermal conductivity and r the heat source.

Let us note that the x coordinate should be Eulerian in this writing. However, for the mechanical description it is more convenient to use a Lagrangian coordinate X (*i.e.* relative to the undeformed state). For small displacements and, small strains and rotations, it is usual not to distinguish both. In the present case, the small strain approximation may be questioned because of the phase transformation (melting and crystallization) where strains can reach 20%. However on both sides of this transition, the small strain approximation is justified, so that the distinction between Eulerian and Lagrangian strains is negligible and will be forgotten. With the transverse confinement, the dilation of the material leads to a simple correspondence $\partial_x T = (1/(1+\epsilon_{XX}))\partial_X T$. As a consequence, the correction factor $(1/(1+\epsilon_{XX}))$ being set by temperature, can be absorbed into a modified conductivity depending on temperature, so as to cover the entire range of experienced temperature. Finally, the only remaining point to clarify is the transport of heat due to the material motion radially (in direction x) that occurs from the phase transformation. The most natural choice for the Eulerian coordinate system is to choose $x = 0$ at the surface and hence the radial (eulerian) velocity remains null at this point. The maximum radial velocity will be given by the velocity of the front times the overall transformation strain. The ratio between the convective and the diffusive contributions expressed through a Peclet number $Pe = UL/D = eL\dot{L}/D$ where U is the velocity, L the transformation front depth, e the transformation strain, D the diffusion coefficient, with $D = k/\rho c_p$. Early in the process $\dot{L}$ is large but L is small. Late L is larger, but $\dot{L}$ is small, and the Peclet number will be checked to be always much smaller than 1, and hence the small strain approximation will be considered as a valid approximation for the heat equation.

The source term r of the heat equation (7.1) can be expressed as

$$r = \dot{\chi} \Delta h_{am-cr} \tag{7.2}$$

where Δh_{am-cr} is the latent heat of fusion and $\dot{\chi}$ is the time derivative of the crystallinity content.

The computation of the temperature has to be done jointly with the computation of the crystallinity content χ due to the coupling coming from r in the heat equation. r is related to χ and χ is also related to temperature.

The evolution of the crystallinity content at fusion is discussed in subsection 2.2 applied to the case of green PTFE heating. The evolution of the crystallinity content at crystallization is detailed in subsection 2.3 and is applied to the case of molten PTFE cooling. Temperature and crystallinity content evolutions are computed for both cases.

2.2 Crystallinity content evolution at fusion

At heating, the crystallinity content χ depends exclusively on the temperature independently on the heating rate. This evolution is only related to the microstructure of nascent PTFE and more particularly on its crystalline lamellae distribution (via Gibbs−Thomson equation (1.1) in Chapter 1).

From DSC measurement at melting in Figure 2.2 in Chapter 2, the peak integration provides the quantitative evolution of the crystallinity content with temperature. This evolution can be fitted by a sigmoid function:

$$\chi(T) = \frac{\chi_0}{1 + \exp\left(a(T - T_m)\right)} \tag{7.3}$$

here χ_0 the crystallinity content of nascent PTFE, T_m the temperature corresponding to half transformation at melting and a a parameter characterizing the temperature span of melting. Due to the shape of the melting peak in DSC, T_m is almost equivalent to the melting temperature where the flux reaches its maximum.

The evolution of the crystallinity content at melting is presented in Figure 7.2 for $\chi_0 = 1$. For the rest of this chapter, the initial crystallinity content χ_0 is set at 100% for as−polymerized PTFE. This approximation is made for simplicity and is not a strong assumption as nascent PTFE is almost fully crystalline.

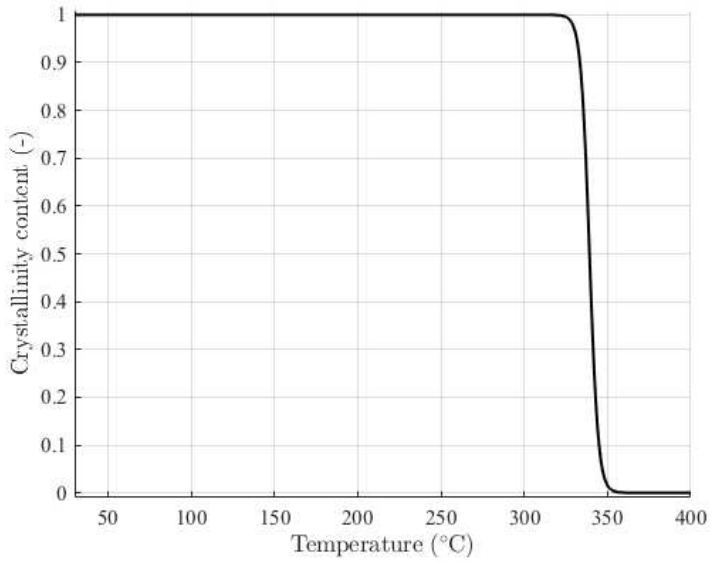

Figure 7.2: Evolution of the crystallinity content at heating as function of temperature for an initial crystallinity content $\chi_0 = 1$. No kinetic effect is expected at melting.

Initially, the semi-infinite PTFE is uniformly at 30°C. At $t = 0$ the free surface $x = 0$ is in contact with an external media at T_{ext}. At the surface $x = 0$

$$-k\frac{\partial T}{\partial t}(x = 0, t) = h\left(T(x = 0, t) - T_{ext}\right) \tag{7.4}$$

with h the heat transfer coefficient taking into account radiative and convective heat transfer. The value of h can be adjusted to mitigate the heating or cooling.

h is fixed at 40 W.m^{-2}.K^{-1} which corresponds to forced convection and therefore $T \approx T_{ext}$. T_{ext} is increasing at 1°C/min from 30 up to 385°C and stay at this temperature for about one hour and a half.

The heat equation (7.1) can be computed simultaneously with the crystallinity content evolution at melting (7.3) using the thermal boundary condition (7.4). Figure 7.3 shows the computed temperature and crystallinity maps (as functions of time and depth along x) obtained at heating. From Figure 7.3b it can be seen that the molten region ($\chi = 0$) is confined in a thin surface layer whose thickness is less than 5 mm at the end of the simulation.

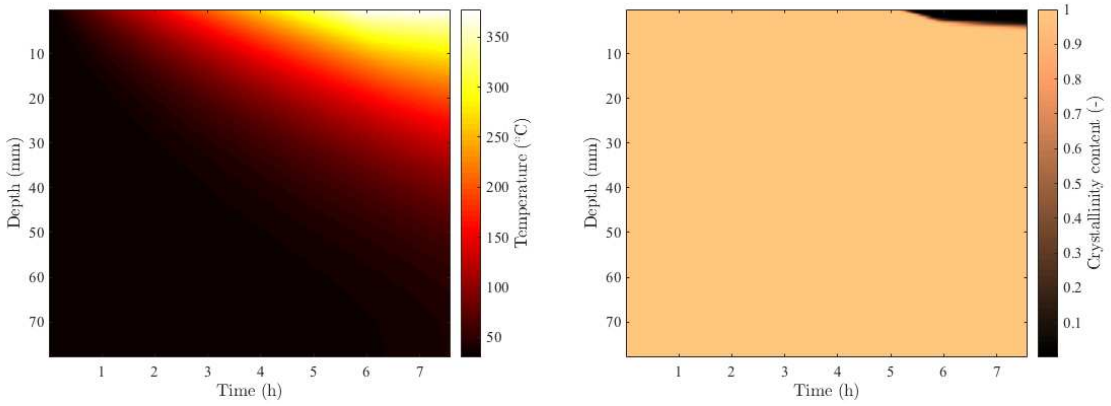

(a) (b)

Figure 7.3: Evolution of the simulated temperature (a) and crystallinity content (a) as functions of time along the depth of the semi-infinite medium during heating of green PTFE.

The evolution of the temperature and of the crystallinity content are shown as functions of time for different depths x in Figure 7.4. The evolution of T_{ext} can be read from the temperature evolution of the surface element ($x = 0$) in Figure 7.4a. For deeper positions, the temperature evolves with a delay compared to the imposed temperature at the surface. In Figure 7.4b, the effect of the thermal gradient is observed on the shape of the crystallinity content. For deeper positions, the melting takes longer to complete due to the thermal gradient.

2.3 Crystallization kinetic model

At cooling, PTFE crystallization obeys a specific kinetic. A model has been developed in Chapter 5. The crystallinity content is expressed as the sum of two terms related to the primary and secondary crystallizations, $\chi = \chi_1^\infty \alpha_1 + \chi_2^\infty \alpha_2$. α_1 and α_2 characterize the transformation level of respectively the primary and the secondary crystallization. They are defined in section 2.3 in Chapter 5 and the same parameters are used for the simulation. The primary crystallization kinetic can be expressed in Nakamura formalism [40] to enable the computation for any thermal cycle. Therefore,

$$\begin{aligned} \alpha_1(t) &= 1 - \exp\left(-\left\{\int_0^t \kappa_1(T(\tau))\mathrm{d}\tau\right\}^n\right) \\ \alpha_2(t) &= 1 - \exp\left(-k_2(T(t))\right) \end{aligned} \tag{7.5}$$

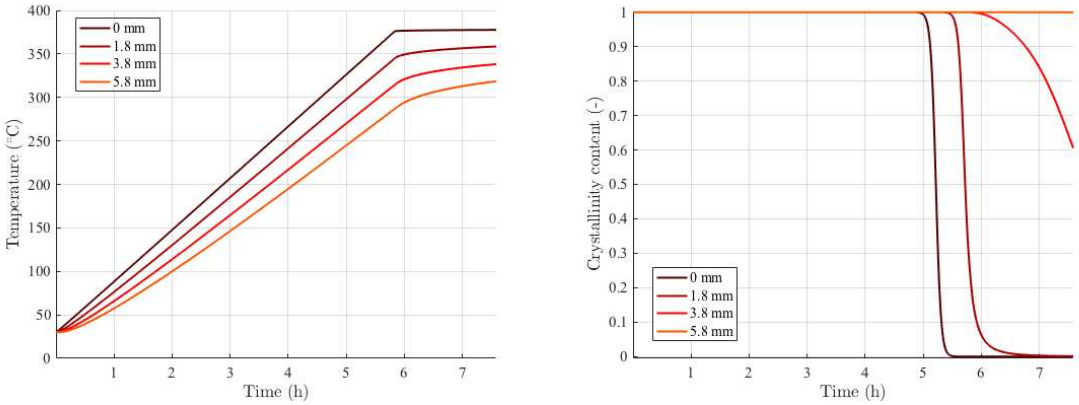

(a) (b)

Figure 7.4: Evolution of the simulated temperature (a) and crystallinity content (a) as functions of time at different depth of the semi-infinite medium during heating of green PTFE.

where κ_1 is the Nakamura kinetic constant for the primary crystallization, n is the Avrami exponent and k_2 is the function of temperature that describes the secondary crystallization.

The primary crystallization is computed incrementally from the differential equation

$$\frac{\mathrm{d}\alpha_1}{\mathrm{d}t} = (1-\alpha_1)\frac{\mathrm{d}\{\kappa_{int}\}^n}{\mathrm{d}t} \tag{7.6}$$

with

$$\kappa_{int}(t) \equiv \int_0^t \kappa_1(T(\tau))\mathrm{d}\tau \tag{7.7}$$

In the simulation κ_1 was computed using a fit of the Ozawa kinetic constant obtained in Chapter 5 with a sigmoid function to simplify the computation.

The secondary crystallization is directly linked to the temperature of each element with $k_2(T)$ and can be computed for each time step.

The cooling of semi-infinite molten PTFE is simulated using the described model. Initially, the entire media is uniformly at 380°C. At $t = 0$ the free surface $x = 0$ is in contact with an external media at $T_{ext} = 30$°C. The equation (7.4) is used to characterize the temperature evolution at $x = 0$ with a coefficient $h = 40$ W.m^{-2}.K^{-1}.

Figure 7.5 shows the computed temperature and crystallinity maps (as functions of time and depth) obtained at cooling of molten PTFE. The evolution of temperature is similar to a diffusive process. The temperature decreases more slowly deeper in the PTFE media than at the surface. The crystallization front is clearly defined between what is still melted (in black) and what recrystallized in color (Figure 7.5b). It follows more or less the isotherm corresponding to crystallization temperature as it does not change too much on cooling rate. Due to lower cooling rates, the final crystallinity content increases with

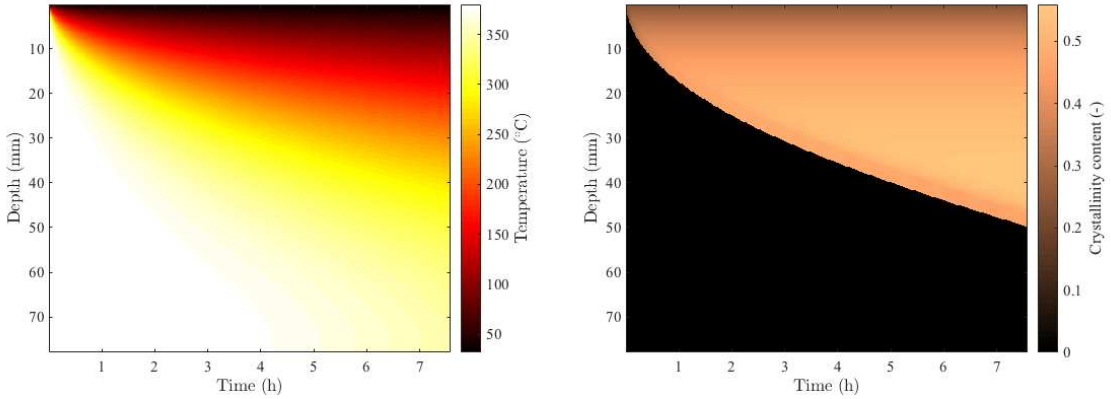

(a) (b)

Figure 7.5: Evolution of the simulated temperature (a) and crystallinity content (a) as functions of time along the depth of the semi-infinite medium during cooling of molten PTFE.

depth.

Note that the simulation was done with a depth increment dx which increased with the depth. It allows to reach final higher depths at a lower computation cost. Then the result is interpolated over a grid with constant dx for the illustration. This interpolation is at the origin of the fluctuations that can be observed in Figure 7.5b on the edge of the crystalline frontier.

The evolution of the temperature and of the crystallinity content are shown as functions of time for different depths x in Figure 7.6. Figure 7.5b confirms that at lower cooling rates (that can be evaluated on Figure 7.5a from the slope of the curves), the final crystallinity content is higher.

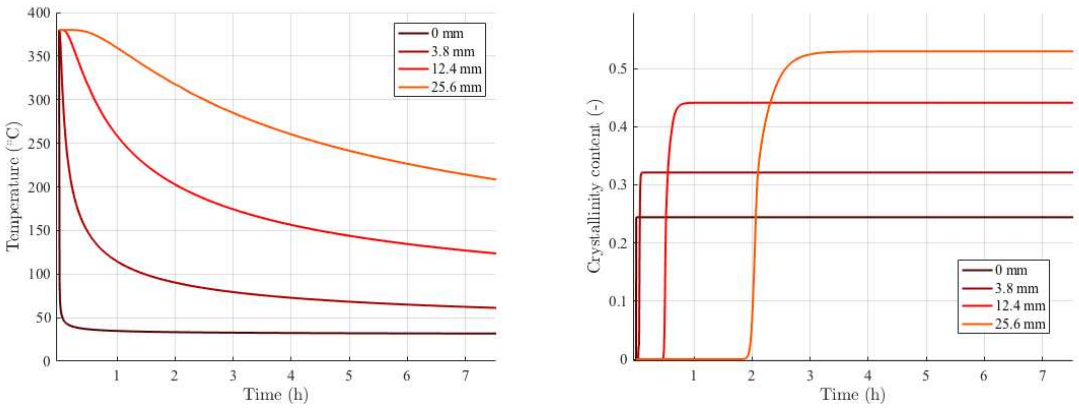

(a) (b)

Figure 7.6: Evolution of the simulated temperature (a) and crystallinity content (a) as functions of time at different depth of the semi-infinite medium during cooling of molten PTFE.

3 Eigenstrain simulation

Once the temporal evolution of the temperature and of the crystallinity content is known everywhere, the eigenstrain can be computed. The different terms coming from the physical mechanisms described in the previous Chapters (3,4 and 5) can be evaluated. The eigenstrain is decomposed as follows

$$\boldsymbol{\varepsilon^* = \varepsilon^{th} + \varepsilon^{phase} + \varepsilon^{vc} + \varepsilon^{r}} \tag{7.8}$$

where $\boldsymbol{\varepsilon^{th}}$ is the thermal expansion, $\boldsymbol{\varepsilon^{phase}}$ the strain due to phase changes, $\boldsymbol{\varepsilon^{vc}}$ the strain due to void closure and $\boldsymbol{\varepsilon^{r}}$ the strain due to residual stress relaxation. The eigenstrain presents a certain anisotropy that is detailed for each term in the next subsections.

3.1 Thermal expansion

The volumetric thermal expansion can be expressed as

$$\varepsilon_v^{th}(T) = \tilde{\beta}(T)\ (T - T_0) \tag{7.9}$$

with $\tilde{\beta}$ the overall volumetric thermal expansion coefficient and T_0 is the reference temperature. $\tilde{\beta}$ depends on the thermal expansion of the amorphous phase and of the crystalline phase and is approximated by a mere mixture law

$$\tilde{\beta} = f\ \beta_{\text{cr}} + (1 - f)\ \beta_{\text{am}} \tag{7.10}$$

where β_{cr} and β_{am} are respectively the volumetric thermal expansion coefficient of the crystalline and amorphous phase and f is the crystalline volume fraction.

Note that in this simulation β_{cr} and β_{am} are constant with temperature. Refinements can easily be made by adding an additional temperature dependence.

From Chapter 3, thermal expansion has a certain anisotropy in the green state and in the molten state. It is due to the orientation of the polymer chains induced by compaction. However in the recrystallized state, the thermal expansion is isotropic. Thus,

$$\varepsilon_i^{th}(T) = R_i^{th}(T)\ \tilde{\alpha}(T)\ (T - T_0) \tag{7.11}$$

where i is the direction either CD or TD, $\tilde{\alpha}$ the overall linear thermal expansion coefficient with $\tilde{\alpha} = \tilde{\beta}/3$ and R_i^{th} is the anisotropy coefficient for the thermal expansion. Due to the transverse isotropy:

$$R_{CD}^{th} = 3 - 2R_{TD}^{th} \tag{7.12}$$

At heating, R_i is equal to $R_i^{\text{m-o}}$ an anisotropy coefficient related to the molecular orientation induced by compaction. At cooling, R_i is equal to $R_i^{\text{m-o}}$ in the molten state and is equal to 1 in the recrystallized state. Therefore at cooling, the proposed evolution of $R_i(T)$ is

$$R_i(T) = \bar{\chi} + (1 - \bar{\chi})R_i^{\text{m-o}} \tag{7.13}$$

where $\bar{\chi}$ is the transformation level at crystallization.

3.2 Phase change

Melting and crystallization induce high strains as the density of crystals is different from the density of the amorphous phase. The volumetric eigenstrain related to phase change ε_v^{phase} is simply related to the crystallinity content by

$$\dot{\varepsilon}_v^{phase} = \dot{\chi}\Delta\varepsilon_{am-cr} \tag{7.14}$$

where $\Delta\varepsilon_{am-cr}$ is the volumetric strain caused by the crystallization. $\Delta\varepsilon_{am-cr} = \log \rho_{am}/\rho_{cr}$ which depends on temperature as it is related to the thermal expansion of the amorphous phase and of the crystalline phase.

The phase change eigenstrain is anisotropic at melting and at crystallization. However at melting the anisotropy is more pronounced and it is probably due the residual stress relaxation as well (see Chapter 3).

Therefore at heating,

$$\dot{\varepsilon}_i^{phase} = R_i^{\text{green}}\dot{\chi}\left[\frac{1}{3}\Delta\varepsilon_{am-cr}\right] \tag{7.15}$$

where R_i^{green} is the anisotropic coefficient relative to melting. This coefficient certainly contains the information on the residual stress relaxation at melting. It is also very likely that this coefficient is higher than the one for crystallization as the crystalline orientation appears to be higher in the green state than in the molten state (see Chapter 5).

At cooling,

$$\dot{\varepsilon}_i^{phase} = (R_i^{\text{m-o}}\dot{\chi}_1 + \dot{\chi}_2)\left[\frac{1}{3}\Delta\varepsilon_{am-cr}\right] \tag{7.16}$$

where $R_i^{\text{m-o}}$ is the anisotropic coefficient relative to molecular orientation. It seems to be the same coefficient than for thermal expansion in the molten state (and in the green state).

A shown in Figure 7.7 the time (and depth) evolution of the volumetric eigenstrain is similar to the crystallinity content as it is responsible for the major part of the strain

The overall volumetric eigenstrain at heating as function of temperature and its decomposition into a thermal expansion component and phase change component are shown in Figure 7.8. The phase change eigenstrain is localized in a more confined temperature region whereas the thermal expansion is occuring all along the heating.

Similarly, the evolution of the overall volumetric eigenstrain at cooling as function of temperature is presented in Figure 7.9. It is obtained from an element located at $x = 20$ mm and that reaches a final crystallinity content of 50%. Figure 7.9b shows the thermal expansion and the phase change eigenstrain. The former is varying linearly with temperature except during the phase change where the slope is modified. The latter is proportional to the evolution of the crystallinity content at crystallization.

At cooling, the eigenstrain can be computed in CD and TD. Figure 7.10 shows the eigenstrain evolution with temperature in CD and TD. It can be noticed that the anisotropy is confined to the molten state and the beginning of the crystallization. Below 315°C, the

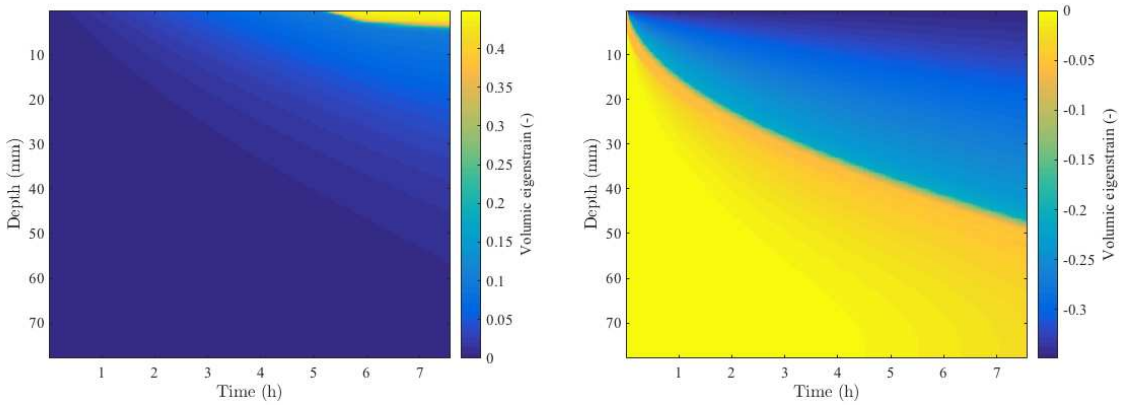

(a) (b)

Figure 7.7: Volumetric eigenstrain simulated for the heating of green PTFE (a) and for cooling of molten PTFE (b).

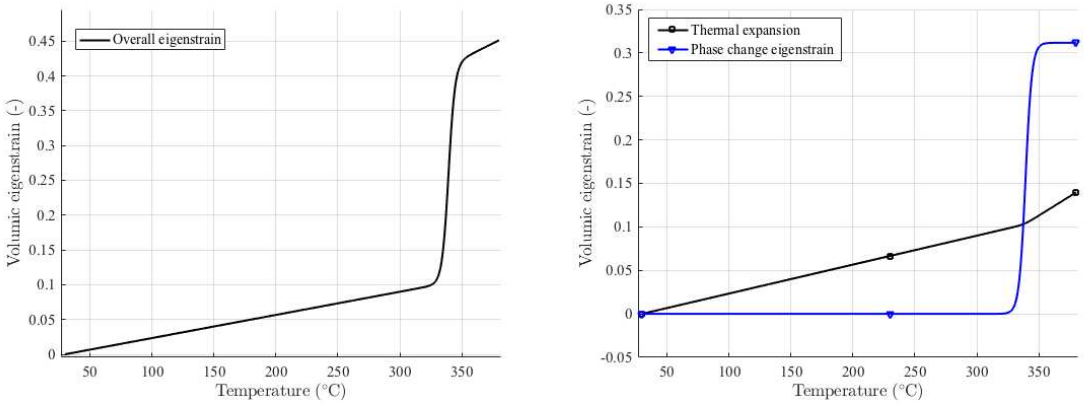

(a) (b)

Figure 7.8: Volumetric eigenstrain simulated for the heating of green PTFE as function of temperature (a). The eigenstrain is decomposed into thermal expansion and phase change eigenstrain components (b). The evolution is obtained for the element at $x = 0$ mm. The eigenstrain is not depending on $\dot{T}$ at heating.

evolution is isotropic.

Using the values of the phase change eigenstrain a Peclet number is computed at the transformation front as function of the depth and shown in Figure 7.11. It shows that the Peclet number Pe is always much smaller than 1 which supports the approximation earlier made that the convective heat transfer due to phase transformation is negligible compared to the diffusive one.

Note that in Figure 7.11, Pe drops when the melting or crystallization front did not reach a certain depth.

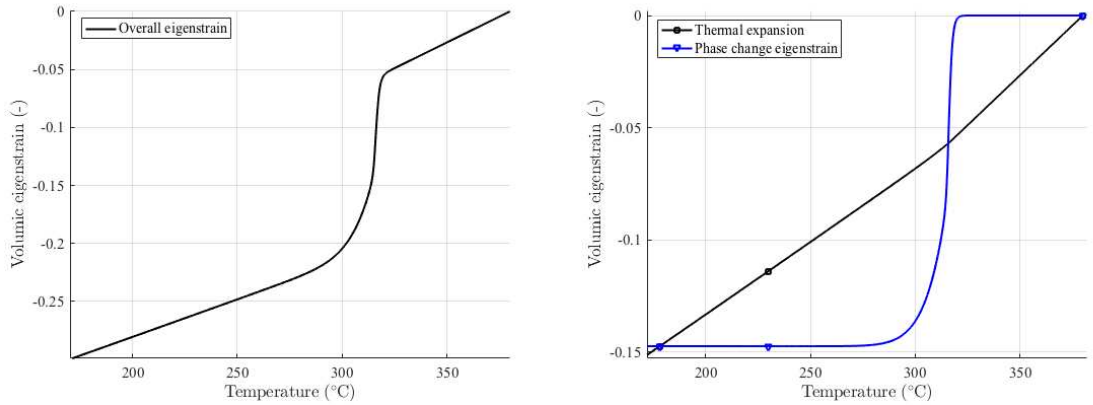

(a) (b)

Figure 7.9: Volumetric eigenstrain simulated for the cooling of molten PTFE as function of temperature (a). The eigenstrain is decomposed into thermal expansion and phase change eigenstrain components (b). The evolution is obtained for the element at $x = 20$ mm with a final crystallinity content $\chi^{\infty} = 50\%$. The eigenstrain depends on $\dot{T}$ at cooling which modifies χ^{∞}.

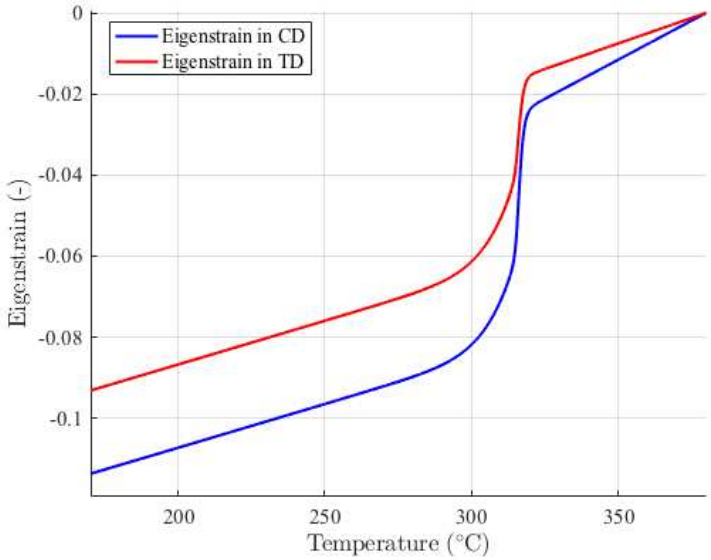

Figure 7.10: Eigenstrain components in CD and TD simulated for the cooling of molten PTFE as function of temperature. The evolution is obtained for the element at $x = 20$ mm with a final crystallinity content $\chi^{\infty} = 50\%$.

3.3 Void closure

The porosity in green PTFE compacts is closed during melting. The void closure is therefore a part of the overall eigenstrain. From Chapter 4, two strains mechanisms were observed. The first is the porosity closure that occurs simultaneous with melting. The second seems to be a porosity closure mechanism due to air diffusion which is time dependent and can thus be confused with a "viscous effect".

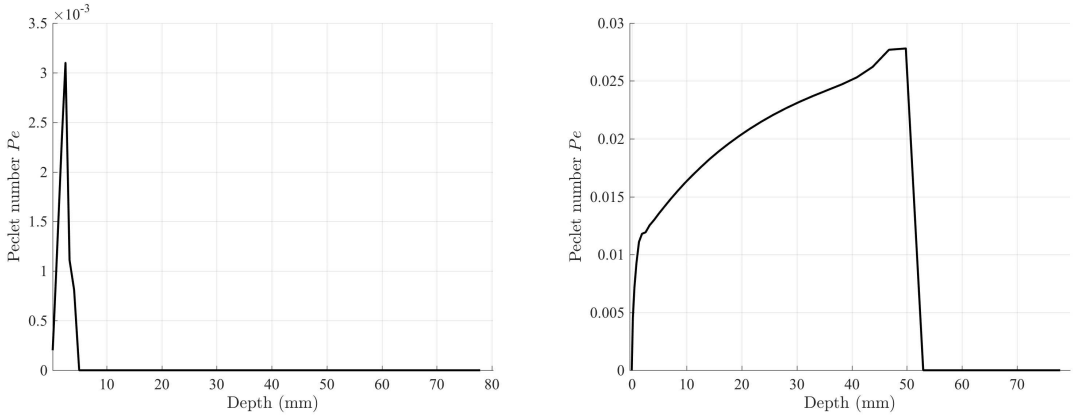

(a) (b)

Figure 7.11: Peclet number computed at the melting and crystallization fronts as functions of the depth, respectively at heating of green PTFE (a) and cooling of molten PTFE (b).

Only the first mechanism will be considered in this model. The total porosity is considered to be closed during melting. Thus the volumetric void closure eigenstrain ε_v^{vc} can be expressed at melting as

$$\varepsilon_v^{vc} = \left(1 - \bar{\chi}\right) \Delta\varepsilon_{max}^{vc} \tag{7.17}$$

where $\bar{\chi} = \chi/\chi_0$ is the relative crystallinity content at melting, with χ_0 the crystallinity content of nascent PTFE and where $\Delta\varepsilon_{max}^{vc}$ is the volumetric strain corresponding to the total closure of the porosities

$$\Delta\varepsilon_{max}^{vc} = \log\left(\frac{\rho_0}{\rho_{max}}\right) \tag{7.18}$$

where ρ_0 is the initial density of the PTFE compact and ρ_{max} is the density of a PTFE compact with no porosity.

The overall volumetric eigenstrain can then be computed for different initial porosity. The porosity is $n \equiv V_p/V_{tot}$ where V_p is the volume of the pores and V_{tot} is the total volume. The porosity can also be expressed as $n = 1 - (\rho_0/\rho_{max})$. Figure 7.12 shows the evolution of the overall eigenstrain at heating for three different initial porosities.

The void closure eigenstrain is anisotropic as well. Its anisotropy results from the anisotropy of the melting eigenstrain. Therefore ε_i^{vc} in the direction i can be expressed as

$$\varepsilon_i^{vc} = R_i^{\text{green}} \; \bar{\varepsilon}_v^{phase} \; [\frac{1}{3}\Delta\varepsilon_{max}^{vc}] \tag{7.19}$$

3.4 Residual stress relaxation strain

Green PTFE relaxes entrapped residual stresses at heating. It results in a very anisotropic apparent thermal expansion. It was shown in Chapter 3 that the behavior below melting can be decomposed into a reversible behavior (the thermal expansion) and an irreversible behavior (the residual stress relaxation). This relaxation also results in the creation of

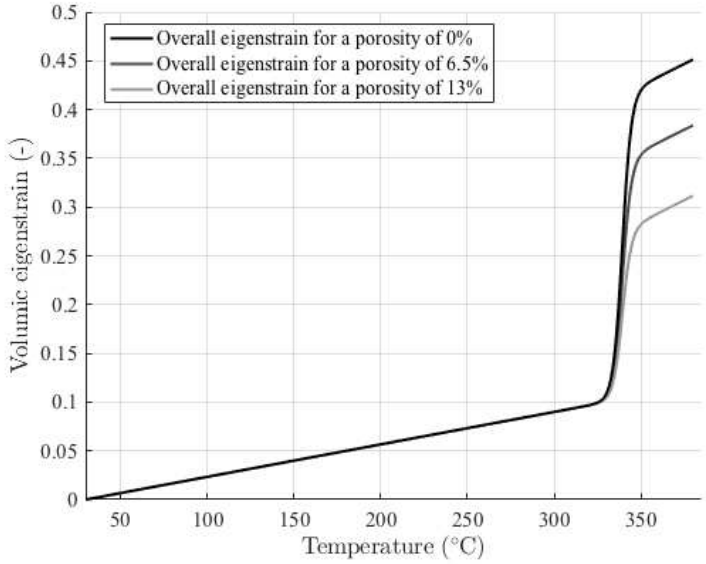

Figure 7.12: Volumetric eigenstrain simulated at heating of green PTFE for different initial porosities (0, 6.5 and 13%).

a small amount of porosities which closes at higher temperature. In this model, this mechanism is considered isovolumetric ($\varepsilon_v^r = 0$) for sake of simplicity.

Therefore the residual stress relaxation eigenstrain ε_i^r in the direction i can be expressed as

$$\varepsilon_i^r(T) = \alpha_i^r \ (T - T_0) \tag{7.20}$$

with α_i^r a residual stress relaxation coefficient relative to the direction i.

From the isovolumetric condition,

$$\alpha_{CD}^r = -2 \ \alpha_{TD}^r \tag{7.21}$$

The overall eigenstrain are simulated at heating in CD and TD as function of temperature in Figure 7.13. The computation is performed for two different porosities. The anisotropy of the void closure strain can be noticed.

If different thermal cycles with cooling below melting were to be computed, the residual stress relaxation eigenstrain would have to depend on the maximum temperature reached. Below this temperature, this eigenstrain component does not vary.

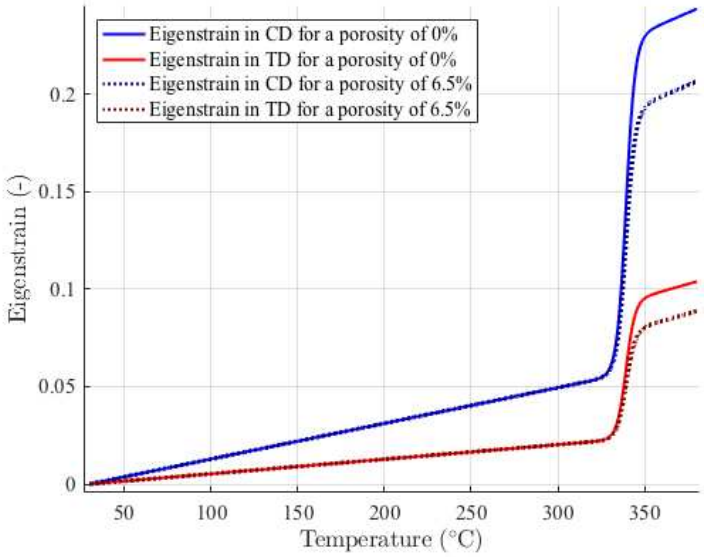

Figure 7.13: Eigenstrain component in CD and TD simulated for the heating of green PTFE as function of temperature for two different porosities (0 and 6.5%).

4 Thermomechanical simulation

The stress generated by the thermal treatment of the semi-infinite media is computed using the boundary conditions. Due to the oedometric conditions, all strain components in the direction perpendicular to x are null and conversely, at the free surface $\sigma_{xi} = 0$, where i corresponds to any direction (x, y and z).

In the following a thermo-elastic model is described for the heating of green PTFE and then a thermo-elasto-plastic model is defined for the cooling of molten PTFE since melt-crystallized PTFE behaves as an elasto-plastic material after its crystallization (as was described in Chapter 6).

4.1 Thermo-elasticity

For the simulation, the elasticity is considered isotropic for the semi-infinite media. Therefore,

$$\boldsymbol{\varepsilon_e} = \frac{1}{E}\left((1+\nu)\boldsymbol{\sigma} \ - \nu \ \mathrm{tr}(\boldsymbol{\sigma})\mathbf{I}\right) \tag{7.22}$$

where $\boldsymbol{\varepsilon_e} = \boldsymbol{\varepsilon} - \boldsymbol{\varepsilon^*}$ is the elastic strain (using equation (6.2) as plasticity is neglected in the green state), E is the Young's modulus, ν the Poisson's ratio and $\mathrm{tr}(\bullet)$ the trace of a tensor.

The projections of relation (7.22) in direction z, which is the compaction direction and in direction y, which is a transverse direction give

$$\begin{array}{rcl} -\varepsilon^*_{CD} & = & \frac{1}{E}\left(\sigma_{zz} - \nu\ \sigma_{yy}\right) \\ -\varepsilon^*_{TD} & = & \frac{1}{E}\left(\sigma_{yy} - \nu\ \sigma_{zz}\right) \end{array} \tag{7.23}$$

Thus,

$$\begin{aligned}\sigma_{zz} &= -\frac{E}{1-\nu^2}\left(\varepsilon^*_{CD} + \nu\,\varepsilon^*_{TD}\right)\\ \sigma_{yy} &= -\frac{E}{1-\nu^2}\left(\varepsilon^*_{TD} + \nu\,\varepsilon^*_{CD}\right)\end{aligned} \tag{7.24}$$

The temperature dependence of the Young's modulus allows one to evaluate the stress during any thermal treatment. The Young's modulus evolution is taken from the measurements made in DMA (see Chapter 6). The stress component σ_{zz} is computed during heating of green PTFE in Figure 7.14 as function of depth and time. The stress obtained is negative because it corresponds to a compression. PTFE expands but is constrained by the oedometric configuration. A compressive zone concentrated in a narrow interval of depth that moves into the solid during heating is observed. Figure 7.15 presents the stress evolution as function of time for the surface element. It can be seen that a minimum appears during the heating phase before melting. This minimum is due to the decrease of the Young's modulus and the eigenstrain increases with temperature. At some point, even if the eigenstrain continues to increase, the abrupt drop of the Young's modulus makes the stress increase back close to 0 . Another local minimum appears at the free surface for higher temperatures due to the large eigenstrain caused by melting.

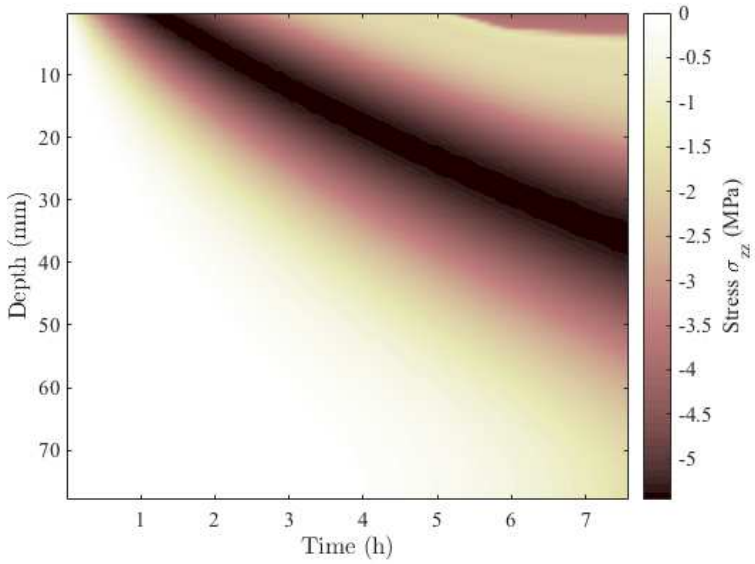

Figure 7.14: Stress simulated in z for the heating of green PTFE.

Similarly, the strain component in x can be evaluated using the elasticity relation (7.22) and the decomposition of the strain tensor (equation (6.2)) as x is a transverse direction,

$$\varepsilon_{xx} - \varepsilon^*_{TD} = -\frac{\nu}{E}\left(\sigma_{yy} + \sigma_{zz}\right) \tag{7.25}$$

Thus, using relations (7.24),

$$\varepsilon_{xx} = \frac{\nu}{1-\nu}\left(\varepsilon^*_{CD} + \varepsilon^*_{TD}\right) + \varepsilon^*_{TD} \tag{7.26}$$

Figure 7.16 shows the total strain along x as function of time and depth. The strain is mainly increasing at melting as it is related to the sum of the eigenstrain in CD ε^*_{CD} and

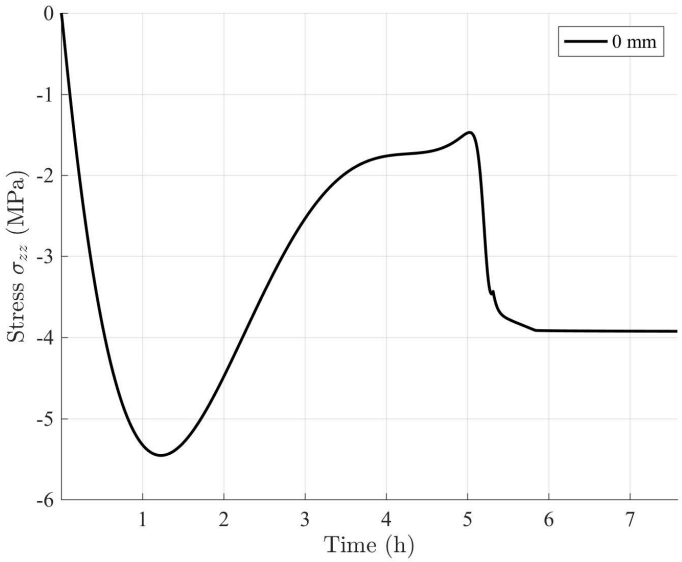

Figure 7.15: Stress component in z simulated as function of time at the surface element ($x = 0$ mm) for the heating of green PTFE.

in TD ε^*_{TD}. It would be equal to the volumetric eigenstrain if PTFE was incompressible ($\nu = 0.5$).

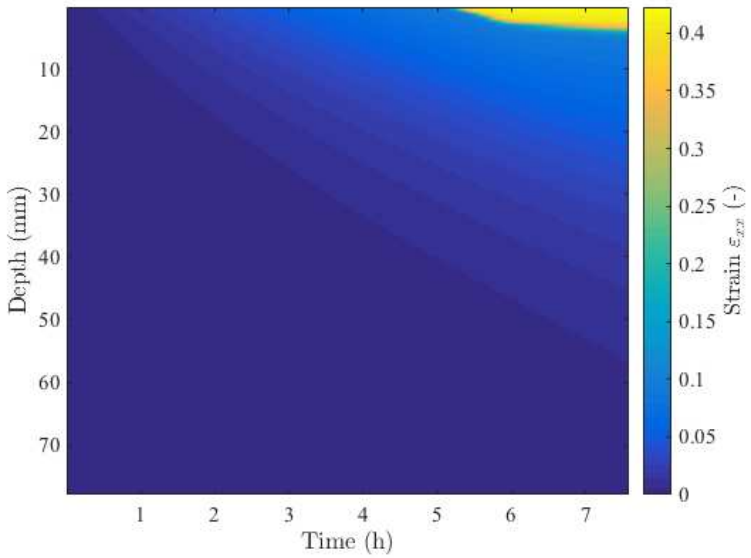

Figure 7.16: Strain component in x simulated for the heating of green PTFE.

4.2 Thermo-elasto-plasticity in the recrystallized state

An elastoplastic behavior was observed for sintered PTFE (see Chapter 6). In the molten state PTFE appears to be mostly elastic and becomes elastoplastic as soon as PTFE crystallizes. A Von Mises plasticity criterion with hardening is proposed according to the

compression tests performed on sintered PTFE at different temperatures. The plasticity criterion $f(\boldsymbol{\sigma})$ is defined by equation (6.9) and the hardening is expressed with equation (6.12) on the plasticity threshold surface σ_s. The evolution of the hardening modulus H with temperature is chosen according to the measurements in Chapter 6 with a correction due to the underestimation of the Young's modulus and with an extrapolation down to 30°C. Figure 7.17 shows the evolution of the Young's modulus E and of the hardening modulus H used for the simulation as function of temperature.

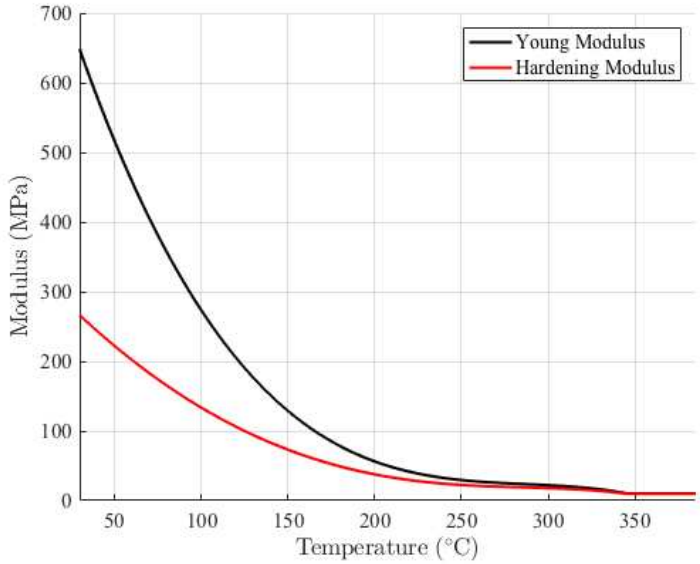

Figure 7.17: Young's modulus E and hardening modulus H chosen for the simulation according to the measurements in Chapter 6, as functions of temperature.

The plasticity appears when $f(\boldsymbol{\sigma}) = 0$ and then the plastic strain rate is aligned with the normal to the yield (stress) surface. Using equation (6.7) and the consistency relation (6.8), the plastic strain increment can be expressed from

$$\mathrm{d}\boldsymbol{\varepsilon}_p = \mathrm{d}p \, \frac{\boldsymbol{\sigma}_d}{\|\boldsymbol{\sigma}_d\|} \tag{7.27}$$

The stress can be computed using the previous relations, the elasticity equation (7.22), the boundary conditions ($\sigma_{xx} = 0$, $\varepsilon_{yy} = 0$ and $\varepsilon_{zz} = 0$) and the fact that the total strain tensor $\boldsymbol{\varepsilon}$ can be decomposed into different terms (equation (6.2)).

The stress component in z can be computed using the hardening law during the cooling of molten PTFE. Figure 7.18 shows the stress as function of time and depth. The stress is higher on the cooled surface as the Young modulus gets more important at lower temperature. It positive value means that it is in tension and that it could potentially induce a crack opening at the surface. A sintering experiment with a preexisting defect in a PTFE block was performed and a crack occurred at surface due to a similar tension (see Chapter 8).

The accumulated plastic strain is also evaluated in Figure 7.19 as functions of time and depth. It follows the evolution of the eigenstrain (and therefore of the crystallinity content). The plasticity is at the origin of a significant reduction of the stress. Without plasticity the computed stress would almost double.

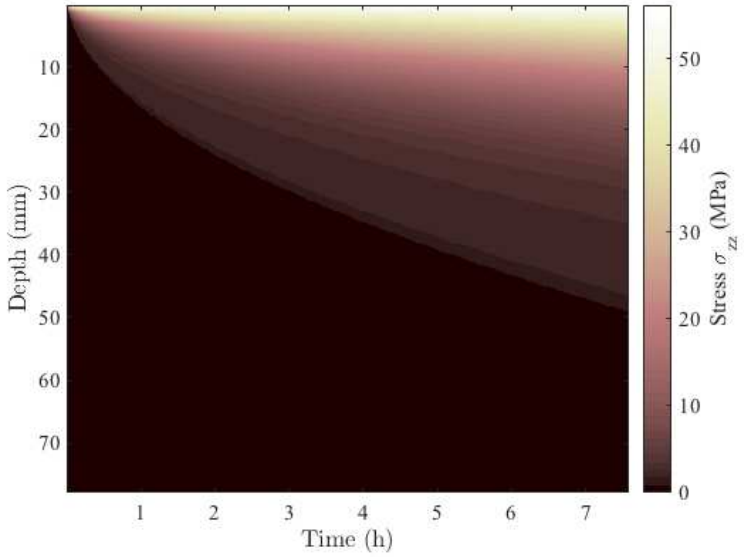

Figure 7.18: Stress component in z simulated for the cooling of molten PTFE.

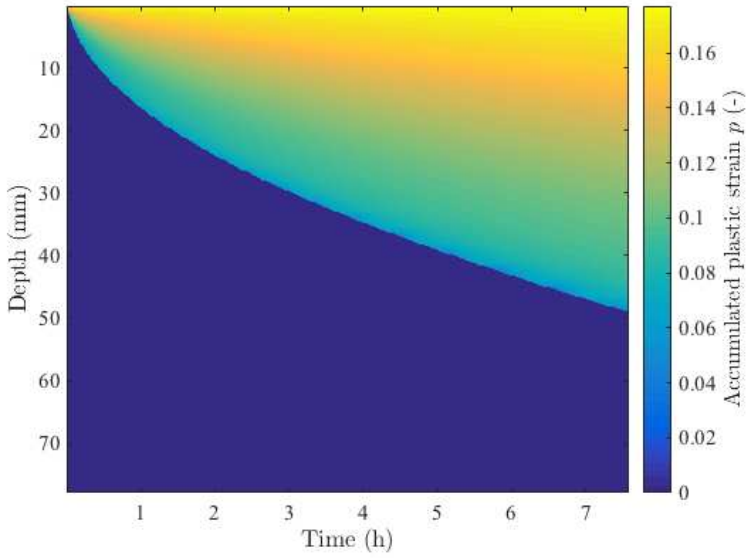

Figure 7.19: Accumulated plastic strain p during the cooling of molten PTFE.

5 Conclusions and perspectives

The complete thermomechanical model for sintering has been detailed in this chapter. A simple simulation case has been treated and used to showcase the different simulation steps.

First, the computation of the heat equation coupled to the crystallinity model gives access to temperature and crystallinity fraction along the thermal treatment. Depending on the type of thermal treatment, the crystallinity model corresponds either to the evolution of the melting as function of temperature, or to the crystallization kinetic model.

Then the eigenstrain is evaluated with the specific model described in the previous chapters. It uses the temperature and crystallinity content simulation to determine the

eigenstrain in both compaction direction and transverse direction.

Finally, the stress and strain are evaluated from the thermomechanical model.

This type of simulation offers a complete simulation of the sintering process. The described model can be implemented in a FE formalism in order to perform simulations as described in the next chapter.

The addition of a failure criterion for PTFE that could depend on various parameters (temperature, initial porosity, green or recrystallized state and crystallinity content) would be very valuable. It could help assessing the possibility of a crack appearance and therefore pave the way to optimize the processing parameters.

Several limits of the model are to be noted. The elastoplastic behavior and even viscoelastic behavior of the green PTFE were not modeled. Their modeling would certainly be necessary in order to more reliably estimate the stress at heating. However, the plasticity in the green state could come from different mechanisms. It could come from the crystal plasticity and from PTFE grain rearrangement. The modeling of the former is also more challenging as its plastic strain vanishes during melting (see memory effect Chapter 6).

The time dependency of the void closure would be interesting and certainly beneficial to model. This effect is related to the initial porosity and increases for lower density. It seems to be related to air trapping during compaction. Its modeling could be necessary to simulate accurately thermal treatments in the case of persistent density inhomogeneities.

Chapter 8

Finite element analysis of the sintering

This chapter presents the finite element (FE) analysis of PTFE compact sintering developed using the elements exposed in the previous chapters. Validations experiments are compared to simulation results. First FE analyses results for different process parameters are shown.

Contents

1 Introduction

Finite element (FE) simulation of PTFE compact sintering have been performed using the models described in the previous chapters. Abaqus® software from Dassault Systèmes was used for the FE simulations.

Different subroutines that have been developed for the simulations are detailed in section 2. Then a validation experiment is described in section 3. The experimental results are analyzed and compared to the simulation results to ensure that the model gives predictive results in section. Additional experiments have been carried out to insist on different properties and are presented in section 4. Last, PTFE billet sintering at a plant scale are simulated in section 5.

2 Finite element simulation

2.1 Solving strategy

Abaqus standard software was used to run the thermal and thermomechanical simulations with an implicit time integration scheme.

The FE analysis is constructed similarly following to the approach detailed in Chapter 7. The three main physical domains involved in these simulations are heat transfer, phase change and mechanics. Couplings exist between these domains that have to be taken into account in the solving strategy. They are described in Figure 8.1. Some of them are strong (e.g., the temperature field is required to estimate the stress and strain field). Other couplings are weak and can be neglected (eg., the stress does not affect the crystallinity content evolution). The influence of the phase change on the heat transfer computation is mostly null except during melting and crystallization where they can delay the heat propagation. Therefe this coupling is considered in the simulation. Figure 8.1 shows the assumptions made for the FE analyses.

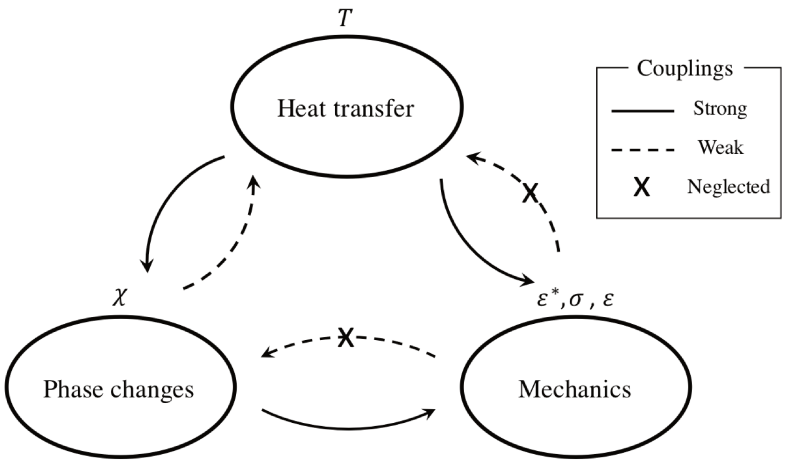

Figure 8.1: Couplings between the different computation elements of the FE analysis.

As the heat transfer is very weakly coupled with the mechanics, the thermal simulation coupled to the evaluation of the crystallinity content χ is made first. The phase change problem is solved at the same time than the heat equation in a specific user subroutine

UMATHT (Figure 8.2). Then, the overall eigenstrain ε^* is computed in a specific user subroutine UEXPAN using as inputs the temperature and the crystallinity fields as functions of time, and the initial porosity field. Finally, the stress σ and the strain ε are obtained from the thermomechanical simulation.

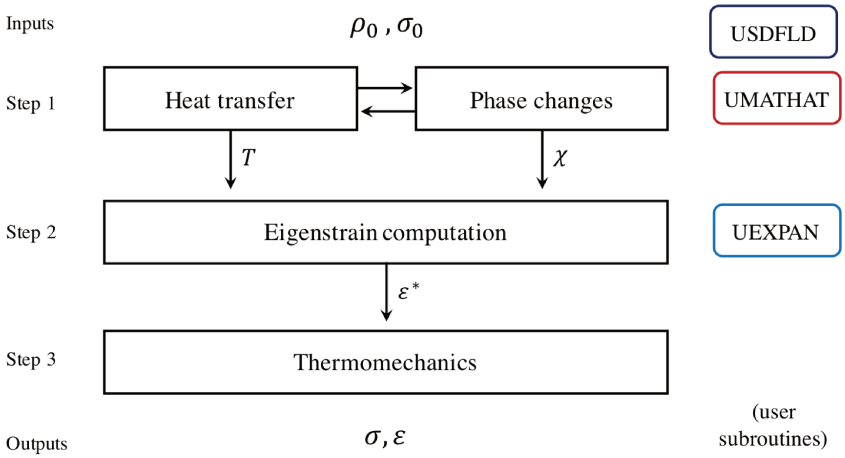

Figure 8.2: FE analysis strategy; First the heat equation is solved at the same time that the phase change problem. Then, the overall eigenstrain is computed. Finally, the stress and strain are obtained from the thermomechanical model.

Remarks:

1) More complexity in the initial state can be introduce using different user subroutines. In this chapter, several simulations were done using the subroutine USDFLD to set an initial density distribution resulting from the compaction process. Defining a non zero initial stresses state caused by the compaction could be introduced using the subroutine SIGINI.

2) A full coupled thermal and thermomechanical analysis can also be run easily. But the computation time is notably increased without significant improvement of the solution for the cases studied.

2.2 Abaqus user subroutines and other material input data

Subroutine UMATHT

This user subroutine allows to define the PTFE thermal constitutive behavior. It is called for each element and at each time t. Input data are the internal variables, time and temperature field at the time t corresponding to the beginning of the increment, as well as material parameters, time increment and temperature increment. Output data at the end of the current time increment $t + \mathrm{d}t$ are internal energy and energy gradients, heat flux and gradients and the internal variables. In this subroutine, the crystallinity content χ is also computed at the end of the increment and the associated state variables (STATEV) are updated. At heating, the evolution of χ is calculated from the sigmoid function in Chapter 7 and at cooling, from the crystallization kinetic model that was implemented. The heat flux and the latent heat associated to the increment of crystallinity content χ are also computed.

Subroutine UEXPAN

This user subroutine allows to define the overall eigenstrain ε of PTFE. It is called for each element and at each time t. Input data are the internal variables, time and temperature at the time t corresponding to the beginning of the increment, as well as material parameters, time increment and temperature increment. The output at the end of the current incremented time $t + dt$ is the increment of the overall eigenstrain which takes into account the different eigenstrain terms discussed in the previous chapters as well as the their anisotropic behavior.

Subroutine USDFLD

This user subroutine allows to define field variable at the material point as function of time. The initial density distribution can thus be specified with this subroutine. The density value is assigned according to the field variable in the material parameters.

2.3 Mechanical properties

The elastic behavior of the PTFE is implemented using Abaqus library (*elastic card). The Young's modulus and Poisson's ratio are defined in a table indicating the temperature dependency. The values are taken from DMA experiment results on sintered PTFE (in Chapter 6). To take into account the evolution of the elastic properties with the initial porosity in the green state (and therefore initial density) an additional dependency is provided in elastic properties. The dependency is made with an internal field variable that corresponds to the initial density. The evolution of the elastic properties with initial void ratio was measured at ambient temperature by Fredy (see Chapter 1). This evolution was extrapolated for any temperature (see Chapter 6).

At cooling of recrystallized PTFE, the plastic behavior described in Chapter 6 is added using Abaqus library (*plastic card) considering Von Mises plasticity criterion and using the associate flow rule. Isotropic hardening option is taken into account. The hardening is described by a tabular function $\sigma_Y = f(p)$, where σ_Y is the yield stress and p the cumulative plastic strain. The data are taken from the compression experiments (see Chapter 6).

3 PTFE plate sintering

Validating the simulation with a specific experiment is mandatory to feel confident with its results. An experiment was designed to compare the FE analysis results with measurements.

First the experiment is described in subsection 3.1, the displacement measurements are analyzed in subsection 3.2, then the determination of temperature using IR thermography is discussed in subsection 3.3 and finally the simulation results are compared to the experimental one in subsection 3.4.

3.1 Experiment description

A green PTFE plate (35 mm × 35 mm × 2 mm) is hanged inside an oven attached to a 40 g load. A cooling system is placed at the top of the plate to create an artificial thermal gradient from top to bottom. Figure 8.3 illustrates the validation experiment setup.

Optical images are recorded from a window parallel to the plate. An IR camera is placed in front of a second window oriented at 45° with respect to the surface of the plate. This latter window is made out of germanium to let the IR radiation pass through.

The interest of such an experiment is that it can be assumed to be a 2D problem as the thickness of the plate is small as compared to the other dimensions. The main thermal gradients are aligned with the mean sample plane. Therefore the two field measurement methods provide access to a complete knowledge of temperature and displacements during the experiment. The FE analysis results can be compared directly to the DIC measurements.

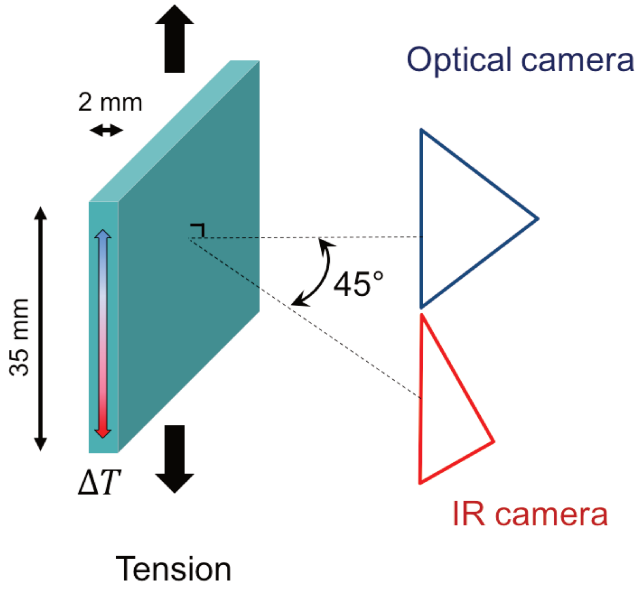

Figure 8.3: Sketch of the validation experiment. A PTFE plate is hanged in an oven and a 40 g mass is attached to the bottom edge of the sample to impose a slight tension. A cooling system is placed close to the top of the plate to set a thermal gradient. The plate is observed from two windows with an optical camera and an infrared (IR) camera. The IR camera is tilted at 45° with respect to the plate surface.

Optical and IR images captured during the experiment are presented in Figure 8.4. The PTFE plate is covered with black speckle (Figure 8.4a) to provide a distribution of gray levels on the image. This speckle pattern is suited to DIC analysis. On the IR image in Figure 8.4b, the intensity is related to the recorded IR flux. The latter depends on the temperature of the object and of its emissivity (see Chapter 2). A circular halo is observed around the plate on the IR image. It corresponds to a Narcissus effect artifact [122]. It is coming from the reflection of the IR camera itself on the germanium glass through which the specimen is observed.

A mesh is superimposed on the PTFE plate in the optical image. From this mesh in white in Figure 8.5a, another mesh is constructed by removing the elements where the plate is hidden or shadowed. This new mesh, in blue in the Figure, is used for the DIC measurement. During the capture, some parts of the plate are no more visible due to the expansion of PTFE. For those reasons, the white mesh does not cover the entire plate at the top and bottom.

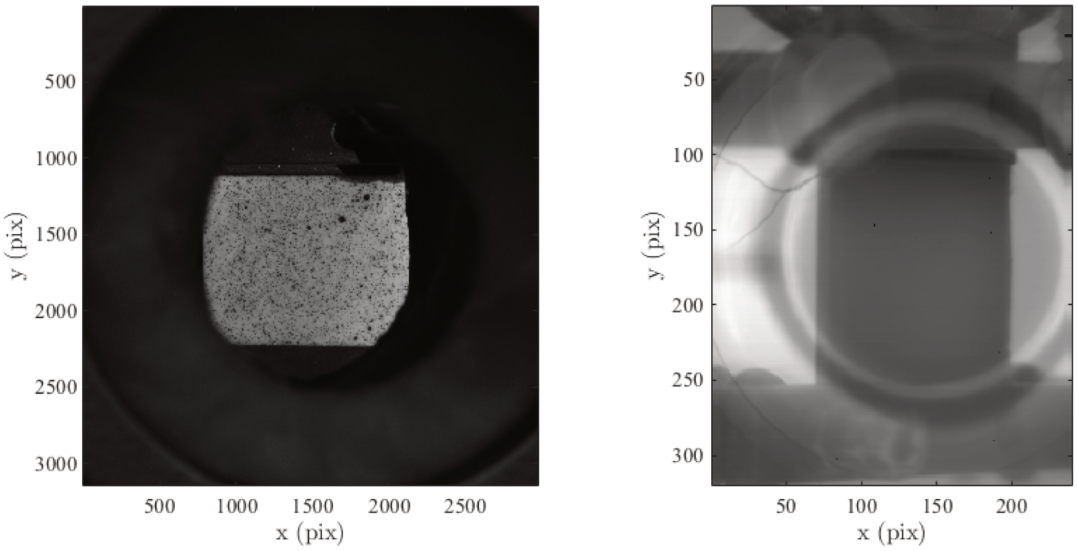

Figure 8.4: Image of the PTFE plate obtained with the optical camera (a) and with the IR camera (b).

The white mesh is projected on the IR image in Figure 8.5b. The perspective effect on the IR mesh is due to the 45° tilt of the IR camera. With the result of the DIC analysis, the mesh is advected with the specimen, and transferred on IR images. Therefore to obtain the corresponding temperature, the IR mesh is deformed all the same with the appropriate projection. Note that the projection is not exact as the out of plane displacement is not measured. This adds some more uncertainties to the temperature measurement.

3.2 Digital image correlation analysis

DIC is performed over the series of optical images. As described in Chapter 2, it provides displacement fields for the different time steps at which images were captured. The brightness and contrast correction option is used to make displacement measurements possible even when PTFE melts and becomes almost translucent. Mechanical regularization is also used for a fast convergence and then the regularization length was progressively tuned down to 0.

The residual is defined as the difference between the current (deformed) image corrected by the measured displacement field and the initial (reference) image. It provides information on the quality of the measurement. Figure 8.6a shows the residual field for frame 100 in the molten state where the residuals are at their highest levels. The residual field is mostly null so that the results are deemed trustworthy. Higher values can reach up to 10% of the gray levels and correspond mainly to the black speckle sprayed on the PTFE plate. This error is due to molten PTFE that becomes translucent. The brightness and the contrast is adjusted to mitigate this effect The root mean square residual for the different frames is shown in Figure 8.6b. It is always below 2.5% of the gray levels. Two peaks can be noticed and can be respectively related to melting and crystallization of the PTFE plate.

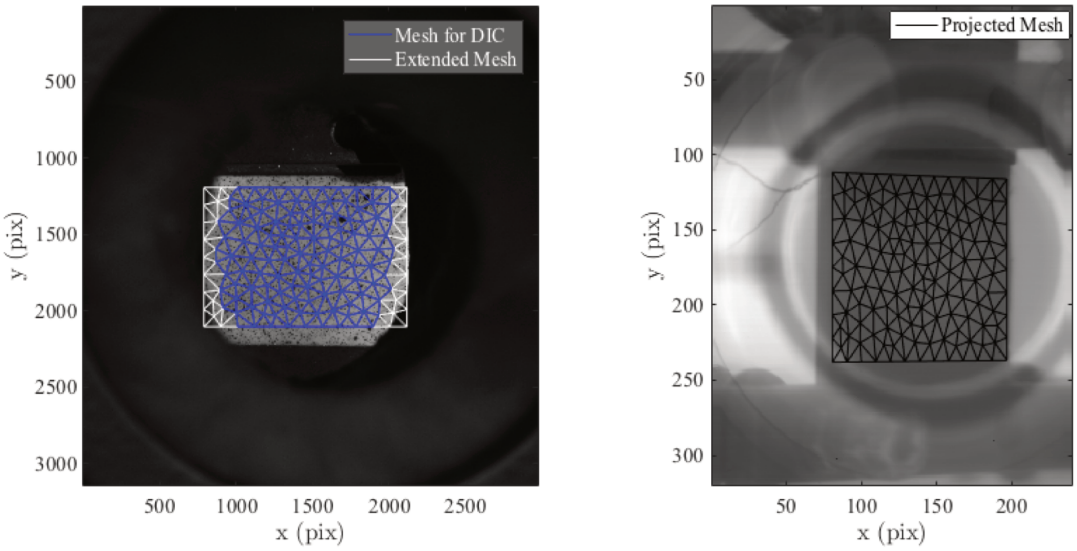

(a) (b)

Figure 8.5: Mesh of the PTFE plate (in white) and restriction of this mesh (in blue) used for the DIC (a). Projection of the mesh on the IR image (b).

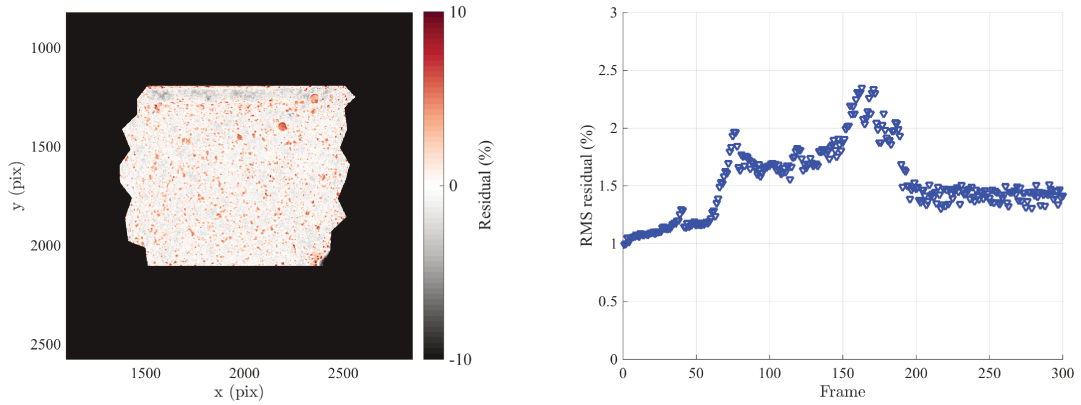

(a) (b)

Figure 8.6: Residual field at frame 100 (a) and root mean square residual as function of the frame number (b). The residual is expressed in percentage of the dynamic range in gray levels.

The DIC measurements obtained on the blue mesh (Figure 8.5a) are extrapolated over the white mesh using the griddedInterpolant function from Matlab. Displacements obtained from DIC in x and y are shown in Figure 8.7 for five different stages (initial stage, heating, plateau, heating and final stage).

The strain can be computed from the measured displacements. The surface strain

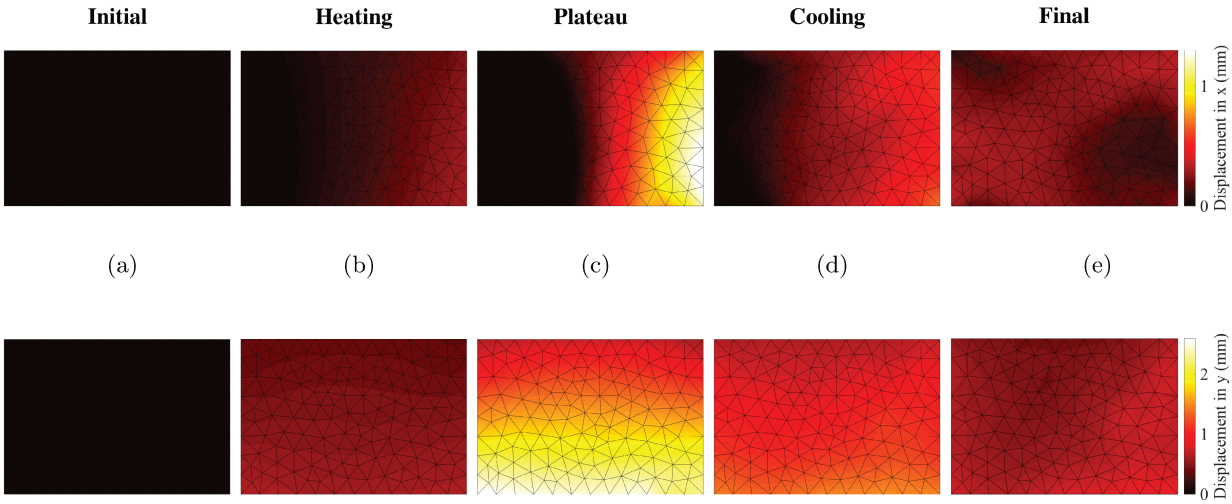

Figure 8.7: Extrapolated DIC measured displacements in x (a, b, c, d, e) and in y (f, g, h, i, j) at different stages of the thermal cycle. (a, f) correspond to the initial stage, (b, g) to heating stage, (c, h) to the plateau, (d, i) to cooling stage and (e,j) to the final capture.

$\varepsilon_s = \varepsilon_{xx} + \varepsilon_{yy}$ (equivalent to the volumetric strain in 2D) is shown in Figure 8.8 for the five different stages along the thermal cycle. It can be seen that the plate is more dilated in the molten state than at the final stage. Spatial variation can also be noticed thanks to these measurements.

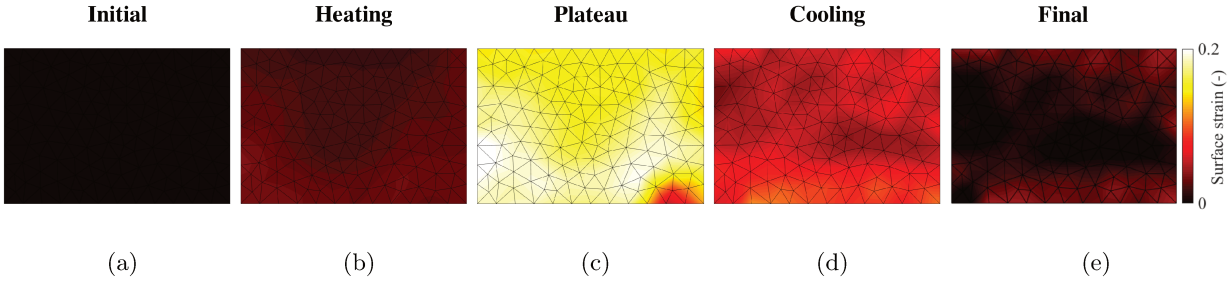

Figure 8.8: Surface strain $\varepsilon_s = \varepsilon_{xx} + \varepsilon_{yy}$ obtained from DIC at different stages of the thermal cycle.

The surface strain are plotted as function of time in Figure 8.9a for different nodes as spotted on the mesh in Figure 8.9b. This evolution is similar to the one observed from TMA experiments (see Figure 4.6 in Chapter 4) with the large expansion corresponding to melting around 35 min and the large shrinkage due to crystallization in the end.

3.3 Infrared thermal camera observation

Infrared measurements give access to the temperature at the surface of the PTFE plate using the preliminary calibration (see Chapter 2). It relates the measured digital level to the temperature of the PTFE specimen. From the different acquired IR images, the

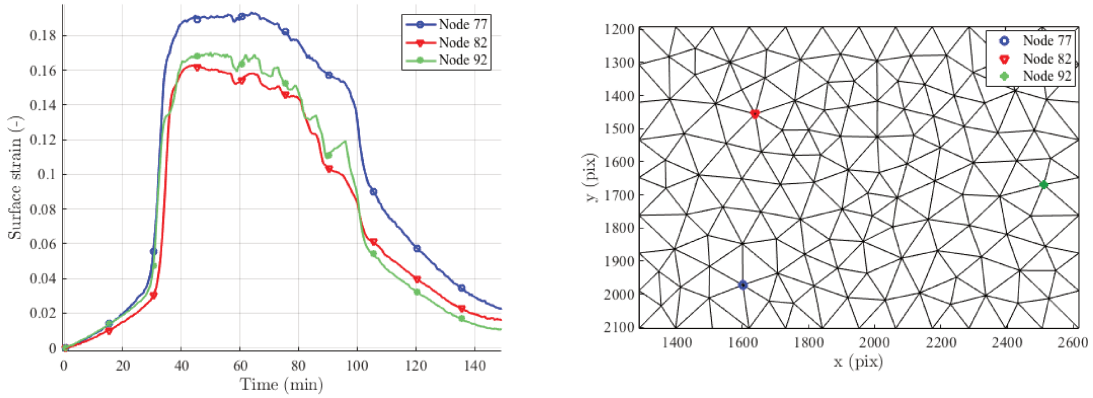

(a) (b)

Figure 8.9: Surface strain ($\varepsilon_{xx}+\varepsilon_{yy}$) obtained from DIC for three different nodes as function of time (a). Position of the three nodes on the mesh (b).

temperature maps can be computed. Figure 8.10 shows the temperature map obtained for the different steps of the applied thermal cycle. It can be seen that a thermal gradient exists between the bottom and the top.

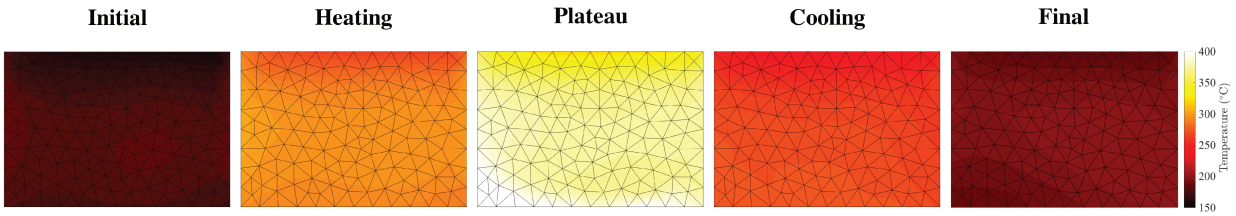

(a) (b) (c) (d) (e)

Figure 8.10: Temperature map obtained at different stages of the thermal cycle from the IR measurements.

The thermal gradient on PTFE surface can be observed within a narrow temperature range (see Figure 8.11). The temperature variation is mainly observed along the y direction but some variations can also be detected in the x direction.

Using the temperature maps at the different steps, the measured displacements and measured strains can be visualized as functions of the temperature. Figure 8.12 shows the surface strain as function of the temperature for the three previously considered nodes (in Figure 8.9). The evolution of the strain is similar to the one observed from dilatometric experiments in Figures 3.2a and 3.2c in Chapter 3. However the behaviors are not superimposed which means that the different nodes were not undergoing the same thermomechanical loading. The challenge for the finite element simulation is to reproduce those differences between the nodes with the developed model using the same boundary conditions.

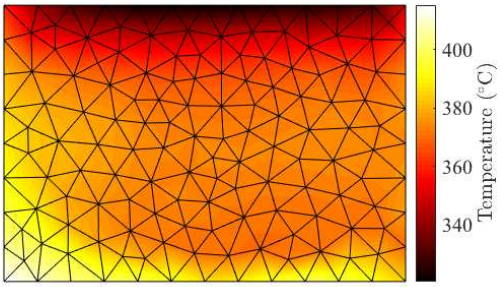

Figure 8.11: Temperature map obtained in a molten state from Figure 8.10c with an adjusted temperature range to identify the thermal gradients.

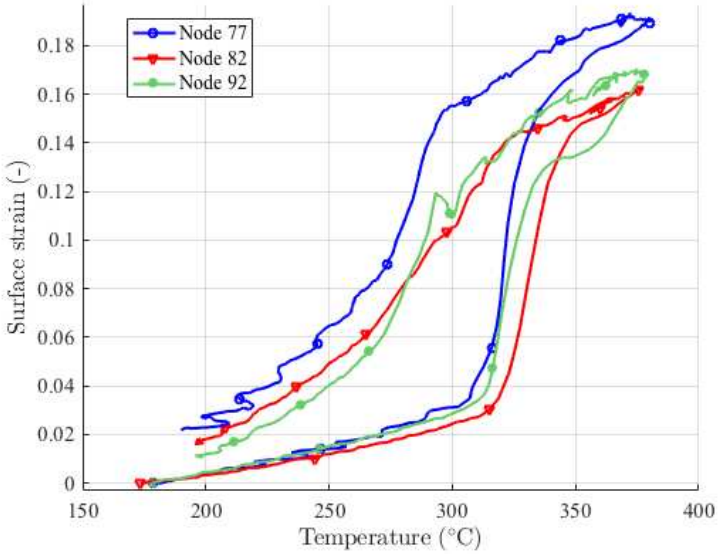

Figure 8.12: Surface strain ($\varepsilon_{xx} + \varepsilon_{yy}$) obtained from DIC for three different nodes (from Figure 8.9) as function of temperature obtained from IR measurements.

3.4 Comparison with simulation

A finite element analysis of the validation experiment is performed. The mesh defined from the optical images is used for the simulation. The temperature is imposed at each node for each time step from the IR measurements. The boundary conditions are set as described in Figure 8.13. The displacement measured from DIC is imposed at the top and bottom edges of the simulated plate. The left and right edges are free edges, therefore their tangential stress component is null ($\boldsymbol{\sigma}.\boldsymbol{n} = 0$). Those boundary conditions enable to get as close as possible from the experiment as they are extracted from the measurements.

Note that displacement conditions (Dirichlet conditions) could have been attached to the left and right edges, however it is more accurate to use the normal stress conditions (Neumann conditions) as they are known to be free edges.

The simulated displacements in x and y directions are presented in Figure 8.14 for the

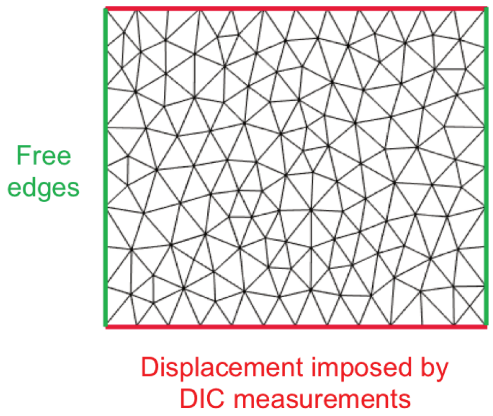

Figure 8.13: Boundary conditions set in the FE simulation on the edges of the PTFE plate.

same time steps as in Figure 8.7. They are comparable to the measured displacements.

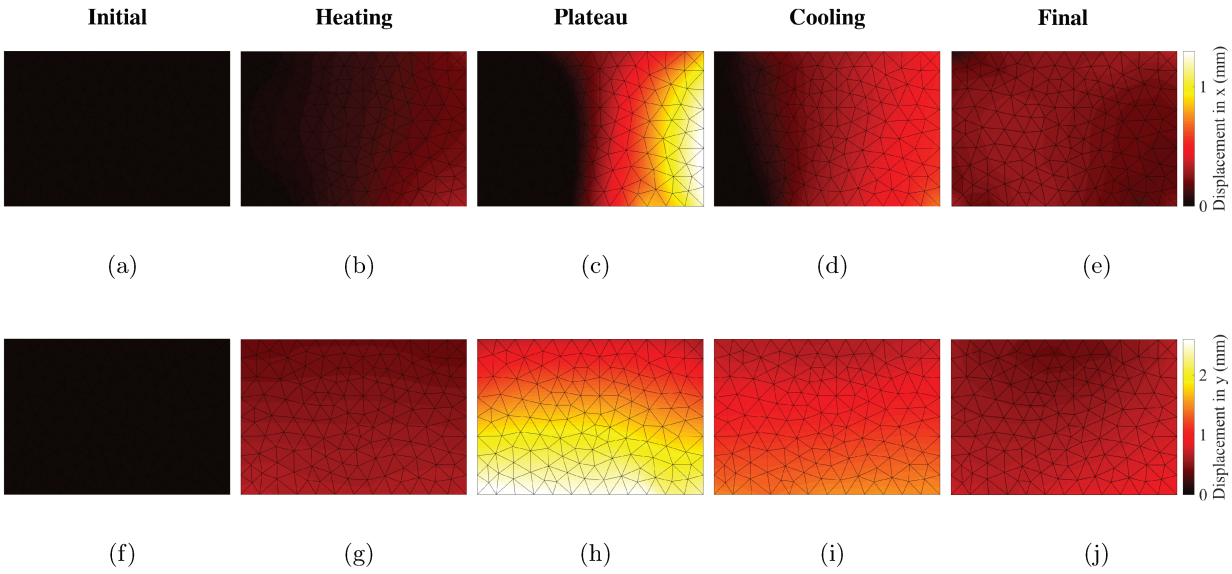

Figure 8.14: Simulated displacements in x (a, b, c, d, e) and in y (f, g, h, i, j) for different stages of the thermal cycle obtained from the FE analysis.

To compare the simulation to the measurements, the difference between the two displacement (called displacement residual) are computed. Those residuals can be easily accessed as they are defined on the same mesh. Figure 8.15 shows the displacement residuals at the same time steps as earlier reported. Their amplitude is quite low and reaches at most 10% of the displacement. No characteristic spatial and temporal evolution is observed meaning that it is mainly related to measurement errors.

The simulation results presented here were obtained by adjusting slightly the model parameters to reduce the residuals. The strain at melting, at crystallization and the melting temperature were modified in the FE analysis. The adjustment of parameters is necessary to correct for the measurement errors (especially on the temperature far from

the calibration temperature span). An optimization loop could be designed to determine the best model parameters.

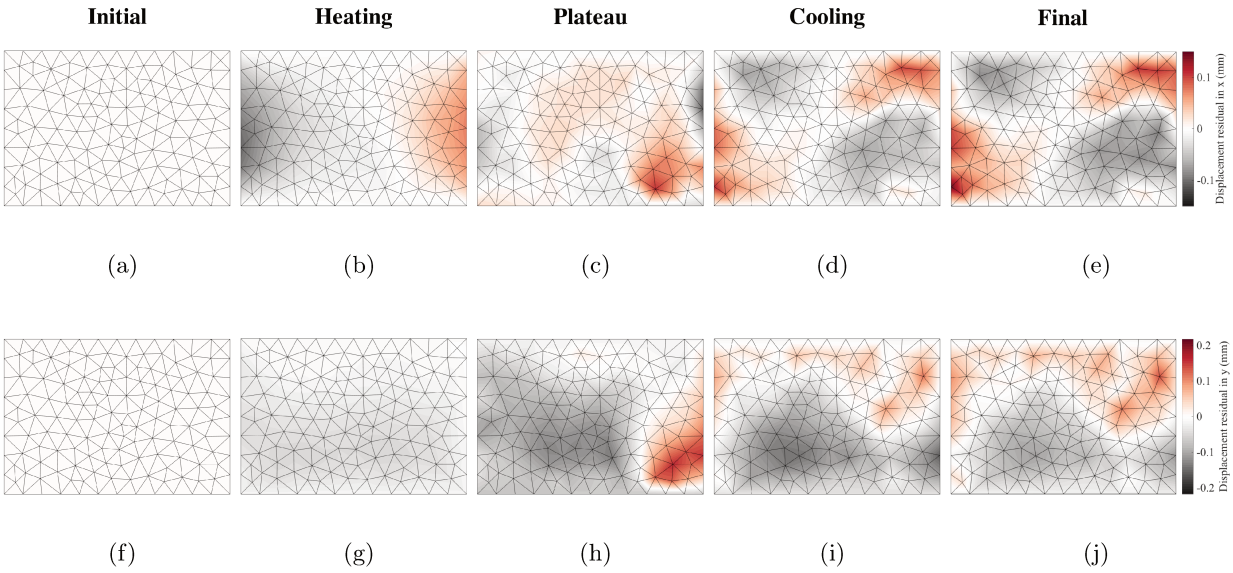

Figure 8.15: Residual displacements in x (a, b, c, d, e) and in y (f, g , h, i, j) between FE simulation and measurement for different stages of the thermal cycle.

The temporal evolution of the displacement residual is proposed in x and y direction for two nodes in Figure 8.16. The measured and simulated displacements are shown as well. It interesting to see that most of the displacement fluctuations are well simulated. They are probably originating from the thermal loading. The displacements are globally very well retrieved by the simulation. The residual displacements are quite low compared to the displacement amplitude.

Note that the lower error is observed in the y direction. This is caused by the fact that the displacements is imposed at the top and bottom edges. Conversely, the x direction has higher errors and even a remaining difference between simulated and measured displacement can be observed at the end of the experiment.

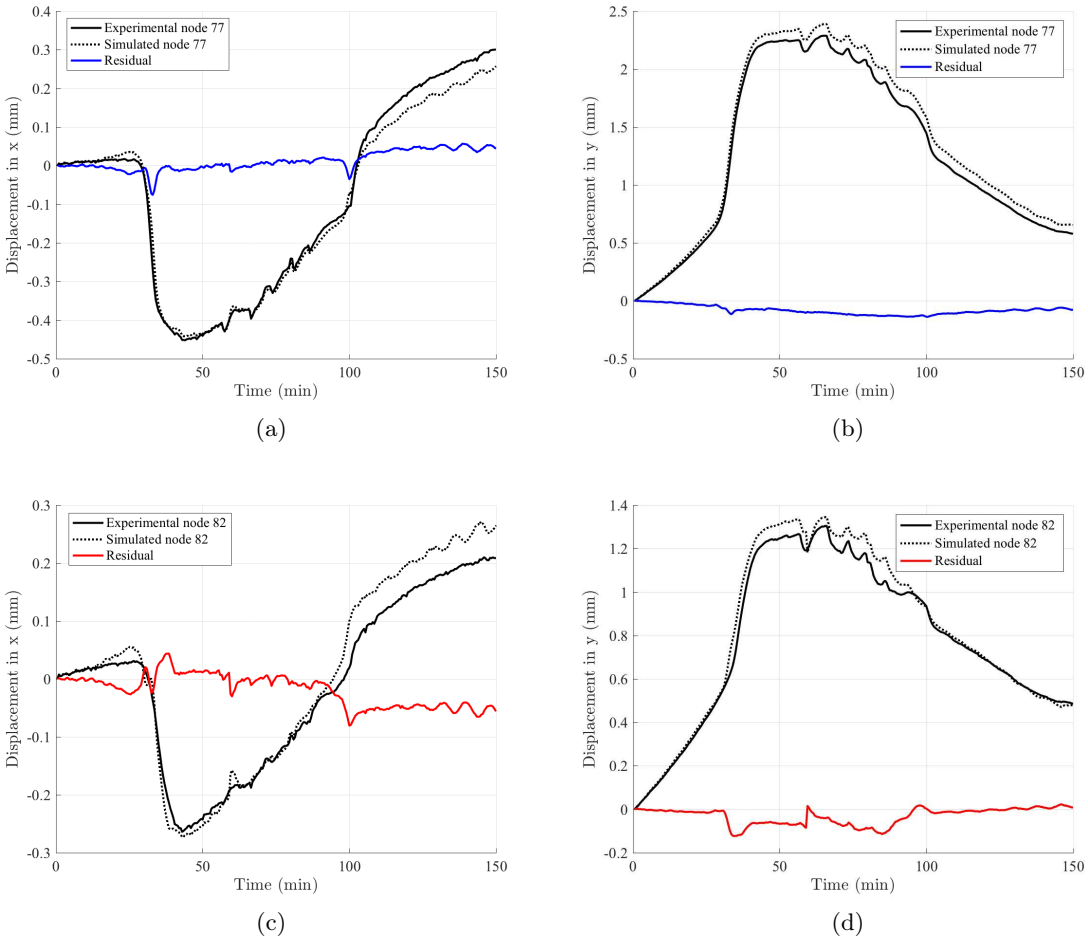

Figure 8.16: Displacements in x and y for two different nodes highlighted in Figure 8.9b obtained from measurement and FE simulation, and their difference (displacement residual).

4 Additional experiments

Two other type of experiments were tested to observe the evolution of PTFE structures during sintering and evaluate the ability of the finite model to correspond to the experimental results. Each test was designed to reproduce a specific situation observed during the manufacturing of pieces by uniaxial compaction and sintering in industrial application.

A first sintering experiment was conducted on a small PTFE sample with an inhomogeneous but controlled density. Density gradients can be observed in pressed billet (see Chapter 1). Other sintering tests were made on samples with initial defect in order to reproduce the behavior of a cracked billet during thermal cycling.

4.1 Sintering of inhomogeneous density PTFE plate

A 3 mm thick PTFE plate (35 mm $\times$ 35 mm) was compacted by a two-step process (see Figure 8.17). First PTFE powder was placed in a mold and was compacted up to 50 MPa. Then powder was added again and the overall PTFE sample was pressed up to 5 MPa. The

obtained PTFE plate had a side with a density related to a 50 MPa compaction (porosity about 5%) and another related to a 5 MPa compaction (porosity about 20 %).

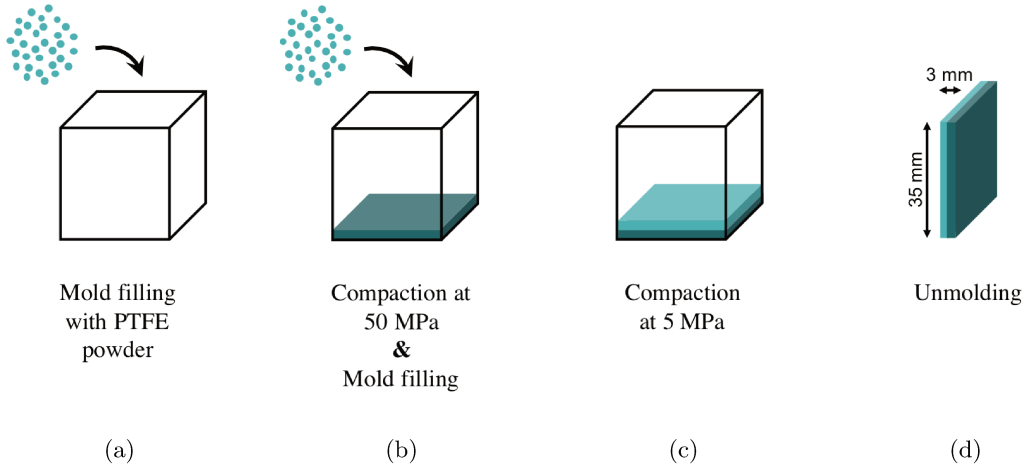

Figure 8.17: Sketch of the pressing of an inhomogeneous plate.

At melting the overall eigenstrain generated (expansion) by the denser layer is expected to be higher than the one of the less dense layer due to void closure (see Chapter 4). Therefore, the plate bends during melting and remains bent after sintering. Figure 8.18 shows the pictures of the straight inhomogeneous plate before and with a curvature after sintering. The curvature of the plate is note perfect, and some defects are noticeable at the interface between the two density regions. Those two parts of the plate seem to delaminate close to the clamp.

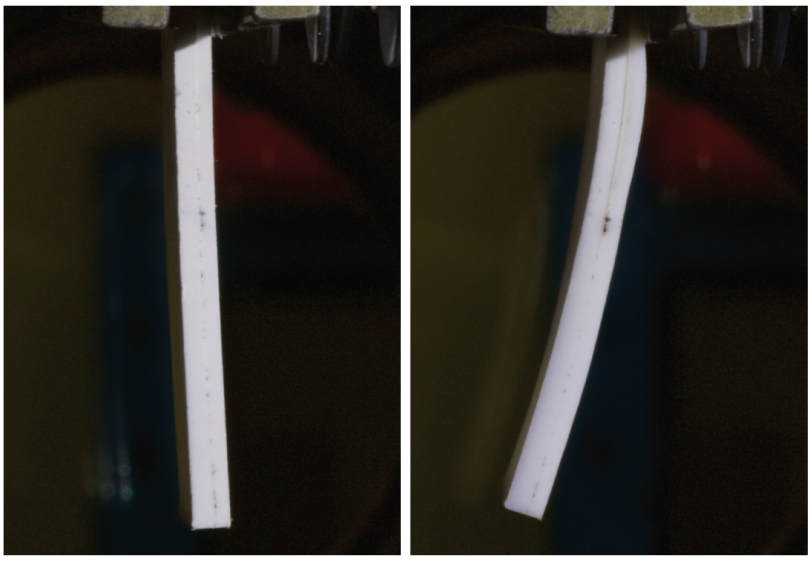

Figure 8.18: Picture of the inhomogeneous plate before (a) and after sintering (b).

A 2D FE analysis of the inhomogeneous plate sintering was performed using the eigenstrain model (i.e. without the mechanical model). The same simulation framework was

used as detailed earlier. The top edge of the plate was clamped ("encastre" in Abaqus) and the other sections were free edges (Figure 8.19a). The same sintering cycle than in the experiment was applied evenly in the plate. The plate was designed with a linear density gradient instead of an abrupt variation to avoid discontinuities for a simpler simulation. The extreme densities were chosen alike.

The results of the simulation are shown in Figure 8.19b. After sintering the shape is very similar to the one observed in the experiment. The curvature is a bit more constant due to the fact that there is no defect in the simulation. We concluded that the FE analysis is in good agreement with the experiment.

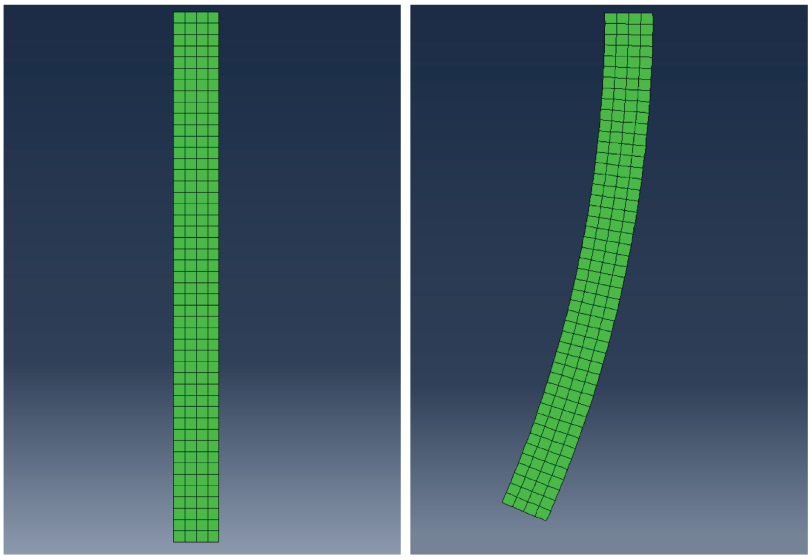

(a) (b)

Figure 8.19: 2D FE simulation of an inhomogeneous plate sintering. Before (a) and after sintering (b).

4.2 Sintering of PTFE compact with defect

To observe the effect of defects in PTFE compacts during sintering, a sample was prepared with a glass inclusion. A PTFE block (25 mm × 35 mm × 35 mm) was pressed with a horizontal glass slide (100 µm × 15 mm × 15 mm) embedded at the center as described in Figure 8.20. After compaction, the unmolded PTFE cube had no visible mark of the defect on the outer surface.

The specimen was then placed in the oven and images were recorded through the glass window. Figure 8.21 shows the PTFE cube at different times of its sintering. At melting the defect started to be visible (Figure 8.21b). A crack appeared on the surface at the defect location during the plateau after that the entire part was melted (Figure 8.21c). During crystallization, the crack continued to open wider (Figure 8.21d). It partly closed up at the end of the cooling (Figure 8.21e).

This experiment illustrates the type of mechanism that could occur in PTFE billet when cracks appear. The glass slide represents a weak interface with a low cohesion. Due to the overall thermal eigenstrain of PTFE and the stress generated from it, the crack opens up. Nevertheless, this phenomenon is difficult to simulate as no information on

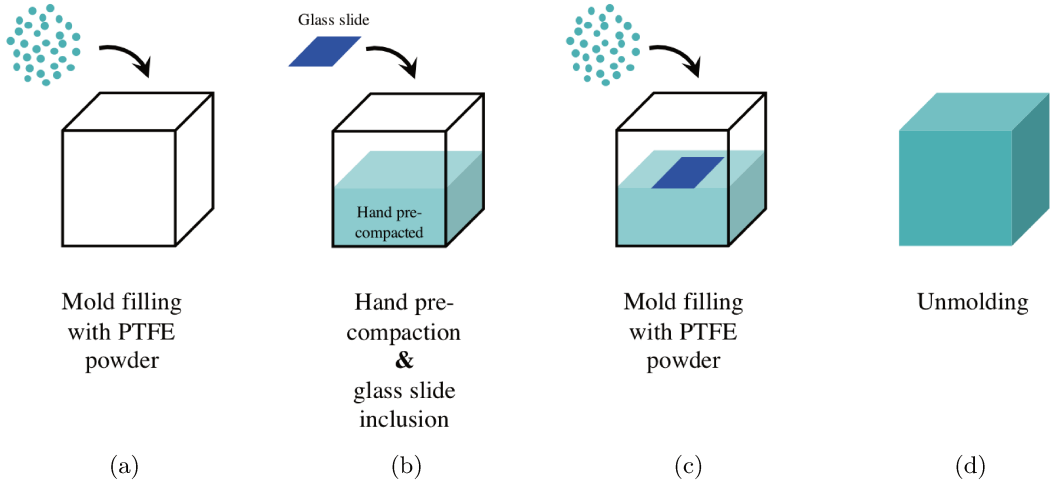

Figure 8.20: Pressing procedure of PTFE compact with an horizontal glass inclusion.

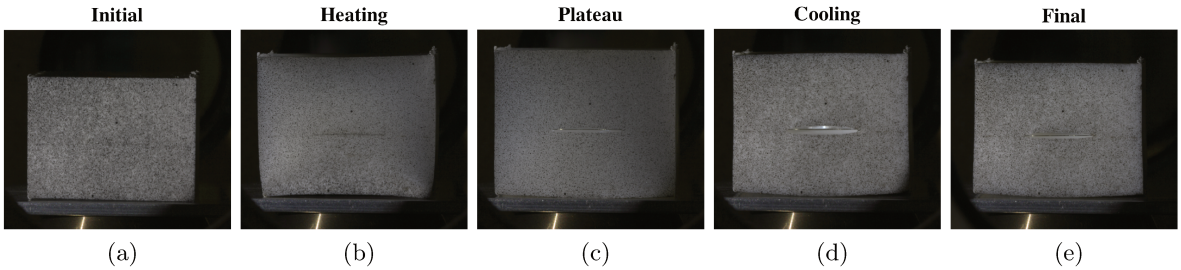

Figure 8.21: Images taken during the sintering of the PTFE compact with an horizontal glass inclusion: in its initial state at ambient temperature (a), during melting (b), during the plateau after complete melting (c), during crystallization (d) and after complete sintering (e).

crack propagation in PTFE is available (and especially at high temperature).

Therefore, another experiment was designed to mimic a billet with an open crack. Two 50 MPa-pressed PTFE cylinders of 20 mm height and 30 mm diameter were superimposed (see Figure 8.22) in an oven. Images are recorded during the sintering of the specimen in Figure 8.23.

At melting the two cylinders expanded from the skin first. They remained in contact at the interface as shown in Figure 8.23b but a gap became visible between the two cylinders in the center. It seems to be caused by a movement out of the symmetry axis. After the complete melting of the two cylinders in Figure 8.23c, the interface seemed to open up from the skin. Some fibrils were visible in the "crack" between the two cylinders, on the left side of the picture. At crystallization in Figure 8.23d, the "crack" opened up wider and closed up at the end of the cooling in Figure 8.23e.

The experiment was simulated with a 2D axisymmetric FE analysis. The interface was modeled with hard contact, no friction and with a perfect thermal contact. The thermal loading was applied at the outer surface, the top and the bottom with a heat transfer coefficient ($h = 40$ W.m^{-2}.K^{-1}) taking inbto account both air convection and thermal radiation. The same thermal cycle than for the experiment was set: a heating at 2°C/min,

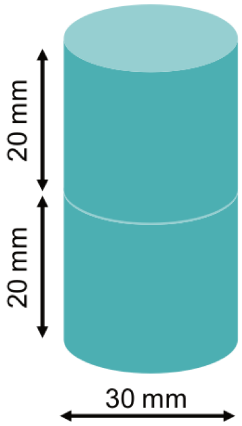

Figure 8.22: Sketch of the two pressed PTFE cylinders representing a PTFE billet with an open crack.

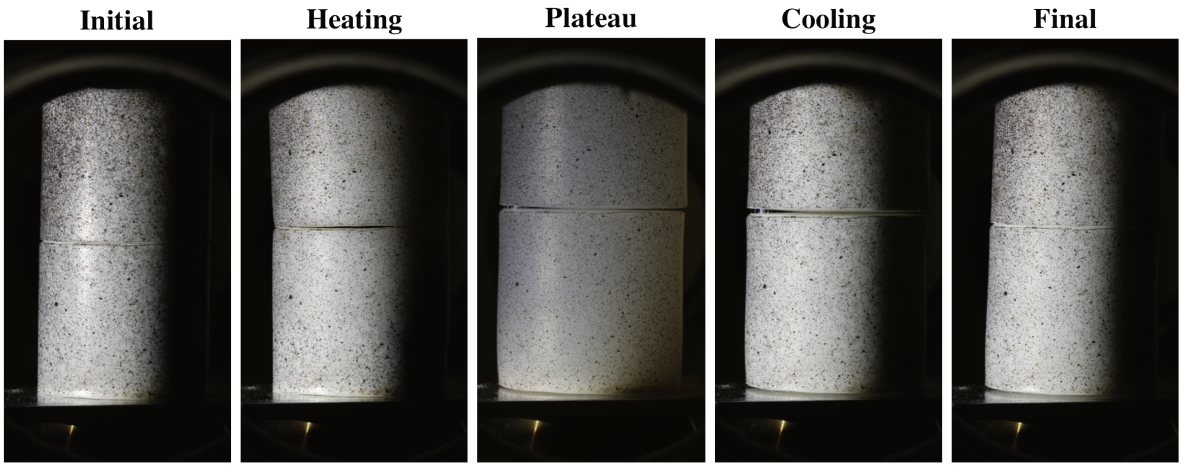

Figure 8.23: Images taken during the sintering of the two superimposed PTFE cylinders: in their initial state at ambient temperature (a), during melting (b), during the plateau after complete melting (c), during crystallization (d) and after complete sintering (e).

a plateau at 370°C for 100 min, a cooling at 2°C/min and a equilibrium plateau at 30°C for 30 min. Gravity was applied to ensure the contact between the two cylinders. The bottom part had no possible motion in the vertical direction (to enforce the contact to the support). The complete model was used for this simulation.

The deformed PTFE cylinders from the FE analysis are presented in Figure 8.24 at different times of the sintering. At melting the system opens up at the center and closes up in the plateau when the whole PTFE samples are molten. At cooling, the cracks re-opens during crystallization and closes up again at ambient temperature when the temperature is homogenized in the sample.

When comparing the experiment to the simulation, it should be impossible to say if the

center opened up during melting as the observation is only on the outer surface. However a gap was observed in the center (Figure 8.23b) that is certainly due to imperfections in the experimental conditions that generated a tilting and revealed the opening at the center. In the simulation, no "crack" opening was predicted at the skin (Figure 8.24c) while it was observed in the experiment (Figure 8.23c). At cooling, the behavior is consistent between the FE analysis and the experiment.

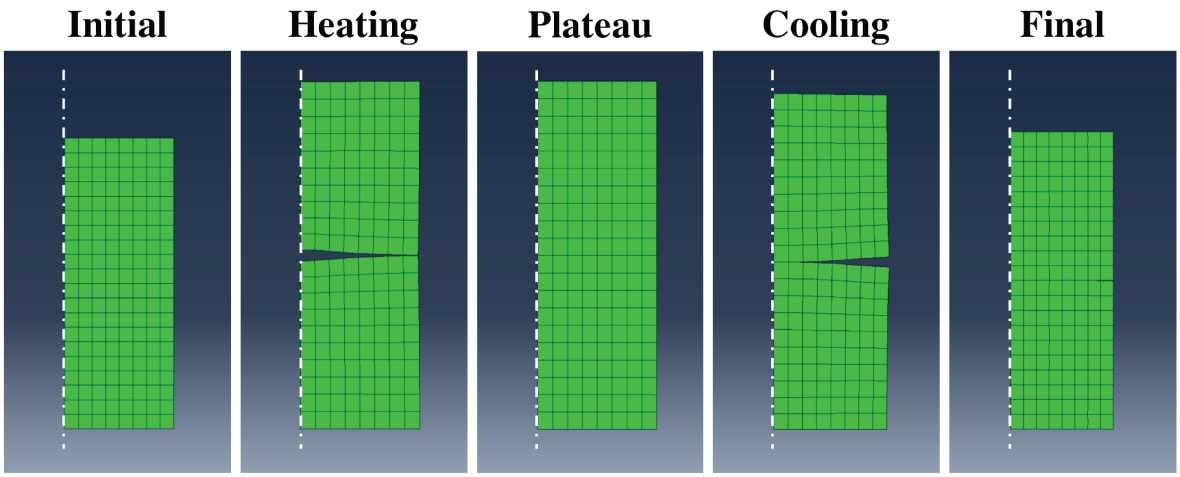

Figure 8.24: Snapshot of the FE analysis of the two superimposed PTFE cylinders sintering: in their initial state at ambient temperature (a), during melting (b), during the plateau after complete melting (c), during crystallization (d) and after complete sintering (e).

There is a relatively good agreement between the simulation and the experiment. However, FE analysis presents some limits due to the incorrect thermal conditions. The lower part of the PTFE cylinder laid on a metallic support and therefore the thermal exchanges may have been different there. Also when the "crack" opens, the thermal exchanges should be considered in the open region. Besides, some friction could be considered as well at the interface and at the contact with the support at the bottom.

5 Billet sintering

5.1 Sintering of a billet with uniform density

A 2D axisymmetric FE analysis of a cylindrical PTFE billet sintering was performed. The dimensions of the billet selected are a height of 1.2 m, an inner diameter of 15 cm and an outer diameter of 42 cm as shown in Figure 8.25a. The part is meshed with an element size of 15 mm (see Figure 8.25b). A preliminary element size study was done to choose it. This size would have to be modify for different thermal cycles, geometries or to observe smaller heterogeneities. In a first step, the billet is considered with an homogeneous initial density (2.15 g/cm^3).

The thermal loading is applied to every surface with a heat transfer coefficient (h = 40 W.m^{-2}.K^{-1}) corresponding to both air convection and thermal radiation. The initial temperature of the part is set to 30°C, then the part is heated at 0.2°C/min up to 385°C,

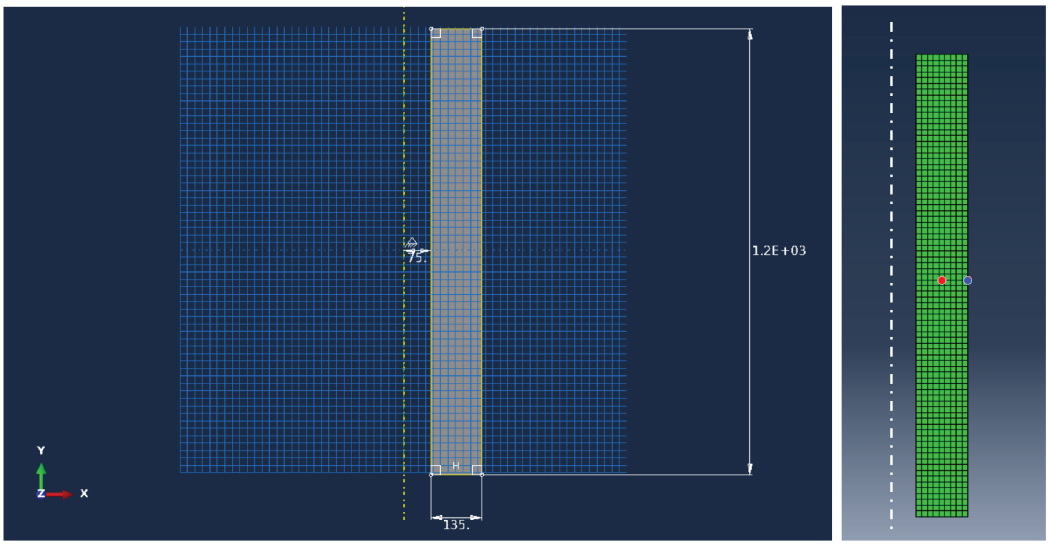

(a) (b)

Figure 8.25: Dimensions of the simulated billet (a) and mesh of the part with highlighted elements at the edge in blue and at the core in red (b).

maintained at this temperature for 1.8 days, then the billet is cooled at 0.2°C/min down to 30°C and maintained at this temperature for 1.8 days. The temperature obtained at the edge and at the core of the billet (respectively blue and red dot in Figure 8.25b) along the thermal cycle is presented in Figure 8.26. The temperature delay observed for the core of the billet is related to the low thermal diffusivity of PTFE. The temperature of the edge is also slightly delayed from the imposed temperature in the plateaus due to the heat transfer coefficient.

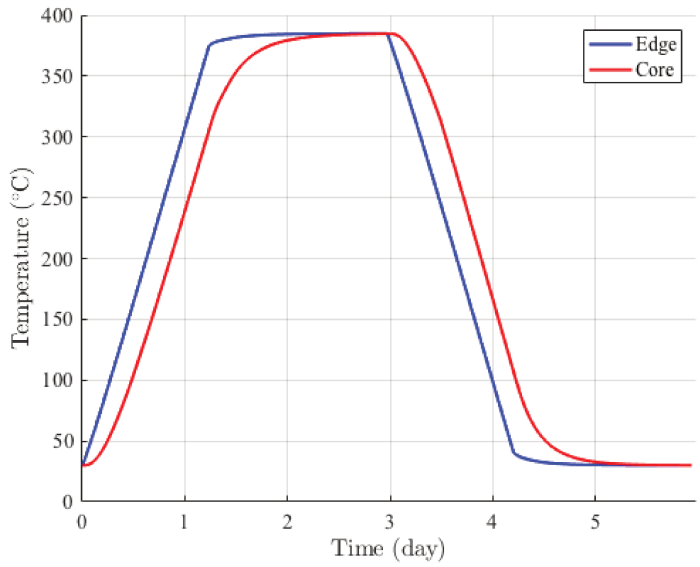

Figure 8.26: Computed temperature at the edge and core of the billet from the FE analysis.

From the FE analysis, the stress state can be evaluated in the PTFE billet along the

thermal cycle. The stress component σ_{yy} corresponding to the axial stress component is considered as variable of interest as usually observed cracks are occurring vertically. Spatial colormaps of the σ_{yy} are presented in Figure 8.27 for different times of the sintering. It appears that the stress is maximal at the end of the cycle where residual stresses are captured. Traction (positive stress) is observed in the core at melting and at the edge during crystallization.

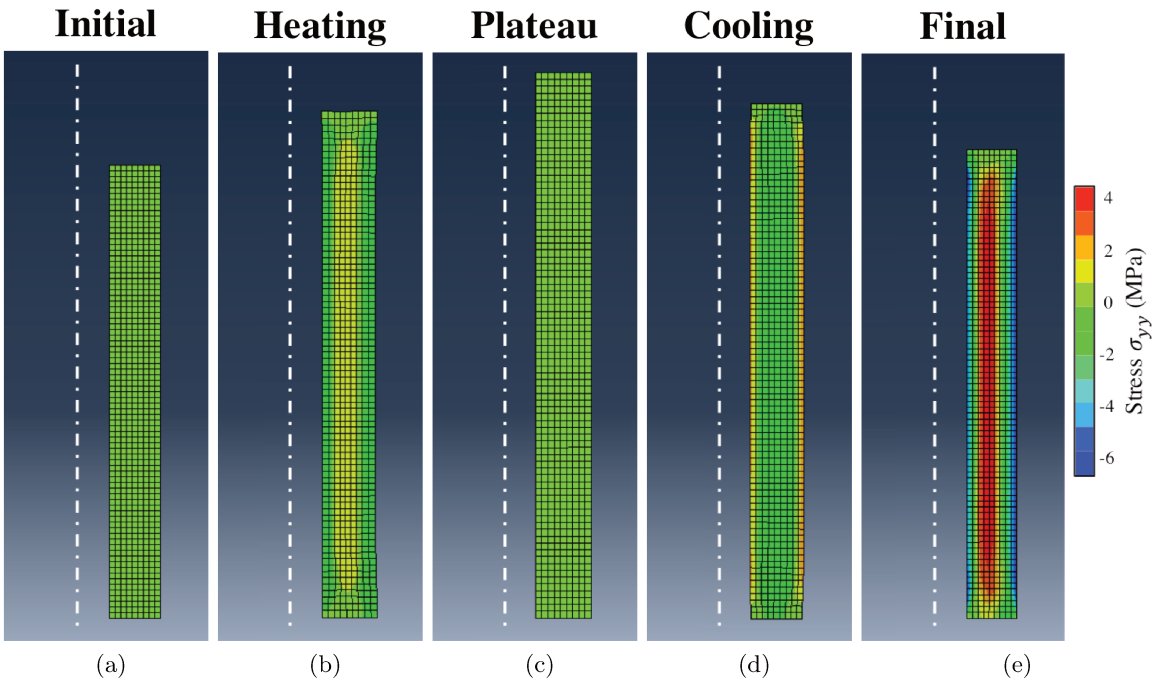

Figure 8.27: Simulated PTFE billet during sintering with the colormap of the axial stress σ_{yy}: in its initial state (a), during melting (b), during the plateau after complete melting (c), during crystallization (d) and after complete sintering (e).

The evolution of the axial component is presented for the edge and the core of the billet in Figure 8.28. At the beginning of the evolution the magnitude of the stress increases due to the thermal expansion. Then it decreases at some point due to the decline of the Young's modulus at higher temperatures. At melting, at about 1.2 days, the magnitude of the stress increases suddenly due to phase change and the same thing happens later at crystallization. The only difference between the stress at melting and at crystallization is the sign of the stress. At heating the edge is in compression at it expands more than the core, and at cooling it shrinks more than the core due to the thermal gradient. However at the end of the thermal cycle, the stress changes of sign as plasticity occurs mainly located on the edge. Plastic strain causes a compression on the edge as long as the core is shrinking due to cooling.

Note that the final stress values are very dependent on the plasticity model that has been chosen. More experiment should be made to validate this. Without any plasticity, the edge should remain in tension and the core in compression.

In order to further validate the FE analysis of billet sintering, it would be interesting to perform post-sintering residual stresses characterization on a billet to compare them with the simulation results. This could be done by cutting sections of the billet and measuring

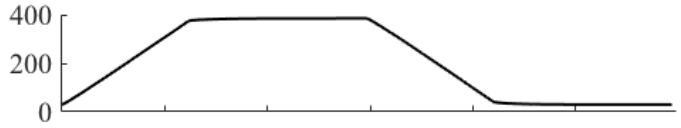

(a)

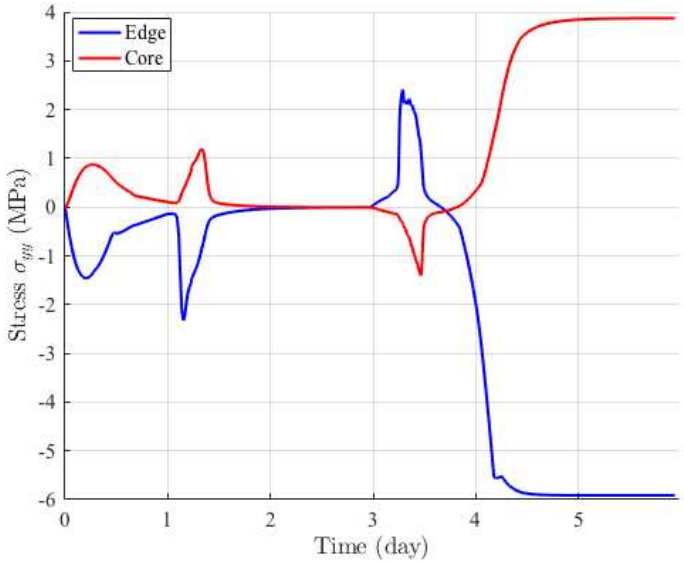

(b)

Figure 8.28: Evolution of the axial stress σ_{yy} with time at the edge in blue and in the core of the billet in red (b). Applied thermal cycle (a).

the dimensions afterwards [60]. These comparisons would be highly beneficial to estimate the chosen quality of the plasticity model.

5.2 Sintering parameters influence

It is now possible to compare the effects of different sintering parameters on the stress (for example) in order to better adjust them.

The initial density is modified step by step 2.0 and to 2.25 g/cm^3. The corresponding axial stresses σ_{yy} at the edge and at the core are plotted as functions of time in Figure 8.29. It appears that changing the initial density has a significant effect at heating. The lower is the density and the lower is the axial stress. It is logical to observe this evolution as both the Young's modulus and the overall eigenstrain at melting are decreasing with the density. After complete melting, the behaviors are similar as the density of the molten PTFE is always the same. The porosity closure is always considered complete and simultaneous with melting in the model. Modifying this part of the model would certainly modify the final behavior depending on the time spent in the plateau above the melting temperature.

The heating and cooling rates is modified by applying a thermal cycle $\times 1.5$ faster than the reference sintering (presented in subsection 5.1) including heating, cooling and plateaus, and a slower thermal cycle ($\times 0.5$ slower than the reference cycle). The temperatures and axial stresses measured at the edge and the core are presented in Figure 8.30 as function of time rescaled with respect to the reference cycle. It appears that faster cycle increase

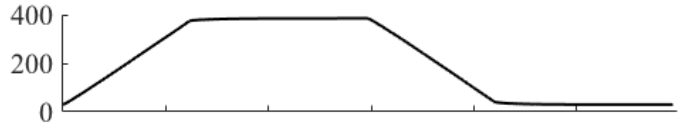

(a)

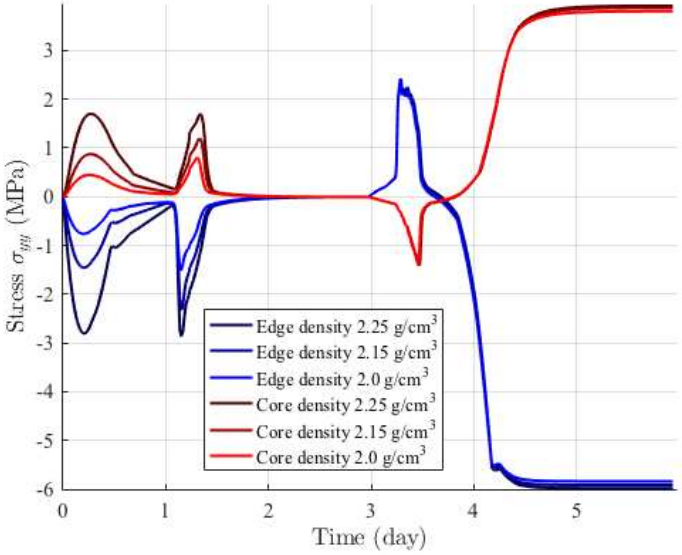

(b)

Figure 8.29: Evolution of the axial stress σ_{yy} with time at the edge in blue and in the core of the billet in red, for different densities: 2.0, 2.15 and 2.25 g/cm^3 from the lighter to the darker colors (b). Applied thermal cycle (a).

the thermal gradient and consequently increases the axial stress magnitude.

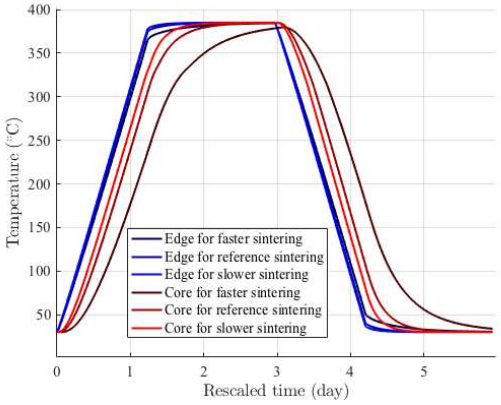

(a)

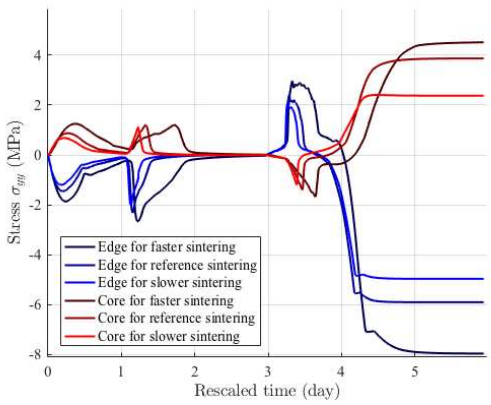

(b)

Figure 8.30: Computed temperature (a) and axial stress (b) at the edge in blue and in the core of the billet in red, for different thermal cycles: $\times 0.5$, $\times 1$ and $\times 1.5$ the reference cycle from the lighter to the darker colors. The results are expressed as function of the time rescaled with respect to the reference cycle for sake of clarity.

Increasing the wall thickness of the billet increases the thermal gradients as well. Figure 8.31 shows the computed evolution of the temperature and the axial stress as function of time for the core and the edge of the billet. The results of the stress are very similar to the one obtained for different thermal cycles (Figure 8.30). This suggests that both effects are mainly driven by the thermal gradient in the PTFE part.

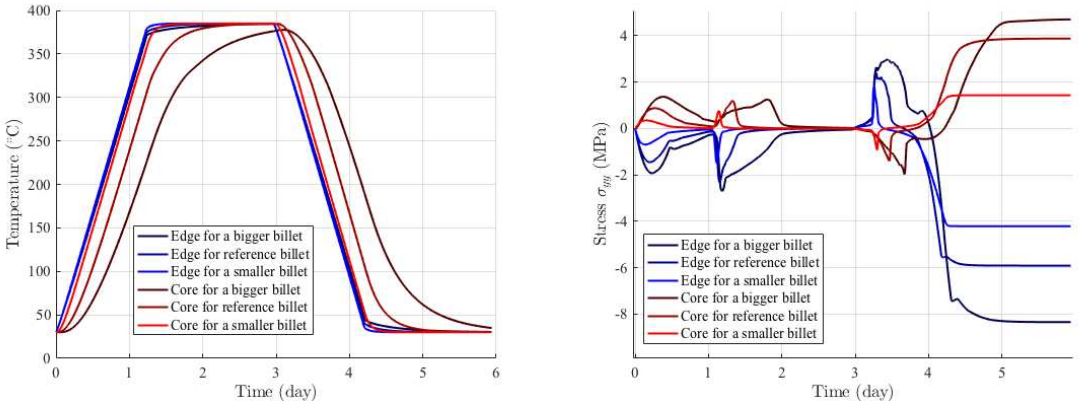

(a) (b)

Figure 8.31: Computed temperature (a) and axial stress (b) with time at the edge in blue and in the core of the billet in red, for different billet wall thickness: $\times 0.5$, $\times 1$ and $\times 1.5$ time the reference wall thickness from the lighter to the darker colors.

5.3 Sintering with density variations

From previous studies on the PTFE compaction [10] it is known that green PTFE compacts have density inhomogeneities (see Figure 1.18 in Chapter 1). Therefore simulating the effect of such density variations is interesting to better understand if it is a critical parameter or not.

For this purpose, sintering simulations were conducted on billets with an initial density gradient. Four cases were studied: two axial density gradients with different amplitudes, and two radial density gradients with different amplitudes. The corresponding density maps are shown in Figure 8.32.

The evolution of the computed axial stress σ_{yy} with time is shown in Figure 8.33 for axial gradients on the left and for the radial gradients on the right. Both gradient types are compared to the case of the homogeneous billet. It appears that the axial gradient does not have a strong effect on the axial stress. It only modifies the stress at heating due to the influence of the initial density as the considered acquisition point is at the middle of the billet (see Figure 8.29). Conversely, the radial gradient seems to increase the axial stress after melting causing significant differences at the end of the sintering. The core part of the billet being less dense, it expands less at melting than the edges and therefore the edges become in compression. This additional compression remains during crystallization causing a higher stress amplitude in the end.

Other type of homogeneities can be imagined. Similarly to the glass inclusion experiment, a billet with a density defect can be sintered numerically. Figure 8.34 shows a PTFE billet with a density anomaly and the resulting final Von Mises stress map after the sintering. The Von Mises stress is defined in equation (6.10) in Chapter 6. It can be seen

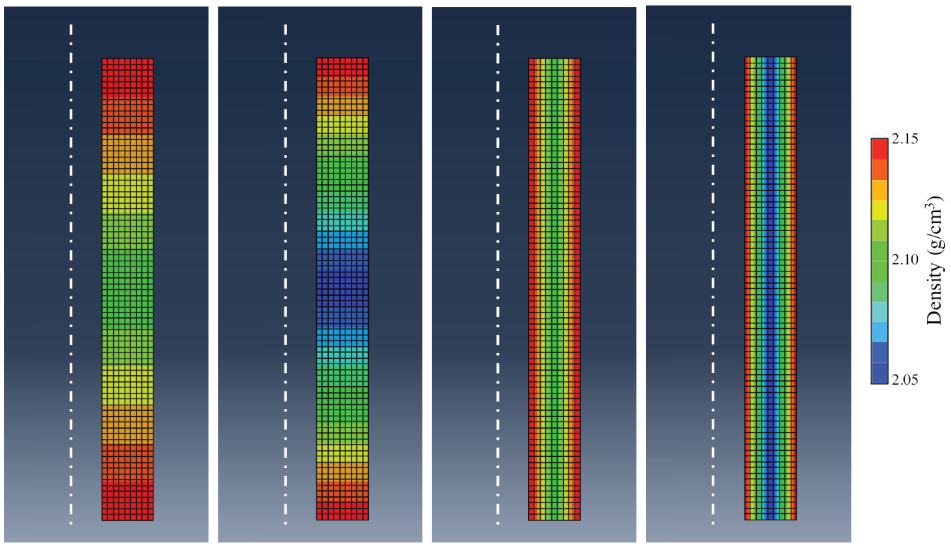

Figure 8.32: Initial density maps of billets chosen to study the influence of density gradients.

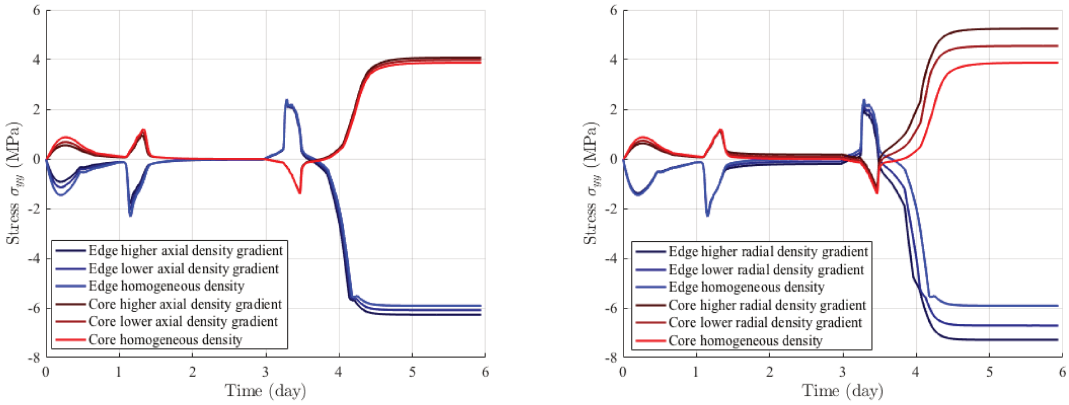

Figure 8.33: Computed axial stress as function of time at the edge in blue and in the core of the billet in red for different initial density gradients: no gradient, a small gradient and a bigger gradient respectively from the lighter to the darker colors (density distribution shown in Figure 8.32). The results are presented for axial gradients (a) and radial gradients (b).

that the initial defect affects significantly the final shape of the billet and presents a very high stress level at the vicinity of its original position.

The axial stress is shown in Figure 8.35 as function of time from an element included in the defect. It appears that the stress level is not so different from the previous experiments before melting. However at cooling, the axial stress increases dramatically to reach high stresses levels. Those type of defects would certainly affect badly a billet and perhaps break it.

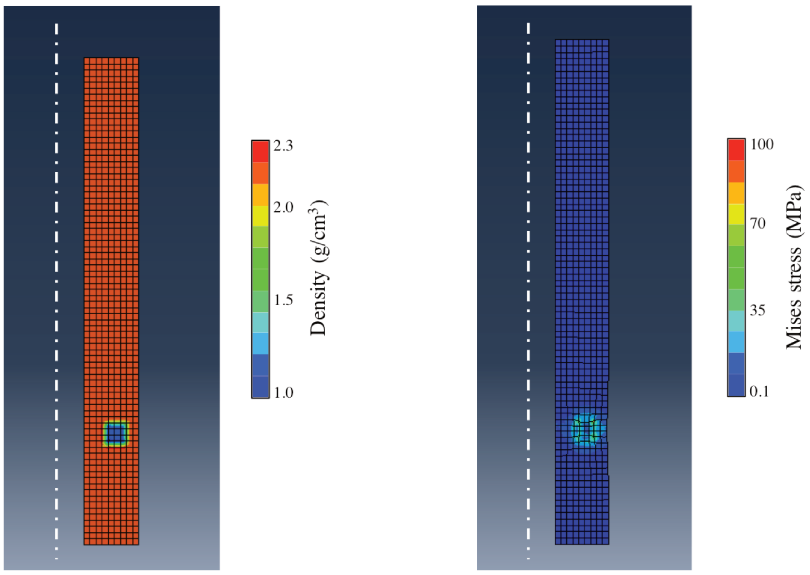

(a) (b)

Figure 8.34: Density map of the billet with a density anomaly (a) and resulting Von Mises stress map at the end of the sintering (b).

(a)

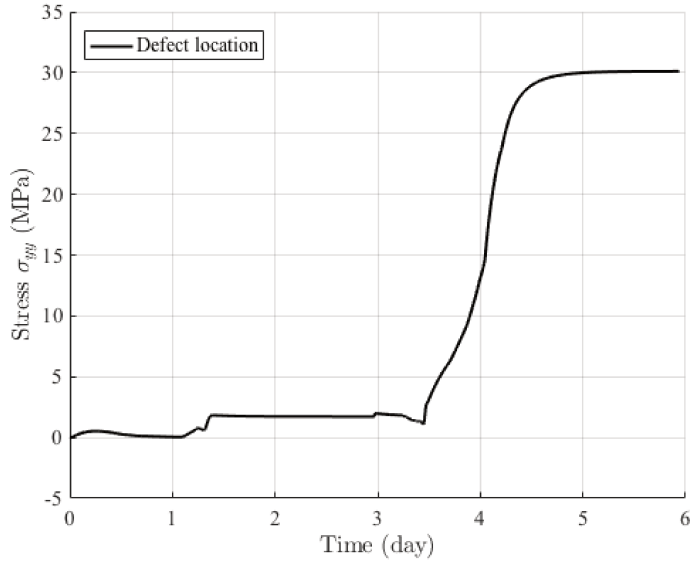

(b)

Figure 8.35: Axial stress as function of time at the vicinity of the density anomaly (b). Applied thermal cycle (a).

6 Conclusions and perspectives

A FE modeling has been designed for PTFE compacts sintering. Thermomechanical constitutive equations for PTFE compacts have been implemented in the FE code Abaqus. They includes the computations of the primary and secondary crystallinity content with the associated latent heat and the different eigenstrains by the use of user subroutines. The mechanical behavior is considered as elastic in the green state and elasto-plastic with isostropic hardening in the recrystallized state. These models are available in the Abaqus library. The evolution of the mechanical properties with temperature and density is also captured.

A validation experiment has been conceived in order to appreciate the quality of the FE analysis. This experiment was monitored by optical and IR cameras giving access to temperature and displacement field measurements. It allowed to compare precisely the results of the simulation with the experiment. By adjusting slightly some of the eigenstrain model parameters, it gives a very good agreement with the experiment. Improving the measurement precision (especially the thermal measurements) could strengthen the confidence in the simulation parameters.

Other specific experiments were performed to gauge the effect of density inhomogeneity and the inclusion of defects on the behavior of PTFE compacts at sintering. Both experiments were computed with FE analyses and confirm the good qualitative agreement. To be more precise on the simulations, knowledge on the exact thermal conditions and on adhesion would valuable. The glass inclusion experiment revealed in particular the ability of the PTFE compacts to open cracks from existing defects. Such phenomena are much likely to happen if for some reasons a defect is present in the billet before sintering. Further studies could be lead to investigate the effect of the size, geometry and defect type on the crack opening.

Finally, FE analyses of plant PTFE billet sintering are presented. The influence of different parameters was explored. It appears that reducing the initial density lower the overall axial stress in the part at heating. Higher thermal gradients obtained with bigger part or with faster sintering cycle increase the overall axial stress level. Radial density gradients in the green part seem to increase the final stress in the part whereas axial density gradients do not seem to have much effect. Simulation of sintering of a PTFE part with an initial density anomaly shows considerable effect on the stress level and on the final shape of the part. This simulation is more qualitative than predictive as failure behavior of PTFE is not taken into account here.

To refine this simulation, different phenomenon would have to be modeled. Looking at the pseudo-viscous component of the void closure strain may be valuable. This mechanism is related to the diffusion of the entrapped air, and therefore would depend on the geometry considered (see Chapter 4). Bigger part would need more time in the high temperature plateau to release the air. Also the impact of entrapped air during cooling would have to be investigate. It could play the role of defects if too important. Similarly, the visco-elastic and visco-plastic behavior of green PTFE could be modeled. The viscous effects are probably originating from the entrapped air as well. The plastic behavior of the green state might be more difficult to handle as it has different origins. It can come from crystal plasticity or PTFE particles rearrangement. The former would vanish at melting whereas the other would remain. Furthermore, this behavior would have to be characterize as function of the porosity fraction.

An attractive output arising from the FE analysis would be the prediction of crack

occurrence in PTFE billets. To do so, a suitable failure criterion for PTFE would have to be characterized. It would have to distinguish the brittle green PTFE and the recrystallized PTFE that can reach high deformations before failing.

Conclusions and perspectives

Sintering PTFE compacts has been practiced successfully for years. Yet, this remarkable know-how has been built over a long experience of different processing conditions. For a more thorough understanding, for accessing more quickly to optimized processes, or for managing fragile compounds, it appeared necessary to step back, and invest some effort in the modeling of PTFE sintering. In the present study different physical mechanisms responsible for the overall thermal eigenstrain of PTFE were analyzed. These observations were turned into a model that was implemented in a thermomechanical simulation. The ambition of this simulation is to be predictive on the stress state inside a PTFE part during the sintering process.

We found experimentally that a residual stress relaxation mechanism is at stake during heating of green PTFE compacted uniaxially. These microscale[1] residual stresses are generated by the (oedometric) compaction due to the deformation of PTFE particles. During heating, an irreversible anisotropic strain occurs and these stresses are relaxed. This result is original and explains a large part of the anisotropic behavior when heating green PTFE (paper published in the journal Polymer Testing [111]).

Another mechanism occurring during sintering is the void closure. It was shown that two different types of void closure signatures seem to take place during melting of PTFE. The first mechanism happens simultaneously with melting and the second one is time-dependent. The latter is more pronounced for a higher porosity content of the green part and is most likely caused by entrapped gas diffusion.

Finally, the mechanism that induces the higher (eigen)strain is the phase change. Either at melting or at crystallization, the volume change due to the transformation of crystals into amorphous phase (and vice-versa) is very significant. The existence of a secondary crystallization that has a very singular evolution was discovered in PTFE. It appears to be independent of the primary crystallization, to have an isotropic eigenstrain signature (unlike the primary for uniaxially compacted PTFE) and to be temperature rate independent. This result was confirmed by X-ray diffraction (XRD) measurements giving access to the crystalline orientation during crystallization. For this study, a project submitted to the European Synchrotron Radiation Facility (ESRF) for an international call for projects, has been accepted. A fast crystalline orientation assessment method from XRD results has been developed to analyze the measurements. These observations on the secondary crystallization mechanism and their influence on the overall eigenstrain of PTFE constitute one of the major results of this thesis. A scientific publication on the crystallization of PTFE and another on the XRD method for the rapid analysis of the crystalline orientation of polymers are currently being submitted to peer-reviewed journals.

[1] Tensions and compressions are balanced at the scale of a few micrometric PTFE particles.

Furthermore, Young's modulus was evaluated as function of temperature for green and sintered PTFE. Highly compacted green PTFE seems to have a higher elastic modulus than sintered PTFE above the second glass transition at 130°C due to its higher crystallinity fraction. It was shown that, unlike what is often believed, molten PTFE is purely elastic. The molecular chains entanglements play the role of permanent crosslinks due to the extremely high molecular weight. As soon as PTFE crystallizes, it becomes elastoplastic. From this behavior, the existence of memory effect properties in PTFE was discovered. Like thermosets, PTFE is able, at cooling, to freeze a "permanent" deformation that has been generated at high temperature, and to recover it after fusion. Nevertheless, it is activated by the crystallization instead of the glass transition for thermosets. More spectacular and unique is the way PTFE is able to recover at high temperature a "permanent" strain generated at low temperature. This original effect was quite unexpected and is yet another key finding of the present work. It significantly changes the common perspective on the mechanical behavior of PTFE in the molten state.

Different models were developed from these observations. A crystallization kinetic model that takes into account the two crystallization mechanisms was built based on the Avrami/Nakamura model. Then, an overall eigenstrain model was assembled gathering the different eigenstrain components as function of temperature, crystallinity content variations and initial porosity. Last, a thermomechanical model was defined based on the mechanical behavior observations on green and sintered PTFE. They were integrated in a simulation code and in finite element (FE) analyses. Specific validation experiments were designed to confront with simulation results. Among them, an experiment was conceived using field measurement methods (digital image correlation and infrared thermography) to better compare the simulation to the experimental results. A good quantitative agreement between FE analysis and the validation experiment was observed. Two experiments were performed to observe crack opening in PTFE compacts due to sintering. Another sintering experiment was conceived to show the influence of density gradients on the thermomechanical behavior of green PTFE. A good qualitative agreement was found between these experiments and their respective simulations. This confirms the potential of these models and of the FE analyses whose development constitutes the initial objective of the PhD project. Already, simulations allow us to study the impact of the different processing parameters (heating and cooling rates, wall thickness or initial density).

To go further from this work, different perspectives can be considered:

A failure criterion could be established to evaluate the crack appearance during sintering. This criterion would depend on temperature and porosity. It would also be very different for green and for sintered PTFE, as the former is much more brittle. Thus, the plastic behavior of green PTFE would have to be characterized as well. Plasticity in green PTFE can originate from crystal plasticity and from grain rearrangements. In addition, viscoelastic or viscoplastic behavior could be taken into account. Especially at higher porosity, where green PTFE is very likely to inherit from gas diffusion a behavior that can be assimilated to visco-elasticity or visco-plasticity. Finally, possible viscoplasticity was neglected for sintered PTFE although it could be taken into account as well. However considering the loading rate, it is more than likely that it has no effect.

Another important effect that would deserve to be investigated is the time-dependent void closure mechanism. This effect seems to be limited by the entrapped gas diffusion. Therefore, such mechanisms depend on the dimension of the PTFE billet (scale effect). If the sintering is carried out too fast to allow the air to diffuse out, defects could form from the remaining porosity. Moreover, skin properties due to uniaxial compaction could also alter stress and the diffusion out of the PTFE billet.

The origins of the residual stress relaxation mechanism could be investigated more closely by studying sintering of green PTFE compacted with different loading paths. For example, isostatic compaction, biaxial compaction or any other compaction could be tested using ASTREE (true triaxial testing machine at LMT). The eigenstrain behavior at heating could provide insights on this relaxation mechanism. One could also imagine that different types of powder could have an impact.

One of the most interesting research direction resulting from this work is the study of PTFE microstructure evolution during secondary crystallization. The reversibility of this crystallization suggests that it is linked to the formation of very small crystals. Furthermore, this crystallization is not related to the primary one that is known to form thick crystalline lamellae. It would be interesting to observe the formation of those crystals with *in-situ* experiments during crystallization. It could be done using either atomic force microscopy or transmission electron microscopy coupled to a heating and cooling device.

Last, another attractive experiment would be to perform *in-situ* sintering in a tomograph. With a fine resolution, it may help tracking the porosity in a low density PTFE compact and observing its evolution with sintering. Above all, this experiment could be used to carry out digital volume correlation (DVC). The results of DVC analysis would provide complete 3D displacement measurements and would be very interesting to compare to the model in 3D case.

References

[1] Sina Ebnesajjad. *Fluoroplastics, Volume 1: non-melt processible fluoropolymers: the definitive user's guide and data book Plastics Design Library*. Elsevier, 2014.

[2] Morton A. Golub and Theodore Wydeven. "Reactions of atomic oxygen (O(3P)) with various polymer films". *Polymer Degradation and Stability* 22.4 (1988), pages 325–338. DOI: 10.1016/0141-3910(88)90004-3.

[3] Enzo Giannetti. "Semi-crystalline fluorinated polymers". *Polymer International* 50.1 (2001), pages 10–26. DOI: 10.1002/1097-0126(200101)50:1<10::AID-PI614>3.0.CO;2-W.

[4] SK Biswas and Kalyani Vijayan. "Friction and wear of PTFE—a review". *Wear* 158.1-2 (1992), pages 193–211.

[5] Jilin Zhang, Jian Li, and Yanchun Han. "Superhydrophobic PTFE Surfaces by Extension". *Macromolecular Rapid Communications* 25.11 (2004), pages 1105–1108. DOI: 10.1002/marc.200400065.

[6] J. M. Cox, B. A. Wright, and W. W. Wright. "Thermal degradation of fluorine-containing polymers. Part I. Degradation in vacuum". *Journal of Applied Polymer Science* 8.6 (1964), pages 2935–2950. DOI: 10.1002/app.1964.070080636.

[7] David Jauffres. "High mechanical performance polymers processed by High Velocity Compaction: sintering mechanisms and process/microstructure/mechanical properties relationships." Theses. INSA de Lyon, 2007.

[8] Rodrigo Bresciani Canto. "Étude théorique et expérimentale du procédé de compaction et frittage du polytetrafluoréthylène (PTFE)". PhD Thesis. Cachan, Ecole normale supérieure, 2007.

[9] Carole Frédy, Rodrigo B. Canto, Nicolas Schmitt, Stéphane Roux, and René Billardon. "Modelling of the mechanical behaviour of two pure PTFE powders during their compaction at room temperature". *AIP Conference Proceedings*. Volume 1542. AIP, 2013, pages 1246–1249. DOI: 10.1063/1.4812164.

[10] Carole Frédy. "Modeling of the mechanical behavior of polytetrafluoroethylene (PTFE) compounds during their compaction at room temperature". PhD Thesis. Université Pierre et Marie Curie-Paris VI, 2015.

[11] Bernhard Wunderlich, Martin Möller, Janusz Grebowicz, and Herbert Baur. *Conformational motion and disorder in low and high molecular mass crystals*. Springer, 1988.

[12] Eric N. Brown and Dana M. Dattelbaum. "The role of crystalline phase on fracture and microstructure evolution of polytetrafluoroethylene (PTFE)". *Polymer* 46.9 (2005), pages 3056–3068. DOI: 10.1016/j.polymer.2005.01.061.

[13] E.N. Brown, D.M. Dattelbaum, D.W. Brown, P.J. Rae, and B. Clausen. "A new strain path to inducing phase transitions in semi-crystalline polymers". *Polymer* 48.9 (2007), pages 2531–2536. DOI: 10.1016/j.polymer.2007.03.031.

[14] E.S. Clark. "The molecular conformations of polytetrafluoroethylene: forms II and IV". *Polymer* 40.16 (1999), pages 4659–4665. DOI: 10.1016/S0032-3861(99)00109-3.

[15] Carleton Angelo Sperati and Howard W Starkweather. "Fluorine-containing polymers. II. Polytetrafluoroethylene". In: *Fortschritte Der Hochpolymeren-Forschung*. Springer, 1961, pages 465–495.

[16] Edward S. Clark. "The Crystal Structure of Polytetrafluoroethylene, Forms I and IV". *Journal of Macromolecular Science, Part B* 45.2 (2006), pages 201–213. DOI: 10.1080/00222340500522265.

[17] M Kimmig, G Strobl, and B Stühn. "Chain reorientation in poly (tetrafluoroethylene) by mobile twin-helix reversal defects". *Macromolecules* 27.9 (1994), pages 2481–2495.

[18] DB Holt and BL Farmer. "Modeling of helix reversal defects in polytetrafluoroethylene: II. Molecular dynamics simulations". *Polymer* 40.16 (1999), pages 4673–4684.

[19] Julian H Gibbs and Edmund A DiMarzio. "Nature of the glass transition and the glassy state". *The Journal of Chemical Physics* 28.3 (1958), pages 373–383.

[20] N. G. McCrum. "An internal friction study of polytetrafluoroethylene". *Journal of Polymer Science* 34.127 (1959), pages 355–369. DOI: 10.1002/pol.1959.1203412728.

[21] Suk Fai Lau, Hidematsu Suzuki, and Bernhard Wunderlich. "The thermodynamic properties of polytetrafluoroethylene". *Journal of Polymer Science: Polymer Physics Edition* 22.3 (1984), pages 379–405. DOI: 10.1002/pol.1984.180220305.

[22] A. V. Tobolsky, D. Katz, and M. Takahashi. "Rheology of polytetrafluoroethylene". *Journal of Polymer Science Part A: General Papers* 1.1 (1963), pages 483–489. DOI: 10.1002/pol.1963.100010142.

[23] Yoshio Araki. "Thermal expansion coefficient of polytetrafluoroethylene in the vicinity of its glass transition at about 400°K". *Journal of Applied Polymer Science* 9.2 (1965), pages 421–427. DOI: 10.1002/app.1965.070090203.

[24] Yoshio Araki. "Stress relaxation of polytetrafluoroethylene in the vicinity of its glass transition temperature at about 130°C." *Journal of Applied Polymer Science* 9.4 (1965), pages 1515–1524. DOI: 10.1002/app.1965.070090426.

[25] Howard W. Starkweather. "The effect of absorbed chemicals on the internal motions in poly(tetrafluoroethylene)". *Macromolecules* 17.6 (1984), pages 1178–1180. DOI: 10.1021/ma00136a013.

[26] F-J Wortmann. "Analysing the relaxation behaviour of poly (tetrafluoroethylene) in the alpha-transition region by applying a two-component model". *Polymer* 37.12 (1996), pages 2471–2476.

[27] Gérard Calleja, Alex Jourdan, Bruno Ameduri, and Jean-Pierre Habas. "Where is the glass transition temperature of poly(tetrafluoroethylene)? A new approach by dynamic rheometry and mechanical tests". *European Polymer Journal* 49.8 (2013), pages 2214–2222. DOI: 10.1016/j.eurpolymj.2013.04.028.

[28] G. Dlubek, A. Sen Gupta, J. Pionteck, R. Häßler, R. Krause-Rehberg, H. Kaspar, and K.H. Lochhaas. "Glass transition and free volume in the mobile (MAF) and rigid (RAF) amorphous fractions of semicrystalline PTFE: a positron lifetime and PVT study". *Polymer* 46.16 (2005), pages 6075–6089. DOI: 10.1016/j.polymer.2005.04.090.

[29] B. Wunderlich. "Extended chain crystals of linear high polymers". *Pure and Applied Chemistry* 31.1-2 (1972), pages 49–64. DOI: 10.1351/pac197231010049.

[30] L. Melillo and B. Wunderlich. "Extended-chain crystals: VIII. Morphology of polytetrafluoroethylene". *Kolloid-Zeitschrift und Zeitschrift für Polymere* 250.5 (1972), pages 417–425. DOI: 10.1007/BF01507508.

[31] J Yang, KL Petersen, RA Williams, PH Geil, TC Long, and P Xu. "Morphology evolution in PTFE as a function of melt time and temperature I: High molecular weight single-and multi-molecule folded chain single crystals and band structures". *Chinese journal of polymer science* 23.02 (2005), pages 123–135.

[32] D.C. Bassett and R. Davitt. "On crystallization phenomena in polytetrafluoroethylene". *Polymer* 15.11 (1974), pages 721–728. DOI: 10.1016/0032-3861(74)90024-X.

[33] L Ferry, G Vigier, R Vassoille, and JL Bessede. "Study of polytetrafluoroethylene crystallization". *Acta polymerica* 46.4 (1995), pages 300–306.

[34] John D. Hoffman, G. Thomas Davis, and John I. Lauritzen. "The Rate of Crystallization of Linear Polymers with Chain Folding". In: *Treatise on Solid State Chemistry: Volume 3 Crystalline and Noncrystalline Solids*. Edited by N. B. Hannay. Boston, MA: Springer US, 1976, pages 497–614. DOI: 10.1007/978-1-4684-2664-9_7.

[35] George W Scherer. "Freezing gels". *Journal of Non-Crystalline Solids* 155.1 (1993), pages 1–25.

[36] Melvin Avrami. "Kinetics of phase change. I General theory". *The Journal of chemical physics* 7.12 (1939), pages 1103–1112.

[37] Melvin Avrami. "Kinetics of phase change. II transformation-time relations for random distribution of nuclei". *The Journal of chemical physics* 8.2 (1940), pages 212–224.

[38] Melvin Avrami. "Granulation, phase change, and microstructure kinetics of phase change. III". *The Journal of chemical physics* 9.2 (1941), pages 177–184.

[39] T. Ozawa. "Kinetics of non-isothermal crystallization". *Polymer* 12.3 (1971), pages 150–158. DOI: 10.1016/0032-3861(71)90041-3.

[40] K. Nakamura, T. Watanabe, K. Katayama, and T. Amano. "Some aspects of nonisothermal crystallization of polymers. I. Relationship between crystallization temperature, crystallinity, and cooling conditions". *Journal of Applied Polymer Science* 16.5 (1972), pages 1077–1091. DOI: 10.1002/app.1972.070160503.

[41] Tadao Suzuki and André J Kovacs. "Temperature Dependence of Spherulitic Growth Rate of Isotactic Polystyrene. A Critical Comparison with the Kinetic theory of Surface Nucleation". *Polymer Journal* 1.1 (1970), pages 82–100. DOI: 10.1295/polymj.1.82.

[42] Rajen M. Patel and Joseph E. Spruiell. "Crystallization kinetics during polymer processing—Analysis of available approaches for process modeling". *Polymer Engineering and Science* 31.10 (1991), pages 730–738. DOI: 10.1002/pen.760311008.

[43] Tanguy Choupin, Bruno Fayolle, Gilles Regnier, C Paris, Jacques Cinquin, and Benoît Brulé. "Isothermal crystallization kinetic modeling of poly (etherketoneketone)(PEKK) copolymer". *Polymer* 111 (2017), pages 73–82.

[44] Tanguy Choupin, Bruno Fayolle, Gilles Régnier, Christophe Paris, Jacques Cinquin, and Benoît Brulé. "A more reliable DSC-based methodology to study crystallization kinetics: Application to poly (ether ketone ketone)(PEKK) copolymers". *Polymer* 155 (2018), pages 109–115.

[45] A.Sh. Yagfarov. "The nature of secondary crystallization in polymers". *Polymer Science U.S.S.R.* 30.1 (1988), pages 88–95. DOI: 10.1016/0032-3950(88)90259-6.

[46] R. Kolb, C. Wutz, N. Stribeck, G. von Krosigk, and C. Riekel. "Investigation of secondary crystallization of polymers by means of microbeam X-ray scattering". *Polymer* 42.12 (2001), pages 5257–5266. DOI: 10.1016/S0032-3861(00)00920-4.

[47] X.F Lu and J.N Hay. "Isothermal crystallization kinetics and melting behaviour of poly(ethylene terephthalate)". *Polymer* 42.23 (2001), pages 9423–9431. DOI: 10.1016/S0032-3861(01)00502-X.

[48] Minqiao Ren, Jianbin Song, Qingxiang Zhao, Yuesheng Li, Qingyong Chen, Hongfang Zhang, and Zhishen Mo. "Primary and secondary crystallization kinetic analysis of nylon 1212". *Polymer International* 53.11 (2004), pages 1658–1665. DOI: 10.1002/pi.1490.

[49] M. J. Jenkins and K. L. Harrison. "The effect of molecular weight on the crystallization kinetics of polycaprolactone". *Polymers for Advanced Technologies* 17.6 (2006), pages 474–478. DOI: 10.1002/pat.733.

[50] O. Verhoyen, F. Dupret, and R. Legras. "Isothermal and non-isothermal crystallization kinetics of polyethylene terephthalate: Mathematical modeling and experimental measurement". *Polymer Engineering & Science* 38.9 (1998), pages 1594–1610. DOI: 10.1002/pen.10330.

[51] Chris N. Velisaris and James C. Seferis. "Crystallization kinetics of polyetheretherketone (peek) matrices". *Polymer Engineering and Science* 26.22 (1986), pages 1574–1581. DOI: 10.1002/pen.760262208.

[52] I. H. Hillier. "Modified Avrami equation for the bulk crystallization kinetics of spherulitic polymers". *Journal of Polymer Science Part A: General Papers* 3.9 (1965), pages 3067–3078. DOI: 10.1002/pol.1965.100030902.

[53] Takeo Ozawa. "Nonisothermal Crystallization of Poly(tetrafluoroethylene)". *Bulletin of the Chemical Society of Japan* 57.4 (1984), pages 952–955. DOI: 10.1246/bcsj.57.952.

[54] Yongsok Seo. "Nonisothermal crystallization kinetics of polytetrafluoroethylene". *Polymer Engineering & Science* 40.6 (2000), pages 1293–1297. DOI: 10.1002/pen.11257.

[55] Xiao Qun Wang, Da Rong Chen, Jie Cai Han, and Shan Yi Du. "Crystallization behavior of polytetrafluoroethylene (PTFE)". *Journal of Applied Polymer Science* 83.5 (2002), pages 990–996. DOI: 10.1002/app.2279.

[56] N. K. J. Symons. "Crystals of polytetrafluoroethylene grown from solution". *Journal of Polymer Science* 51.156 (1961), S21–S25. DOI: 10.1002/pol.1961.1205115622.

[57] Nicolas Bosq, Nathanaël Guigo, Evgeny Zhuravlev, and Nicolas Sbirrazzuoli. "Non-isothermal Crystallization of Polytetrafluoroethylene in a Wide Range of Cooling Rates". *The Journal of Physical Chemistry B* 117.12 (2013), pages 3407–3415. DOI: 10.1021/jp311196g.

[58] Rachele Pucciariello and Vincenzo Villani. "Melting and crystallization behavior of poly(tetrafluoroethylene) by temperature modulated calorimetry". *Polymer* 45.6 (2004), pages 2031–2039. DOI: 10.1016/j.polymer.2004.01.019.

[59] Rene Androsch, Bernhard Wunderlich, and Hans-Joachim Radusch. "Analysis of reversible melting in polytetrafluoroethylene". *Journal of thermal analysis and calorimetry* 79.3 (2005), pages 615–621. DOI: 10.1007/s10973-005-0586-9.

[60] Luca Andena, Marta Rink, and Fabio Polastri. "Simulation of PTFE sintering: Thermal stresses and deformation behavior". *Polymer Engineering and Science* 44.7 (2004), pages 1368–1378. DOI: 10.1002/pen.20132.

[61] DL Kerbow and CA Sperati. *In Polymer Handbook, ; Brandrup, J.; Immergut, EH; Grulke, EA, Eds.* Wiley: New York, 1999.

[62] Daniel Jahier. *Le PTFE, polytétrafluoréthylène: présentation et applications.* CETIM, 1992.

[63] P.J. Rae and D.M. Dattelbaum. "The properties of poly(tetrafluoroethylene) (PTFE) in compression". *Polymer* 45.22 (2004), pages 7615–7625. DOI: 10.1016/j.polymer.2004.08.064.

[64] Kyuichiro Tanaka, Yoshitaka Uchiyama, and Satoru Toyooka. "The mechanism of wear of polytetrafluoroethylene". *Wear* 23.2 (1973), pages 153–172. DOI: 10.1016/0043-1648(73)90081-1.

[65] Xiaoqun Wang, Zhenlu Zhao, Darong Chen, and Shanyi Du. "Friction and Wear of Semi-Crystalline Polytetrafluoroethylene with Spherulitic Micro-Morphology". *Chinese Journal of Chemistry* 28.7 (2010), pages 1296–1300. DOI: 10.1002/cjoc.201090224.

[66] Alfonsius B. Ariawan, Sina Ebnesajjad, and Savvas G. Hatzikiriakos. "Properties of polytetrafluoroethylene (PTFE) paste extrudates". *Polymer Engineering & Science* 42.6 (2002), pages 1247–1259. DOI: 10.1002/pen.11028.

[67] K. Jurczuk, A. Galeski, and E. Piorkowska. "All-polymer nanocomposites with nanofibrillar inclusions generated in situ during compounding". *Polymer* 54.17 (2013), pages 4617–4628. DOI: 10.1016/j.polymer.2013.06.039.

[68] Jennifer L. Jordan, Clive R. Siviour, Jason R. Foley, and Eric N. Brown. "Compressive properties of extruded polytetrafluoroethylene". *Polymer* 48.14 (2007), pages 4184–4195. DOI: 10.1016/j.polymer.2007.05.038.

[69] Akhtar Khan and Haoyue Zhang. "Finite deformation of a polymer: experiments and modeling". *International Journal of Plasticity* 17.9 (2001), pages 1167–1188. DOI: 10.1016/S0749-6419(00)00073-5.

[70] Thomas Kletschkowski, Uwe Schomburg, and Albrecht Bertram. "Endochronic viscoplastic material models for filled PTFE". *Mechanics of Materials* 34.12 (2002), pages 795–808. DOI: 10.1016/S0167-6636(02)00197-7.

[71] J.S. Bergström and L.B. Hilbert. "A constitutive model for predicting the large deformation thermomechanical behavior of fluoropolymers". *Mechanics of Materials* 37.8 (2005), pages 899–913. DOI: 10.1016/j.mechmat.2004.09.002.

[72] Rodrigo Bresciani Canto, Nicolas Schmitt, Jonas De Carvalho, and René Billardon. "Experimental identification of the deformation mechanisms during sintering of cold compacted polytetrafluoroethylene powders". *Polymer Engineering & Science* 51.11 (2011), pages 2220–2235. DOI: 10.1002/pen.21994.

[73] Eugene A. Olevsky. "Theory of sintering: from discrete to continuum". *Materials Science and Engineering: R: Reports* 23.2 (1998), pages 41–100. DOI: 10.1016/S0927-796X(98)00009-6.

[74] Béatrice Perrenot and Georg Widmann. "Polymorphism by differential scanning calorimetry". *Thermochimica Acta* 234 (1994), pages 31–39. DOI: 10.1016/0040-6031(94)85133-6.

[75] C. Schick. "Differential scanning calorimetry (DSC) of semicrystalline polymers". *Analytical and Bioanalytical Chemistry* 395.6 (2009), pages 1589–1611. DOI: 10.1007/s00216-009-3169-y.

[76] NC Parasnis and K Ramani. "Non-isothermal crystallization of UHMWPE". *Journal of Thermal analysis and Calorimetry* 55.3 (1999), pages 709–719.

[77] Peng Zou, Shangwen Tang, Zizheng Fu, and Hanguo Xiong. "Isothermal and non-isothermal crystallization kinetics of modified rape straw flour/high-density polyethylene composites". *International Journal of Thermal Sciences* 48.4 (2009), pages 837–846. DOI: 10.1016/j.ijthermalsci.2008.06.010.

[78] Toshio Mura. "General theory of eigenstrains". In: *Micromechanics of defects in solids*. Springer, 1987, pages 1–73.

[79] EW Fischer. "Small angle x-ray scattering studies of phase transitions in polymeric and oligomeric systems". *Pure and Applied Chemistry* 26.3-4 (1971), pages 385–422.

[80] Benjamin Chu and Benjamin S Hsiao. "Small-angle X-ray scattering of polymers". *Chemical reviews* 101.6 (2001), pages 1727–1762.

[81] E. N. Brown, P. J. Rae, D. M. Dattelbaum, B. Clausen, and D. W. Brown. "In-situ Measurement of Crystalline Lattice Strains in Polytetrafluoroethylene". *Experimental Mechanics* 48.1 (2008), pages 119–131. DOI: 10.1007/s11340-007-9075-3.

[82] James L. White and Joseph E. Spruiell. "The specification of orientation and its development in polymer processing". *Polymer Engineering and Science* 23.5 (1983), pages 247–256. DOI: 10.1002/pen.760230503.

[83] PH Hermans and P Platzek. "Contribution to elucidate the deformation mechanism and the fine structure of hydrate cellulose. IX.: On the theoretical relation between swelling anisotropy and the inherent birefringence of oriented fibers". *Kolloid Z* 88 (1939), pages 68–72.

[84] J. J. Hermans, P. H. Hermans, D. Vermaas, and A. Weidinger. "Quantitative evaluation of orientation in cellulose fibres from the X-ray fibre diagram". *Recueil des Travaux Chimiques des Pays-Bas* 65.6 (1945), pages 427–447. DOI: 10.1002/recl.19460650605.

[85] Zigmond W. Wilchinsky. "Determination of orientation of the crystalline and amorphous phases in polyethylene by X-ray diffraction". *Journal of Polymer Science Part A-2: Polymer Physics* 6.1 (1968), pages 281–288. DOI: 10.1002/pol.1968.160060118.

[86] W. F. Maddams and J. E. Preedy. “X-ray diffraction orientation studies on blown polyethylene films. I. Preliminary measurements”. *Journal of Applied Polymer Science* 22.10 (1978), pages 2721–2737. DOI: 10.1002/app.1978.070221001.

[87] Jianjun Lu and Hung-Jue Sue. “Characterization of Crystalline Texture of LLDPE Blown Films Using X-ray Pole Figures”. *Macromolecules* 34.6 (2001), pages 2015–2017. DOI: 10.1021/ma001031h.

[88] Nada Bou Malhab. “Microinjection Moulding of semi-crystalline polymers”. Theses. Arts et Métiers ParisTech, 2012.

[89] Zigmond W. Wilchinsky. “On Crystal Orientation in Polycrystalline Materials”. *Journal of Applied Physics* 30.5 (1959), pages 792–792. DOI: 10.1063/1.1735235.

[90] R. A. Sack. “Indirect evaluation of orientation in polycrystalline materials”. *Journal of Polymer Science* 54.160 (1961), pages 543–560. DOI: 10.1002/pol.1961.1205416018.

[91] James L. White and Joseph E. Spruiell. “Specification of biaxial orientation in amorphous and crystalline polymers”. *Polymer Engineering and Science* 21.13 (1981), pages 859–868. DOI: 10.1002/pen.760211309.

[92] Zigmond W. Wilchinsky. “Measurement of Orientation in Polypropylene Film”. *Journal of Applied Physics* 31.11 (1960), pages 1969–1972. DOI: 10.1063/1.1735481.

[93] Zigmond W. Wilchinsky. “Orientation in cold-rolled polypropylene”. *Journal of Applied Polymer Science* 7.3 (1963), pages 923–933. DOI: 10.1002/app.1963.070070311.

[94] YD Wang and Mukerrem Cakmak. “Spatial variation of structural hierarchy in injection molded PVDF and blends of PVDF with PMMA. Part II. Application of microbeam WAXS pole figure and SAXS techniques”. *Polymer* 42.9 (2001), pages 4233–4251.

[95] Geun Hyung Kim, Chang-Kwon Kang, Cheol Gyu Chang, and Dae Woo Ihm. “Molecular orientation angle of biaxially stretched poly(ethylene terephthalate) films”. *European Polymer Journal* 33.10-12 (1997), pages 1633–1638. DOI: 10.1016/S0014-3057(97)00053-0.

[96] Shunji Nomura, Hiromichi Kawai, Itsuro Kimura, and Mitsuyasu Kagiyama. “General description of orientation factors in terms of expansion of orientation distribution function in a series of spherical harmonics”. *Journal of Polymer Science Part A-2: Polymer Physics* 8.3 (1970), pages 383–400. DOI: 10.1002/pol.1970.160080305.

[97] Li, Michel H. J. Koch, and Wim H. de Jeu. “Crystalline Structure and Morphology in Nylon-12: A Small- and Wide-Angle X-ray Scattering Study”. *Macromolecules* 36.5 (2003), pages 1626–1632. DOI: 10.1021/ma0257321.

[98] L Salvo, P Cloetens, E Maire, S Zabler, J.J Blandin, J.Y Buffière, W Ludwig, E Boller, D Bellet, and C Josserond. “X-ray micro-tomography an attractive characterisation technique in materials science”. *Nuclear Instruments and Methods in Physics Research Section B: Beam Interactions with Materials and Atoms* 200 (2003), pages 273–286. DOI: 10.1016/S0168-583X(02)01689-0.

[99] J.H. Butler, D.C. Joy, G.F. Bradley, and S.J. Krause. “Low-voltage scanning electron microscopy of polymers”. *Polymer* 36.9 (1995), pages 1781–1790. DOI: 10.1016/0032-3861(95)90924-Q.

[100] C. W. Bunn, A. J. Cobbold, and R. P. Palmer. "The fine structure of polytetrafluoroethylene". *Journal of Polymer Science* 28.117 (1958), pages 365–376. DOI: 10.1002/pol.1958.1202811712.

[101] Kevin P. Menard and Noah Menard. "Dynamic Mechanical Analysis". In: *Encyclopedia of Analytical Chemistry*. Edited by Robert A. Meyers. Chichester, UK: John Wiley & Sons, Ltd, 2017, pages 1–25. DOI: 10.1002/9780470027318.a2007.pub3.

[102] John D Ferry. *Viscoelastic properties of polymers*. John Wiley & Sons, 1980.

[103] Mogon Patel. "Viscoelastic properties of polystyrene using dynamic rheometry". *Polymer Testing* 23.1 (2004), pages 107–112. DOI: 10.1016/S0142-9418(03)00068-0.

[104] TC Chu, WF Ranson, and Mr A Sutton. "Applications of digital-image-correlation techniques to experimental mechanics". *Experimental mechanics* 25.3 (1985), pages 232–244.

[105] G. Besnard, F. Hild, and S. Roux. ""Finite-Element" Displacement Fields Analysis from Digital Images: Application to Portevin–Le Châtelier Bands". *Experimental Mechanics* 46.6 (2006), pages 789–803. DOI: 10.1007/s11340-006-9824-8.

[106] Zvonimir Tomičevć, François Hild, and Stéphane Roux. "Mechanics-aided digital image correlation". *The Journal of Strain Analysis for Engineering Design* 48.5 (2013), pages 330–343. DOI: 10.1177/0309324713482457.

[107] Arturo Mendoza, Julien Schneider, Estelle Parra, Enrico Obert, and Stéphane Roux. "Differentiating 3D textile composites: A novel field of application for Digital Volume Correlation". *Composite Structures* 208 (2019), pages 735–743. DOI: 10.1016/j.compstruct.2018.10.008.

[108] G Gaussorgues. *Infrared thermography (trans Chomet S)*. Chapman and Hall, London, 1994.

[109] Y. Marco, V. Le Saux, L. Jégou, A. Launay, L. Serrano, I. Raoult, and S. Calloch. "Dissipation analysis in SFRP structural samples: Thermomechanical analysis and comparison to numerical simulations". *International Journal of Fatigue* 67 (2014), pages 142–150. DOI: 10.1016/j.ijfatigue.2014.02.004.

[110] V. Le Saux and C. Doudard. "Proposition of a compensated pixelwise calibration for photonic infrared cameras and comparison to classic calibration procedures: Case of thermoelastic stress analysis". *Infrared Physics & Technology* 80 (2017), pages 83–92. DOI: 10.1016/j.infrared.2016.11.008.

[111] Gabriel Guenoun, Jean-Yvon Faou, Gilles Régnier, Nicolas Schmitt, and Stéphane Roux. "Thermal cycling of cold-pressed PTFE compacts: Reversible and irreversible behavior". *Polymer Testing* (2019). DOI: 10.1016/j.polymertesting.2019.01.018.

[112] Ian M Ward. *Structure and properties of oriented polymers*. Springer Science & Business Media, 2012.

[113] F. Li and V.M. Puri. "Measurement of anisotropic behavior of dry cohesive and cohesionless powders using a cubical triaxial tester". *Powder Technology* 89.3 (1996), pages 197–207. DOI: 10.1016/S0032-5910(96)03184-1.

[114] Steve Galen and Antonios Zavaliangos. "Strength anisotropy in cold compacted ductile and brittle powders". *Acta Materialia* 53.18 (2005), pages 4801–4815. DOI: 10.1016/j.actamat.2005.06.023.

[115] S. Nemat-Nasser and M. Hori. *Micromechanics: overall properties of heterogeneous materials*. North-Holland series in applied mathematics and mechanics v. 37. Amsterdam ; New York: North-Holland, 1993.

[116] JM Calo and PJ Hall. "The application of small angle scattering techniques to porosity characterization in carbons". *Carbon* 42.7 (2004), pages 1299–1304.

[117] H.-J. Radusch. "Analysis of reversible melting in polytetrafluoroethylene". *Journal of Thermal Analysis and Calorimetry* 79.3 (2005), pages 615–621. DOI: 10.1007/s10973-005-0586-9.

[118] A Greco and A Maffezzoli. "Polymer melting and polymer powder sintering by thermal analysis". *Journal of thermal analysis and calorimetry* 72.3 (2003), pages 1167–1174.

[119] R.J. Lehnert, P.J. Hendra, N. Everall, and N.J. Clayden. "Comparative quantitative study on the crystallinity of poly(tetrafluoroethylene) including Raman, infra-red and 19F nuclear magnetic resonance spectroscopy". *Polymer* 38.7 (1997), pages 1521–1535. DOI: 10.1016/S0032-3861(96)00684-2.

[120] Jean Lemaitre, Jean-Louis Chaboche, and Paul Germain. *Mécanique des matériaux solides*. Volume 2. Dunod Paris, 1985.

[121] Séverine Humbert, Olivier Lame, Roland Séguéla, and Gérard Vigier. "A re-examination of the elastic modulus dependence on crystallinity in semi-crystalline polymers". *Polymer* 52.21 (2011), pages 4899–4909. DOI: 10.1016/j.polymer.2011.07.060.

[122] Martin Poncelet, Jean-François Witz, Hervé Pron, and Bertand Wattrisse. "A study of IRFPA camera measurement errors: radiometric artefacts". *Quantitative InfraRed Thermography Journal* 8.1 (2011), pages 3–20.

université PARIS-SACLAY

ÉCOLE DOCTORALE
Sciences mécaniques et énergétiques, matériaux et géosciences (SMEMAG)

Titre : Frittage de pièces de Polytétrafluoroéthylène (PTFE) compacté: Mécanismes physiques et modèles

Mots clés : Science des polymères, Thermomécanique, Procédé, Modélisation, Cristallisation

Résumé : Le polytétrafluoroéthylène (PTFE) est un polymère semi-cristallin ayant de nombreuses propriétés remarquables avec notamment une excellente tenue thermique, un coefficient de frottement extrêmement faible et une grande résistance à la corrosion. Ces atouts lui valent d'être utilisé dans de nombreuses applications.
Sa mise en forme s'effectue par des procédés similaires à ceux utilisés pour les poudres métalliques. Dans l'un d'eux, la poudre de PTFE est compactée uniaxialement en pièces cylindriques. L'étape suivante est le frittage de la poudre compactée, au cours de laquelle les pièces sont chauffées au-delà de la température de fusion du polymère. Durant ce cycle thermique, les pièces subissent de grandes déformations causées notamment par la fusion et la recristallisation du PTFE. Les gradients thermiques couplés à ces déformations peuvent engendrer des incompatibilités mécaniques pouvant conduire à l'endommagement, voire à la rupture des pièces.
Cette thèse a permis d'apporter une compréhension plus fine des phénomènes physiques à l'œuvre durant le frittage du PTFE compacté par des observations et analyses microstructurales, et des essais de caractérisation thermique et mécanique. La relaxation de contraintes résiduelles, la fermeture de porosités et un phénomène de cristallisation secondaire ont ainsi été mis en évidence et génèrent des déformations libres de contraintes macroscopiques. Les propriétés mécaniques du matériau en température ont également été déterminées lors du frittage. Un modèle a été développé pour rendre compte de ces observations. Il a été intégré dans une simulation thermomécanique du procédé de frittage d'une pièce de référence. Le modèle a été validé par comparaison des résultats de la simulation à des mesures réalisées sur des expériences de laboratoire.
Enfin, un outil de simulation numérique par éléments finis a été développé. Il permet de déterminer les états de contrainte et déformation ainsi que la répartition des taux de cristallisation et des propriétés thermomécaniques au sein d'une pièce de PTFE compacté durant le cycle de frittage. A terme, cet outil pourrait permettre d'optimiser les paramètres du procédé industriel pour, par exemple, réduire le temps de frittage tout en s'assurant d'avoir des pièces non-endommagées et possédant les propriétés requises.

Title: PTFE compacts sintering: Physical mechanisms and models

Keywords: Polymer science, Thermomechanics, Process, Modeling, Crystallization

Abstract: Polytetrafluoroethylene (PTFE) is a semi-crystalline polymer with many outstanding properties including excellent thermal resistance, extremely low friction coefficient and high corrosion resistance. These advantages make it suitable for many applications.
It is shaped by processes similar to those used for metal powders. In one of them, the PTFE powder is uniaxially compacted into cylindrical parts. The next step is the compacted powder sintering process, in which the parts are heated above the melting temperature of the polymer. During this thermal cycle, the parts undergo large strains caused by the melting and the recrystallization of PTFE. Thermal gradients coupled with these strains induce mechanical incompatibilities that can lead to damage or even failure of the parts.
This study provides a more detailed understanding of the physical mechanisms at work during the sintering of compacted PTFE through microstructural observations and analyses, and thermal and mechanical characterization tests. The relaxation of residual stresses, the closure of porosity and a secondary crystallization mechanism have thus been highlighted and generate macroscopic stress-free strain (called *eigenstrain*). The mechanical properties of the material as function of temperature have been also determined during sintering. A model has been developed to take into account these observations. It has been integrated into a thermomechanical simulation of the sintering process of a reference part. The model has been validated by comparing the simulation results with measurements from a laboratory experiments.
Finally, a finite element numerical simulation tool has been developed. It is used to determine the stresses and strains as well as the distribution of crystallization rates and thermomechanical properties within a PTFE part compacted during the sintering cycle. In the long term, this tool could make it possible to optimize the industrial process parameters to reduce sintering time, for example, while ensuring that the parts are undamaged and have the required properties.

Université Paris–Saclay
Espace Technologique / Immeuble Discovery
Route de l'Orme aux Merisiers RD 128 / 91190 Saint-Aubin, France